UC Irvine
UC Irvine Electronic Theses and Dissertations

Title

Probing Single Molecule Chemistry with a Femtosecond Laser Scanning Tunneling Microscope

Permalink
https://escholarship.org/uc/item/44r5g2bn

Author

Li, Shaowei

Publication Date

2017

Copyright Information
This work is made available under the terms of a Creative Commons Attribution-ShareAlike License, availalbe at https://creativecommons.org/licenses/by-sa/4.0/

Peer reviewed|Thesis/dissertation

eScholarship.org Powered by the California Digital Library
University of California

UNIVERSITY OF CALIFORNIA,
IRVINE

Probing Single Molecule Chemistry with a Femtosecond Laser Scanning Tunneling Microscope

THESIS

submitted in partial satisfaction of the requirements
for the degree of

DOCTOR OF PHILOSOPHY

in Physics

by

Shaowei Li

Dissertation Committee:
Professor Wilson Ho, Chair
Professor Steven R. White
Professor Jing Xia

2017

Portion of Chapter 2 © 2013 American Physical Society
Portion of Chapter 3 © 2015 American Physical Society
All other materials © 2017 Shaowei Li

DEDICATION

To

my family

TABLE OF CONTENTS

Page

LIST OF FIGURES AND TABLES vii

ACKNOWLEDGMENTS ix

CURRICULUM VITAE xi

ABSTRACT OF THE DISSERTATION xv

CHAPTER 1: Introduction 1

1.1 Background and Overview 1

1.2 Principles of STM Techniques 7

1.3 Basic Optical Techniques 14

1.4 Optical Set-up of a Femtosecond Laser STM 21

1.5 Summary of Contents 24

Bibliography 28

CHAPTER 2: Rotational and Vibrational Excitations of a Hydrogen Molecule Trapped within a Nanocavity of Tunable Dimension 31

Abstract 31

2.1 Introduction 32

2.2 Methods 34

2.3 Results and Discussion 35

2.4 Conclusions 44

Bibliography 47

CHAPTER 3: Rotational Spectromicroscopy: Imaging the Orbital Interaction between Molecular Hydrogen and an Adsorbed Molecule 49

Abstract 49

3.1 Introduction 50

3.2 Methods 51

3.3 Results and Discussion 52

3.4 Conclusions 70

Bibliography 78

CHAPTER 4: Single Molecule Mechanochemistry 81

Abstract 81

4.1 Introduction 82

4.2 Methods 83

4.3 Results and Discussion 84

4.4 Conclusions 90

Bibliography 94

CHAPTER 5: Sub-molecular Control of Photo-assisted Activation of a Single C-H Bond 97

Abstract 97

5.1 Introduction 98

5.2 Methods 99

5.3 Results and Discussion 101

5.4 Conclusions 114

Bibliography 115

CHAPTER 6: Probing Coherent Vibration Mediated Structural Transitions of Single Molecules with Space-time Resolution 117

Abstract 117

6.1 Introduction 118

6.2 Methods 122

6.3 Results and Discussion 125

6.4 Conclusions 144

Bibliography 145

CHAPTER 7: Real-space Observation of Nanoelectrical Band Bending and Flattening at a Single Molecule Interface 149

Abstract 149

7.1 Introduction 150

7.2 Methods 151

7.3 Results and Discussion 154

7.4 Conclusions 163

Bibliography 164

CHAPTER 8: Summary and Prospects 167

8.1 Concluding Remarks 167

8.2 Related Research: Hydrogen Rotational Spectroscopy and Microscopy 167

8.3 Related Research: Tunneling Electron Induced Luminescence 170

8.4 Prospects for Future Research 172

Bibliography 176

Appendix A: Hardware Instrumentation 177

Appendix B: Software Development 231

LIST OF FIGURES AND TABLES

Page

FIG. 1.1 Schematic diagrams of NSOM and photo-assisted tunneling. 4

FIG. 1.2 Schematic diagrams of STM-IETS. 11

FIG. 1.3 Kerr-lens mode-locking. 15

FIG. 1.4 Interferometric autocorrelation. 19

FIG. 1.5 Schematic diagram of the femtosecond laser set up. 22

FIG. 2.1 A hydrogen molecule trapped in the tunneling junction of STM. 36

FIG. 2.2 Tunneling spectra taken before and after dosing molecular hydrogen or its isotopes. 39

FIG. 2.3 IETS at different tip-substrate separations. 42

FIG. 2.4 DFT calculations. 45

FIG. 3.1 Reversible electron transfer to a single MgP molecule interacting with H_2 in a double barrier tunnel junction of the STM. 53

FIG. 3.2 Rotational spectra of single H_2 molecule interacting locally with Mg-porphyrin measured by STM-IETS. 56

FIG. 3.3 Single molecule rotational imaging. 58

FIG. 3.4 MgP over NiAl surface. 61

FIG. 3.5 IETS measurements of trapped H_2 at different tip-substrate separations. 65

FIG. 3.6 Calculated partial density of states under different conditions. 68

FIG. 3.7 Spectral shifts over an Au adatom. 71

FIG. 4.1 H_2 adsorption on a Cu(001). 85

FIG. 4.2 Hydrogen dissociation induced by voltage pulses. 88

FIG. 4.3 Hydrogen dissociation induced by mechanical pulses. 91

FIG. 5.1 Bond-selected dissociation of single azulene molecules using energetic tunneling electrons. 102

FIG. 5.2 High-resolution structural images of azulene and its dissociation products. 105

FIG. 5.3 C-H activation induced by photo-assisted tunneling electron. 109

FIG. 5.4 C-H bond activation barrier and azulene electronic structure. 112

FIG. 6.1 Combining femtosecond laser and STM to probe single molecule dynamics. 126

FIG. 6.2 Laser induced conformational change of pyrrolidine on a Cu(001). 128

FIG. 6.3 Femtosecond laser driven coherent oscillations in structural transition of a pyrrolidine monomer on Cu(001). 131

FIG. 6.4 DFT Calculations of low energy vibrations. 135

FIG. 6.5 Topographic images of pyrrolidine dimers with different intermolecular separations. 138

FIG. 6.6 Femtosecond laser driven coherent oscillations in structural transformation of a pyrrolidine dimer on Cu(001). 140

FIG. 6.7 Delay scans and topographic images of three different dimers compared to a monomer. 142

FIG. 7.1 Topographic images of C_{60} molecules over a Si(111) surface. 152

FIG. 7.2 LDOS of a C_{60} molecule and a Si vacancy measured at 80 K. 155

FIG. 7.3 Schematic diagrams of the band bending and laser induced band flattening. 158

FIG. 7.4 LDOS of a C_{60} molecule and a Si vacancy measured at 90 K. 161

TABLE 3.1 DFT results of H_2 adsorption energies at different positions over MgP. 74

ACKNOWLEDGMENTS

I would like to express the deepest appreciation to my advisor, Professor Wilson Ho, who provides me the guidance and financial support to pursue the research presented in this thesis. During these seven years, he has shown me how to conduct research at the frontiers of science and technology. I am especially grateful for being given both academic freedom and scientific instructions and have benefited greatly from his passion for science and extremely high standard of excellence.

I thank Professor Steven White and Professor Jing Xia for serving on my dissertation committee, and Professor Ruqian Wu and Professor Nien-Hui Ge on my advancement committee.

Special thanks to the group members who run experiments with me: Arthur Yu, for his dedication to almost every project presented in this thesis; Dr. Freddy Toledo and Dr. Zhumin Han, for their support in revealing the rotational mode of a single molecule; Greg Czap, for his help in visualizing the intermolecular interaction and photo-activation of azulene; Siyu Chen and Likun Wang, for their contributions to the visualization of coherent structural transition of pyrrolidine.

I would also like to thank my collaborators in Professor Ruqian Wu's group: Dr. Hui Wang, Dr. Haiyan He, and Dr. Dingwang Yuan for the theoretical calculations which provide deep insight into our experimental observations.

During my time in Ho group, I have always been enjoying working with other members: Dr. Qing Huan, Dr. Ying Jiang, Dr. Ungdon Ham and Dr. Chilun Jiang who guided me how to operate the apparatus during my first two years; Dr. Hikari Kimura, Dr. Weicai Cao and Calvin Patel, for their valuable help in operating the laser systems; Dr. Haigang Zhang, Dr. Chen Xu and

HanKyu Lee for their efforts in the instrumentation projects; Jiang Yao, Peter Wagner, Christian Kim for their help and friendship. It is a pleasure to work with all of you in Ho group.

Finally, I would like to thank National Science Foundation Center for Chemical Innovation on Chemistry at the Space-Time Limit (CaSTL) under Grant No. CHE-1414466 and Chemical Science, Geo- and Bioscience Division, Office of Science, U.S. Department of Energy, under Grant No. DE-FG02-04ER15595 for the funding support in carrying out this research.

CURRICULUM VITAE

Shaowei Li

4129 Frederick Reines Hall, **shaoweil@uci.edu**
University of California, Irvine, CA, 92697 **(+1)949-326-8882**

Education

Ph.D in Physics, Department of Physics and Astronomy, UC Irvine (08/2017)
Thesis Title: Probing Single Molecule Chemistry with a Femtosecond Laser Scanning Tunneling Microscope
Thesis Advisor: Wilson Ho
M.S. in Physics, Department of Physics and Astronomy, UC Irvine (12/2015)
Thesis Title: Single Molecule Rotational Inelastic Tunneling Spectroscopy and Microscopy
Thesis Advisor: Wilson Ho
B.S. in Physics (Honors), Department of Physics, Nankai University (06/2010)
Thesis Title: Novel Photon Collection System for a Scanning Tunneling Microscope
Thesis Advisor: Xinghua Lu

Research

- **Wilson Ho Group, University of California, Irvine (07/2010 -08/2017)**

1. **Bond-selected Single Molecule Photochemistry**
   Demonstrated the coupling of photon and tunneling electron at the junction of a scanning tunneling microscope. Visualized the bond-selected and photo-assisted dissociation of single chemical bonds.
2. **Ultrafast Spectroscopy with Sub-Ångström Resolution**
   Probed the ultrafast dynamics of a single molecule using a home-made scanning tunneling microscope combined with a Ti-sapphire femtosecond laser. Demonstrated the single molecule coherence chemistry with simultaneous sub-Ångström spatial resolution and femtosecond temporal resolution.
3. **Single Molecule Rotational Spectroscopy and Microscopy**
   Detected the rotational excitation of single molecules through inelastic electron tunneling spectroscopy and further utilized the rotational motion of a molecule as a force sensor to probe the intermolecular interactions.
4. **Tunneling Electron Induced Luminescence of Single Molecules**
   Studied the emitted photons from a single molecule or metallic nanoparticle excited by tunneling electrons. Visualized the plasmon-electron-orbital coupling in the STM induced photon emission processes using the spatially resolved tunneling electron induced luminescence spectroscopy and microscopy.
5. **Single Molecule Mechanochemistry**
   Observed the mechanical motion induced bond dissociation of a single molecule. Inspected the catalytic effects of single molecule catalysts on the mechanochemical reactions.
6. **Ultra-High Vacuum Related Instrumentation**
   Designed and constructed multiple UHV apparatus including K-cell molecular evaporator, water-cooled molecule/metal evaporator, doser interlock system and portable leak detector.

7. **Software Development**

   Developed a LabVIEW based software that controls the laser and photon detector while communicating with the STM. Upgraded and optimized a C based STM control program.

8. **Helium Recycling**

   Involved in the fabrication of the Ho group home-built Helium recovery and liquefaction system. Constructed two liquefier cold-heads and designed a helium gas purifier.

- **Xinghua Lu Group, Institute of Physics, Chinese Academy of Sciences (07/2009 -07/2010)**

  Designed and fabricated a conical mirror based photon collection system for a scanning tunneling microscope.

Lab Skills

Ultra-high Vacuum: Scanning Tunneling Microscopy and Spectroscopy, Inelastic Tunneling Spectroscopy, Molecular Evaporation and Manipulation, Vacuum Pumps.
Cryogenic: He-4 Continuous Flow Cryostat, He-3 milli-Kelvin Cryostat, GM Cryocooler
Programming, Data Acquisition and Analysis: C, C#, Java, LabVIEW, Mathematica, OriginLab
Lasers and Optics: Pump-probe Spectroscopy, Raman Spectroscopy, Absorption Spectroscopy, Femtosecond Lasers, Kerr-lens Modelocking, Interferometer, Pulse Shaping, Harmonic Generation, CCD-Monochromator.
Design and Instrumentation: Solidworks, Autodesk Inventor
Machining: Mills, Lathes, Grinders, Torches, Band Saws, etc.

Publications

1. **Shaowei Li**, Arthur Yu, Freddy Toledo, Zhumin Han, Hui Wang, H. Y. He, Ruqian Wu, and W. Ho, "Rotational and Vibrational Excitations of a Hydrogen Molecule Trapped within a Nanocavity of Tunable Dimension", **Phys. Rev. Lett.** 111, 146102 (2013)
2. **Shaowei Li**, Dingwang Yuan, Arthur Yu, Gregory Czap, Ruqian Wu, W. Ho, "Rotational Spectromicroscopy: Imaging the Orbital Interaction Between Molecular Hydrogen and an Adsorbed Molecule", **Phys. Rev. Lett.** 114, 206101 (2015)
3. Arthur Yu, **Shaowei Li**, Gregory Czap, and W. Ho, "Single-Molecule Rotational and Vibrational Spectroscopy and Microscopy with the Scanning Tunneling Microscope", **J. Phys. Chem. C.** 119, 14737-14741, (2015)
4. Hui Wang*, **Shaowei Li**, H. Y. He*, Arthur Yu, Freddy Toledo, Zhumin Han, W. Ho, and Ruqian Wu, "The Trapping and Characterization of a Single Hydrogen Molecule in a Continuously Tunable Nanocavity", **J. Phys. Chem. Lett.** 6, 3453-3457 (2015)
5. Arthur Yu, **Shaowei Li**, B. Dhital, H. P. Lu, W. Ho, "Tunneling Electron Induced Charging and Light Emission of Single Panhematin Molecules", **J. Phys. Chem. C** 120, 21099-21103 (2016)
6. Arthur Yu*, **Shaowei Li***, Gregory Czap, and W. Ho, "Tunneling Electron Induced Light Emission from Single Gold Nanoclusters" **Nano Lett.** 16, 5433-5436 (2016)

7. Shaowei Li, Siyu Chen, Jie Li, Ruqian Wu, and W. Ho, "Joint Space-Time Coherent Vibration Driven Structural Transition in a Single Molecule" ***submitted to Phys. Rev. Lett.***
8. Arthur Yu*, **Shaowei Li***, and W. Ho, "Visualization of Nano-Plasmonic Coupling to Molecular Orbital in Light Emission Induced by Tunneling Electrons" ***submitted to Phys. Rev. Lett.***
9. Shaowei Li. Gregory Czap, Hui Wang, Arthur Yu, Siyu Chen, Ruqian Wu, and W. Ho, "Bond-selected Photo-assisted Activation of a single C-H bond" in preparation
10. Shaowei Li, Yanxing Zhang, Arthur Yu, Dingwang Yuan, Gregory Czap, Hikari Kimura, Ruqian Wu, and W. Ho, "Single Molecule Mechanochemistry" in preparation
11. Shaowei Li, Arthur Yu, W. Ho, "Real-space Observation of Nanoelectrical Band Bending and Flattening at a Single Molecule Interface" in preparation

* Equal Contribution

Patents

- **Shaowei Li**, Microwave Laundry Dryer, China National Practical New-type Patent, 200920053803.8
- Xinghua Lu, **Shaowei Li**, Shichao Yan, Xiaodong Guo, Nan Xie, Light Collection System for a Scanning Tunneling Microscope, China National Invention Patent, 201010160542.7

Talks

- **Physical Electronic Conference** at Portland (06/2017)
  Nottingham Prize Contestant's Talk: Single Molecule Photochemistry with a Femtosecond Scanning Tunneling Microscope
- **APS March Meeting** at New Orleans (03/2017)
  Contributed Talk: Single Molecule Coherence Chemistry with Time Resolved Scanning Tunneling Microscope
- **NSF CaSTL Center Newport Award Seminar**, UC Irvine, (05/2016)
  Award Talk: Visualization of Physical and Chemical Processes with Space-Time Resolution
- **Surface Physics Lecture Series**, Institute of Physics, Chinese Academy of Sciences, (12/2014)
  Invited Talk: Rotational Spectromicroscopy with Scanning Tunneling Microscope
- **Physics Today Seminars**, School of Physics, Nankai University, (12/2014)
  Invited Talk: Visualization of Quantum Mechanics
- **ICN+T 2014 International Conference on Nanoscience** at Vail (07/2013)
  Contributed Talk: Controlling Hydrogen Dissociation by the Scanning Tunneling Microscope
  Contributed Talk: Visualization of the Intermolecular Hybridization from Hydrogen Rotation
- **AVS 60th International Symposium and Exhibition** at Long Beach (10/2013)
  Contributed Talk: Real-space Spectroscopy and Microscopy of Tunneling Electron Induced Light Emission from Single Gold Nanoparticle

- **APS March Meeting** at Baltimore (03/2013)
  Contributed Talk: Rotational Spectroscopy at Sub-Ångström Level: Rotational and Vibrational Excitations of Molecular Hydrogen Measured by the Scanning Tunneling Microscope
- **APS California Section Annual Meeting** at San Luis Obispo (10/2012)
  Contributed Talk: Real Space Rotational Spectroscopy: Measurement of the Rotational Excitation of a Single Molecule by the Scanning Tunneling Microscope

---

Honors

- **DCP New Investigator Travel Award**, APS Division of Chemical Physics, (01/2017)
- **Newport Travel Award**, NSF CaSTL Center, UC Irvine, (05/2016)
- **Regents' Fellowship**, UC Irvine, (07/2010)
- **China's National Scholarship** (11/2009)
- **1s Class Outstanding Student Scholarship**, Nankai University (08/2008)

Languages

English, Mandarin Chinese, Cantonese

ABSTRACT OF THE DISSERTATION

Probing Single Molecule Chemistry with a Femtosecond Laser Scanning Tunneling Microscope

By

Shaowei Li

Doctor of Philosophy in Physics

University of California, Irvine, 2017

Professor Wilson Ho, Chair

The goal of the studies presented in this dissertation is to continuously expand the capability of a scanning tunneling microscope (STM) by improving its chemical sensitivity and temporal resolution. It has been demonstrated that the combination of STM with other techniques gains insight into the physical and chemical properties of single molecules. Single molecule rotational spectroscopy and microscopy is demonstrated using STM inelastic tunneling spectroscopy (IETS). We conduct real-space measurements of rotational transitions of gaseous hydrogen molecules physisorbed on surfaces at 10 K. The j=0 to j=2 rotational transition for para-H_2 and HD were observed by STM-IETS. It is also found that the rotational energy is very sensitive to its local environment, we could precisely investigate how the environmental coupling modifies the structure, including the bond length, of a single molecule with sub-Ångström resolution. Due to this high sensitivity, the spatial variation in the potential energy surface can be quantified by the rotational and vibrational energies of the trapped H_2. The ability of the tip to drag along a hydrogen molecule as it scans over another adsorbed molecule combined with the sensitivity of the hydrogen rotational excitation recorded by IETS to its immediate environment lead to the implementation

of rotational spectromicroscopy, which helps us reveal the intermolecular interaction and charge transfer between H_2 and a large molecule. Furthermore, we demonstrate that the H_2 in the STM junction can be dissociated by the mechanical motion of the STM tip. Hydrogen rotational spectroscopy and microscopy provides novels approach toward visualizing and quantifying the local potential energy surface as well as the potential landscape of chemical reactions.

Joint Ångström-femtosecond resolution is achieved by the combination of an STM with a femtosecond laser. We demonstrate the bond-selected, photo-assisted activation of a single C-H bond in an azulene molecule adsorbed on a Ag(110) surface. When the junction is illuminated by femtosecond laser, the electrons in the tip can be photo-excited into higher energy states and dissociate the molecule through a photo-assisted tunneling process. The photon-electron coupling at the junction enables the investigation of coherence molecular transformation with joint fs-Å resolution. We also show the band bending and laser induced band flattening at a molecule-semiconductor interface. More importantly, we observe the photo-induced, reversible conformational change between two structures for a single pyrrolidine molecule on a Cu(001) surface. The conductance changes of the STM junction associated with the structural transitions exhibits oscillates in time with periods corresponding to specific molecular vibrations. The vibrational frequencies and decay time are observed in real-space and real-time. Our laser-STM technique enables the investigation of inhomogeneous environmental effect on the molecular dynamics. We have found that the intermolecular interaction between two pyrrolidine molecules can increase the vibrational period while shortening its decay time. We anticipate that this novel technique would lead to a broad impact in physics and chemistry through direct visualization of coherently driven reactions resolved in space and time.

CHAPTER ONE

Introduction

1.1 Background and Overview

Since its invention, the unparalleled ultra-high spatial resolution makes the scanning tunneling microscope (STM) [1, 2] a powerful tool to investigate the physical and chemical phenomena on surfaces. Numerous efforts have been made to expand the capabilities of STM in addition to its atomic-scale spatial sensitivity. Advancements in instrumentations include the construction of cryogenic low temperature STM [3], He-3 sub-Kelvin STM [4], dilution fridge milli-kelvin STM [5] and closed-cycle cryogen-free STM [6]. Development of experimental methods includes the demonstrations of scanning tunneling microscopy (STS) [7] and inelastic tunneling spectroscopy (IETS) [8]. The combination of STM with other techniques such as strong magnetic field [4] and femtosecond laser [9] further widens the scope of STM studies. Despite the great achievements, the STM still have two major drawbacks: limited chemical sensitivity and poor temporal resolution. This dissertation describes experiments based on a few novel techniques that further expand the capabilities of STM towards overcoming these two obstacles.

One milestone in the evolution of STM is the first demonstration of STM-IETS by Stipe, Rezaei, and Ho [8]. IETS in molecular transport junctions had been extensively studied even before the invention of STM. The signal in early IETS measurements is generated by the excitation of ~10^9 molecules, without the ability to distinguish the signal from individual ones. The recent development of molecular break-junction techniques has produced junctions with a single molecule but is still not able to visualize the molecular conformation. The IETS performed with the STM combines the high spatial resolution of STM and the chemical sensitivity of IETS. It enables the visualization of molecular vibrations at sub-molecular level [10]. The key factors in the achievement of single molecule STM-IETS include the design and construction of an ultra-stable STM system as well as the application of lock-in technique to enhance the signal-noise ratio [11]. Since the first demonstration of vibrational STM-IETS, other inelastic excitations such as phonon [12] and spin flip [13] have soon been reported.

One of the aims of the studies described in this dissertation is to extend STM-IETS into additional systems to further enhance the chemical sensitivity of STM. Besides vibration and spin slip, another important category of inelastic excitations is the molecular rotation. Similar to the molecular vibration, the rotational states can also serve as "molecular fingerprints" [14]. However, the demonstration of single molecule rotational spectroscopy with STM-IETS has met with little success because of the experimental challenges of probing a gaseous molecule on surfaces. In this dissertation, we show experiments that demonstrate the rotational excitation of single hydrogen molecules on different surfaces. These experiments represent the first extension of STM-IETS to the detection of single molecule rotational transitions. Through these measurements, we realized that the rotational energy of a hydrogen molecule can be very sensitive to its local chemical environments. We thus utilize this sensitivity as a chemical probe to visualize the interaction between hydrogen and other large molecules. Moreover, the downshift of rotational energy of a hydrogen in an STM junction compared with free gas phase molecules indicates a weakened H-H bond by the interaction between hydrogen and the STM junction. We further demonstrate that the mechanical movements of the STM tip can break a H-H bond. This study serves as a model system of a mechanochemical process at the single molecule level.

Another focus in STM technology development is to increase the temporal sensitivity. The time resolution of a regular STM is limited by the response time of its feedback loop as well as the resonant frequency of the scanner. To date, the highest time resolution with STM alone is still on the order of 1 to 10 μs, which makes it difficult to probe the molecular dynamics and kinetics happen on the femtosecond to picosecond scales.

The development of femtosecond lasers has led to the rapid advancement of condensed matter studies in time domain [15]. These experiments typically use two time-correlated laser pulses with a variable time delay between them, named pump-probe technique. The temporal sensitivity of the pump-probe technique is mainly determined by the laser pulse width which can be as short as several attoseconds. Pump-probe techniques have also been applied to the studies of molecular dynamics at solid surfaces and interfaces. It reveals valuable information including coherent molecular vibration and electronic excitations [16]. As an optical technique, the biggest obstacle of pump-probe is the difficulty of achieving spatial sensitivity below the laser wavelength due to the diffraction limit. For a widely applied Ti-sapphire laser, the diffraction limit is around 400 nm.

Many approaches have been applied to combine scanning probe techniques with pump-probe with the hope to break the diffraction limit. One important improvement comes from the introduction of near-field scanning optical microscope (NSOM). NSOM techniques can be divided into two categories: aperture or aperture-less. In an aperture-based NSOM as shown in Fig. 1.1.A, a sub-wavelength aperture is placed in close proximity to the surface and used as an optical waveguide to introduce optical field to the objects to be scanned and imaged [17]. The spatial sensitivity is determined by the aperture diameter, typically from 10 nm to 100 nm. On the

FIG. 1.1. Schematic diagrams of NSOM and photo-assisted tunneling. (A) Aperture-based NSOM. (B) Aperture-less NSOM. (C) Photo-assisted tunneling. (D) Energy diagram of photo-assisted tunneling.

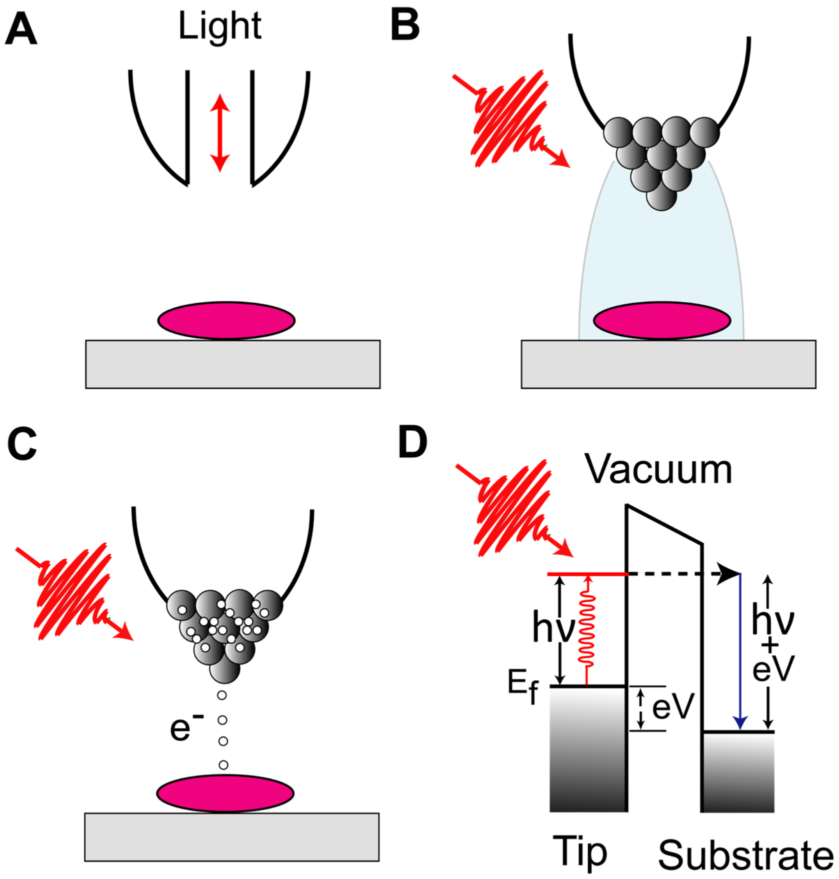
A
Light
B
C
e-
D
Vacuum
hν
Ef
eV
hν
+
eV
Tip
Substrate

contrary, an aperture-less NSOM takes use of the strongly confined electric field near the junction of a metal tip and surface by optically excited the junction plasmons near the tip apex as shown in Fig. 1.1.B [18]. Typical materials used for making tips include silver and gold which sustain strong plasma enhancement in the visible light range. The spatial resolution of an aperture-less NSOM is mainly determined by the radius of the enhanced field, which can reach a few tens nanometers or even a few nanometers with a very sharp tip. The STM can also be used as an aperture-less NSOM for optical measurements. An important application in this direction is the STM tip-enhanced Raman spectroscopy (TERS). Recent results from Dong's group even show that the internal features of an H_2TBPP molecule can be resolved in STM-TERS mappings [19]. However, the spatial resolution of techniques based on field enhancement effect depends heavily on the tip geometry. It is hard to reach atomic-level sensitivity due to the nanometer scale spatial extent of the enhanced filed.

The ultimate spatial-temporal resolution comes from the coupling of femtosecond laser pulses to the tunneling electrons (Fig. 1.1.C). Irradiation of the STM junction with femtosecond laser pulses can generate energetic photo-assisted tunneling electrons as shown by the energy diagram in Fig. 1.1.D. Wu and collaborators have demonstrated that the photo-assisted tunneling electrons can induce the reversible electron transfer into a MgP molecule over Al_2O_3 layers [20,21]. The coupling of the laser to the electron tunneling process combines the unique capabilities from both femtosecond laser and STM. It shatters the diffraction limited resolution in light-induced phenomena and reaches the atomic scale resolution of the STM.

The second aim of the research discussed in this dissertation is to achieve simultaneous spatial and temporal sensitivity by coupling of femtosecond laser pulses to the tunneling junction. Using an STM combined with a femtosecond laser, we investigate the photo induced physical and chemical phenomena at single molecule level and ultimately probe the coherence molecular dynamics with joint femtosecond-Ångström sensitivity. We demonstrate the band bending and photo induced band flattening of a p-type Si(111) surface, and show that the amplitude of the band bending can be modified by molecular doping. We also show that the photo-assisted tunneling electrons can selectively activate individual C-H bonds in an azulene molecule. Electron energy required to break the bond decreases by an amount equals to the laser photon energy under laser illumination, indicating that an electron can be coupled with one photon to induce the reaction. The C-H bond to be activated can be chosen by positioning the tip over the molecule with sub-Ångström resolution. The coupling of femtosecond laser pulses to the tunneling process enables the investigation of coherence chemistry with joint femtosecond-Ångström resolution. We have also observed the coherent vibration driven structural transition of single pyrrolidine molecules. The molecular dynamics, including vibrational frequency and lifetime, are determined to drive the coherent structural transition in the molecule. When two molecules are spatially close to each other, the intermolecular interactions lower the vibrational lifetime and downshift the vibration energy.

1.2 Principles of STM Techniques

The STM operates on tunneling effect between two conducting electrodes who are spatially close to each other. Various of scanner designs have been used by researchers for different purposes. The experiments described in this dissertation are all performed using microscopes adapted in design from the one originally reported by Stipe, Rezaei, and Ho [11]. Several techniques are used to conduct spectroscopic or microscopic measurements.

1.2.1 Topographic Imaging

When the distance between the STM tip and the metal substrate is within a few Ångström and a bias voltage is applied across the junction, a tunneling current can be detected. Within Bardeen's formalism using first order time-dependent perturbation theory [22,23], the tunneling current can be expressed as

$$I = \frac{4\pi e}{\hbar}\int_{-\infty}^{+\infty}[f(E_F - eV + \varepsilon) - f(E_F + \varepsilon)] \times \rho_t(E_F - eV + \varepsilon)\rho_s(E_F + \varepsilon)|M_{st}|^2\, d\varepsilon \qquad (1.1)$$

where *f(E)* is the Fermi-Dirac distribution; ρ_s and ρ_t correspond to the density of states of sample and tip respectively; M_{st} is the tunneling matrix element between the wave-functions of the tip and the sample. For one-dimensional tunneling junction, the tunneling matrix element can be written as a particularly simple form:

$$M_{st} = \frac{\hbar^2}{2m}\int_{L_{st}}(\varphi\frac{\partial\chi^*}{\partial z} - \chi^*\frac{\partial\varphi}{\partial z})dz \qquad (1.2)$$

where φ and χ denote the wave-function of sample and tip respectively, m is the electron mass, and L_{st} denotes the tunneling gap. If we assume the tunneling barrier is a square barrier, with WKB approximation, $|M_{st}|^2$ and be further written as

$$|M_{st}|^2 = e^{-2z\sqrt{2m\Phi}} \qquad (1.3)$$

where z is the distance between tip and sample surface, and Φ is the effective barrier height of the tunneling junction. Therefore, at a fixed sample bias, the tunneling current changes exponentially with the tip-surface gap.

$$I \propto e^{-2z\sqrt{2m\Phi}} \qquad (1.4)$$

Thus, the tunneling current is very sensitive to the z. A change of z by one Ångström will lead to a change in tunneling current by one order. In the experiments described in this dissertation, bias is applied to the sample with the tip as a virtual ground. The STM control electronics use an analog feedback circuit which can maintain a constant value of tunneling current by adjusting z. In a constant-current topographic imaging, we record the z while scanning the tip back and forth across the sample with feedback on. In a constant-height topographic image, the feedback is turned off and we record the current over the scanned area. We prefer constant-current imaging over constant-height, especially over a heavily corrugated surface. In many cases, the topographic images can be intuitively interpreted as the geometric arrangement of the surface. However, features in topographic images are also strongly related to the electronic and vibrational properties of the substrates.

1.2.2 Scanning Tunneling Spectroscopy

Based on Equation 1.1, the tunneling current is strongly related with the density state of the tip and substrate. The common materials used for STM tips including silver and tungsten have a flat density of state near Fermi level. At the low-temperature limit, Fermi distribution can be approximated as a step function. Tersoff and Hamann have shown [22,23] that the tunneling current can be further expressed as

$$I = \frac{4\pi e}{\hbar} \rho_t(E_F) e^{-2z\sqrt{2m\Phi}} \int_0^{eV} \rho_s(E_F + \varepsilon)\, d\varepsilon \qquad (1.5).$$

Therefore, *dI/dV* is proportional to the local density of states (LDOS) of the sample

$$\frac{dI}{dV}\Big|_{eV} \propto \rho_s(E_F + eV) \qquad (1.6).$$

If the tip is fixed at a position, the sample LDOS can be measured by recording the *dI/dV* signal as a function of bias. This technique is known as the scanning tunneling spectroscopy (STS) and was first demonstrated by Feenstra, Stroscio, and Fein [7]. Initially, the *dI/dV* signal was obtained from the numerical derivative of the current vs bias spectrum. The application of lock-in techniques significantly decreases the measurement time and increases the accuracy. One can generate a *dI/dV* mapping by recording the first harmonic output of the lock-in amplifier at various positions while scanning the tip over the surface. *dI/dV* images show the spatial distribution of sample LDOS at energy eV. *dI/dV* spectroscopy and mapping have been widely applied to study the molecular electronic structures as well as the band structure of bulk materials.

1.2.3 Inelastic Tunneling Spectroscopy and Microscopy

When the bias is higher than the threshold energy of an inelastic excitation including vibration, rotation or spin excitation, some of the electrons can lose energy inelastically during tunneling (Fig. 1.2.A). These inelastic processes open a second tunneling channel, provide an additional pathway to the elastic tunneling channel, and change the tunneling current. At the positive side of bias, a slope change in the current vs bias spectrum can be detected at the threshold energy of the excitation, which corresponds to a step change in the *dI/dV* spectrum and a peak or dip in the second derivative of the current to the bias voltage (Fig. 1.2.B). In practice, the slope changes in current and the step changes in *dI/dV* can easily be overwhelmed by the mechanical or electronic noise. We use the peak or dip positions in d^2I/dV^2 spectrum to determine the excitation energy of these inelastic processes.

The inelastic contribution to the current is usually small in traditional transport measurements (~0.1%). However, the inelastic excitations in STM-IETS measurements may change the conductance by an amount from as low as 0.01% to as high as 10% [8,10]. This is attributed to the change in elastic tunneling channel caused by the opening of an inelastic pathway. Lorente and Persson have shown that the change in elastic channel may offset the increase due to inelastic tunneling, which leads to the overall conductance change not measurable for some vibrational modes [24]. The change in elastic tunneling channel is especially significant in the nonadiabatic coupling system where the nuclear movements due to the inelastic excitation are not negligible. Hahn and coworkers have shown that opening an inelastic vibration channel can

FIG. 1.2. Schematic diagrams of STM-IETS. (A) Energy diagram of an inelastic excitation. (B) Sample *I-V*, *dI/dV* and d^2I/dV^2 spectra of an inelastic excitation.

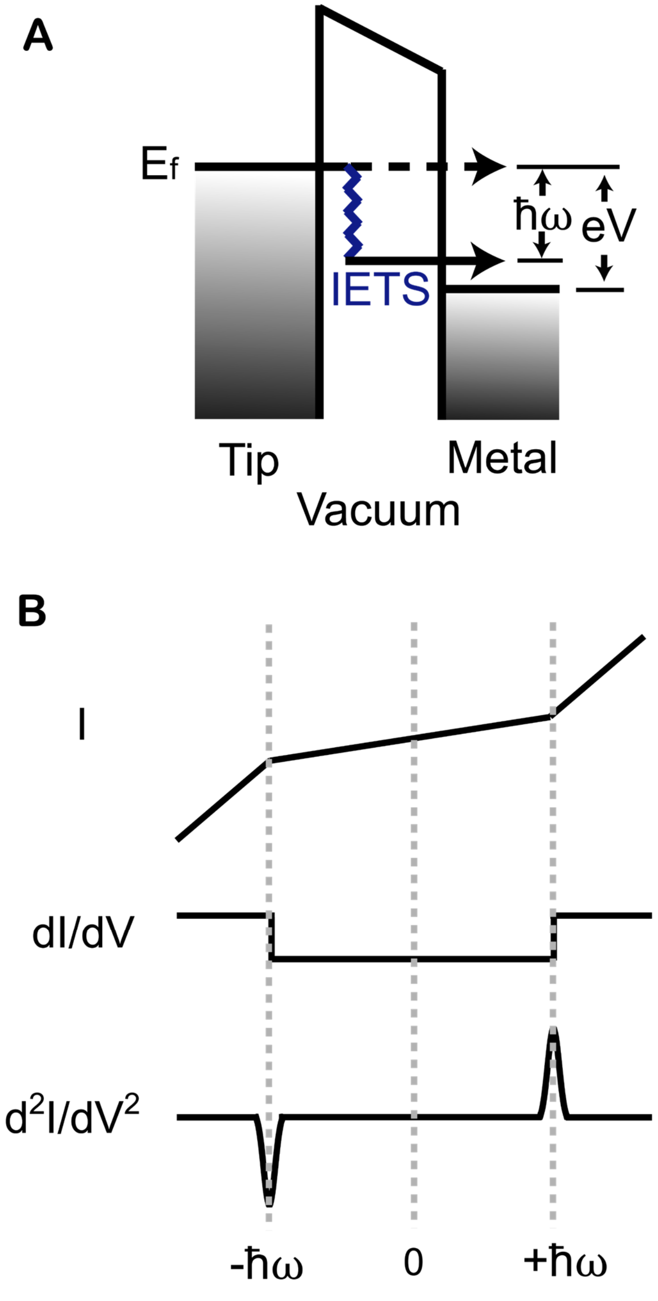
A
Ef
ħω
eV
IETS
Tip
Metal
Vacuum
B
I
dI/dV
d2I/dV2
-ħω
0
+ħω

sometimes decrease the overall conductance [25]. Xu and others have further shown that the competing between elastic tunneling and inelastic tunneling can lead to an asymmetric line shape in the d^2I/dV^2 spectrum [26]. In this dissertation, we will show both the conductance increase and decrease due to different inelastic excitations.

d^2I/dV^2 spectra acquired in this dissertation are all obtained via a lock-in amplifier by recording its second harmonic output while ramping the bias. We have also performed the d^2I/dV^2 mapping by recording the d^2I/dV^2 at a certain bias while scanning the tip over the surface. The d^2I/dV^2 images show the spatial variation of the inelastic excitation signals.

1.2.3 Inelastic Tunneling Probe Microscopy

Based on Equation 1.1, the STM has been shown to reveal the electronic states of the sample. The traditional topographic images often fail to reveal the interior structures of the molecule. The spatial resolution of STM can be enhanced by trapping a hydrogen molecule in the junction or transferring a CO, Xe, or CH_4 molecule to the tip [27-29]. A recent atomic force microscopy (AFM) technique can achieve very high spatial resolution by functionalizing the tip with a CO molecule and detect the shift in the resonance frequency of the quartz tuning fork as the tip scan over the substrate molecule [30]. The clear skeletal structure of the substrate molecule can be resolved. Chiang and coworkers developed a novel technique, named inelastic tunneling probe (itProbe) microscopy, which can obtain ultra-high spatial resolution using STM [31]. In this technique, a CO molecule is transferred to the tip. The low energy hindered translational mode of CO is found to be very sensitive to the change in potential energy surface. As the CO-terminated tip is scanned over the substrate, changes in the energy and intensity of the CO hindered translational mode are measured by recording the d^2I/dV^2 output of a lock-in amplifier at the bias corresponding to the vibration. The spatial resolution arises from variations of the force gradient sensed by the CO as it scans over molecule. Hapala and coworkers have shown that the tilting of the tip-CO sharpens the spatial contrast [32]. The energy shift of the vibration is less than 5 meV, which requires very high spectral sensitivity. All the itProbe images shown in this dissertation are taken using a sub-Kelvin STM operating at 600 mK with a spectral resolution around 0.5 mV.

1.3 Basic Optical Techniques

The combination of STM with femtosecond lasers may assemble the unique capabilities of both techniques: the sub-Ångström spatial sensitivity from STM and the ultra-high temporal resolution from femtosecond lasers. To achieve simultaneous spatial and temporal resolutions, we apply several basic optical techniques including Kerr-lens mode-locking, multiphoton intrapulse interference phase scan, and interferometric autocorrelation.

1.3.1 Kerr-lens Mode-locking

Mode-locking refers to an optical technique by which a laser can be made to produce pulses of extremely short duration. A finite laser resonant cavity usually contains a lot of longitudinal modes depending on the cavity length and laser bandwidth. For a 5 GHz repetition rate Ti-sapphire laser with 125 THz bandwidth, around 25,000 modes can be excited in the cavity. When the laser is operating in the continues wave (CW) mode, each mode oscillates independently without any phase relationship between each other. The basis of mode locking is to induce a fixed-phase relationship between different longitudinal modes. The laser is then 'phase-locked' or 'mode-locked'. The interference between these modes causes the laser to be produced as a series of pulses, with a pulse width as short as a few femtoseconds.

The Kerr-lens mode-locking is a passive mode-locking method that doesn’t require external modulation to the laser [33]. It makes use of the optical Kerr effect to selectively absorb

FIG. 1.3. Kerr-lens mode-locking. (A) Schematic diagram of optical Kerr effect. (B) Schematic diagram of a four-mirror resonator.

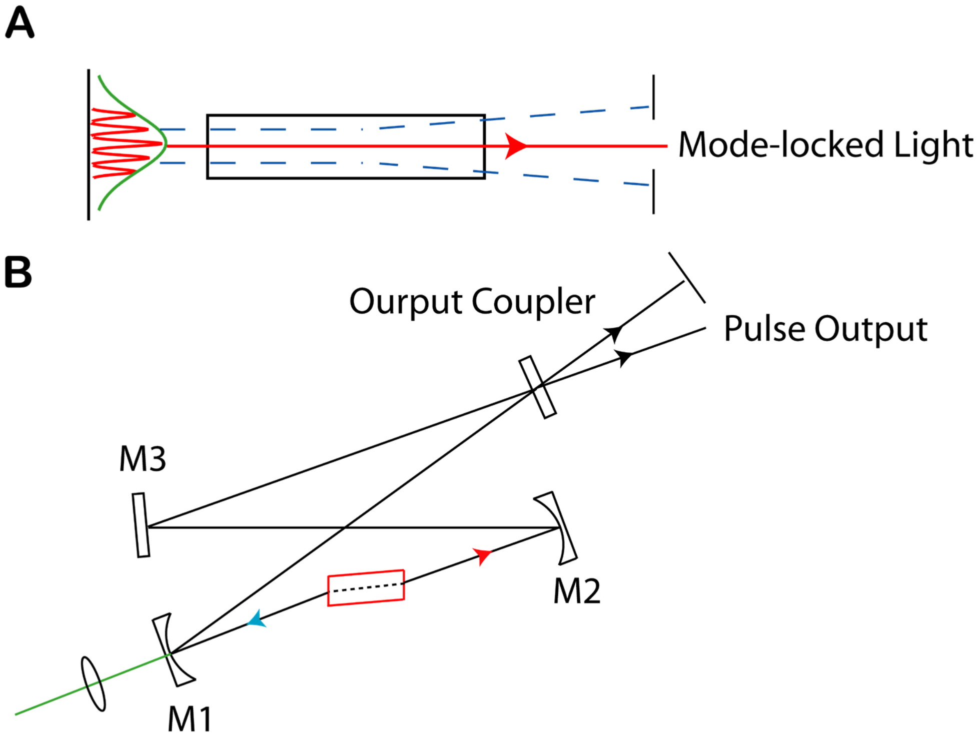
A
Mode-locked Light
B
Ourput Coupler
Pulse Output
M3
M2
M1

the low-intensity CW signals while transmitting the high-power pulse signals. Kerr effect refers to the change in the refractive index of a material in response to an applied electric field. In an optical Kerr effect, the Kerr medium responses to the electric field of incident light. Therefore, the low-intensity CW signals and the high-intensity pulse singles will have different refractive indexes and can be separated in space. In a simple linear optical cavity as indicated Fig. 1.3.A, only the pulse light can pass through the slit while the CW light is blocked. The pulse light can be bounced back to the Ti-sapphire crystal by the end mirror of the cavity and stimulate additional laser signal with the same phase.

We use a *Giga-jet 50* Ti-sapphire resonator manufactured by *Laser Quantum* for all the optical experiment discussed this dissertation. It is a four-mirror resonator as depicted in Fig. 1.3.B. The optical cavity is aligned in the way that the CW light and pulse light will have different optimum focuses and can be separated in space by spherical mirrors M1 and M2. The resonator has two equivalent modes corresponding to the pulses from Ti-sapphire crystal initially travel towards M1 or M2 as indicated by the blue and red arrows. The laser can mode-lock into either direction with equal probability. The mode indicated by the blue arrow is dumped by the resonator housing. Pulse output can only be detected when the resonator is locked to the mode indicated by the red arrow.

Initiation of Kerr-lens mode-locking requires a phase perturbation. For a long cavity contains many longitudinal modes, the random phase relationship in CW operation gives a stable CW output. The 5 GHz resonator we use has a short cavity with relatively fewer modes, the intensity fluctuation due to the beating between a limit number of modes may spontaneously trigger the mode-locking. If mode-locking is not self-started, it can be initiated by shifting the optimum focus while changing the power density. In the *Giga-jet 50* resonator, this can be done by gently shaking the resonator cavity components including M2, output coupler, and Ti-sapphire crystal.

1.3.2 Multiphoton Intrapulse Interference Phase Scan

Multiphoton intrapulse interference phase scan (MIIPS) is a pulse shaping method used in ultrashort laser technology to compress pulse durations [34]. The experiments described in this dissertation use a *MIIPSBox 640* from *Biophotonic Solutions* to perform the pulse compression. In the *MIIPSBox*, the laser pulses are deflected by a diffractive grating into a Spatial Light Modulator (SLM). The SLM applies a phase shift to different frequency based on the signal of second harmonic generation (SHG). The second harmonic signal is generated by a Beta Barium Borate (BBO) crystal and measured in the frequency domain using a spectrometer. Multiple iterations need to be done till optimized pulse profile is reached.

1.3.3 Interferometric Autocorrelation

In the experiments described in this dissertation, we shine 820 nm laser pulses into a Michelson interferometer to create pairs of correlated laser pulses with variable delay time [21]. As shown in Fig. 1.4.A, one arm of the Michelson interferometer is mounted on a motorized linear stage (*Newport UTM100PP*) to control the delay. The other arm is equipped with a home-made piezo shaker. A sine-wave modulation with ~200 nm amplitude (λ/4) is applied to the optical path when the two phase-correlated pulses are temporally overlapped ($|\tau| \leq 100$ fs). This modulation averages the constructive and destructive interferences over one modulation period. A 50/50 beam splitter is used to maintain equal power for both arms to within 10%.

We determine zero delay time and the pulse width from intensity autocorrelation measurement using a BBO crystal. The intensity of SHG can be expressed as

$$I(\tau) = \int_{-\infty}^{+\infty} |[E(t) + E(t+\tau)]^2|^2 \, dt \qquad (1.7)$$

FIG. 1.4. Interferometric autocorrelation. (A) Schematic diagram of SHG autocorrelation. (B) Sample SHG autocorrelation spectrum.

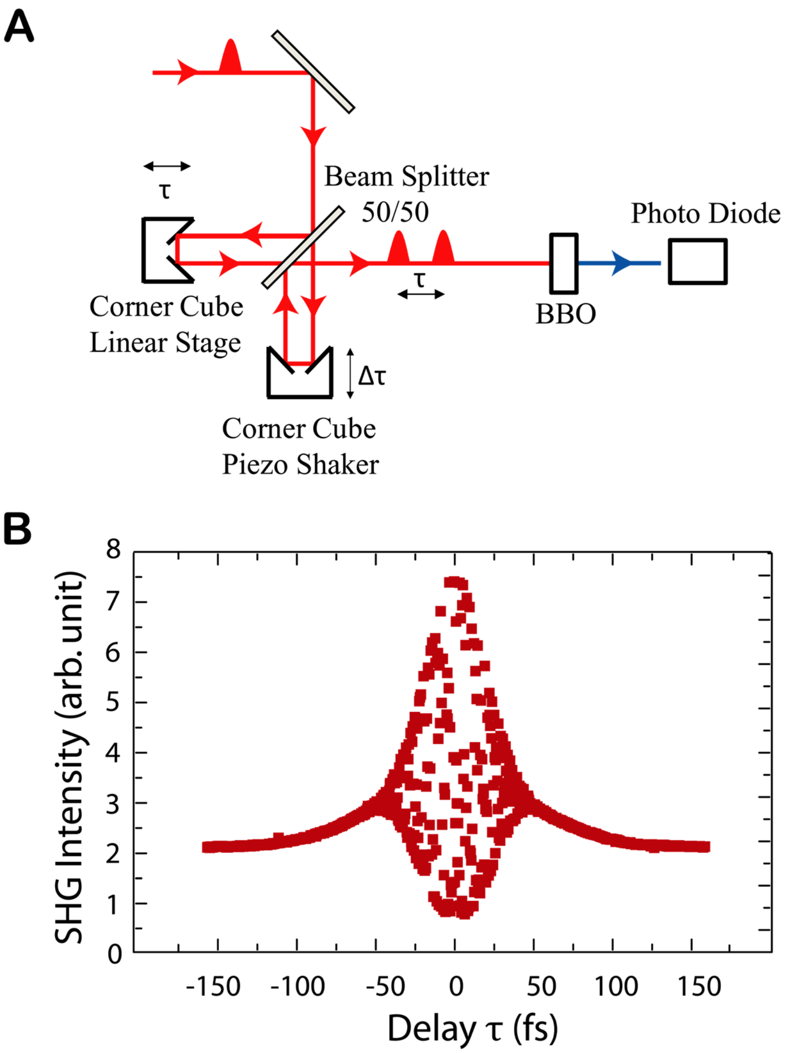
A
τ
Beam Splitter
50/50
Photo Diode
Corner Cube
Linear Stage
τ
BBO
Δτ
Corner Cube
Piezo Shaker
B
SHG Intensity (arb. unit)
0
1
2
3
4
5
6
7
8
-150
-100
-50
0
50
100
150
Delay τ (fs)

where $E(t)$ and $E(t+\tau)$ are the electric fields of a pair of identical pulses separated by a delay time τ. A sample autocorrelation spectrum is shown in Fig. 1.4.B. The position of intensity maximum corresponds to the zero delay. When two pulses are perfectly overlapping in space, zero delay intensity should be eight times of the intensity measured when two pulses are temporally separated. The full width at half maximum (FWHM) of the autocorrelation spectrum is 1.41 times of the pulse duration of Gaussian type pulses, and 1.55 times of the duration of sech^2 type pulse.

1.4 Optical Set-up of a Femtosecond Laser STM

A schematic diagram of the optical layout of the femtosecond laser STM is presented in Fig. 1.5. We use a *Giga-jet 50* resonator to generate 820 nm femtosecond pulses with 800 mW average output power. The resonator is pumped by a *Coherent Verdi V6* diode laser (532 nm and 5.5 W in TEM_{00} mode). An *RD-40* Laser Power Controller from *Brockton Electro-Optics Corp* is used to regulate and stabilize the beam power to 0.03% rms. A *Femtojock MIIPSBOX* from *Biophotonic Solutions* compresses the pulse duration to ~35 fs (FWHM). The compressed pulses are guided into a Michelson interferometer. Zero delay time is determined from SHG interferometry autocorrelation measurement using a BBO crystal outside the UHV chamber and finely adjusted by measuring the tip expansion as a function of delay time when the two pulses are temporally overlapped. The laser beam is focused onto the STM junction by a 3” focal length lens at a 45° angle of incidence and p-polarization. The reflected and scattered light is collected by another 3” focal length lens and imaged by a charge-coupled-device (CCD) camera [20]. The laser is aligned by adjusting the focal lens position using micrometer driven translation and tilt outside the UHV chamber. A strong interference pattern can be captured by the CCD camera when the

FIG. 1.5. Schematic diagram of the femtosecond laser set up.

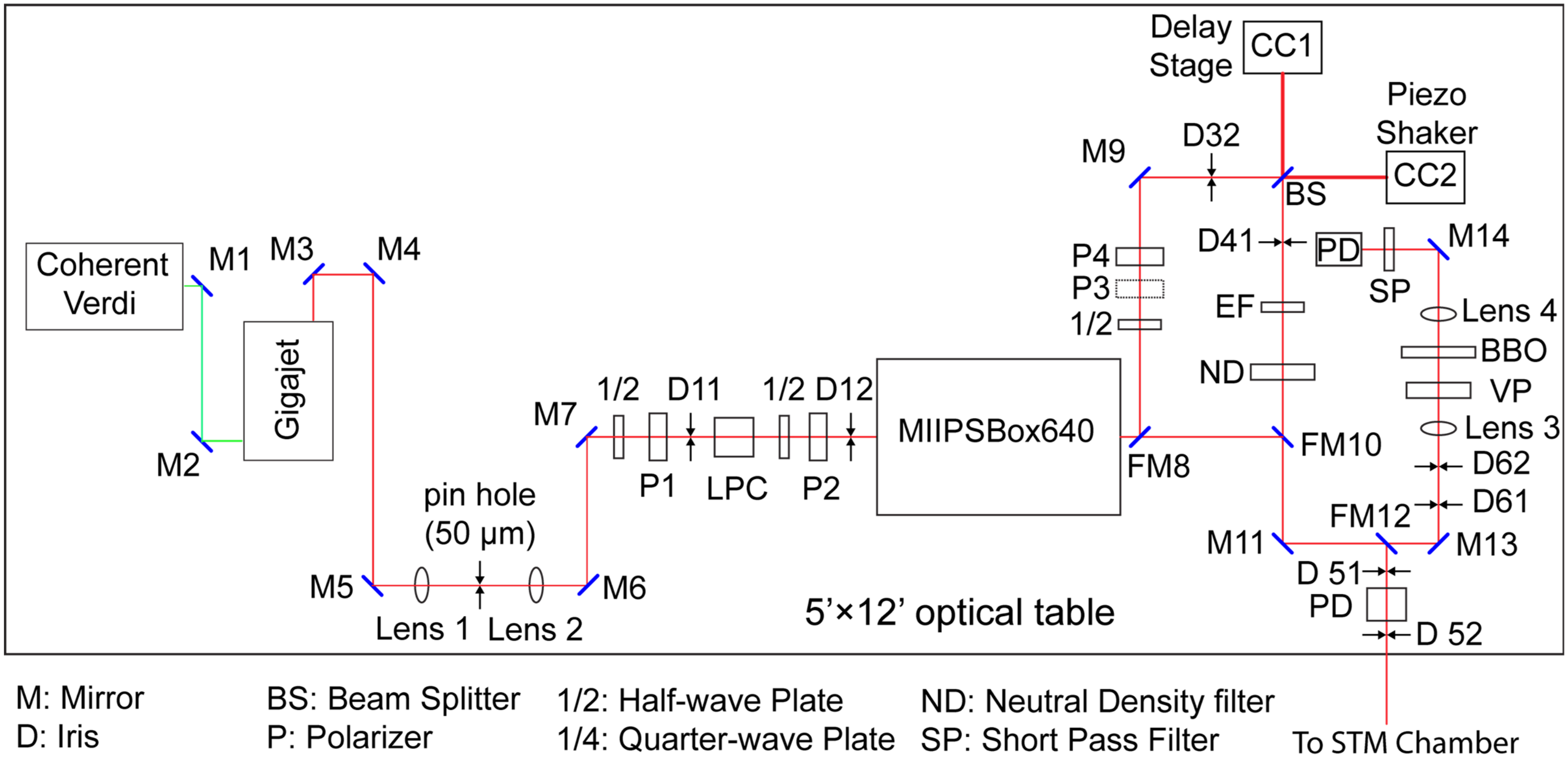
Coherent Verdi
M1
M2
Gigajet
M3
M4
M5
Lens 1
pin hole (50 µm)
Lens 2
M6
M7
1/2
P1
D11
LPC
1/2
P2
D12
MIIPSBox640
FM8
M9
P4
P3
1/2
D32
Delay Stage
CC1
BS
Piezo Shaker
CC2
D41
PD
SP
M14
EF
ND
Lens 4
BBO
VP
Lens 3
FM10
D62
D61
FM12
M11
M13
D 51
PD
D 52
5'×12' optical table
To STM Chamber

M: Mirror
D: Iris
EF: Edge Filter
VP: View Port
BS: Beam Splitter
P: Polarizer
PD: Photodiode
LPC: Laser Power Controller
1/2: Half-wave Plate
1/4: Quarter-wave Plate
CC: Corner Cube
ND: Neutral Density filter
SP: Short Pass Filter
FM: Flip-Mounted Mirror

laser pulses scatter from the STM junction. The laser spot at the junction is estimated to be typically 20–50 μm in diameter [21]. The average power of the laser is measured by a photodiode sensor (*Coherent S120VC*) immediately prior to entering the UHV chamber.

The lens equipped at the output side of the ultrahigh vacuum chamber can also be used to collect and focus the emitted light from the STM junction. The output light is guided to a monochromator with a liquid nitrogen cooled CCD to generate energy resolved emission spectrum. We can also obtain spatially resolved emission imaging by recording the light intensity while scanning the tip over the substrate. This set-up has been used to acquired photon emission spectroscopy and microscopy from artificial metal structures [35,36] and molecules [37-40] on surfaces.

1.5 Summary of Contents

The rest of this dissertation describes a series of experiments using the experimental techniques introduced above to overcome the two obstacles of STM: insufficient chemical sensitivity and poor temporal resolution. Each chapter is a paper that has been published or is awaiting publication. The second and third chapters describe two experiments about using STM-IETS to probe the rotational excitation of the single hydrogen molecule in the STM junction and use the energy shift of hydrogen rotational excitation to characterize the intermolecular interaction. The fourth chapter introduces a study where we use the mechanical motion of STM tip to induce and monitor a mechanochemical reaction. In the fifth and sixth chapters, we combine STM with a femtosecond laser to probe the surface photophysics and photochemistry with simultaneous temporal and spatial sensitivity. In the seventh chapter, we use this laser-STM system to probe the nature of light-matter interaction at a molecule-semiconductor interface. The contents of each chapter are briefly discussed below.

Chapter 2: "Rotational and Vibrational Excitations of a Hydrogen Molecule Trapped Within a Nanocavity of Tunable Dimension" by Shaowei Li, Arthur Yu, Freddy Toledo, Zhumin Han, Hui Wang, H. Y. He, Ruqian Wu, and W. Ho, appearing in *Physical Review Letters*, Volume 111, pages 146102, 2013. In this chapter, we provide the first experimental observation of the rotational transitions of a hydrogen molecule weakly adsorbed on the Au(110) surface at 10 K using STM-IETS. The j=0 to j=2 rotational transition energies for para-H_2, HD, and D_2 indicate that the molecular rotation follows the three-dimensional rigid rotor model as in gas phase. We also notice the H-H bond can be weakened by the interaction between hydrogen and the tunneling junction.

Chapter 3: "Rotational Spectromicroscopy: Imaging the Orbital Interaction between Molecular Hydrogen and an Adsorbed Molecule" by Shaowei Li, Dingwang Yuan, Arthur Yu, Gregory Czap, Ruqian Wu, and W. Ho, appearing in *Physical Review Letters*, Volume 114, pages 206101, 2015. This experiment describes a new technique to probe the intermolecular interaction between a hydrogen molecule and a Mg-porphyrin by imaging the rotational excitation of molecular hydrogen. The preferable interaction between hydrogen and a charge acceptor reveal the donor nature of hydrogen in a certain configuration.

Chapter 4: "Single Molecule Mechanochemistry" by Shaowei Li, Yanxing Zhang, Arthur Yu, Dingwang Yuan, Gregory Czap, Hikari Kimura, Ruqian Wu, and W. Ho, to be submitted. From the experiments introduced in chapter 2 and 3, we realize that the H-H bond of a hydrogen molecule trapped in the tunneling can be weakened by the interaction between hydrogen and the metallic tunneling junction. In this chapter, we show that the H-H bond can be dissociated by the reciprocating movement of the tip of an STM, demonstrating the capability of using STM to induce and monitor the mechanochemical reactions. The catalytic activity of single CO molecules and single gold atoms are also visualized in real-space.

Chapter 5: “Sub-molecular Control of Photo-assisted Activation of a single C-H bond” by Shaowei Li, Gregory Czap, Hui Wang, Arthur Yu, Siyu Chen, Ruqian Wu, and W. Ho, to be submitted. In this chapter, we demonstrate the coupling of femtosecond laser pulses to the tunneling electrons to selectively activate single C–H bonds in individual azulene molecules adsorbed on an Ag(110). The STM bias required to break the bond decreases by 1.5 V under 820 nm laser illumination, indicating that some electrons in the tip can be photoexcited into a higher energy state to induce the reaction. The C-H bond to be dissociated can be accurately chosen by the position of STM tip. This study demonstrates that STM can be used to probe the photochemistry at sub-molecular level.

Chapter 6: “Probing Coherent Vibration Mediated Structural Transitions of Single Molecules with Space-time Resolution” by Shaowei Li, Siyu Chen, Jie Li, Ruqian Wu and W. Ho, submitted for publication in *Physical Review Letters*. The experiment described in this chapter demonstrates the vibration mediated coherent structural transformation of a single pyrrolidine molecule with simultaneous Ångström-femtosecond resolution. The vibration mode of the molecule is excited with a pair of time-correlated femtosecond laser pulses. The molecular dynamics including vibration period and decay time are monitored locally with the STM. We show that the dynamics can be altered by intermolecular interactions in a molecular dimer. This study demonstrates the simultaneous spatial-temporal sensitivity of an STM combined with a femtosecond laser.

Chapter 7: “Real-space Observation of Nanoelectrical Band Bending and Flattening at a Single Molecule Interface” by Shaowei Li, Arthur Yu, and W. Ho, to be submitted. We visualize the band bending and laser induced band flattening of a boron doped Si(111) surface. The energies of both the lowest unoccupied molecular orbital of a single C_{60} and the surface state of a Si atom vacancy can be upshifted by laser irradiation due to the photo induced flattening of the band bending. A larger shift is observed for the C_{60} states due to the electron transfer from Si to the C_{60} molecule. We also find that the laser induced shifts of both states are smaller when the sample temperature is increased from 80 K to 90 K, probably due to the increased charge carrier density and mobility at a higher temperature.

The concluding chapter summarizes this dissertation together with several related studies. Additional experiments to continuously expand the capability of STM are proposed. The appendixes describe the instrumentation projects, including both hardware and software developments which have facilitated the experiments reported in this dissertation. The hardware developments include the design and fabrication of different types of evaporators. The software section describes the modifications to the STM control software and a series of new LabVIEW programs. It also describes the procedures and experimental details of how these programs are used to acquire and process data.

Bibliography

[1] G. Binnig, H. Rohrer, C. Gerber and E. Weibel, Phys. Rev. Lett. **49**, 57 (1982).

[2] G. Binnig, H. Rohrer, C. Gerber and E. Weibel, App. Phys. Lett. **40**, 178 (1982).

[3] D. P. E. Smith and G. Binnig, Rev. Sci. Instrum. **57**, 2630 (1986).

[4] S. H. Pan, E. W. Hudson, and J. C. Davis, Rev. Sci. Instrum. 70, 1459 (1999).

[5] Y. J. Song, A. F. Otte, V. Shvarts, Z. Zhao, Y. Kuk, S. R. Blankenship, A. Band, F. M. Hess, and J. A. Stroscio, Rev. Sci. Instrum. **81**, 121101 (2010).

[6] S. Zhang, D. Huang, S. Wu, Rev. Sci. Instrum. **87**, 063701 (2016).

[7] R. M. Feenstra, J. A. Stroscio and A. P. Fein, Surf. Sci. Lett. **181**, 295 (1987).

[8] B. C. Stipe, M. A. Rezaei, and W. Ho, Science, **280**, 1732 (1998).

[9] L. Bartels, F. Wang, D. Möller, E. Knoesel, T. F. Heinz, Science **305**, 648 (2004).

[10] W. Ho, J. Chem. Phys. **117**, 11033 (2002).

[11] B. C. Stipe, M. A. Rezaei and W. Ho, Rev. Sci. Instrum. **70**, 137 (1999).

[12] Y. Zhang, V. W. Brar, F Wang, C. Girit, Y. Yayon, M. Panlasigui, A. Zettl and M. F. Crommie, Nat. Phys. **4**, 627 (2008).

[13] A. J. Heinrich, J. A. Gupta, C. P. Lutz, and D. M. Eigler, Science **306**, 466 (2004).

[14] R. C. Jaklevic and J. Lambe, Phys. Rev. Lett. **17**, 1139 (1966).

[15] G. C. Cho, W. Kütt, and H. Kurz, Phys. Rev. Lett. **65**, 764 (1990).

[16] K. Watanabe, N. Takagi, and Y. Matsumoto, Chem. Phys. Lett. **366**, 606 (2002).

[17] D. W. Pohl, W. Denk, and M. Lanz, Appl. Phys. Lett. **44**, 651 (1984).

[18] R. Bachelot, P. Gleyzes, and A. C. Boccara, Microsc. Microanal. Microstruct. **5**, 389 (1994).

[19] R. Zhang, Y. Zhang, Z. C. Dong, S. Jiang, C. Zhang, L. G. Chen, L. Zhang, Y. Liao, J. Aizpurua, Y. Luo, J. L. Yang, and J. G. Hou, Nature **498**, 82 (2013).

[20] S. W. Wu, N. Ogawa, and W. Ho, Science **312**, 1362 (2006).

[21] S. W. Wu and W. Ho, Phys. Rev. B **82**, 085444 (2010).

[22] J. Tersoff and D. R. Hamann, Phys. Rev. Lett. **50**, 1998 (1983).

[23] J. Tersoff and D. R. Hamann, Phys. Rev. B **31**, 805 (1985).

[24] N. Lorente and M. Persson, Phys. Rev. Lett, **85**, 2997 (2000).

[25] J.R. Hahn and W. Ho, Phys. Rev. B **80**, 165428 (2009).

[26] C. Xu, C. L. Chiang, Z. Han, and W. Ho, Phys. Rev. Lett. **116**, 166101 (2016).

[27] C. Weiss, C. Wagner, C. Kleimann, M. Rohlfing, F. S. Tautz, and R. Temirov*,* Phys. Rev. Lett. **105**, 086103 (2010).

[28] C. Weiss, C. Wagner, R. Temirov, F. S. Tautz, J. Am. Chem. Soc. **132**, 11864 (2010).

[29] G. Kichin, C. Weiss, C. Wagner, F. S. Tautz, and R. Temirov, J. Am. Chem. Soc. **133**, 16847 (2011).

[30] L. Gross, F. Mohn, N. Moll, P. Liljeroth, and G. Meyer, Science **325**, 1110 (2009).

[31] C. L. Chiang, C. Xu, Z. Han, and W. Ho, Science **334**, 885 (2014).

[32] P. Hapala, R. Temirov, F. S. Tautz, and P. Jelínek, Phys. Rev. Lett. **113**, 226101 (2014).

[33] K. Jamshidi-Ghaleh and N. Mansour, Opt. Commun. **234**, 419 (2004).

[34] V. V. Lozovoy, I. Pastirk, and M. Dantus, Opt. Lett. **29**, 775 (2004).

[35] C. Chen, C. A. Bobisch, W. Ho, Science **325**, 981 (2009).

[36] A. Yu, S. Li, G. Czap, and W. Ho, Nano Letters, **16**, 5433 (2016).

[37] A. Yu, S. Li, B. Dhital, H. P. Lu, and W. Ho, J. Phys. Chem. C **120**, 21099 (2016).

[38] X. H. Qiu, G.V. Nazin, and W. Ho, Phys. Rev. Letts. **92**, 206102 (2004).

[39] X. H. Qiu, G.V. Nazin, and W. Ho, Science **299**, 542 (2003).

[40] C. Chen, P. Chu, C. A. Bobisch, D. L. Mills, and W. Ho, Phys. Rev. Lett. **105**, 217402 (2010).

CHAPTER TWO

Rotational and Vibrational Excitations of a Hydrogen Molecule Trapped Within a Nanocavity of Tunable Dimension[†]

Abstract

The rotational and vibrational transitions of a hydrogen molecule weakly adsorbed on the Au(110) surface at 10 K were detected by inelastic electron tunneling spectroscopy with a scanning tunneling microscope. The energies of the j=0 to j=2 rotational transition for para-H_2 and HD indicate that the molecule behaves as a three-dimensional rigid rotor trapped within the tunnel junction. An increase in the bond length of H_2 was precisely measured from the downshift in the rotational energy as the tip-substrate distance decreases.

[†] This chapter by Shaowei Li, Arthur Yu, Freddy Toledo, Zhumin Han, Hui Wang, H. Y. He, Ruqian Wu, and W. Ho is reprinted with permission from *Physical Review Letters*, Volume 111, pages 146102, 2013.

2.1 Introduction

Rotational and vibrational transitions can reveal structural and energetic properties of molecules [1,2]. Even small changes in the distance between atoms or the masses from isotopic substitution alter the rotational and vibrational transition energies of the molecule. The power of vibrational and rotational spectroscopies has been demonstrated in the frequency [3-5] and time [6-7] domains in the infrared and microwave. The sensitivity of vibrational spectroscopy has reached the single bond level by the detection of vibrationally inelastic electron tunneling process using the scanning tunneling microscope (STM) [8]. However, the detection of rotational transitions in single molecules remains to be demonstrated.

Hydrogen, the lightest element in the universe, plays a particularly important role in the development of quantum mechanics. Exact solutions to the Schrödinger equation can be obtained for atomic and molecular hydrogen. The rotational states of the hydrogen molecule can be analyzed within the rigid rotor model. The smallest mass of hydrogen (H) and the large percent difference in mass from its isotope deuterium (D) yield a high and large shift in energies for the rotational transitions that facilitate detection.

The detection of the rotational transitions of molecular hydrogen using the STM requires that the bonding between molecule and substrate should be sufficiently weak so the adsorbed molecule behaves like a gas phase molecule, but the molecule needs to be sufficiently stable for I-V, dI/dV and d^2I/dV^2 scanning tunneling spectroscopy (STS). On noble metal surfaces such as Au(110), molecular hydrogen is weakly adsorbed at low temperature via van der Waals forces [9,10]. The adsorbed molecules are mobile and can rapidly migrate one by one in and out of the tip-surface tunnel junction, on a time scale much shorter than the imaging time. [10,11]. In the tunneling range, the tip-substrate separation is 6.5 Å to 7.5 Å in our measurement. At the same time, tunneling occurs just below the tip apex, and the tunneling current is confined laterally within sub-Ångström. In such a junction, only a single hydrogen molecule can be trapped at any given time [12,13]. Although the spectroscopic signals are the average over many molecules from the diffusion and trapping processes, each trapped hydrogen molecule is experiencing the same environmental coupling given by the tip-subtract junction, and variations in the configurations and properties of different molecules are expected to be insignificant. The trapped hydrogen molecule dramatically increases the contrast of the STM topographic images, providing new details of complex surface structures [11,12]. In addition, as each trapped molecule is separated from other surrounding molecules, it maintains the essential properties as an isolated molecule that exhibits the rotational and vibrational properties of a nearly free molecule trapped within a nanocavity of tunable dimension.

Here, we demonstrate rotational spectroscopy with the STM. In the inelastic electron tunneling spectroscopy (IETS) with the STM, excitations are characterized by step changes in the *dI/dV* spectrum at the threshold voltage corresponding to these excitations. The STM-IETS of H_2, D_2, and HD molecules weakly adsorbed on the Au(110) surface shows a series of step changes in the *dI/dV* spectra, which correspond to rotational and vibrational excitations. In these *dI/dV* spectra, $j=0\longrightarrow2$ rotational excitations of H_2 and HD are recorded as an increase in conductance while the $v=0\longrightarrow1$ vibrational excitation in the adsorption well of H_2, D_2, and HD shows a decrease in conductance. The coupling of the rotational motions of the hydrogen molecule to its environment given by the metallic tip and substrate is determined by squeezing the tip-substrate separation.

2.2 Methods

The experiments were performed using a home-built STM operating at 10 K and a base pressure of 3×10^{-11} Torr [14]. The Au(110) surface was cleaned by cycles of Ne^+ sputtering and annealing at 680 K. The silver tip was electrochemically etched. The clean surface at 10 K was dosed either with H_2, HD or D_2 at 2×10^{-10} Torr for 5 min. The adsorbed molecule can be completely desorbed by laser illumination at 10 K or raising the sample temperature to 27 K, allowing repeated measurements without the need for tip and sample preparations.

We used the Vienna *Ab-initio* Simulation Package (VASP) [15-17] for electronic structure calculations and structural relaxations. The spin-polarized generalized gradient approximation (GGA), using the Perdew-Burke-Ernzerhof (PBE) functional [18], was employed for the description of electronic exchange and correlation interactions. To correctly describe physisorption systems such as H_2 /Au(110), the van der Waals term was considered through the vdW-DF2 functional that is implemented in VASP [19,20]. We treated H-1s and Au-5d6s as valence states and adopted the projector-augmented wave (PAW) pseudopotentials to represent their ionic cores [21,22]. The Au [110] surface was simulated with a 5-layers slab and a vacuum of about 15 Å thick. Adding a pyramid on the other side of the slab simulated the STM tip. In the lateral plane, we used a (3×3) supercell and fixed the lattice size based on the optimized lattice constant of the bulk Au (a_{Au}=4.17 Å). The energy cutoff of the plane-wave expansion was 700 eV, adequate for the present studies according to our test calculations. A set of 7×7×1 Monkhorst-Pack [23] k-points were used for the geometry relaxation and the determination of electronic and magnetic properties at zero temperature. The tip-surface distance was adjusted by varying the length of the supercell along the z-axis. Positions of all atoms are fully relaxed according to a criterion that requires the force on each atom to be smaller than 0.01 eV/Å and the energy convergence to be better than 10^{-7} eV.

2.3 Results and Discussion

The diffusion and trapping of a molecule in the tunnel junction are illustrated in Fig. 2.1.A. The topographic STM image (Fig. 2.1.B) taken on a hydrogen-free Au(110) surface shows a clear 2×1 reconstruction structure. After dosing H_2, D_2 or HD, the high-resolution image in Fig. 2.1.C reveals single Au atoms on atop sites; the Au atoms in the troughs remain unresolved. The dI/dV image (Fig. 2.1.D) and d^2I/dV^2 image (Fig. 2.1.E) also reveal atomic resolution for atop sites. The increased spatial resolution obtained after dosing H_2, D_2 or HD indicates that a single hydrogen molecule can be trapped between the tip and an atop Au atom. In this paper, all the STS spectra were recorded above atop Au atoms.

The rotational motion of adsorbed molecules can either be free or hindered, depending on the depth of the adsorption well. Previous STM studies have investigated the rotational motion of molecules stably adsorbed on the surface and can be imaged [24-26]. In these studies, the molecules are highly constrained to be within the adsorption well and the rotations are described as hindered vibrational modes. However, if the adsorption potential well is shallow, the rotational motion of the adsorbed molecule is "unhindered" [27] and is characteristic of a rigid three-dimensional (3D) free rotor. The rotational energy is given by $j(j+1)\hbar^2/2\mu r_b^2$, where $j=0,1,2,\ldots$, μ is the reduced mass of the molecule, and r_b is the distance between the two atoms in the molecule (the bond length for H_2). In the STS spectra taken on H_2, a step change in dI/dV spectrum is observed (Fig. 2.2.A), with a corresponding peak in the d^2I/dV^2 spectrum (Fig. 2.2.B) at 42.0 mV. This energy agrees with the $j=0\longrightarrow2$ rotational excitation of a para-H_2 as a 3D rigid rotor, indicating

FIG. 2.1. A hydrogen molecule trapped in the tunneling junction of STM. (A) Schematic diagram of the diffusion and trapping of a hydrogen molecule in the tunnel junction. The average lifetime of each trapped molecule in the junction is estimated to be far shorter than the response time of STM electronics. The spectroscopic signals arise from the average of many such diffusion and trapping processes. (B) STM topographic image of bare Au(110) 2×1 reconstructed surface obtained at constant current mode prior to dosing with hydrogen. Imaging conditions: tunneling gap set with sample bias V_B=13.5 mV and tunneling current I_T=2 nA. (C) STM topographic image obtained under the same conditions as (B) but after dosing with H_2 molecules. (D) dI/dV image at 0 mV bias and (E) d^2I/dV^2 image at 10 mV bias for surface adsorbed with H_2. Tunneling gap setting conditions: V_B =50 mV and I_T =2 nA for (D), V_B =100 mV and I_T =10 nA for (E).

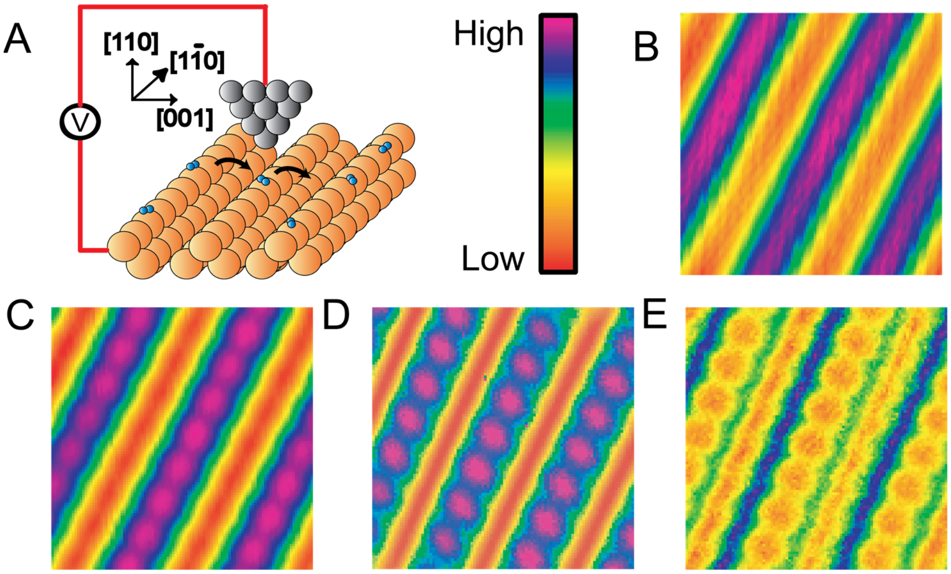
A
[110]
[1$\bar{1}$0]
[001]
V
High
Low
B
C
D
E

that the H_2 molecules on Au(110) behave like in the gaseous phase. For the HD, this inelastic rotational signal shifts down to 31.5 mV, which is 0.75 times the measured transition energy of H_2, in agreement with the value of 3/4 according to the 3D rigid rotor model. Since the two atoms in HD are distinguishable, the j=0⟶1 excitation is allowed. However, this excitation is difficult to resolve since its energy is expected to be at 10.5 mV, where the signal is dominated by the v=0⟶1 vibrational transition. For the same reason, the j=0⟶2 excitation energy of ortho-D_2 at 21 mV is similarly difficult to be resolved. On the other hand, the j=1⟶3 rotational excitation at 70 mV for ortho-H_2 and 35 mV for para-D_2 is not visible in the STS spectra. These results are in agreement with prior measurements by electron energy loss spectroscopy (EELS), showing that hydrogen molecules are weakly adsorbed on noble metal surfaces at low temperature and rapidly convert into the j=0 state (the para-H_2 or ortho-D_2) [9,25,29]. Thus the presence of ortho-H_2 or para-D_2 is unlikely on Au(110) at 10 K. Nevertheless, our data for H_2 and HD are sufficient to indicate that molecular hydrogen on Au(110) behaves as a 3D rigid rotor.

The strong signals at lower energies in the tunneling spectra are assigned to the vibrational excitations in the physisorption potential well. In the harmonic approximation, the vibration energies are given by $h\nu_0(v+1/2)$ with v=0,1,2,... In the tunneling spectra of H_2, the large step down at 11.4 mV in the *dI/dV* spectrum (Fig. 2.2.A) and the corresponding asymmetric dip in the d^2I/dV^2 spectrum (Fig. 2.2.B) are assigned to the v=0⟶1 excitation of the hydrogen vibrational motion bouncing between the tip and substrate. In the tunneling spectra of HD and D_2, the v=0⟶1 transition energy is shifted down to 8.9 mV and 8.2 mV, respectively. The ratios of these transition energies are 1.3 between H_2 and HD and 1.4 between H_2 and D_2, in agreement with the quantum harmonic oscillator.

FIG. 2.2. Tunneling spectra taken before and after dosing molecular hydrogen or its isotopes. The tunneling gap is set with V_B=50 mV and I_T=2 nA for all the spectra. The bias for the x-axis in the spectra has been shifted up by 1 mV to compensate for the instrumental offset. (A) From the top to the bottom: *dI/dV* spectra of H_2, HD, D_2, and clean gold surface (Background). (B) From the top to the bottom: d^2I/dV^2 spectra of H_2, HD, D_2, and clean gold surface (Background). The magnified line shapes for the rotational excitation are also presented. The excitation energies are marked by arrows. The signal at ±42.0 mV in H_2 spectra and the signal at ±31.5 mV in HD spectra are assigned to the $j=0\longrightarrow2$ rotational excitation. The small structure around ±42 mV in HD and D_2 spectra is attributed to contamination from co-adsorption of background H_2 in the vacuum chamber. The strong signals at ±11.4 mV, ±8.9 mV, ±8.2 mV in the spectra for H_2, HD, D_2 are assigned to the $v=0\longrightarrow1$ vibrational excitation within the physisorption potential well.

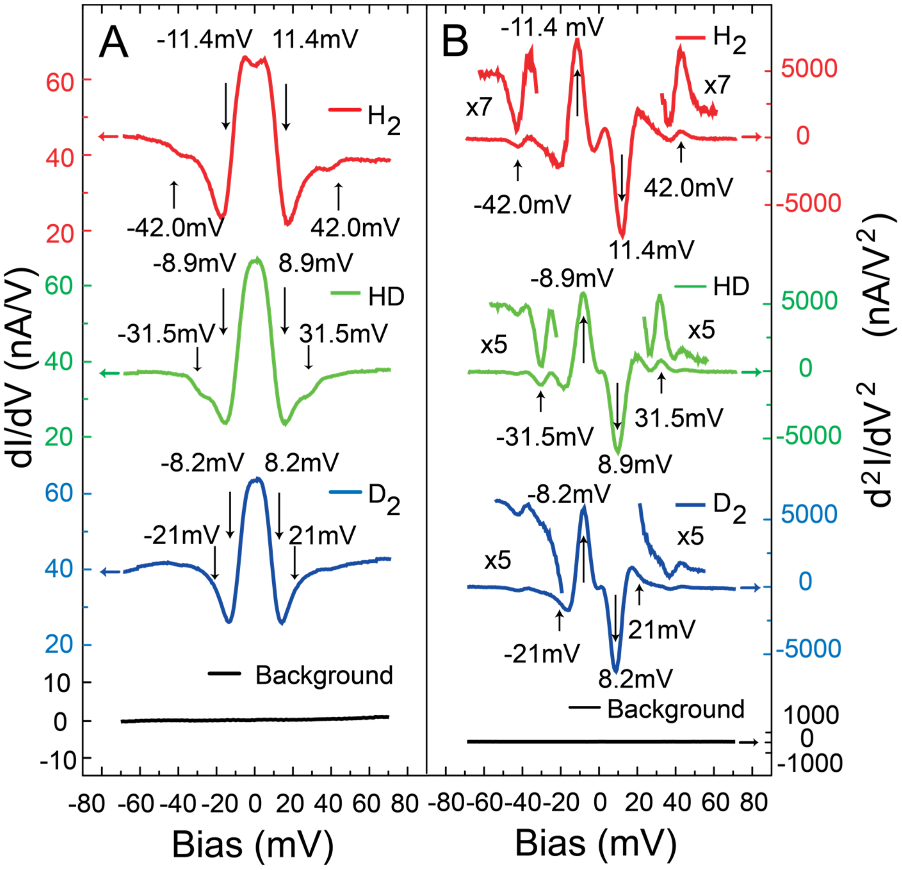A
B
-11.4mV
11.4mV
H2
-42.0mV
42.0mV
-8.9mV
8.9mV
HD
-31.5mV
31.5mV
-8.2mV
8.2mV
D2
-21mV
21mV
Background
dI/dV (nA/V)
60
40
20
10
0
-10
Bias (mV)
-80 -60 -40 -20 0 20 40 60 80
-11.4 mV
x7
11.4mV
x5
5000
0
-5000
1000
-1000
d2I/dV2 (nA/V2)

The rotational energy is directly related to the principal moment of inertia of the molecule and, therefore, to its structure [30]. Rotational spectroscopy with the STM can be used to probe changes in the structure of a single molecule due to its coupling to its environment. The rotational excitation energies in Fig. 2.2 are slightly smaller than the theoretical result for a free molecule (42.0 vs. 43.9 mV for H_2 and 31.5 vs. 33.1 mV for HD) or the experimental data measured for an ensemble of molecules by EELS (44 mV for H_2 [9,31]). These deviations are presumably caused by changes in the molecular structure due to the coupling of the molecule to the tip. The effect of this coupling can be systematically investigated by varying the tip-substrate separation which is controlled by setting the sample bias and tunneling current. As the sample bias decreases from 120 mV to 5 mV while keeping the tunneling current constant at 2 nA, the tip is moved toward the surface by approximately 1 Å (the tip-substrate separation changes from 7.5 Å to 6.5 Å). Both the vibrational and rotational excitation energies change during this process. The v=0⟶1 vibrational excitation energy of H_2 increases from 7.5 mV to 18 mV (Fig. 2.3.D). The tunneling spectra for HD show similar trend when the tip-substrate separation is changed [Fig. 2.3(b)]. The increase of vibration energy suggests an increased binding of the molecule to the substrate, which weakens the H-H bond strength and increases the bond length as predicted by theoretical calculations [32, 33]. DFT calculations of the adsorption energy and H-H bond length at different tip-substrate separations have been performed (Fig. 2.4.A) using the Viena *ab-initio* simulation package (VASP) at the level of vdW-DF2. A Morse potential like adsorption energy curve is revealed which further confirms that van der Waals interactions are dominant in this weakly bonding system. According to the calculation, the H-H bond length increases from 0.750 Å to 0.765 Å when the tip-substrate separation decreases from 7.5 Å to 6.5 Å. In agreement with the DFT calculations, the rotational excitation energy of H_2 decreases from 43 mV to 41 mV (Fig. 2.3.C) as the tip-substrate separation

FIG. 2.3. IETS at different tip-substrate separations. (A-B) d^2I/dV^2 spectra taken at different tip-substrate separation for H_2(A) and HD (B). The sample bias V_B is changed from 5 mV (bottom) to 120 mV (top) in (A) and from 5 mV (bottom) to 70 mV in (B). I_T is kept at 2 nA for all these spectra. A z-V curve is measured to convert the change in V_B to the corresponding change in the tip-substrate separation (△z). The tunneling gap distance at V_B=5 mV and I_T=2 nA is used as the reference point (△z=0). The uncertainty in △z is around 0.095 Å. The shifting of the rotational and vibrational excitation energies is indicated by the dashed lines. The magnified line shapes of the rotational excitation are also presented. (C) The j=0⟶2 excitation energy increases from 41 mV to 43 mV as △z increases by 1 Å. The horizontal dashed line indicates for reference the excitation energy of a free molecule. (D) The v=0⟶1 excitation energy decreases from 18 mV to 7.5 mV as △z increases by 1 Å for H_2, and from 15 mV to 8mV as △z increases by 0.8 Å for HD.

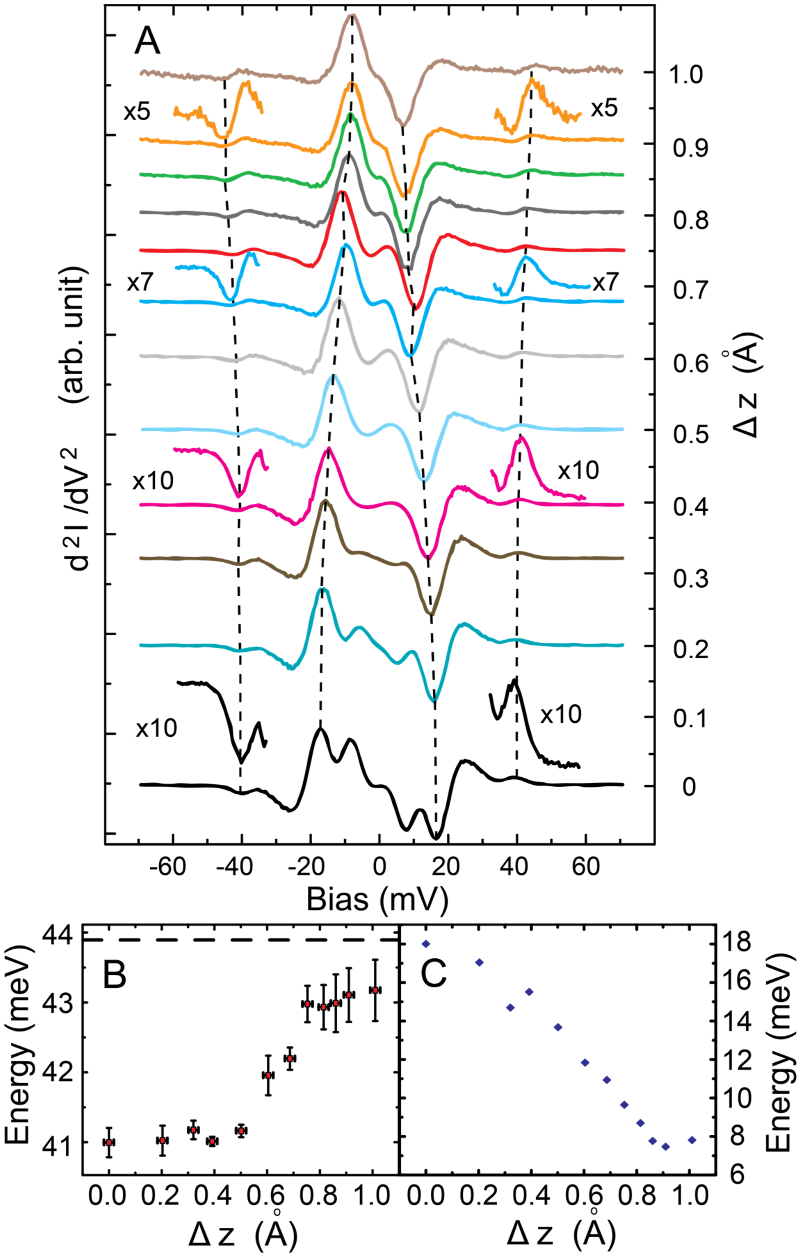
A
x5
x5
x7
x7
x10
x10
x10
x10
d²I /dV² (arb. unit)
Δz (Å)
1.0
0.9
0.8
0.7
0.6
0.5
0.4
0.3
0.2
0.1
0
-60
-40
-20
0
20
40
60
Bias (mV)
B
Energy (meV)
41
42
43
44
0.0
0.2
0.4
0.6
0.8
1.0
Δz (Å)
C
Energy (meV)
6
8
10
12
14
16
18
0.0
0.2
0.4
0.6
0.8
1.0
Δz (Å)

decreases by ~1 Å, indicating that the H-H bond length increases from 0.746 Å to 0.766 Å (Fig. 2.4.B). DFT calculations also identified the observed vibrational mode as the bouncing motion of H_2 confined between the Au(110) surface and the tip.

2.4 Conclusions

In summary, the STM has been extended to the study of the rotational excitations of weakly adsorbed molecules, in addition to the detection of vibrational transitions. Rotational spectroscopy at the single molecule level opens a new avenue for chemical identification and measurement of the bond length in a single bond. By squeezing a trapped hydrogen molecule in the tip-substrate junction by decreasing the dimension of the nanocavity, structural changes in a single molecule can be observed by altering the potential experienced by the molecule.

FIG. 2.4. DFT calculations. (A) DFT calculations of the interaction energy between the trapped molecule and the tunneling junction, and H-H bond length at different tip-substrate separation. The blue shaded area indicates the approximate range probed by STM. (B) The H-H bond length, derived from the measured j=0⟶2 excitation energies, decreases from 0.766 Å to 0.746 Å as Δz increases by 1 Å. The dashed line indicates for reference the H-H bond-length of a free molecule.

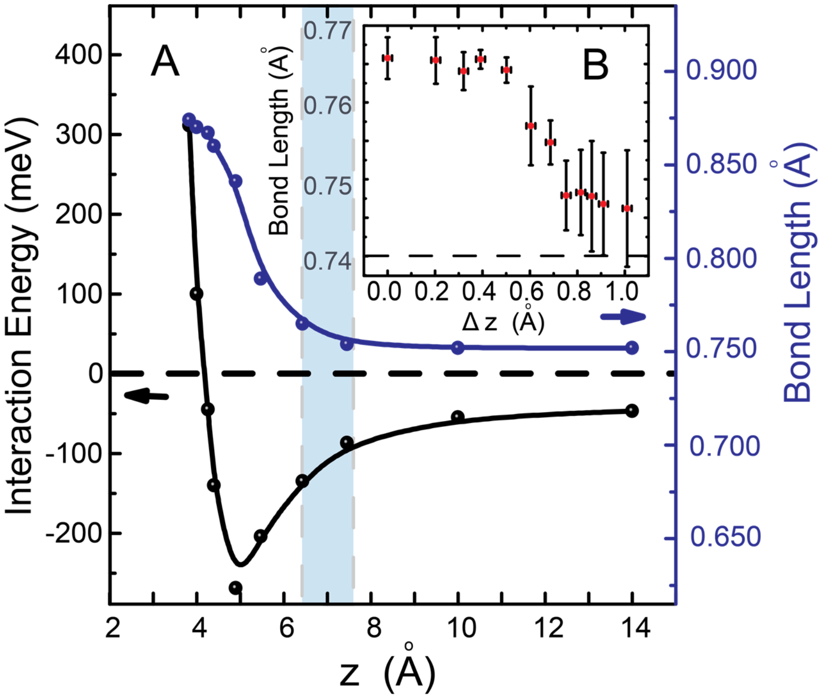
A
B
Interaction Energy (meV)
Bond Length (Å)
z (Å)
Δz (Å)
400
300
200
100
0
-100
-200
2
4
6
8
10
12
14
0.900
0.850
0.800
0.750
0.700
0.650
0.77
0.76
0.75
0.74
0.0
0.2
0.4
0.6
0.8
1.0

Bibliography

[1] R. C. Jaklevic and J. Lambe, Phys. Rev. Lett. **17**, 1139 (1966).

[2] E. B. Wilson Jr., Science **162**, 59 (1968).

[3] P. O. Stoutland, R. B. Dyer, and W. H. Woodruff, Science **257**, 1913 (1992).

[4] R. S. McDonald, Anal. Chem. **58**, 1906 (1986).

[5] P. R. Griffiths, Science **222**, 297 (1983).

[6] K. K. Kohli, Gordon Davies, N. Q. Vinh, D. West, S. K. Estreicher, T. Gregorkiewicz, I. Izeddin, and K. M. Itoh, Phys. Rev. Lett. **96**, 225503 (2006).

[7] C. Schröter, K. Kosma, and T Schultz, Science **333**, 1011 (2011).

[8] B. C. Stipe, M.A. Rezaei, and W. Ho, Science **280**, 1732 (1998).

[9] K. Svensson and S. Andersson, Surf. Sci. **92**, L40 (1997).

[10] J. A. Gupta, C. P. Lutz, A. J. Heinrich, and D. M. Eigler, Phys. Rev. B **71**, 115416 (2005).

[11] J. R. Hahn and W. Ho, Phys. Rev. Lett. **87**, 196102 (2001).

[12] C. Weiss, C. Wagner, C. Kleimann, M. Rohlfing, F. S. Tautz, and R. Temirov, Phys. Rev. Lett. **105**, 086103 (2010).

[13] W. H. A. Thijssen, D. Djukic, A. F. Otte, R. H. Bremmer, and J. M. van Ruitenbeek, Phys. Rev. Lett. **97**, 226806 (2006)

[4] B. C. Stipe, M. A. Rezaei, and W. Ho, Rev. Sci. Instrum. **70**, 137, (1999).

[15] G. Kresse and J. Hafner, Phys. Rev. B **47**, 558 (1993).

[16] G. Kresse and J. Hafner, Phys. Rev. B **49**, 14251 (1994).

[17] G. Kresse and J. Furthmuller, Phys. Rev. B **54**, 11169 (1996).

[18] J. P. Perdew, K. Burke, and M. Ernzerhof, Phys. Rev. Lett. **77**, 3865 (1996).

[19] J. Klimeš, D. R. Bowler, and A. Michaelides, Phys. Rev. B **83**, 195131 (2011).

[20] J. Klimeš, D. R. Bowler, and A. Michaelides, J. Phys.: Cond. Matt. **22**, 022201 (2010).

[21] P. E. Blochl, Phys. Rev. B **50**, 17953 (1994).

[22] G. Kresse and D. Joubert, Phys. Rev. B **59**, 1758 (1999).

[23] H. J. Monkhorst and J. D. Pack, Phys. Rev. B **13**, 5188 (1976).

[24] B. C. Stipe, M.A. Rezaei, and W. Ho, Science **279**, 1907 (1998).

[25] L .J. Lauhon and W. Ho, J. Chem. Phys. **111**, 5633 (1999).

[26] J. K. Gimzewski, C. Joachim, R. R. Schlittler, V. Langlais, and H. Tang, I. Johannsen, Science **281**, 531 (1998).

[27] I. F. Silvera, Rev. Mod. Phys. **52**, 393 (1980)

[28] E. Ilisca, Prog. Surf. Sci. **41**, 217 (1992).

[29] P. Avouris, D. Schmeisser, and J. E. Demuth, Phys. Rev.Lett. **48**, 199 (1982).

[30] B. C. Dian, G. G. Brown, K. O. Douglass, F. S. Rees, J. E. Johns, P. Nair, R. D. Suenram, and B. H. Pate, Proc. Natl. Acad. Sci. U.S.A. **105**, 12696 (2008).

[31] K. Svensson and S. Andersson, Phys. Rev. Lett. **78**, 2016 (1997). .

[32] S. Sakong and A. Groβ, Surf. Sci. **525**, 107 (2003).

[33] A. Groβ, Appl. Phys. A **67**, 627 (1998).

CHAPTER THREE

Rotational Spectromicroscopy: Imaging the Orbital Interaction between Molecular Hydrogen and an Adsorbed Molecule[†]

Abstract

A hydrogen molecule can diffuse freely on the surface and be trapped above an adsorbed molecule within the junction of a scanning tunneling microscope. The trapped hydrogen molecule exhibits the properties of a free rotor. Here we show that the intermolecular interaction between molecular hydrogen and Mg-porphyrin (MgP) can be visualized by imaging the j=0 to 2 rotational excitation of hydrogen. The interaction leads to a weakened H-H bond and modest electron donation from the hydrogen to the lowest unoccupied molecular orbital of MgP, a process similarly observed for the interaction between dihydrogen and an adsorbed Au atom.

[†] This chapter by Shaowei Li, Dingwang Yuan, Arthur Yu, Gregory Czap, Ruqian Wu, and W. Ho is reprinted with permission from in *Physical Review Letters*, Volume 114, pages 206101, 2015.

3.1 Introduction

The nature of the interaction between molecules underlies the understanding of chemistry in diverse fields of chemical synthesis, drug design and molecular electronics [1-3]. The strong covalent bond between molecules has been manipulated and characterized at the single molecule level using the scanning tunneling microscope (STM) [4,5]. The real-space microscopic features possibly resembling the weak intermolecular hydrogen bonds have also been observed using non-contact atomic force microscopy [6], scanning tunneling hydrogen microscopy (STHM) [7], and inelastic tunneling probe (itProbe) [8]. However, the application of real-space visualization of chemical bonding could be enhanced by extending the control and quantifying the intermolecular interactions [9], especially for non-planar geometries between the interacting molecules.

Orbital hybridization and charge transfer are two key mechanisms underlying the interaction between two molecules [4]. The magnesium porphyrin (MgP) molecule can participate as an electron acceptor. In one such instance, a negative ion (MgP^-) is formed by tunneling electrons from the STM tip. This single molecule electron transfer is reversible and can be controlled by choosing the bias between STM tip and substrate [10,11]. In contrast, molecular hydrogen can be an electron donor. Dihydrogen cations (H_2^+) are formed abundantly in the universe from ionization of neutral hydrogen molecules by cosmic rays. The electron from the occupied σ orbital of neutral H_2 ($\sigma_{H\text{-}H}$) can be transferred to an acceptor if the two molecules have a favorable geometry [12, 13]. Consequently, MgP and H_2 can potentially form a donor-acceptor pair and investigation of the interaction between them may reveal insight into the mechanism of intermolecular hybridization and charge transfer.

STM has been used effectively to investigate and manipulate single atoms and molecules. The STM tip and substrate form a nano-cavity in which molecular hydrogen can be trapped at low temperature by van der Waals forces [14-17]. The trapped H_2 is sensitive to its local environment and the spatial variation in the potential energy surface can be quantified by changes in its rotational and vibrational energies [14]. Consequently, we can use the trapped H_2 as a sensor of its environment, such as over another adsorbed molecule to investigate the intermolecular interaction by monitoring the rotational excitation of H_2. The trapping potential moves with the scanning tip. Spatial imaging of the intermolecular interaction between the trapped hydrogen and the underlying molecule can be obtained by rotational spectromicroscopy.

In this letter, we probe the $j=0\longrightarrow2$ rotational excitation of a trapped H_2 over neutral MgP and anionic MgP^- molecules adsorbed on bi-layer alumina (Al_2O_3) grown on NiAl(110) surface. The Al_2O_3 serves as a decoupling layer to suppress the orbital hybridization between adsorbed molecules and the metal substrate (Fig. 3.1.A). The rotational and vibrational spectra of H_2 trapped above a Au adatom on NiAl(110) are also investigated for comparison to MgP adsorbed on alumina. The rotational and vibrational excitation energies are measured by inelastic electron tunneling spectroscopy (IETS) with the STM. The existence of the rotational spectra and the measured energies suggest that the trapped H_2 behaves like a free three-dimensional (3D) rigid rotor, freely translating and rotating on the surface at 10 K. However, the rotational and vibrational energies and line shapes in the d^2I/dV^2 spectra vary as the trapped H_2 experiences spatially dependent interactions with the underlying surface.

3.2 Methods

The experiments were performed using a home-built STM operating at 10 K and a base pressure of 3×10^{-11} Torr [18]. The preparation of the NiAl(110) surface and Al_2O_3 patches follows previously reported procedures [19]. The Ag tip was electrochemically etched. The clean surface at 10 K was dosed *in situ* with MgP and Au. As hydrogen molecules have limited residence time on the Al_2O_3/NiAl(110) surface at 10 K, a background pressure of H_2 is kept at 1×10^{-10} Torr throughout the experiment to maintain a constant population of adsorbed H_2 on the surface following an initial dose at 5×10^{-10} Torr for 5 min. A bias voltage V_B is applied to the sample with the tip connected to the current amplifier at virtual ground.

The calculations are performed using the plane-wave based Vienna ab initio simulation package (VASP) [20-22]. The interaction between the ion and core electrons is described by the projector augmented wave (PAW) method [23]. Plane waves with an energy cutoff of 500 eV are used to expand the Kohn-Sham wave functions. The Ag STM-tip is constructed with 29 Ag atoms, consisting of two Ag(111) layers and an Ag adatom (Fig. 3.4.A). To simulate the adsorption of H_2 molecule in the junction of Ag STM-tip and MgP molecule, we use a cubic supercell of 20 Å in each dimension. To correctly describe the adsorption of H_2 in the junction, the van der Waals correction is included using the optB86b-vdW functional [24,25]. For the large supercell, single Gamma point is used to sample the small Brillouin zone during geometrical optimization, whereas a set of 3×3×3 Monkhorst-Pack k-points is employed [26] for the electronic structure calculations. In our DFT calculations, the distance between the tip and MgP varies from 6.0 to 4.5 Å along the tunneling gap. Most results we discuss in the text are for the tip-molecule distance of 4.5 Å, which best reproduces the experimental conditions.

3.3 Results and Discussion

Due to the inhomogeneity of the alumina film grown on NiAl(110), the MgP molecules adsorb in a variety of geometries, including those which can become negatively charged by

FIG. 3.1. Reversible electron transfer to a single MgP molecule interacting with H_2 in a double barrier tunnel junction of the STM. (A) Schematic diagram of a single molecule double-barrier junction with temporarily trapped H_2. The spectroscopic signal arises from the average of many diffusion and trapping processes for H_2. (B) *dI/dV* spectra measured over a MgP molecule undergoing reversible single electron transfer in the geometry sketched in (A). The inset shows the topographic image of the charged molecule taken with a gap set with $V_B = 1.5$ V and $I_T = 0.1$ nA. The position for recording the *dI/dV* spectra is marked in the topographic image. The red curve is the *dI/dV* spectrum taken when the sample bias is ramped from low to high (Forward) while the black curve is taken with the bias ramped from high to low (Backward). The two vertical arrows mark the positions of sudden conductance change during the forward and backward scans, corresponding to the charging and discharging of the molecule, respectively. The onset of the LUMO of MgP is around 0.5 V, and the onsets for the SUMO and SOMO of MgP^- are around 0.6 V and −0.5 V, respectively.

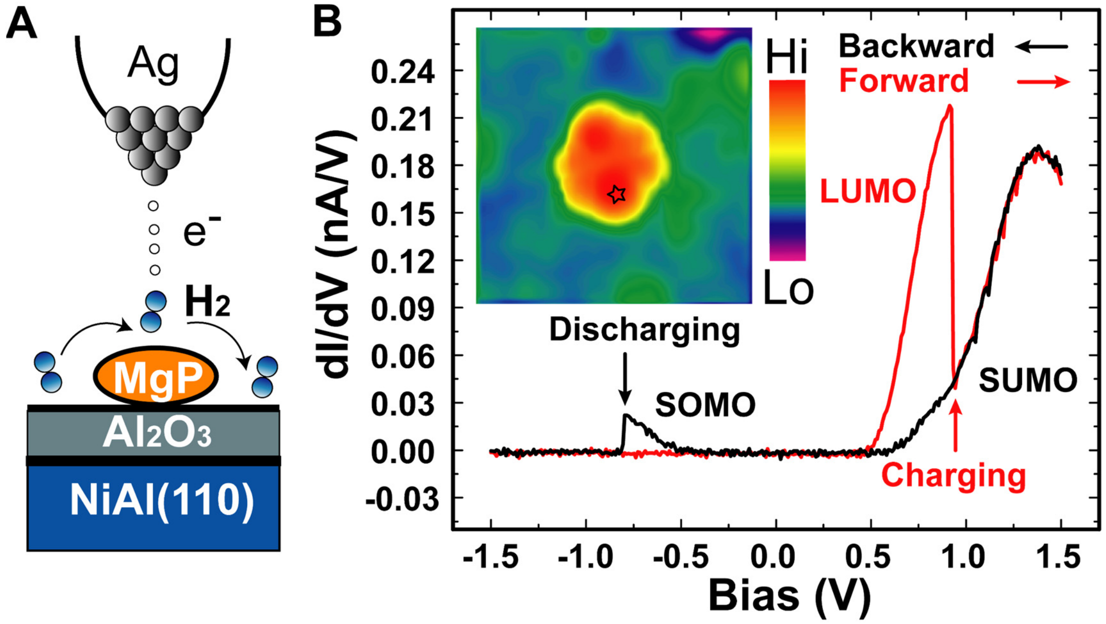
A
Ag
e-
H2
MgP
Al2O3
NiAl(110)
B
Backward ←
Forward →
Hi
Lo
LUMO
Discharging
SOMO
SUMO
Charging
dI/dV (nA/V)
0.24
0.21
0.18
0.15
0.12
0.09
0.06
0.03
0.00
-0.03
-1.5
-1.0
-0.5
0.0
0.5
1.0
1.5
Bias (V)

capturing a tunneling electron from the STM tip [11]. The differential conductance (*dI/dV*) spectra measured over a chargeable MgP show hysteresis during forward and backward scans (ramping V_B up and down). The step-down in the conductance (red vertical arrow in Fig. 3.1.B) appears after the onset of the lowest unoccupied molecular orbital (LUMO, 0.5 V for the molecule shown in Fig. 3.1), indicating that an electron transfer to MgP has occurred through the injection of an electron into the LUMO. The MgP^- is reverted back to the neutral molecule by transferring an electron from its singly occupied molecular orbital (SOMO) to the tip at a negative bias, as indicated by the step-down in the conductance when the bias is ramped backward (black vertical arrow in Fig. 3.1.B). Because the STM images closely follow the electronic structure, the topographic images taken at 0.5 V (LUMO, Fig. 3.2.A) for MgP and 0.9 V [singly unoccupied molecular orbital (SUMO), Fig. 3.2.B] for MgP^- show similar 10-lobes patterns that are in agreement with density functional theory (DFT) calculations [27].

After dosing H_2, IETS measurement over the bare alumina surface shows an inelastic excitation signal at 45.1 meV. This signal is attributed to the $j=0\longrightarrow2$ rotational excitation of molecular hydrogen and has previously been confirmed by isotopic substitution [14, 28]. When the tip is located over one of the prominent lobes in the LUMO of MgP, the $j=0\longrightarrow2$ rotational excitation energy shifts to 42.0 meV. The change in rotational excitation energy can be an indicator of a change in the H-H bond length [14]. The downshift of the rotational excitation indicates a stretched and weakened H-H bond, in response to variations in the interaction potential surface. If the tip is moved toward the center of MgP, spectral features in the IETS become progressively weaker and are not resolved directly over the center of MgP. DFT calculations suggest the 3D rotor behavior of H_2 can only exist over the rim of MgP molecule. The rotational motion is

FIG. 3.2. Rotational spectra of single H_2 molecule interacting locally with MgP measured by STM-IETS. (A-B) Topographic images taken at the onset of MgP LUMO (A) and the onset of MgP^- SUMO (B). The set points are $V_B = 500$ mV, $I_T = 0.1$ nA for (A) and $V_B = 800$ mV, $I_T = 0.1$ nA for (B). (C) The IETS spectra of trapped H_2 taken over different positions over MgP and alumina, as marked in (A). The vertical dashed line indicates the energy of j=0⟶2 rotational excitation of H_2 measured over position 1 of MgP. For all the spectra, the tunneling gap is set with $V_B = 50$ mV and $I_T = 0.1$ nA, and the sample bias is modulated at 345 Hz and 5 mV rms. The spectra are the result of an average of 10 scans. (D) The IETS spectra taken under same set point conditions as in (C) for positions over MgP^- as marked in (B). The spectra are the result of an average of 50 scans. The vertical dashed line indicates the j=0⟶2 rotational excitation of H_2 measured over alumina background.

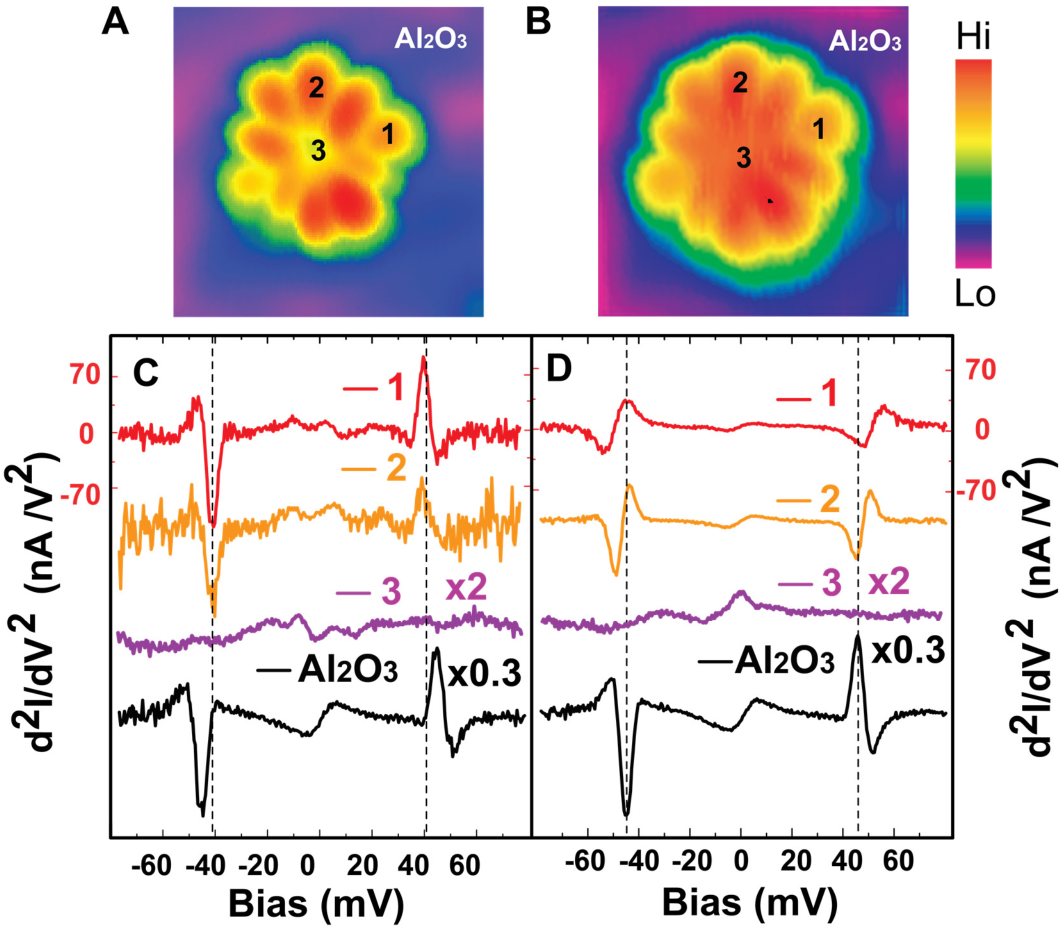
A
B
Al2O3
Al2O3
1
2
3
Hi
Lo
C
D
— 1
— 2
— 3
x2
— Al2O3
x0.3
70
0
-70
d2I/dV2 (nA /V2)
-60 -40 -20 0 20 40 60
Bias (mV)

FIG. 3.3 Single molecule rotational imaging. (A) Constant current topographic image of MgP taken at $V_B = 50$ mV, $I_T = 0.1$ nA. (b-c) Topographic images showing the (B) LUMO of MgP imaged at $V_B = 500$ mV, $I_T = 0.1$ nA, and (C) SUMO of MgP^- imaged at $V_B = 800$ mV, $I_T = 0.1$ nA. The structure of the molecule is superposed on the images. (D) d^2I/dV^2 images taken at 37 mV which is off-resonance of the $j=0\longrightarrow2$ rotational excitation energy of H_2. The image doesn't show obvious structure. (E) d^2I/dV^2 image taken at 42 mV on MgP showing the multi-lobes feature, and additionally the overall size of the image closely follows the molecular skeletal structure superimposed in (B) and (C). (f) d^2I/dV^2 on-resonance image taken at 45 mV on MgP^-. The image also does not reveal clear structure. (G) Calculated partial density of states (PDOS) of the tip-MgP junction (top) and tip-H_2-MgP junction with configuration (*5-d)* in TABLE 3.1. The calculated image of the LUMO for MgP is shown in the inset. The two new features of MgP states (blue solid peaks) in resonance with H_2 states (red dashed peaks) are indicated by arrows in the bottom panel. (H) top view and (I) side view of the charge density difference in the tip-H_2-MgP junction. Yellow region indicates charge accumulation while blue regions indicate charge depletion. The value of isosurface for the charge difference is 0.0004 $bohr^{-3}$. The results repeat in the other three quadrants of the molecule.

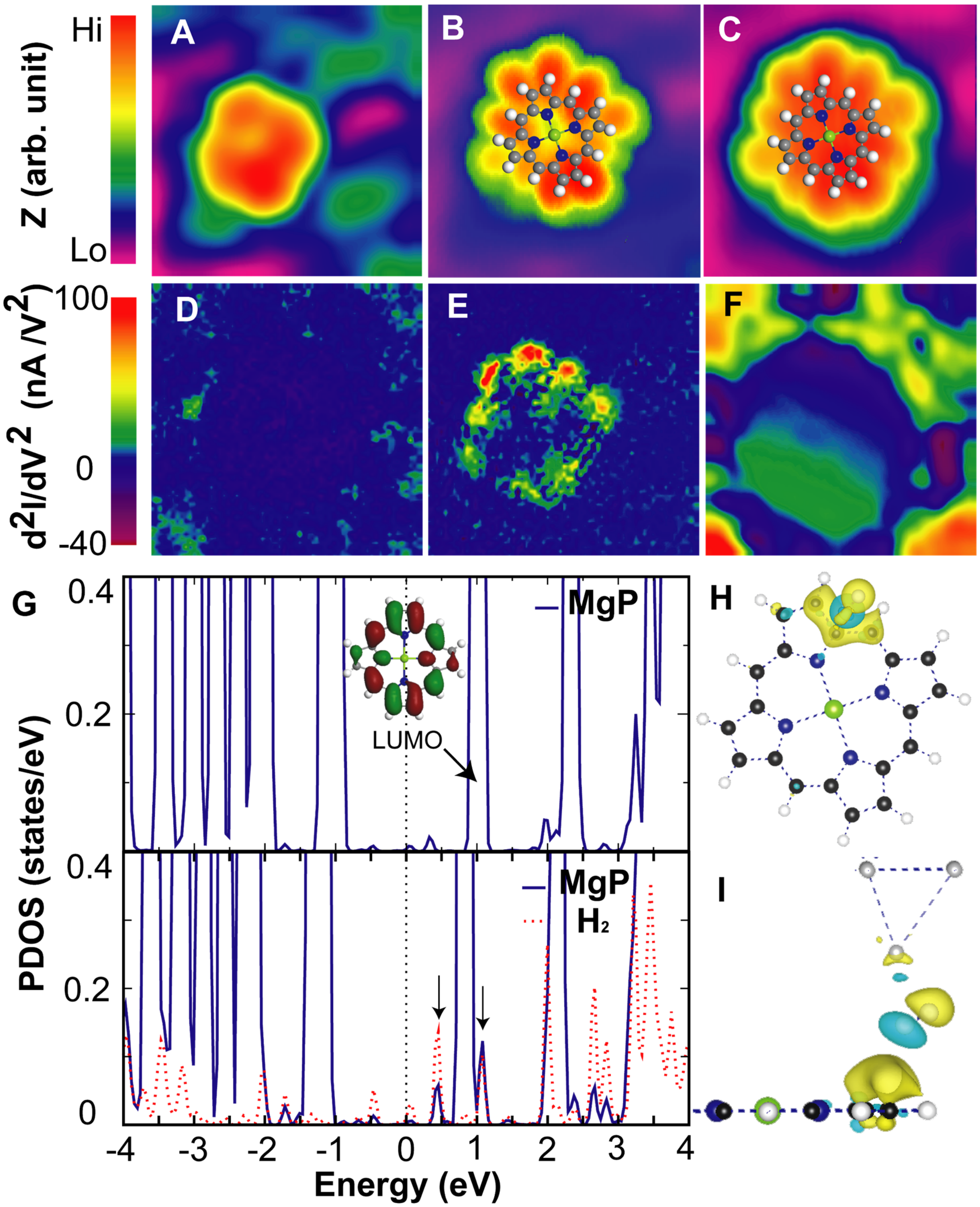
Hi
Z (arb. unit)
Lo
A
B
C
d^{2}I/dV^2 (nA /V^2)
100
0
-40
D
E
F
G
MgP
LUMO
H
PDOS (states/eV)
MgP
H₂
I
0.4
0.2
0
-4
-3
-2
-1
0
1
2
3
4
Energy (eV)

suppressed at the center of MgP due to the large anisotropy energy between the vertical and horizontal adsorption geometries of H_2 in the tunnel junction, causing the absence of the rotational signal in IETS. Variation in the measured rotational excitation energy is not significant over different outer lobes of a MgP molecule [Fig. 3.2(c)]. However, variation in the intensity between the lobes indicates that the interaction between hydrogen and MgP is affected by the anisotropy in the adsorption geometry of MgP.

Rotational imaging reveals the role of molecular orbitals in the interaction between H_2 and MgP by measuring the spatial distribution of the second derivative signal d^2I/dV^2 at the rotational energy of 42 meV (Fig. 3). The junction gap is set with 50 mV sample bias and 0.1 nA tunneling current, followed by disabling the feedback and decreasing the bias to 42 mV to record the second derivative rotational signal which is proportional to the second harmonic output of the lock-in amplifier. The rotational image at 42 mV (Fig. 3.3.E) shows a multi-lobes pattern that closely resembles the LUMO image (Fig. 3.3.B), but is significantly different from the constant-current topographic image taken at 50 mV and 0.1nA (same set point as the rotational image) (Fig. 3.3.A). The spatial contrast can only be observed with the sample bias in resonance with the rotational excitation. The off resonance image at 37 mV is nearly featureless (Fig. 3.3.D). The spatial similarity between the hydrogen rotational image at 42 mV and the MgP LUMO image at 500 mV indicates that the intermolecular hybridization of MgP and H_2 is dominated by the interaction between MgP LUMO and hydrogen orbitals.

The role of charge transfer between MgP and H_2 is further investigated by rotational analysis of the charged MgP^-. The $j=0 \longrightarrow 2$ rotational excitation signal in the IETS over MgP^- is significantly different than over MgP and alumina. The intensity of the rotational excitation signal is lower, possibly because the interaction between MgP^- and H_2 is less attractive. The line shape

FIG. 3.4. MgP over NiAl surface. (a) Schematic diagram of the structural model of DFT calculations. The light blue, gray, dark blue, green, and white balls represent Silver, Carbon, Nitrogen, Magnesium, and Hydrogen atoms, respectively. (b) The five positions where the adsorption energy of H_2 over MgP are calculated. (c) The constant current topographic image of a MgP molecule adsorbed on NiAl(110) surface. $V_B = 50$ mV, $I_T = 0.1$ nA (d) The d^2I/dV^2 spectra taken with a trapped H_2 at different positions over a MgP molecule adsorbed on NiAl(110) as indicated by positions A, B, and C in (c), and over the NiAl substrate. The set point is $V_B = 50$ mV, $I_T = 1$ nA.

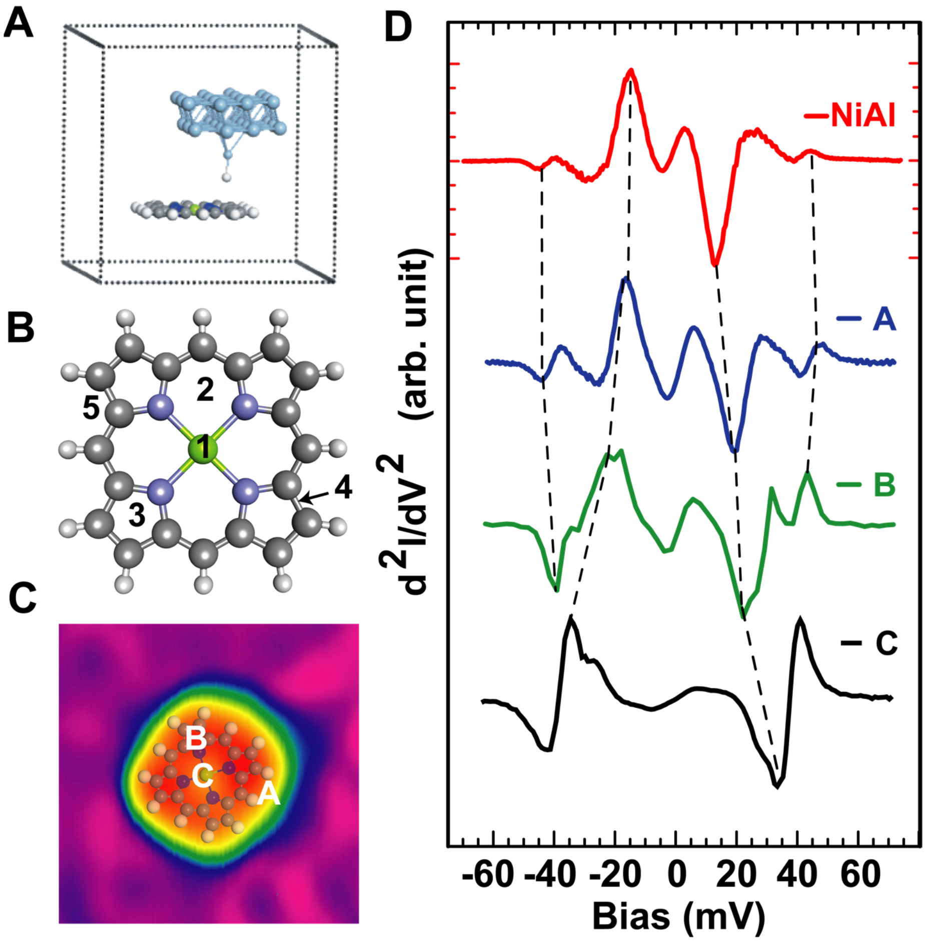
A
B
2
5
1
4
3
C
B
C
A
D
NiAl
A
B
C
d^{2}I/dV^2 (arb. unit)
-60 -40 -20 0 20 40 60
Bias (mV)

of the rotational feature in the d^2I/dV^2 spectrum at positive bias changes from a peak with a side dip (Fig. 3.2.C) into a dip with a side peak (Fig. 3.2.D) with the expected behavior at negative bias, which is possibly due to the change in the coupling of the inelastic and elastic tunneling processes or the local variation of surface potential [29, 30]. Aside from the changes in signal intensity and line shape, the excitation energy doesn't change significantly when the tip is moved from alumina to over MgP^-. The rotational image at 45 mV (Fig. 3.3.F) does not reveal clear features within the molecule. The mismatch between the rotational and the SUMO images demonstrates that the singly unoccupied orbital contributes negligibly to the interaction between H_2 and MgP^-. The major difference in the interaction with H_2 is that MgP is an electron acceptor while MgP^- is an electron donor. In contrast to the SUMO of MgP^-, the LUMO of MgP readily accepts an electron. In the interaction of H_2 with MgP, electrons in the $\sigma_{H\text{-}H}$ partially transfer to the LUMO of MgP [31]. DFT calculations of the projected density of state (PDOS) (Fig. 3.3.G) and charge density difference (Fig. 3.3.H and I] have been performed for the tip-H_2-MgP junction. The Fermi level shifts towards the LUMO when interacting with H_2, compared to the H_2-free junction. Two extra peaks (two vertical arrows in Fig 3.3.G) next to the LUMO of MgP confirm the hybridization between the MgP-LUMO and H_2 orbitals. Calculated charge density difference confirms the electron transfer from H_2 to MgP. The spatial distribution of the transferred charge closely follows the LUMO lobes (Fig. 3.3.H and I).

The intensity in the rotational image [Fig 3(e)] is observed to lie in the outer region of the molecule. The j=0⟶2 rotational excitation signal in the IETS becomes progressively weaker and is not detected over the center of MgP. The Ag tip is situated at five positions over the MgP molecule, as indicated in Fig. 3.4.B, to investigate the interaction between the H_2 and MgP with DFT. The results calculated for the interaction are tabulated in Table. 3.1. The adsorption energy of H_2 (E_{ad}) is determined by $E_{ad} = E_{H_2/tip+MgP} - E_{tip+MgP} - E_{H_2}$, where $E_{H_2/tip+MgP}$, $E_{tip+MgP}$, and E_{H_2} are the total energies of the tip-H_2-MgP junction, tip-MgP junction, and isolated H_2, respectively. The positions of atoms in the Ag tip and the MgP molecule are fixed during the optimization of the adsorption configuration of H_2. Calculations indicate that the adsorption energy of H_2 sensitively depends on the orientation of H-H bond at positions 1-4, where the rotation of H_2 is effectively hindered due to large energy anisotropy. At the edge of MgP (position 5), H_2 interacts with MgP but may still freely rotate due to the smallest energy anisotropy. Therefore, the intensity of the rotational image of MgP (Fig 3.3.E) is very low near the center of MgP.

The d^2I/dV^2 spectra of H_2 over MgP adsorbed on NiAl(110) are presented in Fig. 3.4.D. Besides the rotational signal around 44 mV, the spectra also show strong vibrational features of H_2 over MgP. The vibrational energy significantly increases as the tip moving from the edge toward the center of MgP; this trend is also observed as the tip moving toward the center of an Au atom adsorbed on the NiAl(110) surface. The weak H_2 rotational feature is eventually overwhelmed by the vibrational signal over the Mg atom. The increase of vibration energy can be correlated with an increase of H_2 adsorption energy, which would hinder the rotational motion of H_2 near the center of MgP, leading to the suppression of the rotational excitation signal. Since the selection rule of STM-IETS is still being discussed in the literature [32], the reason for the absence of vibrational signals over Al_2O_3 requires further theoretical investigation beyond the scope of the present work.

The MgP molecules are adsorbed on an inhomogeneous Al_2O_3 layer grown on NiAl(110). The asymmetry of the multiple lobes in the rotational image of Fig. 3.3.E is due to the non-uniform coupling of MgP to the inhomogeneous substrate, resulting in a non-planar geometry for the MgP and hence asymmetric interaction with the hydrogen. The asymmetry is not due to tip effect or

FIG. 3.5. IETS measurements of trapped H_2 at different tip-substrate separations over MgP (A) and MgP^- (B). The bottom spectra are taken at $V_B = 50$ mV and $I_T = 0.1$ nA. The change in tip-substrate separation (Δz) is converted from the exponential dependence of the potential barrier height and the tunneling current. The spectra in (A) are the result of an average of 10 scans. The middle and bottom spectra in (B) are the result of an average of 50 scans, while the top spectrum is from a single scan. (C-D) Rotational d^2I/dV^2 images taken over two different MgP molecules at the same set point as Fig. 3.3.E. Multiple lobes are resolved but the molecules are less stable and switched during the scan. (E) Rotational d^2I/dV^2 image taken over the same MgP as for Fig. 3.3.E at 43 mV, with a larger tip-substrate gap set by $V_B = 100$ mV and $I_T = 0.1$ nA, hence the inferior quality of the image.

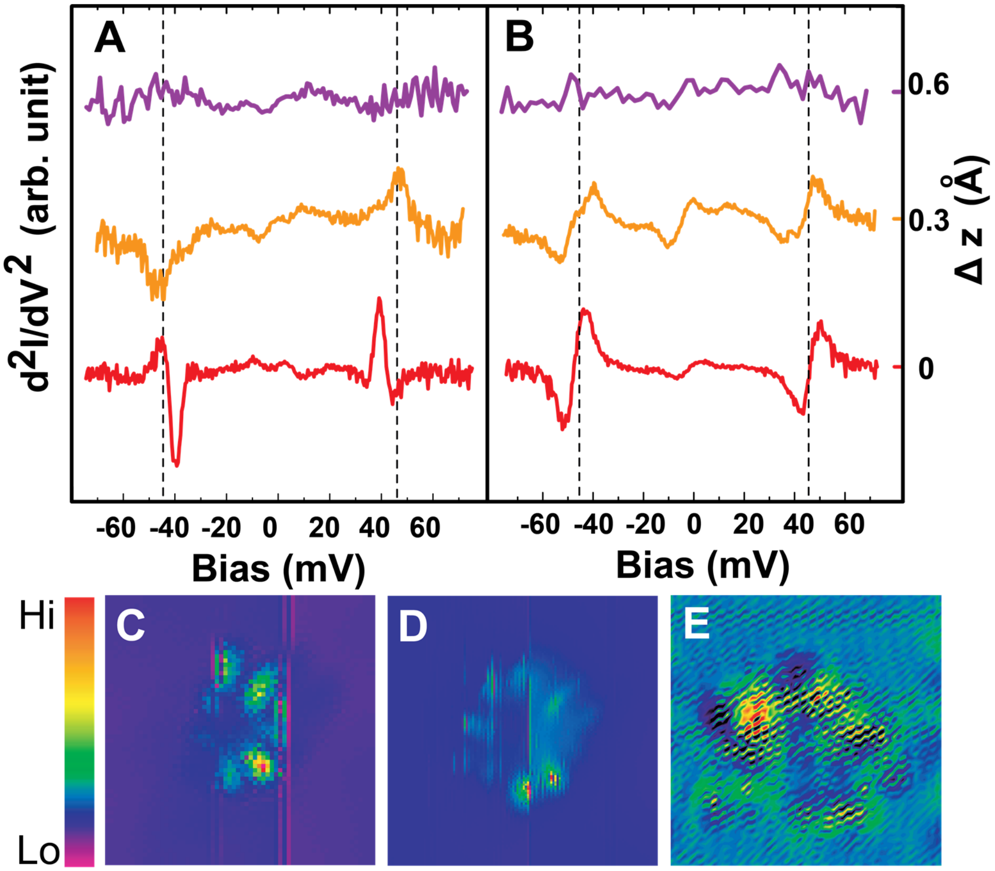
A
B
d^2I/dV^2 (arb. unit)
Δ z (Å)
0.6
0.3
0
-60 -40 -20 0 20 40 60
Bias (mV)
-60 -40 -20 0 20 40 60
Bias (mV)
Hi
Lo
C
D
E

lack of quality of the image and is a real effect. We used different tip-substrate distance and the image shown in Fig. 3.3.E has the best qualify corresponding to the optimized tip-substrate distance. The inhomogeneous Al_2O_3 surface also causes variations in the adsorption geometry and stability of different molecules, leading to the observed changes in the relative intensity of the lobes in the rotational image for different molecules.

The interaction between trapped H_2 and MgP is also sensitive to the distance between two molecules. The precise control of STM tip position allows us to modify the intermolecular distance by changing the tip-substrate separation. The IETS measurement of trapped H_2 over MgP and MgP^- at different tip-substrate separations are shown in Fig. 3.5. When the tip-substrate separation increases from $V_B = 50$ mV and $I_T = 0.1$ nA set point by 0.3 Å, the H_2 rotational excitation energy shifts from 42meV to around 45 meV over MgP. However, the change in spectral features over MgP^- is less obvious when the tip-substrate separation is changed by the same amount. The changes of rotational spectra with tip-substrate separation provide another indication that H_2-MgP interaction is stronger than H_2-MgP^- interaction. If the tip-substrate separation increases by 0.6 Å, both the spectra over MgP or MgP^- become structureless, possibly due to the low probability of trapping a hydrogen molecule in the tip-substrate gap when the separation is large. Faint multiple lobes in the rotational image over MgP start to appear at $V_B = 100$ mV and $I_T = 0.1$ nA set point (Fig. 3.5.E), and become more prominent when the tip-substrate distance decreases (Fig. 3.5.C-D, Fig. 3.3.E). However, the molecules become unstable as the tip-substrate distance continues to decrease, thus limiting spectromicroscopic measurements.

The calculated partial densities of states at different tip-substrate separations are presented in Fig. 3.6. The presence of H_2 in the junction also shifts the Fermi level of MgP towards its

FIG. 3.6. Calculated partial density of states under different conditions for the tip-MgP junction (A) and tip-H_2-MgP junction (B-C). The distance between tip and MgP is set at 4.5 Å for (A) and (C), and 6 Å for (B). The Fermi level is indicated by the black dashed line. The H_2 molecule follows the configuration *(5-d)* in TABLE 3.1.

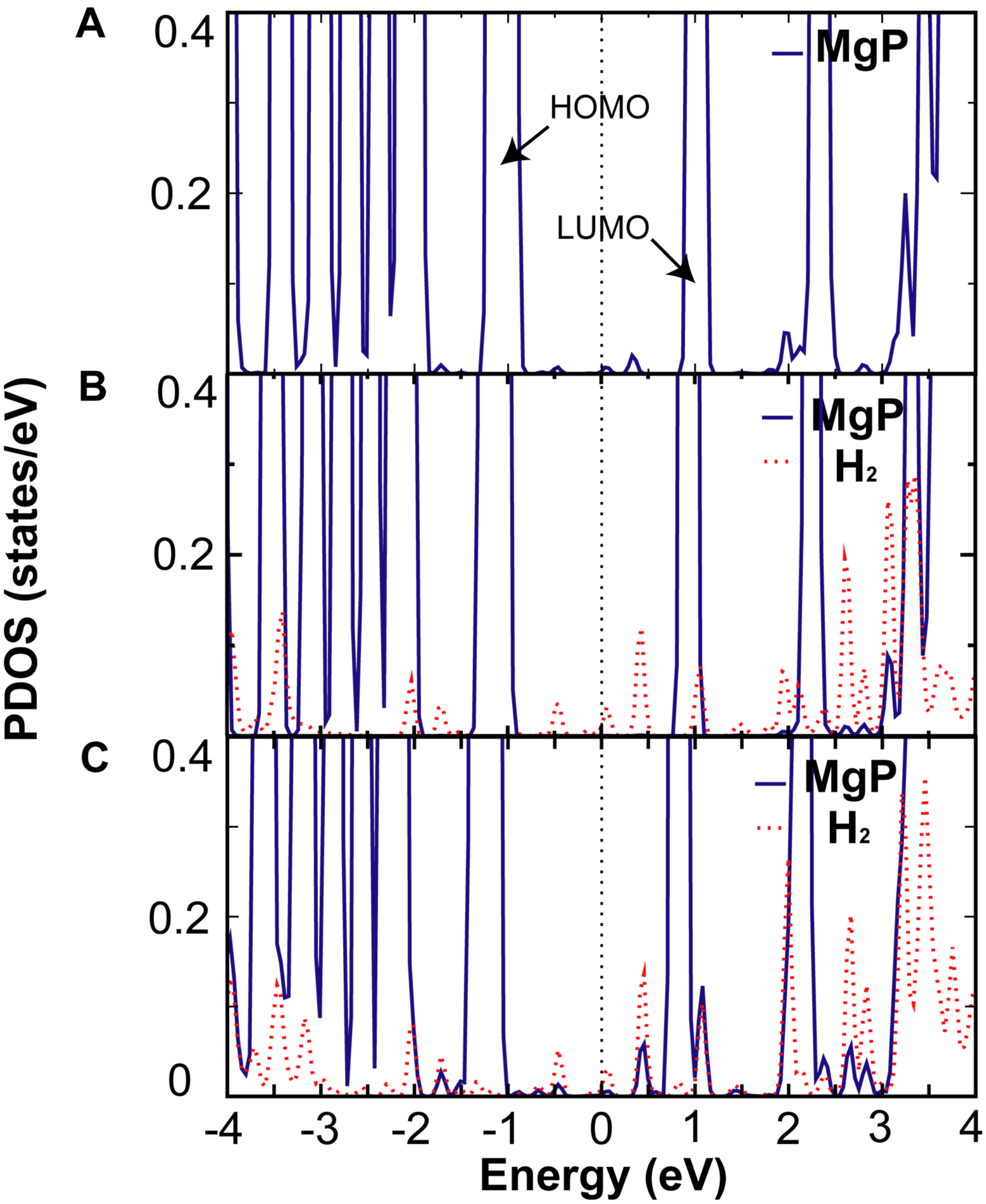
A
B
C
0.4
0.2
0
MgP
H₂
HOMO
LUMO
PDOS (states/eV)
-4
-3
-2
-1
0
1
2
3
4
Energy (eV)

LUMO at 6 Å tip-substrate distance compared to the H_2-free junction at 4.5 Å tip-substrate distance demonstrating the change in electrostatic level is due to the MgP-H_2 interaction instead of MgP-tip interaction. A larger shift is observed when MgP is interacting with H_2 in a 4.5 Å separation junction. This further demonstrates that the interaction mainly depends on the distance between MgP and H_2, and the hybridization with STM tip is not important.

We also study the interaction between H_2 and a single Au atom, another electron acceptor, to further validate H_2 as an electron donor. Electron transfer to a single Au atom to form Au^- has been shown to occur on the surface of NaCl film grown on Cu(100) [33]. The IETS measurement over NiAl(110) shows strong vibrational excitation signal at 15.2 mV for the H_2-surface bouncing mode and a relatively weaker rotational feature at 44.8 mV [Fig. 3.7]. When the tip is located over an Au atom adsorbed on NiAl(110), the rotational excitation energy decreases to 40.1 meV and the vibrational excitation energy increase to 20.0 meV [Fig. 3.7.A]. The increase in the vibrational energy coupled to the decrease in the rotational energy suggests a strengthened H-metal bond and a weakened H-H bond when the tip is positioned over the Au adatom [14]. These results strengthen the conclusion that the H_2 molecule acts as an electron donor and favorably interacts with an electron acceptor.

3.4 Conclusions

In summary, hydrogen rotational spectromicroscopy provides a novel approach for visualizing and quantifying the intermolecular interaction between H_2 over another adsorbed molecule. The ability of the tip to trap a hydrogen molecule as it scans over another adsorbed molecule combined with the sensitivity of the hydrogen rotational excitation recorded by IETS to

FIG. 3.7. Spectral shifts over an Au adatom. (A) d^2I/dV^2 spectra of H_2 trapped over NiAl(110) substrate (top spectrum) and an Au adatom (middle spectrum). The j=0⟶2 rotational excitation energy of H_2 is 44.8 meV over NiAl(110) substrate and 40.1 meV over Au adatom. The v=0⟶1 vibrational excitation energy of the H_2-surface bouncing mode is 15.2 meV over NiAl(110) substrate and 20.0 meV over Au adatom. The d^2I/dV^2 spectra (BK) taken before dosing H_2 and over NiAl (bottom spectrum) is nearly featureless. All the spectra are taken with set point V_B = 50 mV, I_T = 1 nA. (B) Topographic image of Au adatoms on NiAl(110); Au adatom (marked by dotted box) appears as a small round protrusion. The larger square protrusions are adsorbed MgP molecules. (C) Zoom in topographic image of the Au adatom marked in (B). The set point is V_B = 100 mV, I_T = 0.1 nA for both (B) and (C).

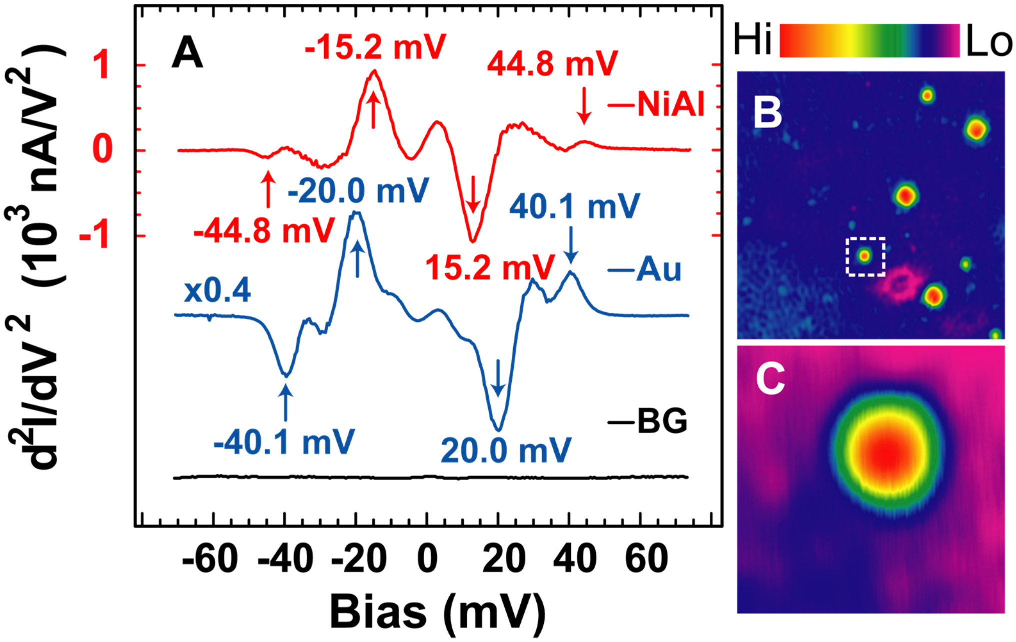
A
-15.2 mV
44.8 mV
—NiAl
-44.8 mV
-20.0 mV
15.2 mV
40.1 mV
—Au
x0.4
-40.1 mV
20.0 mV
—BG
1
0
-1
d^2I/dV^2 (10^3 nA/V^2)
-60 -40 -20 0 20 40 60
Bias (mV)
Hi
Lo
B
C

its immediate environment leads to the implementation of rotational spectromicroscopy. Here we apply this new probe to image the interaction between a hydrogen molecule on top of (instead of next to) a MgP on Al_2O_3 surface. The similarity between the hydrogen rotational image and the LUMO image of MgP suggests that hydrogen orbitals interact with the LUMO of MgP. This conclusion is based on the expectation that the rotational intensity tracks the preferable location of the freely rotating hydrogen over the molecule, and the shift in the rotational energy reflects the change in H-H bond strength. In contrast, the coupling is not favored between hydrogen and the SUMO of anionic MgP^{-}. The electron transfer from σ_{H-H} to the empty LUMO in the neutral MgP is critical in this donor-acceptor interaction. The σ-donor nature of H_2 is further confirmed by DFT calculations as well as its interaction with an electronegative Au atom adsorbed on the NiAl(110) surface. The rotational spectromicroscopy extends the study of intermolecular interactions in the direction perpendicular to the surface.

TABLE 3.1. DFT results of H_2 adsorption energies at different positions over MgP as indicated in Fig. 3.4.B. The distance between tip and substrate is set at 4.5 Å.

	H-H parallel to the MgP plane	**H-H tilted from the MgP plane**	
Tip at position 1	$1-a$ $E_{ad}=-0.167$ eV 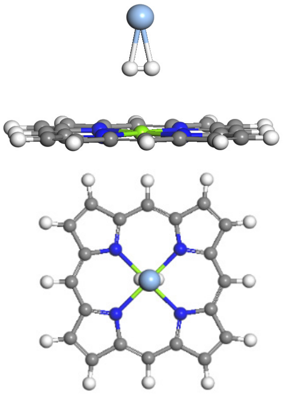	$1-b$ $E_{ad}=-0.116$ eV 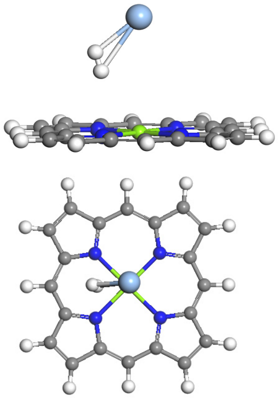	
Tip at position 2	$2-a$ $E_{ad}=-0.176$ eV 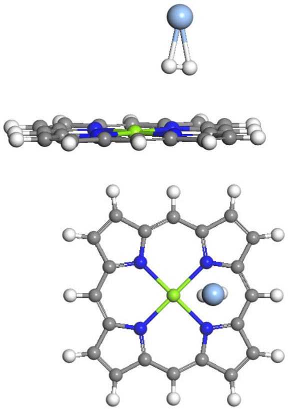	$2-b$ $E_{ad}=-0.156$ eV 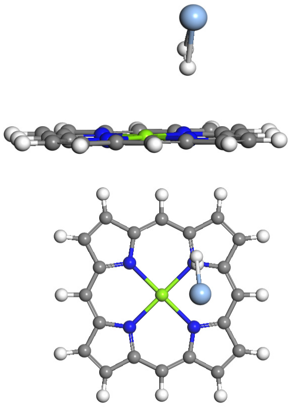	$2-c$ $E_{ad}=-0.137$ eV 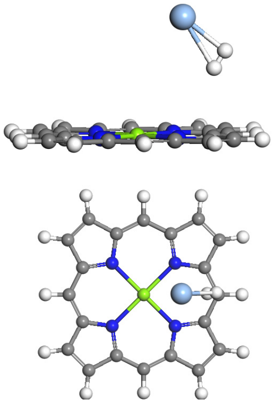
		$2-d$ $E_{ad}=-0.151$ eV 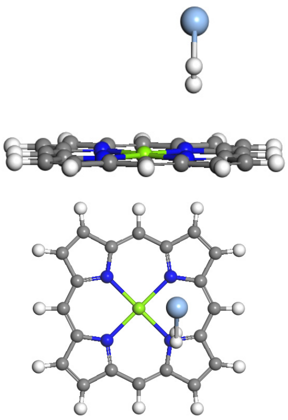	$2-e$ $E_{ad}=-0.158$ eV 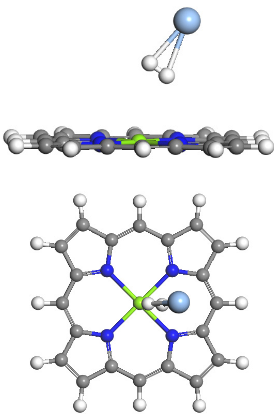

	H-H parallel to the MgP plane	**H-H tilted from the MgP plane**	
Tip at position 3	$3-a$ $E_{ad}=-0.200$ eV 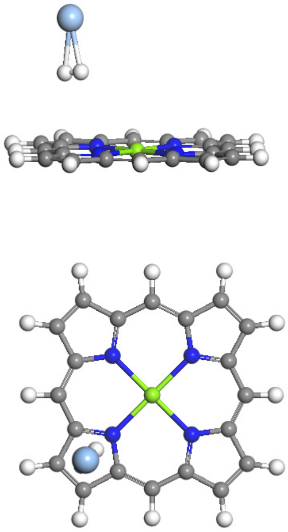	$3-b$ $E_{ad}=-0.126$ eV 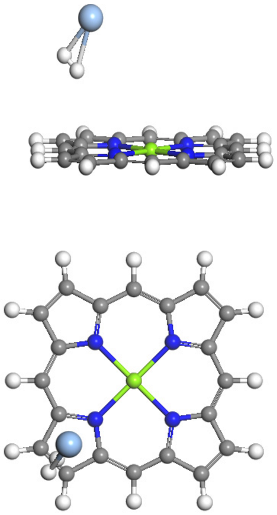	$3-c$ $E_{ad}=-0.150$ eV 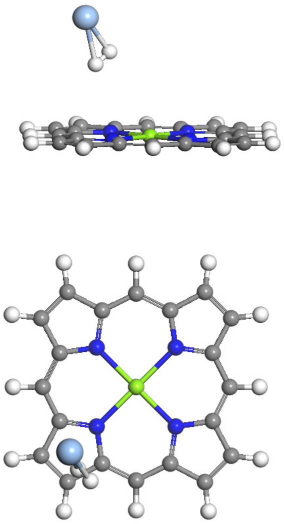
		$3-d$ $E_{ad}=-0.165$ eV 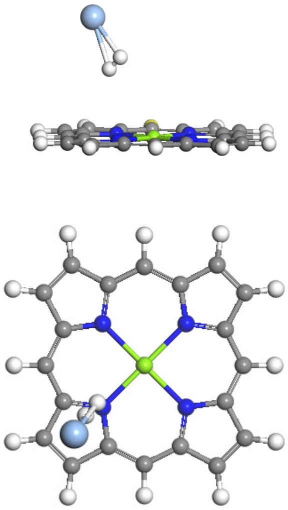	$3-e$ $E_{ad}=-0.149$ eV 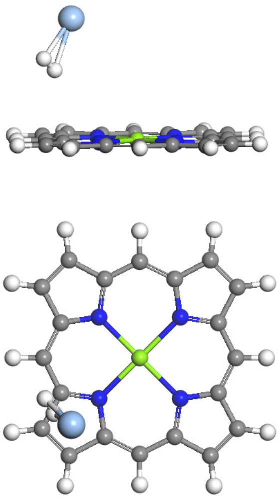

	H-H parallel to the MgP plane	**H-H tilted from the MgP plane**	
Tip at position 4	$4-a$ $E_{ad} = -0.168$ eV 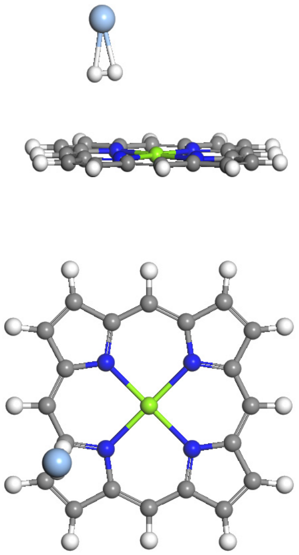	$4-b$ $E_{ad} = -0.140$ eV 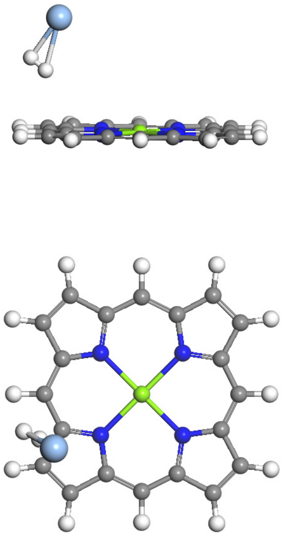	$4-c$ $E_{ad} = -0.162$ eV 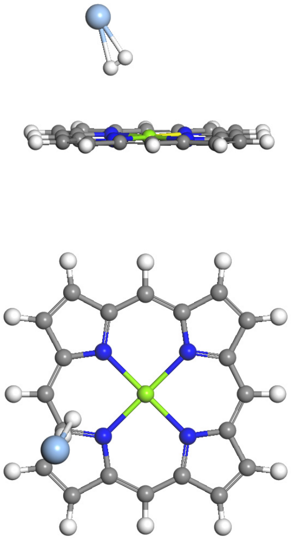
		$4-d$ $E_{ad} = -0.181$ eV 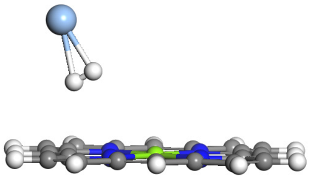	$4-e$ $E_{ad} = -0.125$ eV 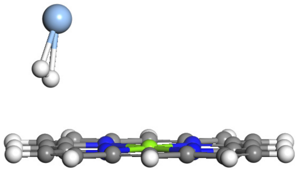

	H-H parallel to the MgP plane	**H-H tilted from the MgP plane**	
Tip at position 5	$5-a$ $E_{ad} = -0.143$ eV 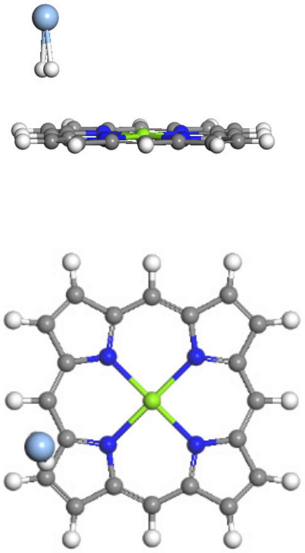	$5-b$ $E_{ad} = -0.156$ eV 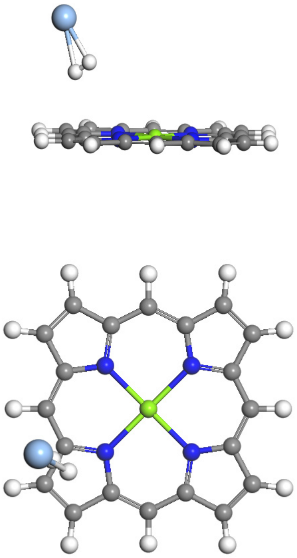	$5-c$ $E_{ad} = -0.129$ eV 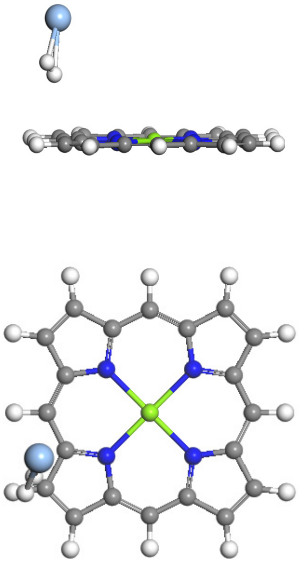
		$5-d$ $E_{ad} = -0.148$ eV 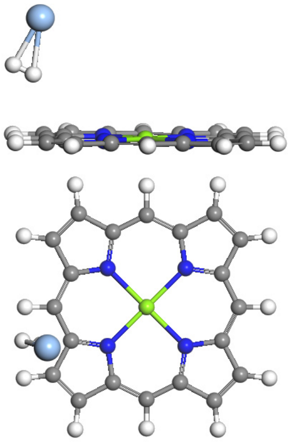	$5-e$ $E_{ad} = -0.148$ eV 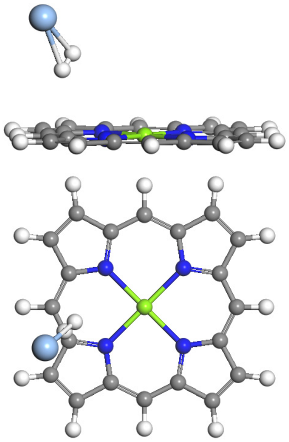

Bibliography

[1] S. L. Cockrofta and C. A. Hunter, Chem. Soc. Rev. **36**, 172 (2007).

[2] J. K. Gimzewski and C. Joachim, Science **283,** 1683 (1999).

[3] A. E. Reed, L. A. Curtiss, and F. Weinhold, Chem. Rev. **88**, 899 (1988).

[4] H. J. Lee and W. Ho, Science **26**, 1719 (1999).

[5] Y. Jiang, Q. Huan, L. Fabris, G. C. Bazan, and W. Ho, Nature Chem. **5**, 36 (2013).

[6] J. Zhang, P. Chen, B Yuan, W. Ji, Z. Cheng, and X. Qiu, Science **342**, 611 (2013).

[7] C. Weiss, C. Wagner, R. Temirov, and F. S. Tautz, J. Am. Chem. Soc. **132**, 11864 (2010).

[8] C. Chiang, C. Xu, Z. Han, and W. Ho, Science **344**, 885 (2014).

[9] C. A. Hunter, Angew. Chem. Int. Ed. **43**, 5310 (2004).

[10] S. W. Wu, N. Ogawa, and W. Ho, Science **312**, 1362 (2006).

[11] S. W. Wu, N. Ogawa, G. V. Nazin, and W. Ho, J. Phys. Chem. C, **112**, 5241 (2008).

[12] W. L. Yim, J. S. Tse, and T. Iitaka, Phys. Rev. Lett. **105**, 215501 (2010).

[13] C. S. Carr and J. B. Hughes, Environ. Sci. Technol., **32**, 1817 (1998).

[14] S. Li, A. Yu, F. Toledo, Z. Han, H. Wang, H. Y. He, R. Wu, and W. Ho, Phys. Rev. Lett. **111**, 146102 (2013).

[15] J. A. Gupta, C. P. Lutz, A. J. Heinrich, and D. M. Eigler, Phys. Rev. B **71**, 115416 (2005).

[16] C. Weiss, C. Wagner, C. Kleimann, M. Rohlfing, F. S. Tautz, and R. Temirov, Phys. Rev. Lett. **105**, 086103 (2010).

[17] G. Kichin, C. Wagner, F. S. Tautz, and R. Temirov, Phys. Rev. B **87**, 081408 (2013).

[18] B. C. Stipe, M. A. Rezaei, and W. Ho, Rev. Sci. Instrum. **70**, 137, (1999).

[19] X. H. Qiu, G.V. Nazin, and W. Ho, Science **299**, 542, (2003).

[20] G. Kresse and J. Hafner, Phys. Rev. B **47**, 558 (1993).

[21] G. Kresse and J. Hafner, Phys. Rev. B **49**, 14251 (1994).

[22] G. Kresse and J. Furthmuller, Phys. Rev. B **54**, 11169 (1996).

[23] P. E. Blochl, Phys. Rev. B **50**, 17953 (1994).

[24] J. Klimeš, D. R. Bowler, and A. Michaelides, Phys. Rev. B **83**, 195131 (2011).

[25] J. Klimeš, D. R. Bowler, and A. Michaelides, J. Phys.: Cond. Matt. **22**, 022201 (2010).

[26] H. J. Monkhorst and J. D. Pack, Phys. Rev. B **13**, 5188 (1976).

[27] J. B. Maddox, U. Harbola, K. Mayoral, and S. J. Mukamel, Phys. Chem. C **111**, 9516 (2007).

[28] F. D. Natterer, F. Patthey, and H. Brune, Phys. Rev. Lett. **111**, 175303 (2013).

[29] N. Lorente and M. Persson, Phys. Rev. Lett. **85**, 2997 (2000).

[30] F. D. Natterer, F. Patthey, and H. Brune, ACS Nano **8**, 7099 (2014).

[31] G. J. Kubas, Proc. Natl. Acad. Sci. U.S.A. **104**, 6901 (2007).

[32] N. Lorente, M. Persson, L. J. Lauhon, and W. Ho, Phys. Rev. Lett. **86**, 2593 (2001).

[33] J. Repp, G. Meyer, F.E. Olsson, and M. Persson, Science **305**, 493 (2004).

CHAPTER FOUR

Single Molecule Mechanochemistry[†]

Abstract

Bond dissociation by scanning tunneling microscope (STM) has traditionally been induced by energetic tunneling electrons. In contrast, we found that the reciprocating movement of the tip of an STM can also be used to initiate the dissociation of a single hydrogen molecule sandwiched between the silver tip and copper substrate. The extraordinary catalytic activity was measured for a single carbon monoxide molecule, while a single gold atom is found to be an inhibitor. This work provides insight into mechanochemistry at the atomic scale and shows that a single diatomic molecule can act as a molecular catalyst to enhance the reaction rate on a surface.

[†] This chapter by Shaowei Li, Yanxing Zhang, Arthur Yu, Dingwang Yuan, Gregory Czap, Hikari Kimura, Ruqian Wu, and W. Ho is in preparation for submission.

4.1 Introduction

Mechanochemistry refers to the coupling of mechanical motion (e.g., squeezing, shearing, stretching, grinding and milling) and chemical reaction at the molecular level. Growing interests about mechanochemical activation of the catalyst are driven by the potential needs for energy production and environmental protection applications [1-3]. Although significant progress has been made through fundamental and industrial explorations, the underlying mechanism of mechanochemistry is still somewhat elusive due to the technical difficulties to control and visualize the reaction processes in most experimental measurements [4]. The scanning tunneling microscope (STM), an apparatus originally designed for imaging surface structures with atomic scale resolution but later adapted for spectroscopic and dynamic studies, offers an opportunity for the understanding of mechanochemistry by controlling and observing chemical reactions in nanocavities formed by STM tip and the substrate [5, 6,]. In general, the tip and substrate can act as two grinding balls in a mill jar, and the mechanical motion of the tip can effectively squeeze molecules under it [7, 8]. An unparalleled advantage of STM over traditional tools for studying mechanochemistry is its spatial resolution at the single molecule scale. It provides the means to separately probe the effect of various factors on a mechanochemical reaction to establish clear physical insight into its mechanism.

Hydrogen dissociation is one of the simplest chemical reactions and is the precursor step for many hydrogenation reactions that are of great importance in chemical science, nano science and life science [9, 10, 11, 12]. Here, we use hydrogen dissociation on Cu(001) as a prototypical reaction for studies of mechanochemistry and demonstrate that the mechanical motion and hot electron injection from the tip can both initiate the H-H bond activation. Since the occupation of the antibonding σ orbital of H_2 plays a key role in the bond breaking [13], we modify the local electron density of Cu(001) by adding carbon monoxide (CO) and Au atoms into the tip-substrate nanocavity [14, 15]. Interestingly, the presence of CO molecules significantly increases the hydrogen dissociation rate. In particular, H_2 may easily swap its electrons with CO as being squeezed by the STM tip. Our studies reveal that the mechanical motion of STM tip continuously modifies the chemical environment of the trapped hydrogen, and leads to charge redistribution, structural relaxation, and bond breaking.

4.2 Methods

The experiments were performed using a home-built STM operating at 10 K and a base pressure of 3×10^{-11} Torr [16]. Cu(001) surface was cleaned by cycles of Ne^+ sputtering and annealing at around 800 K. The silver tip was electrochemically etched. The clean surface at 10 K was dosed with Au, CO, and H_2. Au atoms are evaporated from a Knudsen cell doser. CO and H_2 are introduced into the chamber through a variable leak valve. The topographic images are taken under constant current mode by recording z with feedback on. The dI/dV and d^2I/dV^2 spectra are done by recording the first and second harmonic outputs of the lock-in amplifier.

We have found that the molecular hydrogen will spontaneously desorb from Cu surfaces at 10K [17-22]. The measured reaction rate depends on the density of H_2 on the surface. A background pressure of H_2 is kept at 5×10^{-10} Torr during the whole experiment to maintain a constant population of the adsorbed molecules on the surface after an initial dose at 8×10^{-10} Torr for at least 5 min. To avoid the inaccuracy due to the variation in the H_2 population and tip condition, the measurement presented in this work is conducted under similar H_2 population and tip conditions.

4.3 Results and Discussion

After dosing Au adatoms and CO molecules onto the Cu(001) substrate, they can be easily distinguished from either STM topographic images or IETS spectra (Fig. 4.1). Au adatoms appear as protrusions sitting at the hollow sites of Cu(001) while CO molecules appear as depressions sitting at the top sites (Fig. 4.1.B). Without H_2, the IETS spectra taken over the Cu(001) surface and Au atoms are structureless. Two fingerprinting IETS features can be observed over CO which correspond to the hindered translational and hindered rotational excitations, respectively (Fig. 4.1.E) [23]. Once dosed, H_2 diffuses freely on the Cu surface but may temporarily be trapped in the STM junction. The CO molecule imaged with a trapped H_2 in the tip-substrate junction has an outer ring of 2.95 Å in radius (Fig. 4.1.C). The d^2I/dV^2 spectra taken over the Cu surface and Au adatoms are dominated by the H_2 rotational and vibrational excitations [19,21] (Fig 4.1.D-E). The spectrum taken above CO now shows a combination of CO and H_2 features, whereas the spectrum taken over the outer ring around CO is similar to that on the bare Cu surface aside from the much stronger signal for H_2 rotation (Fig 4.1.F). No sign of spontaneous H_2 dissociation can be identified in STM images with 50 meV bias and 0.1 nA tunneling current (tip-substrate gap distance is larger than 7 Å [24]).

To break apart H_2 molecules by electrons in the fixed tunneling gap, we apply voltage pulses to the sample bias to generate energetic tunneling electrons. During a voltage pulse, the tunneling gap is preset at 50 mV bias and 0.1 nA tunneling current, and suddenly increase the bias for a short time with feedback off. Fig. 4.2 shows the topographic images taken before and after applying a 540 mV and 500 ms voltage pulse over the bare Cu surface. About 20 small depressions are generated by the pulse. IETS measurement over these depressions reveals the same vibrational

FIG. 4.1. H_2 adsorption on a Cu(001). (A) Schematic diagram of a hydrogen molecule trapped in the STM junction. (B-C) topographic images taken before (B) and after (C) dosing hydrogen at 50 mV, 1 nA set point. (D-F) d^2I/dV^2 taken over bare Cu(001) surface (D), Au atom (E) and CO molecule (F) before and after dosing hydrogen. The spectroscopic features observed at 44 mV after H_2 dosage are the rotational excitation of H_2. The features at 5 mV for bare Cu and 18 mV for Au atom are the vibrational bouncing mode of H_2. The spectra taken over the center of CO before dosing H_2 shows the CO hindered translational mode at 5mV and hindered rotational mode at 36 mV. The spectrum at the same position with H_2 also shows CO hindered rotational features at 36 mV, but the features at 5 mV are different which may arise from the mixture of H_2 vibrational and CO hindered translational features. The spectrum taken over the outer ring feature of CO shows H_2 rotational and vibrational signatures similar to the bare Cu surface, but with a much stronger signal for the rotational mode.

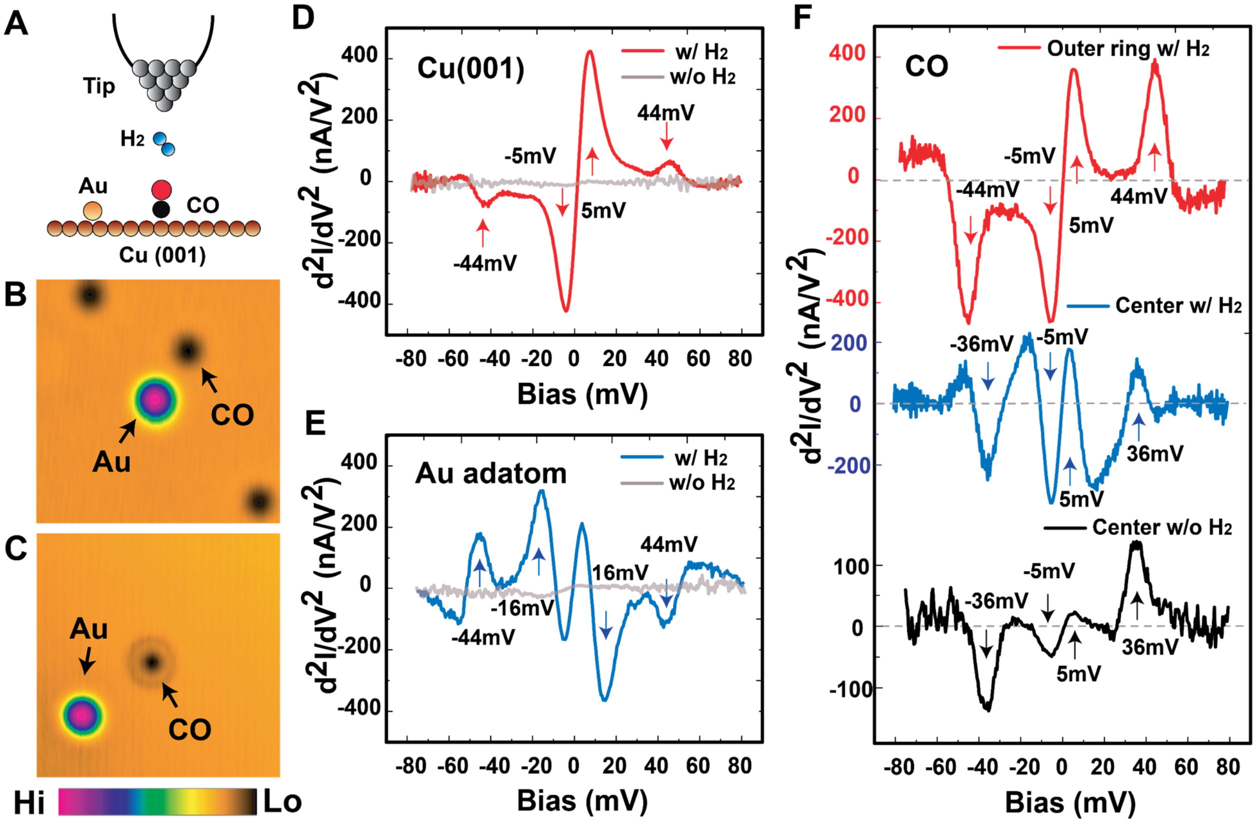
A
Tip
H2
Au
CO
Cu (001)
B
CO
Au
C
Au
CO
Hi
Lo
D
Cu(001)
w/ H2
w/o H2
-5mV
5mV
44mV
-44mV
d^{2}I/dV^2 (nA/V^2)
400
200
0
-200
-400
-80 -60 -40 -20 0 20 40 60 80
Bias (mV)
E
Au adatom
w/ H2
w/o H2
44mV
16mV
-16mV
-44mV
F
CO
Outer ring w/ H2
-5mV
-44mV
5mV
44mV
Center w/ H2
-36mV
-5mV
5mV
36mV
Center w/o H2
-5mV
-36mV
5mV
36mV
100
0
-100

features as obtained from hydrogen atoms dissociated from acetylene [25, 26], confirming their chemical identity as atomic hydrogen. These hydrogen atoms can spill over as far as 3 nm away from the pulse center, possibly due to their relatively high kinetic energy acquired from the hot electrons. The number of hydrogen atoms produced from a single voltage pulse is found to decrease as either the voltage amplitude or pulse duration are decreased. We find that no hydrogen atoms are produced under a threshold amplitude of around 510 meV which can be assigned as the activation barrier (E_a) for hydrogen dissociation on Cu(001). This value is smaller than both the previous experimental report (680 meV) [27]. The small reduction of E_a in our STM measurement is probably due to the presence of the tip even though it is assumed to be quite reasonably far away. The same measurements are repeated over CO and Au atoms. 16 hydrogen atoms were generated by one 540 mV pulse on top of an Au atom as shown in Fig. 4.2.E, whereas more than 130 hydrogen atoms were generated by one 540 mV voltage pulse over CO as shown in Fig. 4.2.F.

To mechanically drive the hydrogen dissociation, we squeeze the trapped hydrogen molecule by suddenly decreasing the tip substrate separation. During one mechanical pulse, the tip substrate gap is preset at 5 mV bias and 0.1 nA tunneling current, and is suddenly decreased by around 3 to 4 Å for 500 ms (Fig. 4.3.B). To rule out dissociation induced by tunneling electrons, the sample bias is decreased to nearly 0 meV during the mechanical pulse, the tunneling current, in this case, is mainly produced by the work function difference between the silver tip and the copper substrate (Fig. 4.3.C) [28]. Fig. 4.3.E is the topographic image after 1000 sequential mechanical pulses applied over the bare Cu(001) surface. Two hydrogen atoms are generated in the region close to the pulse center. The production rate measured over Au atoms is similar to that on the bare Cu surface (Fig. 4.3.D). Strikingly, when the mechanical pulse is applied above the outer ring of the CO molecule, 32 hydrogen atoms are generated (Fig. 4.3.F) [29, 30]. In all three

FIG. 4.2. Hydrogen dissociation induced by voltage pulses. (A) The production rate over bare Cu(001) (red), Au atom (blue) and CO molecule (black) as a function of bias during the voltage pulse. The production rate is defined as the number of H atoms generated by one 500 ms duration voltage pulse divided by the current during the pulse. The inset is the topographic image taken before applying mechanical pulses. (B). Schematic diagram of the hot electron induced hydrogen dissociation. (C) The current measured during a 540mV and 500 ms voltage pulse. (D-F) Topographic images taken after applying one 540 mV and 500 ms voltage pulse over bare Cu (D), Au atom (E), and CO molecule (F). The H atoms can be swept out from the scanning area by scanning at 1 V, 1 nA tunneling set point which allows us to repeat the measurement over the same area. The positions where the pulses are applied are marked by red circle (Cu), blue triangle (Au) and black square (CO) respectively.

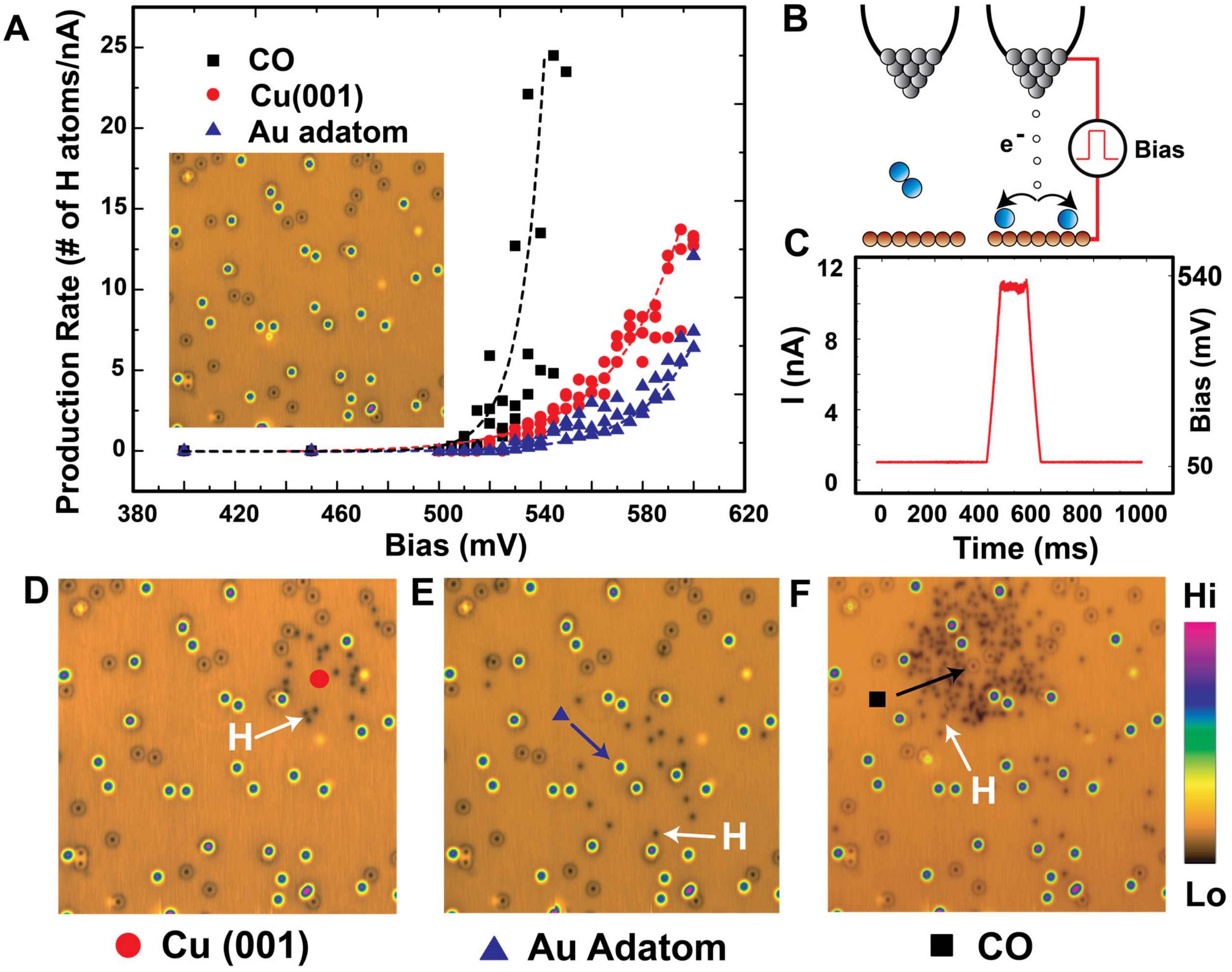
A
Production Rate (# of H atoms/nA)
25
20
15
10
5
0
380
420
460
500
540
580
620
Bias (mV)
■ CO
● Cu(001)
▲ Au adatom
B
e⁻
Bias
C
I (nA)
12
8
4
0
540
Bias (mV)
50
0
200
400
600
800
1000
Time (ms)
D
H
E
H
F
H
Hi
Lo
● Cu (001)
▲ Au Adatom
■ CO

cases, the reaction rate increases as the tip-substrate gap shrinks (Fig. 4.3.A). When the pulses are applied over Au adatom or bare Cu, almost no dissociation event can be observed if the gap distance is larger than 3.8 Å during the mechanical pulses. However, dissociation events can be observed even with 4 Å gap when the pulses are applied over the outer ring of CO, indicating the benefit of using CO to assist the mechanochemical H_2 dissociation.

While it is clear that the mechanical motion of the STM may noticeably enhance the reaction rate of H_2 dissociation and, in general, including other reactions, we believe this is not done through the direct transferring of mechanical (kinetic) energies to the reactants. The mechanical motion of STM tip occurs in a much longer time scale (ms to μs) than that for bond breaking (ps to ns) and the energy transfer through electron-phonon coupling is inadequate for meaningful chemical reactions. Instead, the mechanical motion of the tip modifies the interaction energy of the trapped H_2 to its environment, and continuously drives the trapped molecule towards the state where H-H bond tends to be cleaved [31]. Based on our results, the essence of mechanochemistry in this system is derived from the continuous evolution of the catalytic environment from inert to active as the hydrogen molecule is guided mechanically toward the surface. This offers new opportunities for tuning the performance of nanocatalysts by selecting the pace of motion and special dopants.

4.4 Conclusions

In conclusion, we demonstrate that the mechanical motion of STM tip induces one of the simplest chemical reactions: hydrogen dissociation. This brings the study of mechanochemistry to the single molecule level, with unmatched controllability and visibility. The electronic and vibrational properties of both reactants and products can be characterized and quantified quickly

FIG. 4.3. Hydrogen dissociation induced by mechanical pulses. (A) The production rate over bare Cu(001) (red), Au atom (blue) and CO molecule (black) as a function of gap distance during the voltage pulse. The production rate is defined as the number of H atoms generated per 1000 mechanical pulses. The topographic images taken before applying mechanical pulses are shown as insets. (B). Schematic diagram of the mechanical pulse induced hydrogen dissociation. (C) The current measured during four mechanical pulses. (D-F) Topographic images taken after applying 1000 mechanical pulses over Au atom (D), bare Cu (E), and CO molecule (F). The positions where the pulses are applied are marked by red circle (Cu), blue triangle (Au) and black square (CO) respectively. The gap distance during the pulses is set at around 3.1 A. The vertical stripes in the images arise from the creeping of piezo tube induced by the repeated mechanical movement.

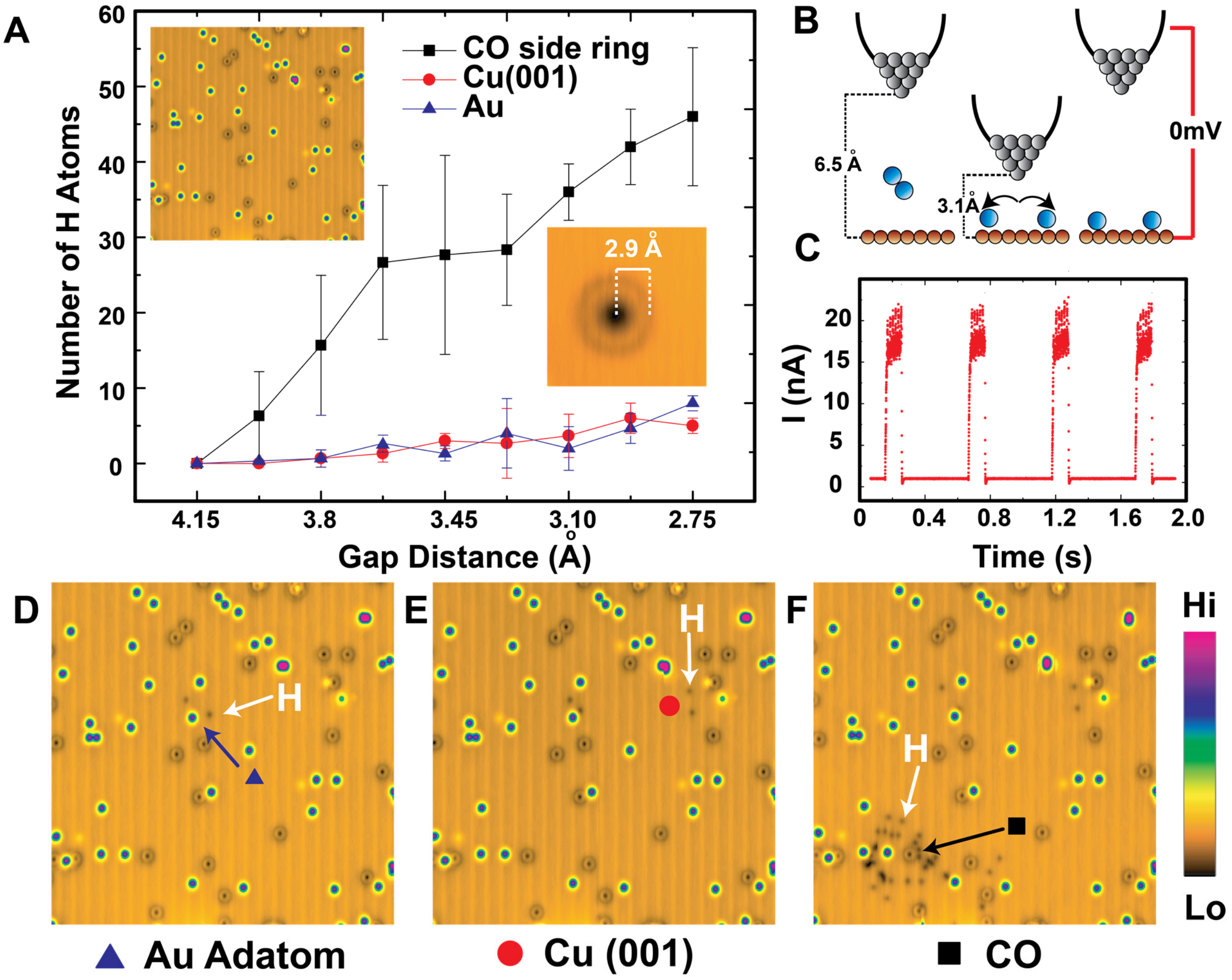
A
B
C
D
E
F
Number of H Atoms
Gap Distance (Å)
0
10
20
30
40
50
60
4.15
3.8
3.45
3.10
2.75
CO side ring
Cu(001)
Au
2.9 Å
6.5 Å
3.1 Å
0mV
I (nA)
Time (s)
0
5
10
15
20
0
0.4
0.8
1.2
1.6
2.0
H
H
H
Hi
Lo
▲ Au Adatom
● Cu (001)
■ CO

by real-space spectroscopy and microscopy. Our results indicate that the mechanochemical processes rely on the constant generation of active chemical environments during the mechanical motion for different steps of chemical reactions. We anticipate that more extensive investigations of mechanochemistry at the single molecule level will open a new vista for the design of efficient nano-catalysts.

Bibliography

[1] M. K. Beyer, H. Clausen-Schaumann, Chem. Rev. **105**, 2921 (2005).

[2] J. N. Brantley, K. M. Wiggins, C. W. Bielawski, Science **333**, 1606 (2011).

[3] C. R. Hickenboth et al., Nature **446**, 423-427 (2007).

[4] P. Baláž et al., Chem. Soc. Rev. **42**, 7571-7637 (2013).

[5] H. J. Lee, W. Ho, Science **286**, 1719-1722 (1999).

[6] S. W. Hla, K. H. Rieder, Annu. Rev. Phys. Chem. **54**, 307 (2003).

[7] S. Stöttinger, G, Hinze, G. Diezemann, I. Oesterling, K. Müllen, T. Basche, Nat. Nanotechnol **9**, 182 (2014).

[8] A.-S. Duwez, S. Cuenot, C. Jérôme, S. Gabriel, R. Jérôme, S. Rapino, F. Zerbetto, Nat. Nanotechnol. **1**, 122 (2006)

[9] I. F. Silvera, Rev. Mod. Phys. **52**, 393 (1980).

[10] G. Kyriakou et al., Science **335**, 1209 (2012).

[11] A. A. Khajetoorians, M. Valentyuk, M. Steinbrecher, T. Schlenk, A. Shick, J. Kolorenc, A. I. zichtenstein, T. O. Wehling, R. Wiesendanger, J. Wiebe, Nat. Nanotechnol. **10**, 958 (2015).

[12] D. Serrate, M. Moro-Lagares, M. Piantek, J. I. Pascual, M. R. Ibarra, J. Phys. Chem. C 118, 5827 (2014).

[13] J. Harris, S. Andersson, Phys. Rev. Lett. **55**, 1583 (1985).

[14] B. Hammer, Y. Morikawa, J. K. Nørskov, Phys. Rev. Lett. **76**, 2141 (1996).

[15] J. Repp, G. Meyer, F. E. Olsson, M. Persson, Science **305**, 493 (2004).

[16] B. C. Stipe, M. A. Rezaei, W. Ho, Rev. Sci. Instrum. **70**, 137, (1999).

[17] J. A. Gupta, C. P. Lutz, A. J. Heinrich, D. M. Eigler, Phys. Rev. B **71**, 115416 (2005).

[18] S. Li, A. Yu, F. Toledo, Z. Han, H. Wang, H. Y. He, R. Wu, and W. Ho, Phys. Rev. Lett. **111**, 146102 (2013).

[19] C. Weiss, C. Wagner, C. Kleimann, M. Rohlfing, F. S. Tautz, and R. Temirov*,* Phys. Rev. Lett. **105**, 086103 (2010).

[20] S. Li, D. Yuan, A. Yu, G. Czap, R. Wu, W. Ho. Phys. Rev. Lett. **114**, 206101 (2015).

[21] F. D. Natterer, F. Patthey, H. Brune, Phys. Rev. Lett. **111**, 175303 (2013).

[22] A. Yu, S. Li, G. Czap, and W. Ho, J. Phys. Chem. C **119**, 14737 (2015).

[23] L.J. Lauhon, W. Ho, Phys. Rev. B **60**, 8525 (1999).

[24] The shortest distance between two neighbor Cu atoms in a crystal is 2.6 Å. Here we refer the tip-substrate gap distance in point contact condition where the tip and substrate start to exchange atoms as 2.6 Å to estimate the absolute gap distance.

[25] L. J. Lauhon, W. Ho, Phys. Rev. Lett. **85**, 4566 (2000).

[26] Single H atoms are very mobile on a Cu(001) surface, the STM-IETS over these small depressions shows an inelastic excitation at 74 mV which matches the energy of the bouncing vibrational mode of a single H atom on a Cu(001) surface.

[27] G. Binnig, H. Rohrer, C. Gerber, E. Weibel, Phys. Rev. Lett. **49**, 57 (1982).

[28] J. M. Campbell, C. T. Campbell, Surf Sci.**259**, 1 (1991).

[29] M. Emmrich et al., Phys. Rev. Lett. **114**, 146101 (2015).

[30] When the STM tip and the H_2 molecule is placed right above the CO molecule, H_2 and CO repel each other and CO is pushed aside as the gap shrinks, which explains the lateral hopping of CO reported in reference 24 and also in our own experimental observations.

[31] H. Wang, S. Li, H. He, A. Yu, F. Toledo, Z. Han, W. Ho, R. Wu, J. Phys. Chem. Lett., **6**, 3453 (2015).

CHAPTER FIVE

Sub-molecular Control of Photo-assisted Activation of a Single C-H Bond[†]

Abstract

We demonstrate the bond-selected and photo-assisted activation of a single C-H bond in individual azulene molecules adsorbed on a Ag(110) surface using a scanning tunneling microscope combined with a femtosecond laser. The electrons in the STM tip can be photo-excited when irradiated by femtosecond laser pulses, and dissociate the individual C-H bonds in the STM junction through photo-assisted tunneling processes. The electron energy required to break the bond decreased by 1.5 eV under 820 nm laser illumination, indicating that an electron can be coupled with one photon to induce the reaction. The C-H bond to be activated can be chosen by positioning the tip over the molecule with sub-Å resolution. The inelastic tunneling probe (itProbe) images taken before and after the reaction provide unambiguous structural identifications of the reaction products. The demonstration of a chemical reaction induced by photo-assisted tunneling electrons opens a new avenue to probe the photochemistry at sub-molecular level.

[†] This chapter by Shaowei Li, Gregory Czap, Hui Wang, Arthur Yu, Siyu Chen, Ruqian Wu, and W. Ho is in preparation for submission.

5.1 Introduction

The controlled activation of inert carbon-hydrogen (C-H) bonds in saturated hydrocarbons has been a ubiquitous theme in organic chemistry [1]. Replacing the hydrogen atom by other functional groups can turn the low cost and abundant hydrocarbon feedstocks into much more valuable and synthetically useful compounds [2]. Multiple methods have been applied in this direction. Thermal cracking and dehydrogenation can convert alkanes to more active products but is generally energy intensive and requires harsh reaction conditions [3]. Use of 'brute-force' reagents such as highly reactive radicals and super acids can also cleave C-H bonds but they are in general expensive and demanding [4]. The heterogeneous catalysis methods use solid metallic materials to react with C-H bonds, but the efficiency of the reaction is often compromised [5]. There is a sharp increase of interest in catalytic reactions using metal atoms or complexes containing rhodium or platinum to bring about oxidative additions for C-H activation [6]. Photocatalyzed reactions are especially appealing among these studies since they can utilize the energy from visible light to induce the reactions which are thermodynamically unfavorable [7]. However, a common difficulty with all these methods is how to selectively activate the desired C-H bond [8]. Searching for an experimental approach to precisely provide energy to the high-energy C-H bonds without damaging other active functional groups remains challenging.

The scanning tunneling microscope (STM) provides a wealth of information on low dimensional molecular systems. It has been shown to be an ideal tool to induce and detect the bond-selected chemistry with sub-molecular precision [9]. Due to the atomic-scale localization and meV scale energy tunability of the tunneling electron, STM can be used to break and form specific bonds selectively [10,11]. Additionally, the sub-Ångström spatial resolution of a STM provides identification of molecular structure [12,13], orbital hybridization [14,15], and intermolecular bond orientation [16,17]. It contributes to our understanding of material composition, molecular organization, intra- and intermolecular coupling, and chemical kinetics and dynamics. A recent advance in STM provides a new inelastic tunneling probe technique (itProbe) based on mapping out the vibration of a CO molecule attached to the STM tip. Images of molecules obtained with this technique show features directly related to the positions of atoms and bonds which provide the unambiguous evidence to the molecular structures [18]. Moreover, the coupling of the laser with STM allows it to probe photo-induced chemical transformations such as charge transfer [19,20] and nuclear motion of single molecules [21,22], and enables the bond-selected photochemistry with sub-molecular accuracy.

Here, we demonstrate the coupling of femtosecond laser pulses with tunneling electrons to induced the dissociation of a single C-H bond in the STM junction through a photo-assisted tunneling process. An electron in the tip is photo-excited to a higher energy level and then tunnels to the molecule in the junction, inducing the reaction. The reaction can be visualized by the distinct change of the molecule in constant current topographic images as well as high-resolution itProbe images. The photo-assisted tunneling electrons are highly spatially localized. In most cases, only the molecule underneath the tip can be dissociated. The bond to be dissociated can be chosen by positioning the tip within the molecule with sub-Ångström spatial sensitivity.

5.2 Methods

The experiments are conducted with a home-made ultrahigh-vacuum (UHV) STM at a base temperature of 9 K with an electrochemically etched silver tip [21]. The femtosecond laser pulses are focused on to the STM junction using a 3” focal length spherical lens. The laser we use is a Ti-Sapphire (820 nm) with 5 GHz repetition rate and 35 fs pulse duration. A laser power controller is used to modulate the laser intensity and reduce the power fluctuation to <0.1%. The power of the laser is measured just before the entrance of UHV chamber, and maintained at 1.3 mW throughout the experiment. The base temperature increases by less than 10 mK resulting from laser illumination.

The high-resolution structural images are taken separately with a different STM running at 600 mK using the itProbe technique reported previously [11]. Three different operational modes of itProbe can be used. In constant current mode, the feedback is turned off at the same tunneling set point for every pixel, followed by setting the sample bias to the imaging value. In constant height mode, feedback is turned off at the center of each image and remains off during the whole imaging process. In constant current mode, STM tends to maintain a constant gap between the tip and the molecule, thus the images can resolve the overall structures of molecules in a non-planar configuration. On the contrary, constant height images show the tomographies of the molecule that different height. If the molecule has strong electronic feature near the image set point, the constant current image may reflect the convolution of its molecular orbital and skeletal structure. This can be avoided by using the third image mode, semi-constant height mode. In this mode, the feedback is turned off at a tunneling set point with large tip sample separation and then move towards the surface by a certain distance at each image pixel. The set point bias can be chosen to avoid the energy of the electronic features of the molecule. In this study, we find that azulene has strong electronic structures near Fermi level. The structural images are obtained using constant height mode or semi-constant height mode. Detailed descriptions of the different itProbe operational modes can be found in ref 11.

5.3 Results and Discussion

The azulene molecule we studied is a simple metal-free dye molecule and widely involved in photo-chemical processes. The molecule consists of a seven-membered ring and a five-membered ring with eight C-H bonds. Individual azulene molecules are sublimed on to the 9 K Ag(110) surface through a variable leak valve using its vapor pressure at room temperature. The azulene molecules appear as a pear shape on the Ag(110) surface. They adsorb in two equivalent geometries with their long axis along the (001) direction. A low coverage of CO molecules is co-adsorbed on the surface to allow more detailed structural determination with CO terminated tip. Without laser illumination, the molecules can be consistently converted to different species when the bias is set higher than 2.4 V. The type of the species it is converted to depends on the position of STM tip. When the tip is positioned near the middle of the long axis and the edges of the short axis of a molecule, the molecule can be reproducibly converted into a crescent-type product (Fig. 5.1). The Z vs bias curve recorded over the molecule shows a stepwise change as the bias ramps from low to high with feedback on. For the molecule presented in Fig. 5.1.E, the tip suddenly moved towards the surface when the bias reached 2.8 V, indicating a dramatic conductivity change of the molecule in the junction. The topographic image taken immediately after the Z vs bias scan indicated that the molecule had been converted into a crescent-type product. The conversion is irreversible, such that the molecule will not return to its original state when the bias is ramped back down. The bias when the step changes occur may vary among different molecules, but is always higher than 2.4 V. If we repeat the Z vs bias measurement over the other edge of the short molecular axis of the crescent shape product as indicated by the white dot in the left top inset of Fig. 5.1.F, another step change can be observed with the bias as low as 1.8 V. The topographic image taken

FIG. 5.1. Bond-selected dissociation of single azulene molecules using energetic tunneling electrons. (A-D) A series of STM topographic images taken before and after dissociating several nearby azulene molecules with laser illumination. The arrows indicate the molecules where the tip was parked to induce the reaction. The dissociation processes are highly localized. In most cases, only the molecule underneath the tip is dissociated while the neighbor molecules are not affected. The majority of the molecules turn into a crescent shape as shown in (B) and (C). The crescent type species indicated by the arrow in (C) can be further dissociated into a peanut shape as shown in (D). All the images are taken with 0.5 V and 1 nA set points in constant current mode. (E) The Z vs bias curve taken when an intact azulene molecule is dissociated into a crescent type product. The bias is ramped from 1 V to 3 V with feedback on. The sudden drop in Z near 2.8 V is the sign of dissociation occurrence. The dissociation bias varies in different scans but is always higher than 2.4 V. The left inset is the topographic image of an intact molecule before dissociation. The white dot indicates the position where the tip is parked. The right inset is the topographic image of the dissociated product. (F) Z vs bias spectrum taken when a crescent type molecule is dissociated into a peanut type. The white dot in the left top inset indicates the tip position. The right bottom inset is the topographic image of the peanut type product. The threshold bias to convert a crescent type product into the peanut type is near 1.9 V.

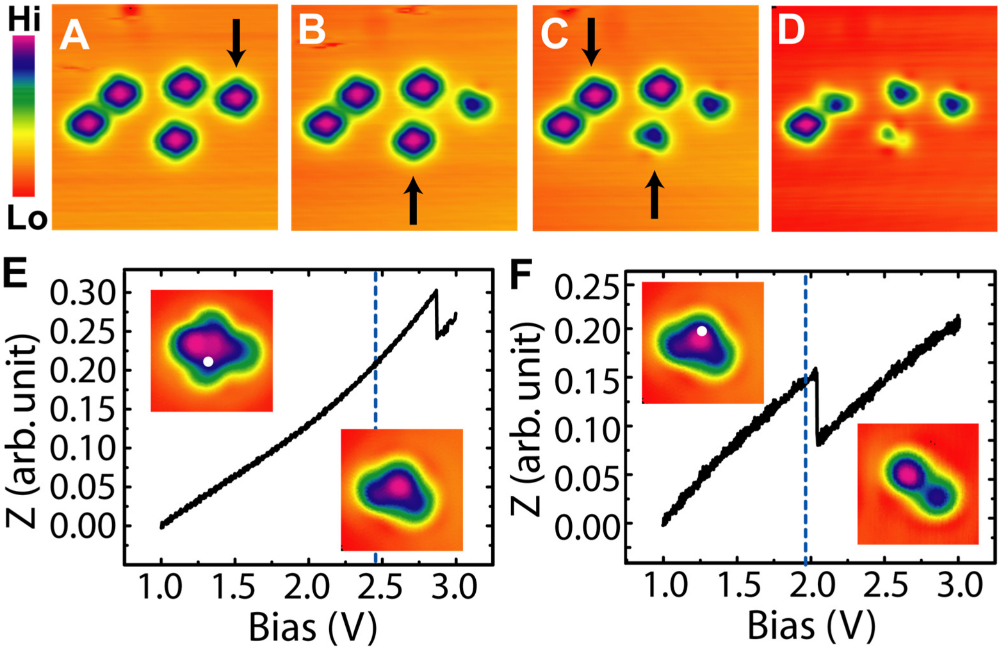
Hi
Lo
A
B
C
D
E
Z (arb. unit)
0.30
0.25
0.20
0.15
0.10
0.05
0.00
1.0
1.5
2.0
2.5
3.0
Bias (V)
F
Z (arb. unit)
0.25
0.20
0.15
0.10
0.05
0.00
1.0
1.5
2.0
2.5
3.0
Bias (V)

immediately afterward showed that the molecule was converted into a peanut-type product, which is relatively stable and hard to be converted to another species. Occasionally, an azulene can be converted to peanut-type directly by one bias ramp when the current is set at 2 nA.

The irreversible change in molecular topographic structure indicates the molecule could have undergone a chemical transformation. The itProbe images taken with semi-constant height mode resolve the skeletal structures of the azulene molecule and its products. The image of an intact azulene molecule shows clear seven-membered and five-membered rings and the relatively weaker C-H features. DFT calculations have reproduced the adsorption geometries of azulene/Ag(110) and two types of products as shown in Fig. 5.2.E-F. Compared to the intact molecule whose long molecular axis is along the (001) direction, the crescent-type product shown in the middle column of Fig 5.2 is rotated by 30 degrees clockwise. A relative prominent line at the bottom side of the seven-membered ring is resolved in the image of the crescent-type product in Fig. 5.2.B. This new feature indicates the formation of a chemical bond between the carbon atom of the seven-membered ring and a substrate Ag atom after activating the C-H bond. The DFT calculation indicates the binding energy of the molecule to the Ag substrate increases from 1.33 eV to 4.36 eV due to the C-Ag bond. The top side of the molecule in the image is also tilted upward, which contributes to the slightly distorted ring features in the middle semi-constant height image of Fig. 5.2.B. The peanut-type product is rotated by another 30 degrees clockwise compared to the crescent-type product. Two prominent lines correspond to the C-Ag bonds are resolved at the both side of the seven-membered ring replacing the weak C-H features. DFT calculations show that the molecule is now strongly bonded to the substrate with 5.0 eV binding energy.

FIG. 5.2. High-resolution structural images of azulene and its dissociation products. (A) Constant current STM topographic images taken at 50 mV bias and 0.1 nA of an intact azulene (left), a crescent shape product (middle) and a peanut shape product (right). (B) semi-constant height itProbe images showing detailed structures of the molecules in (A). (C-E) Constant height itProbe images taken at different tip-substrate distances from far (C) to close (E). (F) Top views and (G) side views for molecular structures obtained from DFT calculations.

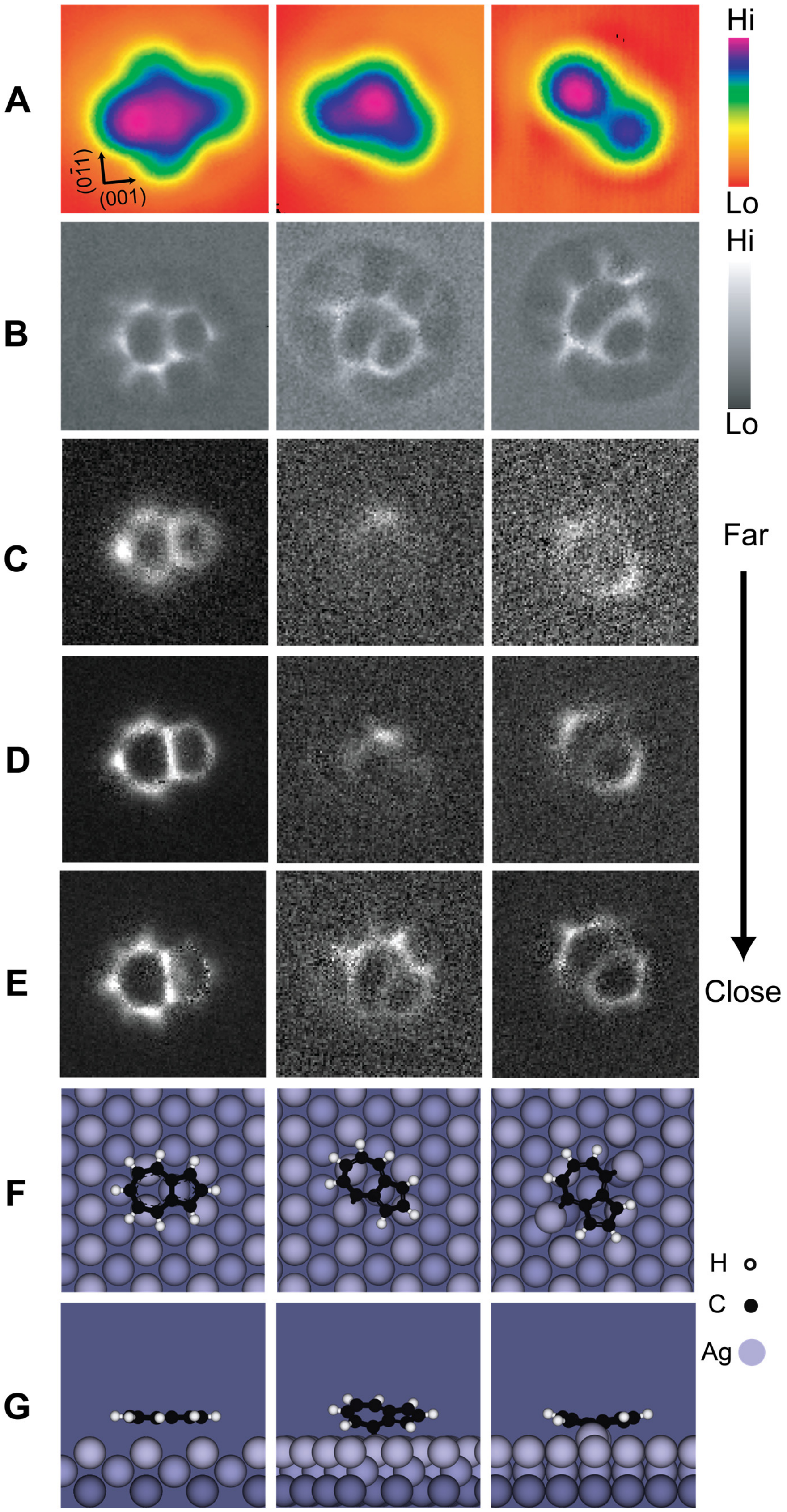
A
(01̄1)
(001)
Hi
Lo
B
Hi
Lo
C
Far
D
E
Close
F
H
C
Ag
G

The molecule adsorbed in a boat shape with both ends tiled upward as shown in the third column of Fig. 5.2.G. The tilting of the molecule after C-H activation can be better resolved in the itProbe tomography images taken with the constant-height mode. As the tip moves closers to the surface, the intact molecule shows an overall planar feature. For the crescent type product, the top part of the molecule can be resolved at a further tip-substrate distance, confirming the side tilted geometry given by the DFT calculation. For the peanut type product, two ends of the molecule are resolved before the middle section, matching the calculation results. The good agreement between itProbe images and the DFT calculations further confirms the identities and structures of the dissociation products.

Without laser illumination, the C-H activation cannot be induced when the bias is below 2.4 V. However, with the junction illuminated by femtosecond laser pulses, we have observed dissociation of the molecule at a much lower bias such as in the Z vs bias scan presented Fig. 5.3.D. The reaction rate is strongly correlated to the laser power, focus, and alignment. To quantify this photon-induced chemical transformation, we have compared the C-H bond dissociation rate at different sample bias with and without laser illumination. The dissociation rate is defined as the average number of azulene molecules that can be dissociated into crescent-typed products per second. To measure the dissociation rate at a certain electron energy, we ramp the bias to the corresponding bias voltage over the background and move the tip to 10 different azulene molecules with feedback on. The tip is parked over the position indicated by the white dot in the left top inset of Fig. 5.1.E within each molecule. If the molecule is dissociated, the STM tip will noticeably move towards the surface to compensate the current drop due to the molecular structural change, a stepwise change like the ones in Fig. 5.1.E and Fig. 5.1.F can be observed in Z. The time it took to dissociate each molecule is recorded and averaged. The dissociation rate is given by the reciprocal of the average dissociation time. The rate is set as zero if no molecule can be dissociated in 30 minutes.

The dependence of the dissociation rate on sample bias shows an obvious threshold both with or without laser irradiation. Reactions can be observed at a bias as low as 0.9 V when the junction is irradiated with 820 nm light, in sharp contrast to the threshold bias of 2.4 V without light (Fig.5.3.B). The energy difference between these two thresholds (1.5 eV) closely matches the energy of one photon of 820 nm laser light, indicates the photons couple quantum mechanically to the tunneling electrons. The reaction rate increases exponentially with bias. The fitted pre-exponential factor for the reaction rate without laser illumination is larger than the one with laser illumination by three orders of magnitude, indicating roughly 0.1% of the tunneling electrons can obtain energy from the photons to induce the reaction (Fig. 5.3.C).

The exact one-photon-to-one-electron quantum coupling can be explained by the photo-assisted tunneling model as shown in Fig. 5.3.A. An electron in the STM tip is excited to a state with *hv* energy higher than the Fermi level by absorbing a photon. The lifetime of the photoexcited electrons in the tip (~10-100 fs) [23] is much longer than the time scale of electron tunneling (<10 fs) [24], allowing them to tunnel through the junction without relaxation. Another potential mechanism is that the laser directly couples to the molecule in the junction by exciting it to a higher molecular state, and then interact with the tunneling electron to induce a reaction. However, this mechanism is not feasible since the molecule in its bounded excited state is expected to relax to a lower vibrational or electronic level in a time scale much shorter than the required time for it to couple to the tunneling electron. The relaxation is expected to be expedited on metal surfaces due to the hybridization between molecule and substrate [25]. The fact that the dissociation thresholds with and without laser illumination differ by an energy exactly equals to the photon energy

FIG. 5.3. C-H activation induced by photo-assisted tunneling electrons. (A) A schematic diagram of the photo-assisted tunneling process. (B) The azulene dissociation rates as a function of bias with (Red) or without (Black) laser illumination. To measure the dissociation rate at certain electron energy, we ramp the bias to corresponding voltage over the background and move the tip over the center of 10 different azulene molecules, and record the time it took for each molecule to dissociate. The dissociation rate is defined as the average number of molecules that can be dissociated per second. The red and black lines are the fitted exponential curves to the data. (C) The semi-log plot of the data in (B). (D) The Z vs bias curve taken when an intact azulene molecule is dissociated into a crescent type product under laser illumination. The threshold bias for dissociation is decreased to 0.9 V.

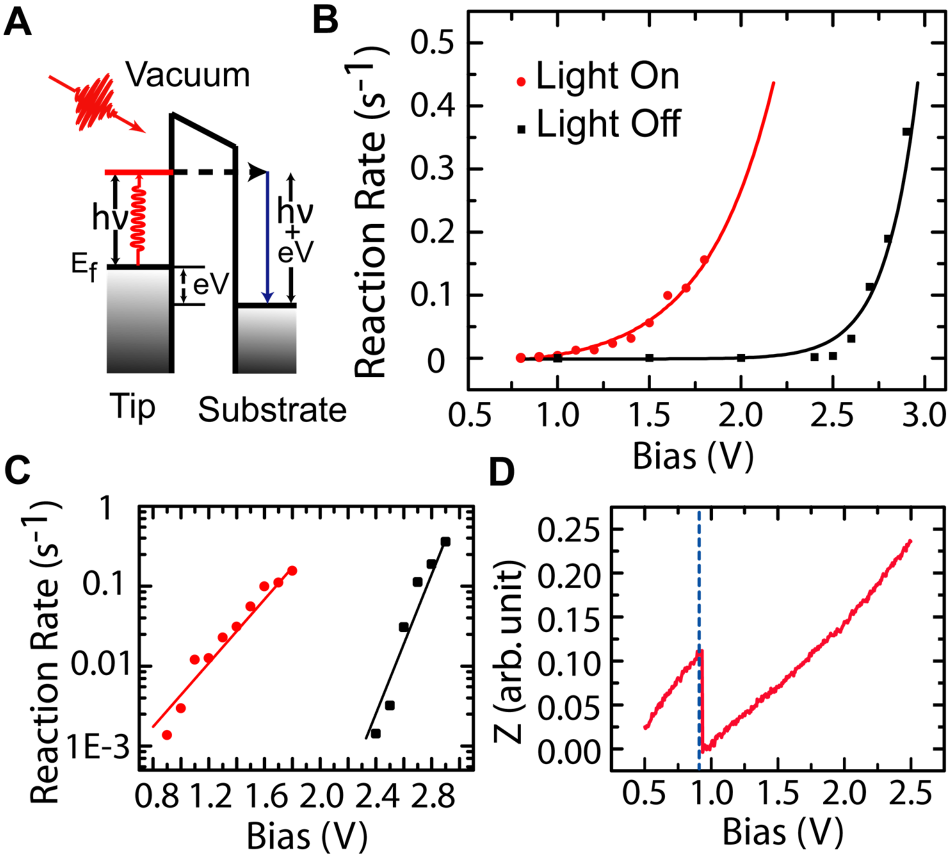
A
Vacuum
hν
E$_f$
eV
hν + eV
Tip
Substrate
B
Reaction Rate (s^{-1})
Light On
Light Off
Bias (V)
0.5 1.0 1.5 2.0 2.5 3.0
0 0.1 0.2 0.3 0.4 0.5
C
Reaction Rate (s^{-1})
1 0.1 0.01 1E-3
0.8 1.2 1.6 2.0 2.4 2.8
Bias (V)
D
Z (arb. unit)
0.00 0.05 0.10 0.15 0.20 0.25
0.5 1.0 1.5 2.0 2.5
Bias (V)

indicates that there is no energy lost due to such relaxations. Moreover, no obvious change was observed in the *dI/dV* spectrum after molecule irradiated by the laser, indicating the laser illumination has a minor effect on the molecular electronic structure. The photo-assisted tunneling model described here is also different with the mechanism in photo-induced rectification current observed in the microwave or THz frequency range, where the electric field of the electromagnetic wave directly adds on to the electric field from junction bias to induce the tunneling [21,26]. The period of 820 nm laser is too short compared to microwave and THz. Therefore, the photo-assisted tunneling process described here is expected to be the dominant mechanism.

The molecular orbitals should also be important in this tunneling electron induced dissociative reaction. Even though they are not expected to be directly involved in the photo-excitation, these orbitals serve as the final states for the resonance electron tunneling. It is widely accepted that the LUMO of azulene doesn't contribute its photo-dissociation in gas phase experiments due to an ultrafast internal relaxation to the ground state. The second excited state, LUMO+1, is believed to play an important role in the H elimination dissociation pathway. Experimentally, we observe a broad electronic peak spanning from 0.3 V to 1 V and centering around 0.5 V in the *dI/dV* spectra recorded at the center of an azulene molecule. The *dI/dV* image shows a four-lobed molecular electronic structure. In general, the molecular orbitals are hard to be resolved over metal surface due to the broadening from strong hybridization between molecule and metal surface. The distinct *dI/dV* feature with moderate broadening in our measurement indicates a relatively weak hybridization between azulene and Ag(110) near Fermi level. The week hybridization is explained by the low density of states of Ag near Fermi level given by DFT calculations as shown in Fig. 5.4.C. The LUMO is calculated at 0.5 eV above the Fermi level with a sizable broadening from 0.3 eV to 1 eV, and matches the peak we resolve in the *dI/dV*

FIG. 5.4. C-H bond activation barrier and azulene electronic structure. (A) Activation barriers of dissociating an azulene into a crescent type product (black) and dissociating a crescent type product into a peanut type product (red) base on DFT calculations. (B) Calculated density of states of an azulene adsorbed on Ag (110). The hyperdilation between azulene and the s electrons of Ag substrate is found to be weak near Fermi level. The azulene HOMO is found at 1.3 eV below the Fermi level. The LUMO and LUMO+1 are found at 0.5 eV and 1.3 eV above the Fermi level respectively. The spatial distributions of HOMO, LUMO, and LUMO+1 are shown as insets. (C) *dI/dV* spectra taken over the center of an azulene molecule (red) and Ag(110) background (black). The inset is the *dI/dV* image taken at 1.0 V. (D-E) Top views (top) and side views (bottom) of the calculated molecular structures in the transition states during the first (D) and second (E) C-H dissociations. The corresponding energies and positions along the reaction coordinate are labeled in (A).

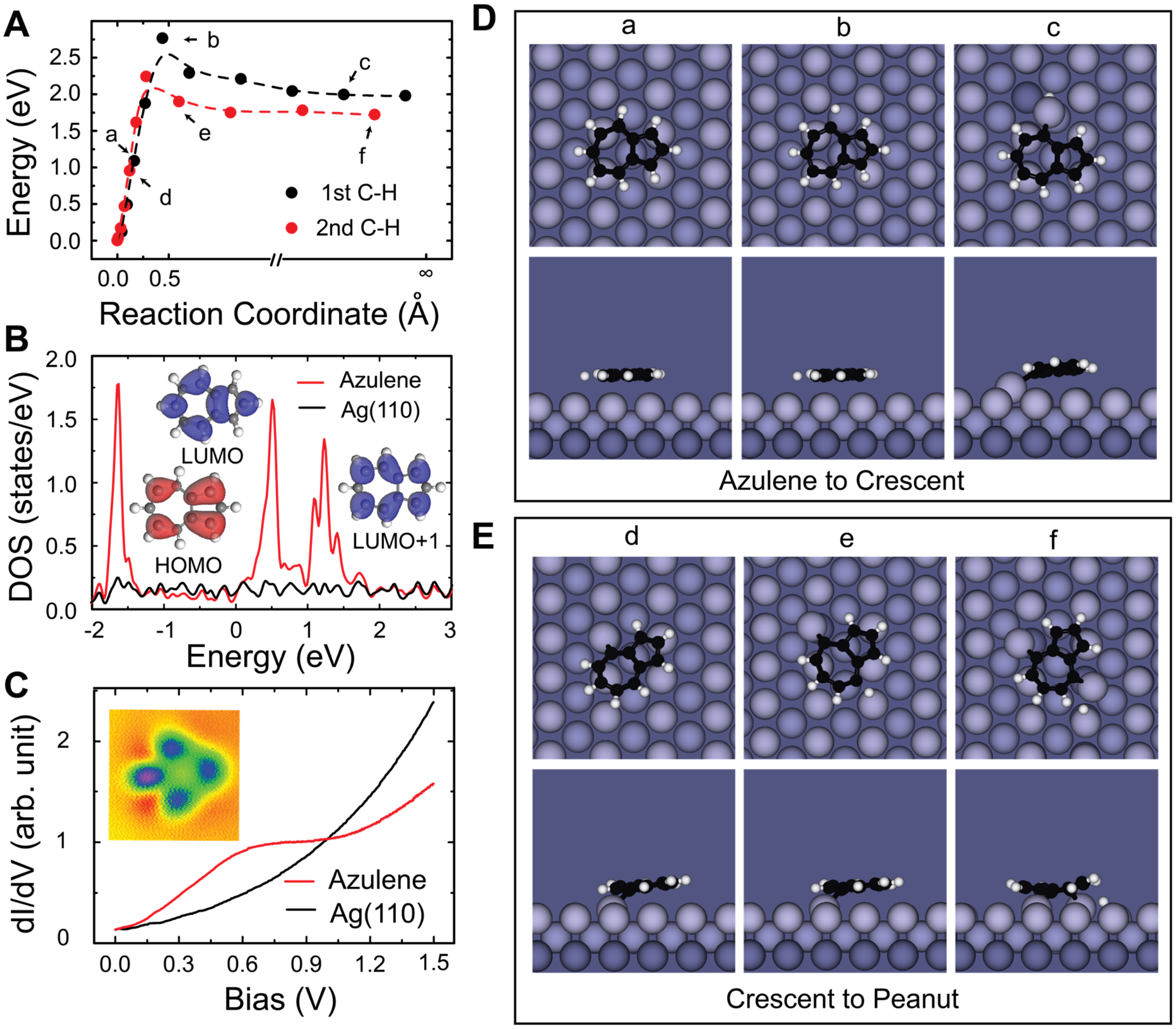
A
Energy (eV)
2.5
2.0
1.5
1.0
0.5
0.0
a
b
c
d
e
f
1st C-H
2nd C-H
0.0
0.5
∞
Reaction Coordinate (Å)
B
DOS (states/eV)
2.0
1.5
1.0
0.5
0.0
LUMO
HOMO
LUMO+1
Azulene
Ag(110)
-2
-1
0
1
2
3
Energy (eV)
C
dI/dV (arb. unit)
2
1
0
Azulene
Ag(110)
0.0
0.3
0.6
0.9
1.2
1.5
Bias (V)
D
a
b
c
Azulene to Crescent
E
d
e
f
Crescent to Peanut

spectrum. The spatial distribution of LUMO density also closely resembles the *dI/dV* image shown as the inset of Fig. 5.4.C. The LUMO+1 is calculated to be near 1.3 eV with a tail all the way to 2.0 eV. The higher energy orbitals such as LUMO+2 are all found to be more than 4 eV above the Fermi level and are less likely to contribute to the dissociation reaction induced by an electron with energy slightly above 2.4 eV. The electronic tail of the LUMO+1 is most likely to be the final state of the tunneling electrons. The calculated density of LUMO+1 concentrates near the 6 C-H bonds as shown in the Fig. 5.4.D right inset, probably accommodating the favorable activation of these C-H bonds. Activation barrier for converting an azulene to a crescent type product is found to be near 2.6 eV by DFT calculations as shown in Fig. 5.4.A, very close to the measured reaction threshold around 2.4 V without laser illumination. DFT also show that the energy required to break the second C-H bond decreased by 0.55 eV, in close agreement with the experimental measurement.

5.4 Conclusions

In summary, we have demonstrated the selective activation of a single C-H bond assisted by laser photons. The realization of the coupling of femtosecond laser pulses to the tunneling process enables the studies of photochemistry with submolecular resolution. The ability to precisely locate and inject photo-excited electrons using the STM tip allows the selected photo-activation of individual chemical bonds. Furthermore, the photo-assisted tunneling occurs in an ultrashort time scale, thus providing photo-assisted tunneling electrons both the temporal sensitivity from femtosecond pulses and the spatial resolution from tunneling. The combination of a femtosecond laser to the STM enable the exploration of laser induced chemical transformation with simultaneous spatial and temporal resolution.

Bibliography

[1] T. W. Lyons and M. S. Sanford, Chem. Rev., **110**, 1147–1169 (2010).

[2] L. McMurray, F. O'Haraa, and M. J. Gaunt, Chem. Soc. Rev. **40**, 1885-1898 (2011).

[3] B. S. Greensfelder, H. H. Voge, and G. M. Good, Ind. Eng. Chem. **41**, 2573–2584 (1949).

[4] J. A. Labinger and J. E. Bercaw, Nature **417**, 507-514 (2002).

[5] A. A. Latimer, A. R. Kulkarni, H. Aljama, J. H. Montoya, J. S. Yoo, C. Tsai, F. Abild-Pedersen, F. Studt, J. K. Nørskov, Nat. Mater. **16**, 225–229 (2017).

[6] T. Gensch, M. N. Hopkinson, F. Glorius and J. Wencel-Delord, T. Gensch, M. N. Hopkinson, F. Glorius, and J. Wencel-Delord, Chem. Soc. Rev. **45**, 2900-2936 (2016).

[7] N. A. Romero and D. A. Nicewicz, Chem. Rev. **116**, 10075−10166 (2016).

[8] Z. Zhang, K. Tanaka, and J. Q. Yu, Nature **543**, 538–542 (2017).

[9] W. Ho, Acc. Chem. Res. **31**, 567-573 (1998).

[10] H. J. Lee and W. Ho, Science, **286**, 1719-1722 (1999).

[11] Y. Jiang, Q. Huan, L. Fabris, G. C. Bazan, and W. Ho, Nat. Chem. **5**, 36–41 (2013).

[12] C. Weiss, C. Wagner, C. Kleimann, M. Rohlfing, F. S. Tautz, and R. Temirov, Phys. Rev. Lett. **105**, 086103 (2010).

[13] L. Gross, N. Moll, F. Mohn, A. Curioni, G. Meyer, F. Hanke, and M. Persson, Phys. Rev. Lett. **107**, 086101 (2011).

[14] Z. Han, G. Czap, C. Xu, C. L. Chiang, D. Yuan, R. Wu, and W. Ho, Phys. Rev. Lett. **118**, 036801 (2017).

[15] S. Li, D. Yuan, A. Yu, G. Czap, R. Wu and W. Ho, Phys. Rev. Lett. **114**, 206101 (2015).

[16] G.V. Nazin, X.H. Qiu, and W. Ho, Science **302**, 77-81 (2003).

[17] C. Weiss, C. Wagner, R. Temirov, and F. S. Tautz, J. Am. Chem. Soc. **132**, 11864 (2010).

[18] C. L. Chiang, C. Xu, Z. Han, and W. Ho, Science **334**, 885 (2014)

[19] S. W. Wu, N. Ogawa, and W. Ho, Science **312**, 1362 (2006).

[20] S. W. Wu and W. Ho, Phys. Rev. B **82**, 085444 (2010).

[21] T. L. Cocker, D. Peller, P. Yu, J. Repp, and R. Huber, Nature **539**, 263 (2016).

[22] L. Bartels, F. Wang, D. Moeller, E. Knoesel and T. Heinz, Science **305**, 648 (2004).

[23] M. Aeschlimann, M. Bauer, S. Pawlik, R. Knorren, G. Bouzerar, K. H. Bennemann, Applied Phys. A **71**, 485–491(2000).

[24] A. van Houselt and H. J. W. Zandvliet, Rev. Mod. Phys. **82**, 1593–1605 (2010).

[25] K. Kuhnke, C. Große, P. Merino, and K. Kern, Chem. Rev. **117**, 5174–5222 (2017).

[26] X. Tu, J. Lee, and W. Ho, J. Chem. Phys. **124**, 021105 (2006).

CHAPTER SIX

Probing Coherent Vibration Mediated Structural Transitions of Single Molecules with Space-time Resolution[†]

Abstract

Single-molecule coherent conformational changes are observed with joint Ångström-femtosecond resolution using a Ti-sapphire femtosecond laser combined with a scanning tunneling microscope (STM). The conductance change of STM junction associated with the laser induced reversible structural transitions between two adsorption geometries of a single pyrrolidine molecule on a Cu(001) surface is detected STM in real-space. The transition rate exhibits coherent oscillatory patterns with periods corresponding to specific molecular vibrations. The dynamics of this vibration mediated structural transition depends sensitively on the local molecular environment. We have found that the intermolecular interaction between two pyrrolidine molecules can increase the vibration period while shortening its decay time.

[†] This chapter by Shaowei Li, Siyu Chen, Jie Li, Ruqian Wu and W. Ho is submitted for publication in *Physical Review Letters*.

6.1 Introduction

Femtosecond lasers have been used to reveal quantum beat phenomena in the time domain which have led to a valuable understanding of the energy and dynamics of various states in a system [1]. By tailoring the amplitude and phase of a pair of laser pulses, quantum-mechanical constructive and destructive interferences between different coherent excited states can be modified and monitored [2]. This raises the fascinating possibility of coherent control of molecular reactions by choosing the excitation pathway that leads to a desired final product. One hurdle in achieving this goal arises from the inhomogeneity of molecules in the ensemble [3,4]. Each individual molecule could be influenced by its local environment and requires a specific driving pulse profile. A new approach with Ångström (Å) scale spatial resolution and femtosecond (fs) scale temporal sensitivity is necessary to probe the coherent response of individual molecules beyond the ensemble average.

Pump-probe technique has been used to probe the coherent properties of solid state matter by monitoring changes in the linear reflectivity [5,6], the generation of second harmonic or sum frequency [7-10], and the emission of electrons [11]. Due to the diffraction limited spatial resolution, these studies can only probe the homogeneous properties of the ensemble. It became possible to record the absorption [12] and fluorescence [13] of single molecules embedded in solids. The spatial resolution has been reduced through the advancement of super-resolution technique [12, 14,15] and near-field optical microscopy [16-18]. Although these laser-based probes have been able to detect individual molecules, the resolution of their internal structure remains elusive. The combination of laser with a scanning tunneling microscope (STM) can overcome this limitation. The efficiency of electron transfer to a single molecule adsorbed on a solid surface exhibited spatial variation within the molecule [19, 20]. By using circularly polarized light, spin coherence in GaAs quantum wells has been detected by the STM with ~1 nm resolution [21]. Most recently, the coherent vibration of single adsorbed molecules was detected by monitoring the photo-induced rectification of the tunneling current in the STM irradiated with THz laser pulses [22]. Still, the possibility of monitoring the nuclear motion that corresponds to a single-molecule reaction driven by coherent electronic or nuclear excitation has yet to be demonstrated.

One important category of molecular reaction is the structural transition where a molecule reversibly switches between two or more semi-stable conformational states. The transition may be triggered by various effects, such as heat, light, change in pH, interaction to other molecules, magnetic or electrical fields. Studies of molecular conformational transition as draw intense attention due to its far-reaching industrial applications. One example is the pH indicators where the dye molecules switch between different structural states in response to the pH changing of a medium. Each of these states has a distinct absorption and therefore the molecules change their color corresponding to the pH value [23]. The structural transformation such as cis-trans or ring opening isomerization can also be triggered thermally. Molecules containing stilbene as one of their fragments may rapidly undergo cis-trans isomerization when heated. Currently, single molecular switches are particularly of interest in the field of nanoscience for application toward miniaturization in future technology. Various single molecule devices ranging from triggering switch to molecular motors have been proposed and fabricated. For example, Wilson and co-workers have synthesized a system in which a small molecular ring is continuously transported directionally around a cyclic molecular track. The reversible motion of the molecular ring is powered by an irreversible reaction of 9-fluorenylmethoxycarbonyl chloride [24]. Molecular structural transitions are also important to in biology. For example, the mechanism of vision base on the cis-trans transformations of retinal in eyes. Upon visible light irradiation, the cis-retinal at the photo receptor site of an opsin quickly convert to trans-retinal within a few picoseconds. The transition triggers a nerve impulse carried by sensory neurons to the spinal cord or brain. Another biological function based on molecular structural transformation is the allosteric regulation where the enzyme subunits switch between a tensed conformation and a relaxed conformation. The relaxed subunits more readily bind to substrates and therefore are more active.

Among the studies of molecular conformational changes, photo-induced reversible structural transitions are particularly attractive. One of the most widely studied fields is photochromism where light irradiation induces reversible changes between two states with different absorption spectra. In the case of azobenzene photoisomerization, the trans-azobenzene can be converted to the cis under the irradiation with ultra-violet light. A different wavelength in the visible blue regime can be used to convert the molecule back to the trans form. The photoisomerization happens within a few picoseconds, while the thermal relaxation from cis to trans takes seconds to hours. Due to the fast response of photo-induced molecular switching, it has been applied to fabricate high-efficiency molecular devices. For example, Jiang and collaborators demonstrate the nanoscale architecture of a macromolecule system can be quickly changed even with very low energy photon in the infra-red range through a multi-photon absorption process [25]. Bissel and coworkers fabricate a nanoscale molecular shuttle that a super-molecule can translate between two non-degenerated recognition sites [26]. Photoinduced conformational change is also important in the catalytic processes. Wurthner and Rebek have shown that an azobenzene-based molecule can switch from one isomer to the other when irradiated with light of wavelength 366 nm. The product isomer is catalytically active and increases the reaction rate for amide bond formation between modified adenine units a factor of 10 [27]. The molecular structural transition is also important in the photoinduced charge transport systems. The reversible photoisomerization of azobenzene derivatives can transduce the optical signals into electronic signals, which have been implemented into the design of different fluorescence sensors [28]. Photoinduced molecular conformational change can also be used to modify the surface properties of materials. Tachibana and coworkers report that the structural change of TCNQ (7,7,8,8-tetracyanoquinodimethane) monolayer over conductive Langmuir-Blodgett films under UV light irradiation can be used to control the conductivity of the material [29]. More recently, molecular conformational change shows a rising potential to be applied in the next generation digital optical data systems. Single molecules can be used as memory elements where the recording of information is carried out by light.

STM has been widely applied to study the molecular conformational change due to its ability to image the structures of individual molecules. Using a variable temperature STM, the thermally induced structural change of single molecules has been studied in real-space. Piantek and coworkers [30] have observed a distinct structural change of spiropyran deposited on cold Au(111) from an ordered self-assembled domains at 240K to molecular chains at 300 K due to thermally activated ring opening isomerization. The electric field created by the bias between tip and sample can also trigger the conformational change. Alemani and collaborators show the reversible trans−cis isomerization of single azobenzene derivatives adsorbed on a Au(111) surface induced by the localized electric field in the junction [31]. Gaudioso and Ho also show that the tunneling electron can also excite the switching of a molecule, and can be mediated by molecular vibrations. Su and coworkers use an STM break junction technique and demonstrated the conformational change can be due to stereoelectronic effect [32]. By combining STM with lasers, the photoinduced molecular structural transitions can also be probed at single molecule level [33].

Comstock *et al.* observed the photo-isomerization of individual tetra-tert-butyl azobenzene molecules by irradiating the STM junction with UV light [34].

Here, we demonstrate the coherent vibration driven conformational change of a single molecule using the combination of a femtosecond laser with an STM. Individual pyrrolidine (C_4H_8NH) molecules in the junction of an STM undergoes conformational changes when excited by femtosecond laser photons. The structural transitions can be visualized as two distinct tip height states using STM in the constant height mode. The structural transition rate shows oscillatory patterns corresponding to the vibrational quantum beat between vibration excited states and the ground states. The coherent oscillations decay within a few picoseconds. We also show that the molecular dynamics can be modified by intermolecular interaction when two molecules are separated by 7.21 Å. The interactions between two molecules lower the decay time and increase the oscillation period. The combination of sub-Ångström spatial resolution of STM and the femtosecond temporal resolution of ultrafast laser opens the possibility to probe coherent chemistry at single molecule level.

6.2 Methods

The experiment is performed using a home-built, low temperature, ultra-high vacuum (UHV) STM operating at 8.6 K and 2.3×10^{-11} torr [35]. The microscope is cooled by a continuous flow liquid helium cryostat (ARS Hilitran LT3B) with helium supplied by a flexible transfer line connected to a 100 L dewar. Fig. 6.1.A is the schematic diagram of the STM junction illuminated by the femtosecond laser consists of 35 fs pulses at 5 GHz repetition rate, 820 nm wavelength, and bandwidth of 25 nm. Additional detail of the optical step has been previously described in *Chapter 1.4.* Electrochemically etched silver (Ag) tip is used to obtain high plasma enhancement of the optical field near 800 nm. The Cu(001) surface is cleaned by cycles of Ne^+ sputtering, followed by annealing to around 800 K [36]. The pyrrolidine sample (98% purity ordered from Spectrum Chemical) is further purified by more than 20 freeze-pump-thaw cycles. The molecules are dosed onto the Cu(001) surface at 8.6 K through a variable leak valve with vapors from the room temperature liquids in a glass tube [33]. No noticeable pressure change is measured in the UHV chamber during dosing. Low molecular coverage (< 0.1 ML) is targeted to have most of the pyrrolidines isolated from each other. Some pyrrolidine molecules form dimers with different intermolecular separations upon adsorption on the cold surface.

The topographic images are taken under constant current mode by recording changes in the tunneling gap (Δz) with feedback on. The bias voltage is applied to the sample with the tip connected to the current amplifier at virtual ground. The atomic resolved topographic images are recorded with a H_2 molecule trapped in the tunneling junction. Hydrogen molecules in the background of the UHV chamber can adsorb onto the surface at low temperature [37]. The adsorbed hydrogen molecules remain mobile but can be trapped in the tunneling junction at a set point of 3 mV sample bias and 7 nA tunneling current. Enhanced spatial resolution in the topographic image can be obtained when the STM is scanned with H_2 in the tunneling gap [38]. However, H_2 molecules desorb under laser illumination, thus keeping pyrrolidine molecules free from contaminants [39].

To record the time trace of molecular transitions in a delay scan, the STM tip is positioned over the maximum height of a pyrrolidine molecule with tracking function to compensate lateral drifting. The tip samples the molecule at eight points on a circle of 0.2 Å radius, senses the gradient and adjusts its position toward the maximum junction gap position every 1 ms during tracking [40]. Both tunneling current (I) and junction gap (z) signals are recorded using a Data Acquisition

Device (National Instrument DAQ) with a home-made LabVIEW program which also controls the motorized linear stage. The program starts recording only when the molecule is in the high state. When two pulses are temporally separated ($|\tau|>100$ fs), the time trace of the z value is recorded for 12 seconds at each delay of a given pass. Multiple passes are averaged to counter effects due to long term laser power fluctuations. When two pulses are temporally overlapped ($|\tau|\leq 100$ fs), the shaker is turned on. We wait for 60 s after stepping to a new delay to allow the junction to stabilize from thermal drifting, followed by 60 s acquisition of the Δz time trace. The unidirectional repeatability and minimum incremental motion of the linear stage are both 0.3 μm (equivalent to 2 fs delay time). P-polarized light with E field vector in the incident plane is used in all the delay scans reported in this study. The incident plane contains the tip axis and the laser beam propagation direction. The total average power for the two laser pulses at the entrance to the UHV chamber is maintained at 1.5 mW, which increases the equilibrium sample temperature by 70 mK from 8.6 K. The temperature fluctuations are within 2 mK either in the dark or under laser irradiation. The temperature drift becomes too large for average powers greater than 10 mW, and the tunnel junction becomes unstable [19,20]. However, average powers less than 2 mW are used in laser-STM experiments, due largely to the plasmonic enhancement of the laser field in the tunnel junction by using Ag tips.

Density Functional Theory (DFT) calculations were carried out using the Vienna ab-initio simulation package (VASP) at the level of the generalized-gradient approximation (GGA) with the Perdew-Burke-Ernzerhof (PBE) exchange-correlation functional. The nonlocal van der Waals density functional was included in self-consistent calculations. The interaction between valence electrons and ionic cores was described within the framework of the projector augmented wave (PAW) method. The energy cutoff for the plane wave basis expansion was set to 700 eV, which is sufficient according to test calculations. A large (5x5) supercell in the lateral plane was used to calculate the single molecule adsorption geometries on Cu(001). A 5×5 k-grid mesh was used to sample the two-dimensional Brillouin zone. All atoms were fully relaxed using the conjugated gradient method for the energy minimization until the force on each atom became smaller than 0.01 eV/Å.

6.3 Results and Discussion

The pyrrolidine molecules adsorb on a Cu(001) surface appearing as protrusions in constant current STM topographic images (Fig. 6.1.C). Both DFT calculations and atomic resolved topographic images show that Pyrrolidine molecules adsorb on the atop sites of Cu atoms (Fig. 6.1.E). Calculations also suggest the molecule bonds with the metal substrate through the nitrogen electron lone pair, in consistent with the previous deuterium exchange studies over transition metal catalysts. The spikes like noise apparent in the image are due to the switching of molecules as the tip scans across them. At low applied bias without laser excitation, two distinct states as indicated in Fig. 6.1.B can be clearly imaged as shown in Fig. 6.1.C and cross-sectional cuts in Fig. 6.1.D. Clear structural transitions of a molecule can be observed at fixed sample bias by monitoring changes in the tunneling gap in constant current mode (feedback on) or by changes in the tunneling current at a fixed gap (feedback off, constant height mode). The switching between state I and II can be clearly seen in the time dependent changes of tunneling gap (Δz trace) recorded over the center of a pyrrolidine molecule with feedback on (Fig. 6.2). The residence times in either state I or II, obtained from the time traces, are exponentially distributed, as shown in the Fig. 6.2.C-D, in agreement with a Poisson random process. The transition rate can then be taken as the number of

FIG. 6.1. Combining femtosecond laser and STM to probe single molecule dynamics. (A) Schematic diagram of the STM junction illuminated by pairs of phase-correlated femtosecond laser pulses. (B) Reversible transitions between two structural states I and II for pyrrolidine on Cu(001). (C) Topographic images revealing the two states. (D) The vertical line cut across the state I of the upper molecule (red dashed lines in c and d); vertical line cut (black dashed line of state II) and horizontal line cut (blue solid lines in c and d showing I to II and II to I transitions) across the lower molecule. (E) Energetics landscape along the pathways for structural transition and the optimized structures for the states I and II and the transition state between them given by DFT calculations.

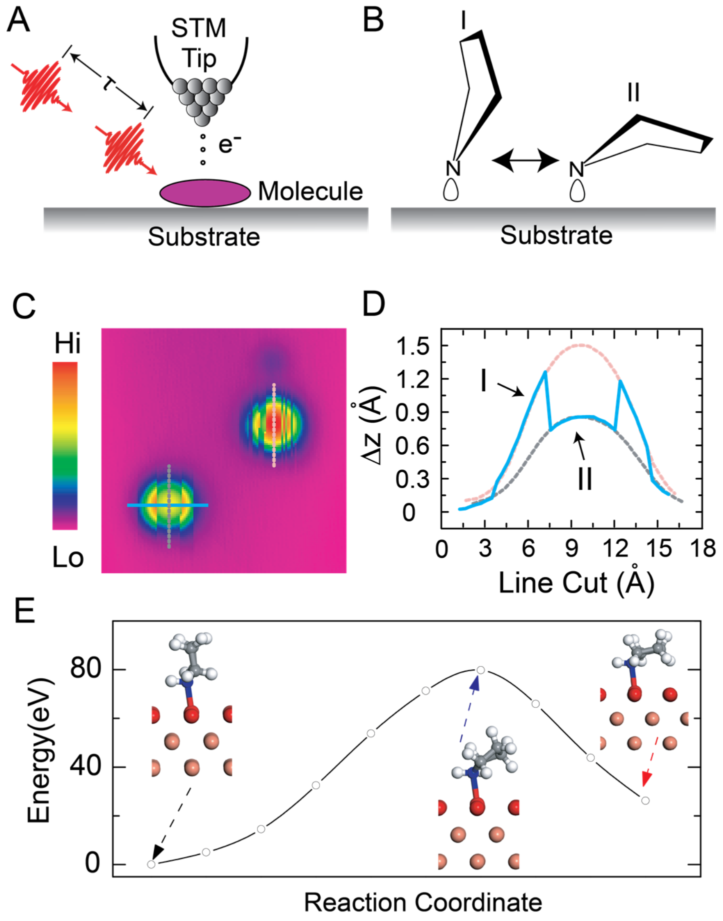
A
τ
STM
Tip
e-
Molecule
Substrate
B
I
II
N
N
Substrate
C
Hi
Lo
D
1.5
1.2
0.9
0.6
0.3
0
Δz (Å)
I
II
0
3
6
9
12
15
18
Line Cut (Å)
E
80
40
0
Energy(eV)
Reaction Coordinate

FIG. 6.2. Laser induced conformational change of pyrrolidine on a Cu(001). (A) Topographic images and corresponding time traces of changes in the tunneling gap (Δz) recorded over positions marked by circular symbol, from top to bottom: isolated pyrrolidine molecule without light; isolated pyrrolidine irradiated by laser; lower molecule in the dimer with laser; center of the dimer with laser. Tunneling gap set at 30 mV sample bias, 50 pA tunneling current, and with the feedback on. A transition cycle consists of I to II and back to I. (B) Binned residence time of state I (high z state). (C) The binned residence time of state II (low z state). The data are extracted from a time trace of 20 minutes duration recorded over a monomer under femtosecond laser irradiation with the delay time set at 600 fs and 1.5 mW laser power. Bin size is 40 ms. The red line indicates an exponential fit of the data. The mean residence time is 322 ms for the state I and 83 ms for the state II. The exponential distribution of the residence time means the average residence time is the same as the 1/e decay time of the exponential function. This result validates the counting of number of cycles per min as the transition rate for events following Poisson statistics, with an event being a cycle of transition from state I to state II and back to state I. (D) Topographic image showing the 17 locations where transition rate was obtained in (E) from Δz trace recorded for 300 s.

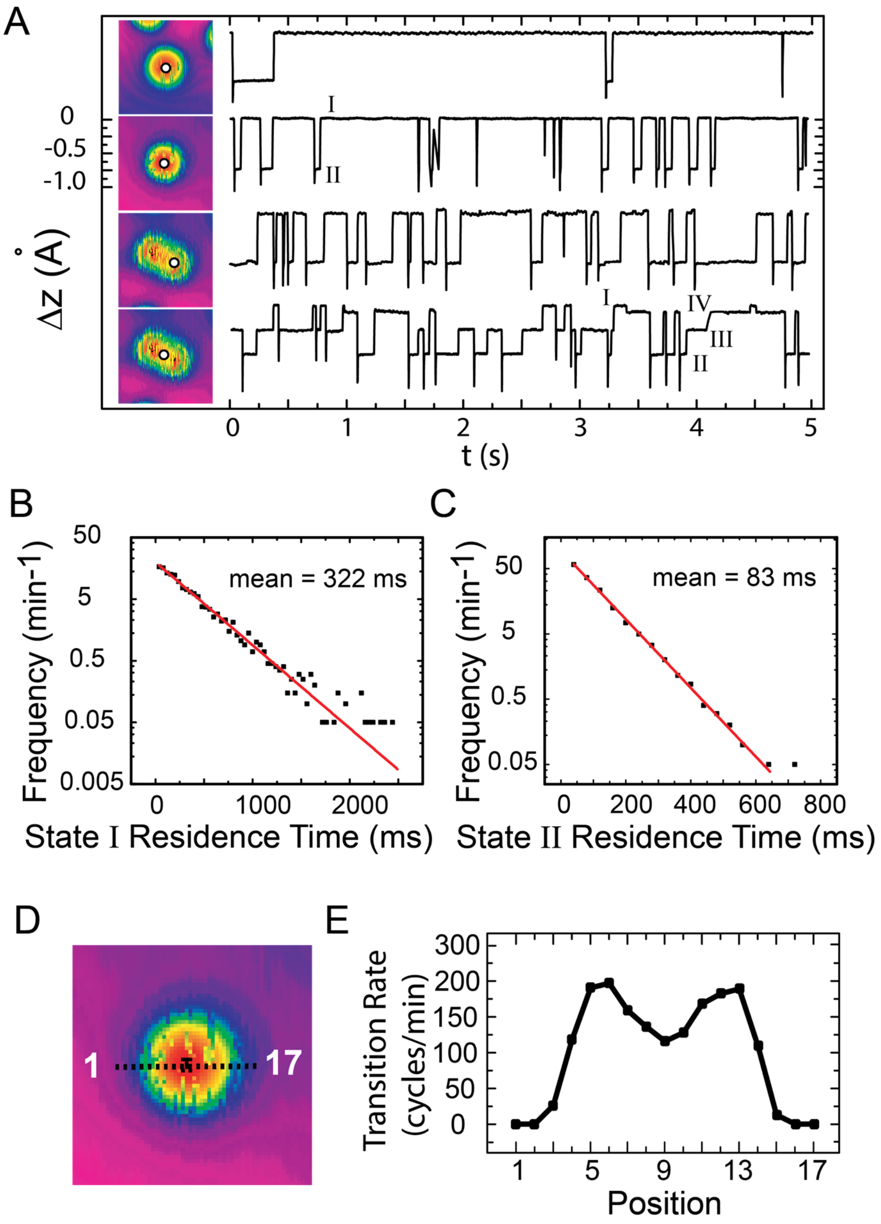
A
0
-0.5
-1.0
Δz (Å)
I
II
I
IV
III
II
0
1
2
3
4
5
t (s)
B
50
5
0.5
0.05
0.005
Frequency (min-1)
mean = 322 ms
0
1000
2000
State I Residence Time (ms)
C
50
5
0.5
0.05
Frequency (min-1)
mean = 83 ms
0
200
400
600
800
State II Residence Time (ms)
D
1
17
E
300
200
150
100
50
0
Transition Rate (cycles/min)
1
5
9
13
17
Position

cycles of down and up changes in Δz per unit time. The isolated pyrrolidine spends 75% time in state I. The DFT calculations in Fig. 6.1.E reveals a difference of 26 meV between the binding energies of state I (0.639 eV) and state II (0.613 eV) and an energy barrier of 79 meV from the state I to the transition state at the top of the barrier. The five-member ring of the pyrrolidine in the transition state is tilted at an angle between the state I and II. The structures of the molecule in states I, II, and the transition state given by DFT calculation are shown as insets of Fig. 6.1.E.

We've studied this system in detail and characterized the conformational change that can be driven by molecular vibration excited by inelastic tunneling electrons in the absence of light [34]. The rate of structural transition can be decreased by lowering the energy of the tunneling electrons as determined by the sample bias. In this study, we found that the transition rate of an isolated pyrrolidine molecule significantly increases when the STM junction is irradiated by femtosecond laser pulses (Fig. 6.2.A). Further increase in the transition rate is observed when two molecules are in close proximity (dimer). Additionally, four distinct levels (I-IV) corresponding to the four possible combinations of states of the two molecules are observed when the STM tip is positioned over the center of the dimer. Measured transition rates vary as the tip positioned over different points of the molecule, probably due to the local chemical potential changed by the STM tip.

To reveal the coherent dynamics in these molecular conformational changes, we perform delay scans over the center of a molecule by counting the transition rate at different delay time between a pair of time-correlated pulses. Coherent oscillations are observed in the delay scan taken over a monomer as shown in Fig. 6.3A, and are not seen in the control experiments performed in dark or with a laser operating at continuous wave (CW) mode. The scan is symmetric over zero

FIG. 6.3. Femtosecond laser driven coherent oscillations in the structural transition of a pyrrolidine monomer on Cu(001). (A) Delay scan (red dots, −3500 fs to +3500 fs in 2 fs steps) over the center of a monomer. The sign of the delay reflects the temporal order of the two pulses. Transition rate is determined from the sum of 5 passes, each pass with Δz trace recorded for 12 s at every delay, except one pass of 60 s at each delay for $|\tau| \leq 100$ fs. The black dashed line is the fit using equation 6.1. The two insets above (blue dots) show delay scans from the sum of 10 passes; the same fit is shown. The green dots plot transition rate vs. delay for continuous wave (CW) irradiation (laser not mode-locked) with only one arm of the Michelson interferometer and the same total power of 1.5 mW. The black dots are for transition rate vs. delay in the dark. The two control scans show no oscillations and the "delay" refers to having the same linear translator position as the scan with the femtosecond laser pulses. (B) Fourier transform of the data presented in A, showing a dominant peak (145 ± 4 fs, 6.9 ± 0.2 THz, or 28.5 ± 0.7 meV) and a weak peak (365 ± 44 fs, 2.7 ± 0.3 THz, or 11.3 ± 1.4 meV). The uncertainty of the 6.9 THz peak is obtained from fitting the delay scan to the dominant sinusoidal function at 6.9 THz. The uncertainty of the 2.7 THz peak is the step size in the FFT spectrum. Inset shows the topographic image of the molecule for all the data in this figure. (C) Topographic image taken in the dark with gap set at 3 mV, 7 nA, and with molecular hydrogen in the background and trapped in the STM junction to enhance resolution. Center of each pyrrolidine molecule coincides with a Cu atom of the substrate surface.

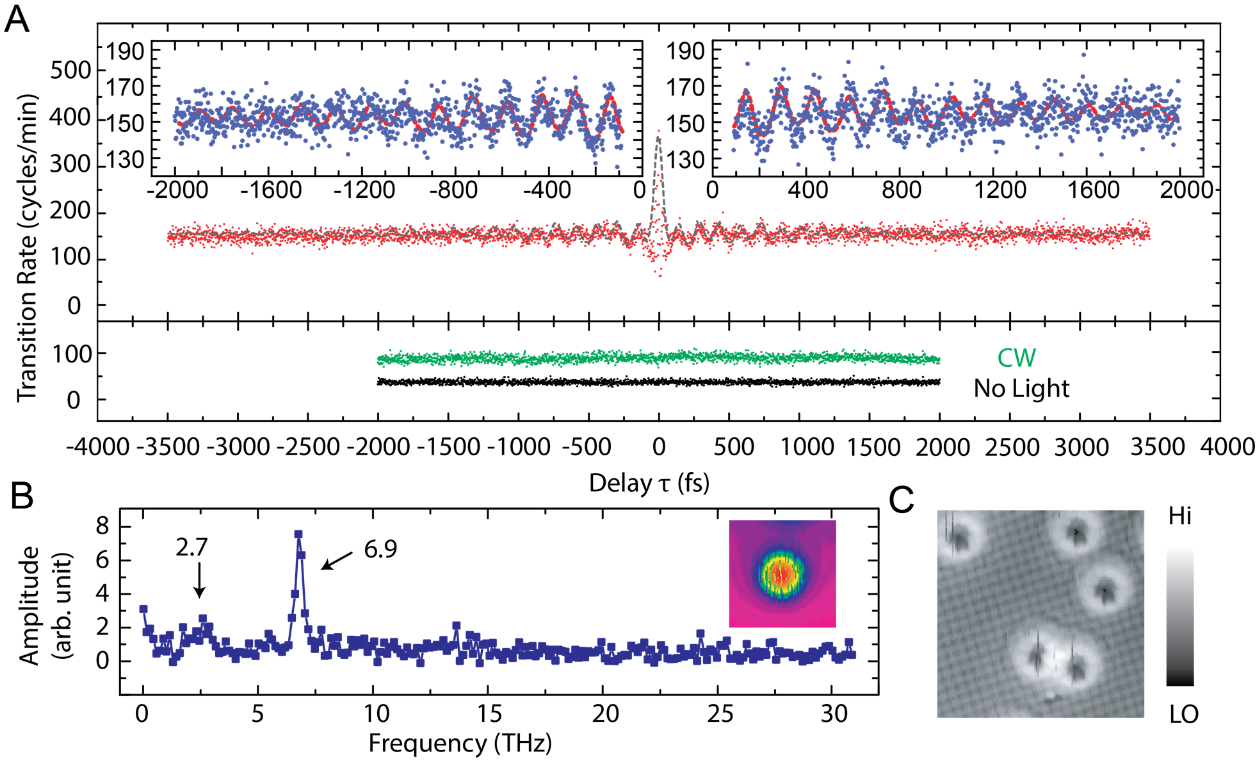
A
Transition Rate (cycles/min)
500
400
300
200
100
0
190
170
150
130
-2000
-1600
-1200
-800
-400
0
400
800
1200
1600
2000
100
0
CW
No Light
-4000 -3500 -3000 -2500 -2000 -1500 -1000 -500 0 500 1000 1500 2000 2500 3000 3500 4000
Delay τ (fs)
B
Amplitude (arb. unit)
8
6
4
2
0
2.7
6.9
0
5
10
15
20
25
30
Frequency (THz)
C
Hi
LO

delay time since each time-correlated pulse pair consists of two identical laser pulses. The negative delay time corresponds to the reversed pulse order. In the zoom in the spectrum shown in the insets of Fig. 6.3.A, weak beating effect can be seen at both positive and negative sides of the spectrum. Fast Fourier transform (FFT) of the time delay scan in Fig. 6.3.B reveals two peaks at 6.9 THz (28.5 meV) and 2.7 THz (11.3 meV) in the frequency domain. These two frequencies fall in the typical regime of molecular vibrations. We thus believe the oscillatory pattern resolved in the delay scan origins from the quantum beat of molecular vibrations. The coherent transitions rate only accounts 10 to 15% of the total transition rate, and decay within a few picoseconds as the coherent vibrations decay. Most of the transitions are excited by the incoherent photo-generated hot carriers that can induce photochemistry through electronic excitation and electron-vibrational coupling [41]. The laser induced switching under CW irradiation is solely from these incoherent excitations. Near zero delay time where two pulses are temporally overlapping, the transition rate exhibits an autocorrelation interference of the electric fields of the two laser pulses. The center feature can be fitted with a Gaussian envelope like a field autocorrelation spectrum.

We can fit the delay scan by the sum of three parts in equation 6.1: a coherent transition rate R_{coh} of two exponentially decaying sinusoidal functions, a constant incoherent switching rate R_{inc}, and a Gaussian function R_{Gauss} accounts for the auto-correlation signal near zero delay:

$$\mathrm{R} = R_{coh} + R_{inc} + R_{Gauss}$$

$$= \sum_{i=1}^{2}[A_i \sin(2\pi f_i \tau + \varphi)] e^{-|\tau|/T} + constant + A e^{-\tau^2/(2\sigma^2)} \qquad (6.1).$$

The oscillation frequencies f_1 (2.7 ± 0.3 THz) and f_2 (6.9 ± 0.2 THz) are determined from the peaks in FFT spectrum in Fig. xx. The partition coefficient A_1 is set as (2.6/7.9) A_2 where 2.6 and 7.9 are the FFT amplitudes at f_1 and f_2 obtained directly from Fig. 6.3.B. We assumed the phase and decay constant to be the same for both vibrations to reduce the number of fitting parameters. This assumption is validated by the overall good fit to the experimental data. The decay constant *T* obtained from equation 6.1 is 1.30 ± 0.17 ps for the isolated pyrrolidine shown in Fig. 6.3, which is approximately half the values measured for the higher energy stretch vibrations of an ensemble of molecules on metal surfaces [42,43]. In our study, the molecular vibration modes we found are within the copper phonon bands [44]. The decay channel due vibration-phonon interaction may contribute to the faster vibrational decay.

Density Functional Theory (DFT) calculations provide a deeper understanding of the nature of these two molecular vibrations that drive the structural transition. Eight normal vibrational modes are identified with energies less than 50 meV, as shown in Fig. 6.4 (A-H). We assign the 6.9 ± 0.2 THz oscillation to the mode in Fig. 6.4.G (27.2 meV), corresponding to an overall bending motion of the molecule. Since the structural transition between state I and II involves a folding and unfolding of the molecule, the bending vibrational mode is believed to be readily correlated with the structural switching. The weaker mode around 2.7±0.3 THz (11.3 ± 1.4 meV) is assigned to the mode in Fig. 6.4.A (11.8 meV). This mode involves the overall bouncing motion of the molecule against the surface. The excitation of this mode leads to a nucleus motion in the order of 0.2 Å, which is the largest amount all 8 normal modes. The variation of molecule-substrate distance can modify the activation energy of this structural transition and change the switching rate.

Traditionally, coherent vibrational oscillation visualized for the molecules in the gas phase are excited through Frank-Condon scattering, where a broadband laser pulse excites the superposition of multiple vibrionic excited states [4]. However, for the molecules adsorbed on the metal surface, the strong hybridization between molecule and substrate broadens the molecular electronic states and shortens their lifetimes. We believe the vibration modes in this study are

FIG. 6.4. DFT Calculations of low energy vibrations. (A-H) The eight vibrations of a single pyrrolidine adsorbed as state I on the Cu(001) surface with energies smaller than 50 meV (11.85, 12.91, 13.36, 13.57, 17.32, 18.85, 27.24, and 46.51 meV). Green arrows show directions and amplitudes of atom motions of each eigenmode. Mode A (11.85 meV) and mode G (27.24 meV) are assigned to the two peaks in Fig. 6.3.B (11.3 meV and 28.5 meV).

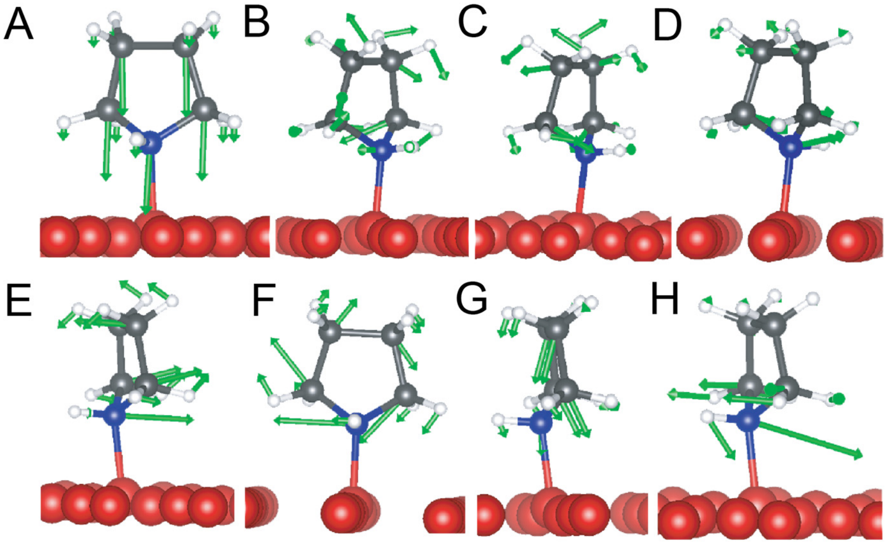
A
B
C
D
E
F
G
H

excited through an impulsive stimulated Raman process. The femtosecond laser operates at a central wavelength of 820 nm, 25 nm bandwidth (46 meV energy spread), and has a 35 fs pulse width that is shorter than the period of the observed oscillations. The laser pulses can excite a superposition of the ground and first excited states of low energy vibrations in the ground electronic state [45]. The populations of the excited state would have an oscillatory component at a frequency corresponding to the vibrational energy difference between the v=0 and v=1 states [46]. The excited state population can influence the transition rate through the attempt frequency in the pre-exponential factor and leads to the coherent oscillatory pattern resolved in the delay scan.

The sub-Å special resolution of STM allows the assessment of the local chemical environment on the molecular dynamics. We have found that the coherent oscillations can be modified by the intermolecular interaction. Pyrrolidine molecules can adsorb in dimers with different intermolecular separations (Fig. 6.5). The dimer is shown in Fig. 6.6 with 7.21 Å intermolecular separation exhibits a nearly 70% increase in the transition rate compared to the monomer. The delay scan taken over the same dimer reveals only one oscillation frequency at 6.0 THz with a decay time constant of 0.90 ± 0.16 ps. Therefore, the delay scan reveals that the energy of the main vibrational mode driving the structural transition decreased by 3.7 meV due to the intermolecular interaction. The faster decay time is probably due to the additional energy decay channel opened up by the interaction between two molecules. The delay scans taken over other dimers are shown in Fig. 6.7. The variation of vibration periods measured between these molecules highlight the importance of single molecule measurement where the inhomogeneous properties of each individual molecules can be investigated.

FIG. 6.5. Topographic images of pyrrolidine dimers with different intermolecular separations. (A-F) Left to right: topographic images, atom-resolved topographic images, with a superimposed schematic of Cu(001) surface atoms, and schematic models of surface atoms and positions of pyrrolidine monomer and different dimers. The dotted circles outline the size of molecules in atom-resolved topographic images. The intermolecular separations from B to F dimers are 5.70 Å, 7.21 Å, 7.65 Å, 8.06 Å, and 9.19 Å. Tunneling gap set points are 30 mV, 50 pA for topographic images and 3 mV, 7nA for atomically resolved topographic images.

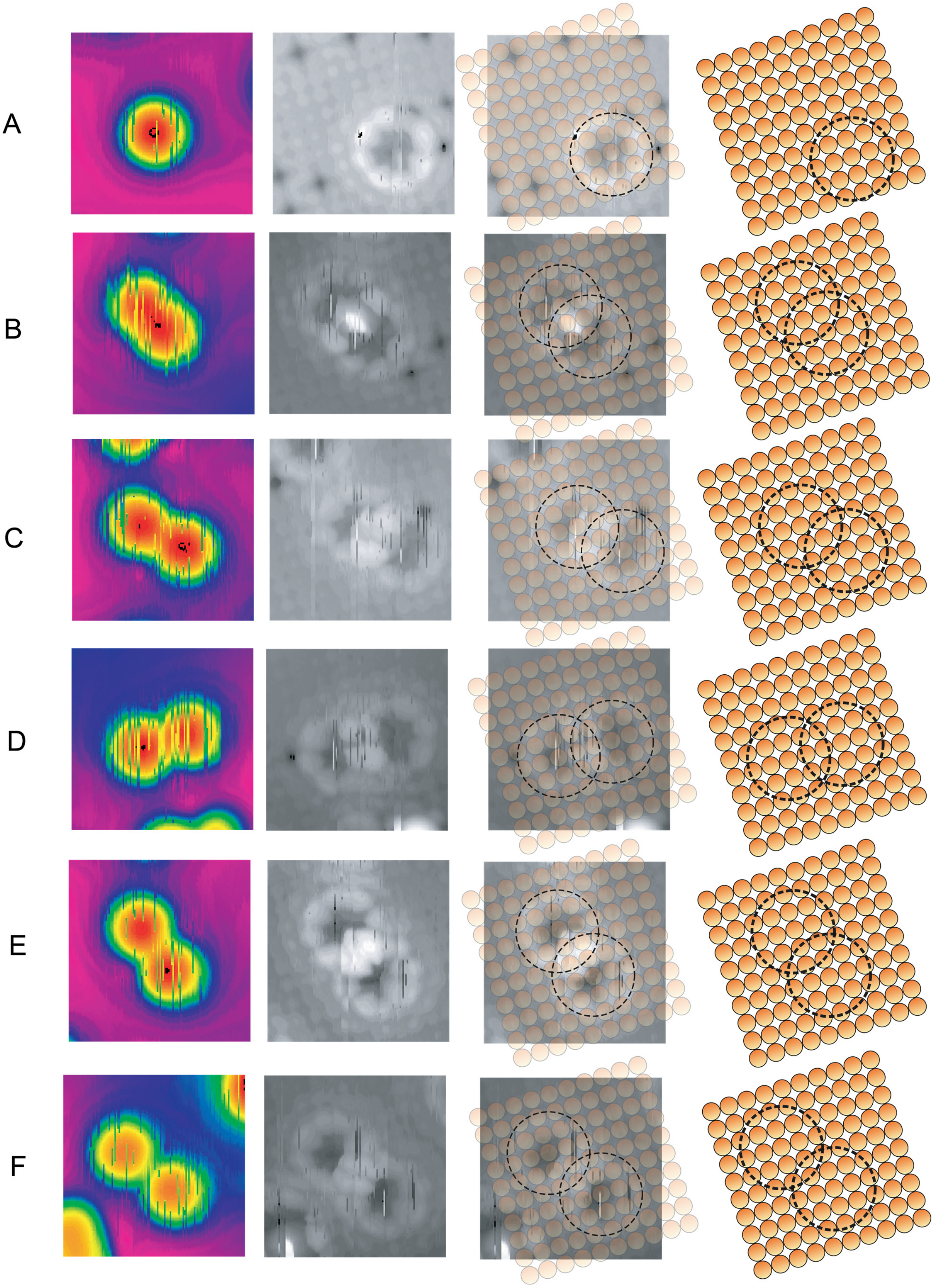
A
B
C
D
E
F

FIG. 6.6. Femtosecond laser driven coherent oscillations in structural transformation of a pyrrolidine dimer on Cu(001). (A) Delay scan over the center of one of the pyrrolidine molecule in a dimer with separation of 7.21 Å between the two molecules (red dots), taken under the same conditions as Fig. 6.3A. The black dashed line is the fit using equation 6.1. Insets are delay scans taken under the same conditions as insets in Fig. 6.3A. The horizontal dashed line indicates transition rate recorded in the dark over the same molecule in the dimer, showing background count of ~51 counts min^{-1} driven by incoherent tunneling electrons. (B) Fourier transform of time domain data in A, revealing one peak at 6.0 ± 0.2 THz (167 ± 4 fs period and 24.8 ± 0.6 meV energy; uncertainty obtained from the sinusoidal fit to the delay scan). The insets are the topographic image (left), an atom-resolved topographic image with a superimposed schematic of substrate surface atoms (right). (C) Atom-resolved topographic image.

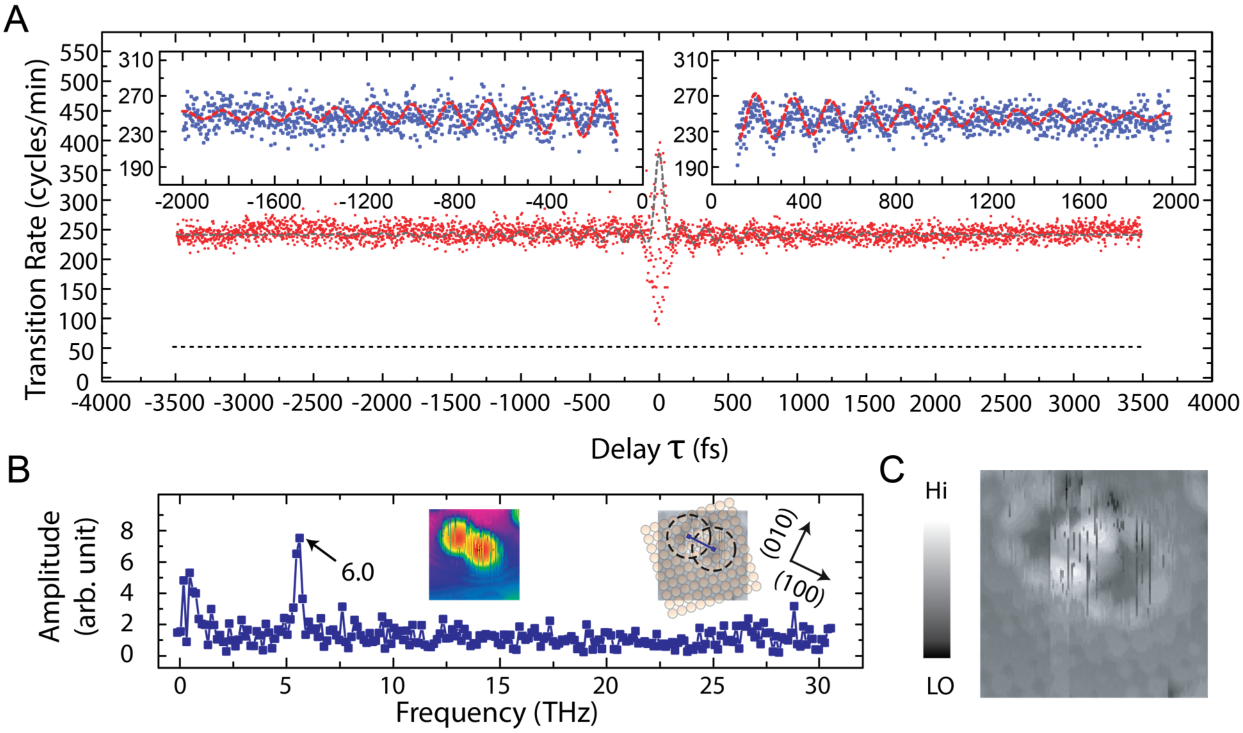
A
Transition Rate (cycles/min)
550
500
450
400
350
300
250
200
150
100
50
0
-4000
-3500
-3000
-2500
-2000
-1500
-1000
-500
0
500
1000
1500
2000
2500
3000
3500
4000
Delay τ (fs)
310
270
230
190
-2000
-1600
-1200
-800
-400
0
310
270
230
190
0
400
800
1200
1600
2000
B
Amplitude (arb. unit)
8
6
4
2
0
6.0
(010)
(100)
0
5
10
15
20
25
30
Frequency (THz)
C
Hi
LO

FIG. 6.7 Delay scans and topographic images of three different dimers compared to a monomer. The dashed lines are the fits using damped sine function. The oscillation period and separation between molecules in dimer: (A) 164.9 ±3.4 fs, 7.21 Å, (B) 147.2 ± 5.6 fs, 8.06 Å, (C) 147.6 ± 6.2 fs, 9.19 Å. For the monomer: (D) 146.1 ± 5.7 fs. For b and c, no difference in the period is resolved, suggesting that the intermolecular interactions have reduced and do not affect the vibrational energy. The adsorption sites for the molecules are obtained from atom-resolved topographic scans as in Fig. 6.7. The center of the topographic images for molecules is directly over a copper surface atom of the Cu(001) surface.

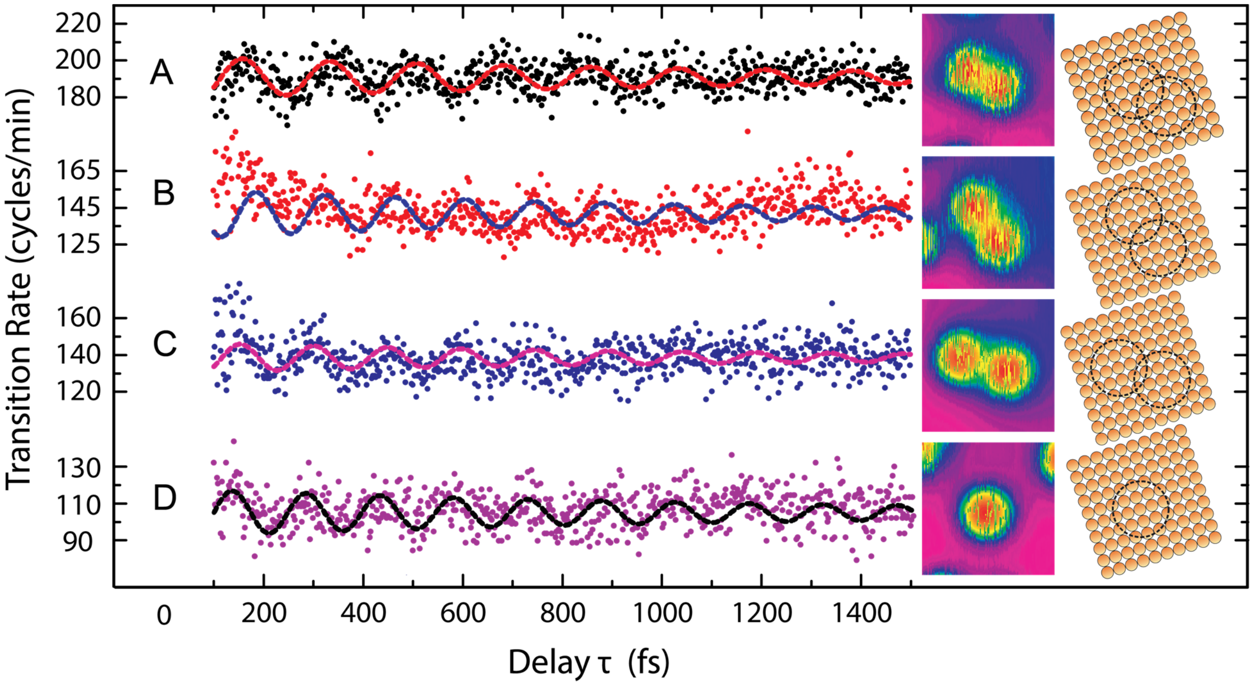
Transition Rate (cycles/min)
220
200
180
165
145
125
160
140
120
130
110
90
A
B
C
D
0
200
400
600
800
1000
1200
1400
Delay τ (fs)

6.4 Conclusions

In summary, the studies of ultrafast molecular dynamic are now extended to sub-molecular scale through the combination of femtosecond laser and scanning tunneling microscope. A single-molecule reaction driven by coherent vibrational excitation is demonstrated with joint Å-fs resolution. This technique enables the investigation of inhomogeneous environmental effect on molecular dynamics. We anticipate that this novel technique will soon be extended to other chemical transformations such as reversible proton motions, phase transitions, bond dissociations, and would lead to a broader impact in chemistry through direct visualization of coherence chemistry in space and time [47,48].

Bibliography

[1] A. H. Zewail, J. Phys. Chem. A. **104**, 5660 (2000).

[2] X. Xie et al., Phys. Rev. Lett. **109**, 243001 (2012).

[3] H. Rabitz, R. de Vivie-Riedle, M. Motzkus, and K. Kompa, Science **288**, 824 (2000).

[4] L. Piatkowski, N. Accanto, and N. F. van Hulst, ACS Photonics, **3**, 1401 (2016).

[5] G. C. Cho, W. Kütt, and H. Kurz, Phys. Rev. Lett. **65**, 764 (1990).

[6] T. K. Cheng, S. D. Brorson, A. S. Kazeroonian, J. S. Moodera, G. Dresselhaus, M. S. Dresselhaus, and E. P. Ippen, Appl. Phys. Lett. **57**, 1004 (1990).

[7] Y. M. Chang, L. Xu, and H. W. K. Tom, Phys. Rev. Lett. **78**, 4649 (1997).

[8] D. Star, T. Kikteva, and G. W. Leach, J. Chem. Phys. **111**, 14 (1999).

[9] A. N. Bordenyuk, H. Jayathilake, and A. V. Benderskii, J. Phys. Chem. B **109**, 15941 (2005).

[10] K. Watanabe, N. Takagi, and Y. Matsumoto, Chem. Phys. Lett. **366**, 606 (2002).

[11] U. Höfer, I. L. Shumay, C. Reuß, U. Thomann, W. Wallauer, and T. Fauster, Science **277**, 1480 (1997).

[12] W. E. Moerner and L. Kador, Phys. Rev. Lett. **62**, 2535 (1989).

[13] M. Orrit and J. Bernard, Phys. Rev. Lett. **65**, 2716 (1990).

[14] S. W. Hell and J. Wichmann, Opt. Lett. **19** 780 (1994).

[15] E. Betzig, G. H. Patterson, R. Sougrat, O. W. Lindwasser, S. Olenych, J. S. Bonifacino, M. W. Davidson, J. Lippincott-Schwartz, H. F. Hess, Science **313** 1642 (2006).

[16] D. W. Pohl, W. Denk, and M. Lanz, Appl. Phys. Lett. **44**, 651 (1984).

[17] E. Betzig, M. Isaacson, and A. Lewis, Appl. Phys. Lett. **51**, 2088 (1987).

[18] E. Betzig, J. K. Trautman, T. D. Harris, J. S. Weiner, R. L. Kostelak, Science **251** 1468

(1991).

[19] S. W. Wu, N. Ogawa, and W. Ho, Science **312**, 1362 (2006).

[20] S. W. Wu and W. Ho, Phys. Rev. B **82**, 085444 (2010).

[21] S. Yoshida, Y. Aizawa, Z.-H. Wang, R. Oshima, Y. Mera, E. Matsuyama, H. Oigawa, O. Takeuchi, and H. Shigekawa, Nature Nanotechnol. **9**, 588 (2014).

[22] T. L. Cocker, D. Peller, P. Yu, J. Repp, and R. Huber, Nature **539**, 263 (2016).

[23] B. L. Feringa, R. A. van Delden, N. Koumura, and E. M. Geertsema, Chem. Rev. **100**, 1789 (2000).

[24] M. R. Wilson, J. Solà1, A. Carlone1, S. M. Goldup, N. Lebrasseur, and D. A. Leigh, Nature **534**, 239, (2016).

[25] D. L. Jiang and T. Aida, Nature **388**, 454, (1997).

[26] R. A. Bissel, E. Cordova, A. E. Kaifer, J. F. Stoddart, Nature **369**, 133 (1994).

[27] F. Wurthner, H. Rebek, Angew. Chem., Int. Ed. Engl. **34**, 446 (1995).

[28] R. A. Bissel, A. P. de Silva, H. Q. N. Gunaratne, P. L. M. Lynch, G. E. M. Maguire, K. R. A. S. Sandanayake, Chem. Soc. Rev. **21**, 187 (1992).

[29] H. Tachibana, Y. Kawabata, H. Kozumi, E. Manda, M. Matsumoto, T. Nakamura, H. Niino, A. Yabe, A. J. Am. Chem. Soc. **111**, 3080 (1989).

[30] M. Piantek, G. Schulze, M. Koch, K. J. Franke, F. Leyssner, A. Kruger, C. Navio, J. Miguel, M. Bernien, M. Wolf, W. Kuch, P. Tegeder, and J. I. Pascual, J. Am. Chem. Soc. **131**, 12729 (2009).

[31] M. Alemani, M. V. Peters, S. Hecht ,K. H. Rieder, F. Moresco, and L. Grill, J. Am. Chem. Soc. **128**, 14446 (2006).

[32] T. A. Su, H. Li, M. L. Steigerwald, L. Venkataraman, and C. Nuckolls, Nature Chem. **7**, 215 (2015).

[33] J. Gaudioso, L. J. Lauhon, and W. Ho, Phys. Rev. Lett. **85**, 1918 (2000).

[34] M. J. Comstock, N. Levy, A. Kirakosian, J. Cho, F. Lauterwasser, J. H. Harvey, D. A. Strubbe, J. M. J. Fréchet, D. Trauner, S. G. Louie, M. F. Crommie, Phys. Rev. Lett. **99**, 038301 (2007).

[35] B. C. Stipe, M. A. Rezaei, and W. Ho, Rev. Sci. Instrum. **70**, 137 (1999).

[36] B. C. Stipe, M. A. Rezaei, and W. Ho, Science **280**, 1732 (1998).

[37] J. A. Gupta, C. P. Lutz, A. J. Heinrich, and D. M. Eigler, Phys. Rev. B **71**, 115416 (2005).

[38] C. Weiss, C. Wagner, C. Kleimann, M. Rohlfing, F. S. Tautz, and R. Temirov, Phys. Rev. Lett. **105**, 086103 (2010).

[39] S. Li, A. Yu, F. Toledo, Z. Han, H. Wang, H. Y. He, R. Wu, and W. Ho, Phys. Rev. Lett. **111**, 146102 (2013).

[40] L. J. Lauhon and W. Ho, J. Chem. Phys. **111**, 5633 (1999).

[41] Laser Spectroscopy and Photochemistry on Metal Surfaces, Part I and Part II, H.-L. Dai and W. Ho, Eds. (World Scientific, Singapore, 1995).

[42] A. L. Harris, L. Rothberg, L. H. Dubois, N. J. Levinos, and L. Dhar, Phys. Rev. Lett. **64**, 2086 (1990).

[43] M. Morin, N. J. Levinos, and A. L. Harris, J. Chem. Phys. **96**, 3950 (1992).

[44] E. C. Svensson, B. N. Brockhouse, and J. M. Rowe, Phys. Rev. 155, 619 (1967).

[45] S. Ruhman, A. G. Joly, and K. A. Nelson, J. Chem. Phys. **86**, 6563 (1987).

[46] M. J. Rosker, F. W. Wise, and C. L. Tang, Phys. Rev. Lett. **57**, 321 (1986).

[47] H. Petek, ACS Nano, 8, 5 (2014).

[48] W. Ho, J. Chem. Phys. **117**, 11033 (2002).

CHAPTER SEVEN

Real-space Observation of Nanoelectrical Band Bending and Flattening at a Single Molecule Interface[†]

Abstract

The surface band bending and photo induced band flattening are observed in real-space using a variable temperature scanning tunneling microscope combined with a Ti-sapphire laser. The lowest unoccupied molecular orbital of a single C_{60} over a boron doped Si (111) surface and the surface state of a Si atom vacancy are measured with the scanning tunneling spectroscopy. Laser irradiation is found to up-shift the defect state due to the photo induced flattening of the band bending. Larger shifts are observed for the C_{60} states, which are attributed to enlarged local band bending due to the electron transfer from Si to C_{60} molecules. The laser induced shifts of both states are found to be smaller at an elevated temperature.

[†] This chapter by Shaowei Li, Arthur Yu, and W. Ho is in preparation for submission.

7.1 Introduction

The ultimate task in molecular electronics is to use individual molecules as active electronic components to fabricate industrial level devices [1]. However, miniaturization of semiconductor devices presents fundamental and technological challenges for fabricating and characterization of the desired band structure with controlled atomic composition [2]. As the size of a semiconductor moves towards nano-scale, the carrier recombination at surfaces or interfaces places an important role in determining the efficiency of the device [3]. Recently, increased attentions have been paid on understanding and controlling the surface recombination of a molecular-semiconductor interface to design and fabricate durable and efficient device at single molecule level [4-6].

Understanding the band bending at a surface or interface is especially important in designing P-N junctions which are the basic building blocks of semiconductor industry [7]. When materials with different Fermi levels come into contact, electrons will transfer from the one with the higher energy Fermi level to the other until the Fermi levels at the interface are equilibrated. The surface or interface of the semiconductors thus become ionized which establishes an electric field and bend the valence band and the conduction band with respect to the Fermi level. Band bending of bulk semiconductor materials has been widely studied using surface photovoltage (SPV) measurements [8], X-ray photoelectron spectroscopy (XPS) [9] or ultraviolet photoelectron spectroscopy (UPS) [10]. But the lack of spatial resolution limits their application at the single molecule scale.

Scanning tunneling microscope (STM) is an ideal tool to study the surface electronic structure at the single molecule level due to is unparalleled spatial resolution [11]. The local density of state of the substrate can be detected by scanning tunneling spectroscopy (STS) [12]. It contributes to our understanding of the fundamental properties of semiconductors including surface reconstructions [13], band structures [14], and surface states [15] and molecular orbitals [16]. The combination of STM with a laser allows the investigation of light-matter interaction in real-space, benefiting the realization of efficient conversion of solar energy, and the design of optoelectronics devices [17-21].

Here use a variable temperature STM combined with a Ti-sapphire laser to probe the band bending induced by single molecule dopants on Si(111) surface. Laser induced band flattening is resolved near both a single C_{60} molecule and a Si atom vacancy. C_{60} is found to increase the amplitude of the band bending locally. Reduced band bending is observed when the temperature is increased from 80 K to 90 K. This study reveals the fundamental mechanisms of how light can be efficiently coupled to a molecule-semiconductor interface.

7.2 Methods

The experiment is carried out with a home-built variable temperature scanning tunneling microscope running at a base pressure of 3×10^{-11} torr [22]. The bias is provided to the STM tip with the sample as a virtual ground. The STM is equipped with a spherical lens focusing at the tunneling junction which can be used to illuminate the junction with laser beams. The electrochemically etched silver tip is used in the experiment due to its strong plasma enhancement in the visible light range. The p-type Si(111) sample is cleaned by cycles of Ne^+ ion bombardments and annealing as reported previously until clear 7×7 reconstructed surface structure can be imaged with STM (Fig. 7.1). The sample is cooled by a continuous flow liquid helium cryostat. The temperature of the sample can be controlled from 8 K to room temperature by regulating the helium flow rate. The Si sample becomes non-conductive below 40 K, preventing the STM measurements.

FIG. 7.1. Topographic images of C_{60} molecules over a Si(111) surface. (A) Large area topography scan of Si(110) surface, showing the coverage of C_{60} molecules. (B) Zoom in image taken over an isolated C_{60}. (C) Zoom-in image over a bare Si(111) surface showing clear 7×7 reconstruction. (D) A Si atom vacancy and a Si atom created by parking the tip over a Si atom at $V_B = 2.0$ V, $I_T = 0.5$ nA. (E) The Si adatom can move around when taking topographic images. All the images are taken under constant current mode at $V_B = 1.5$ V, $I_T = 0.1$ nA.

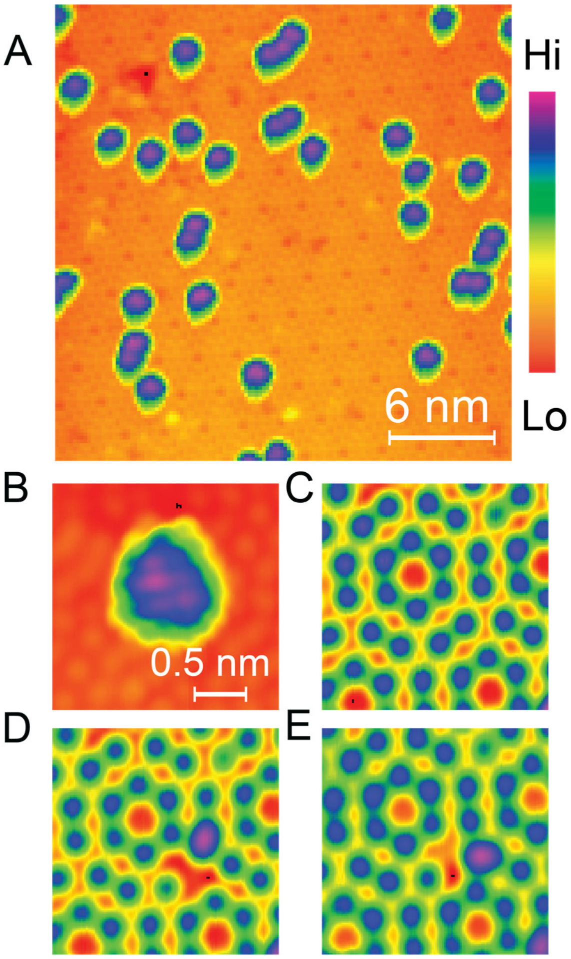
A
Hi
Lo
6 nm
B
0.5 nm
C
D
E

All the measurements presented in this study are preformed above 70 K. Scanning tunneling spectroscopy measurements are done by recording the first derivative output of a lock-in amplifier. C_{60} molecules purchased from Sigma Aldrich are sublimated to the clean Si(111) surface at room temperature from a Knudsen cell evaporator. A Ti-sapphire laser operating at continuous wave (CW) mode and 800 nm center wavelength is used in the experiment. Details of the optical set up have been described previously in *Chapter 1.4.* The laser spot size on the sample is estimated to be around 20 μm. The power of the laser before entering the STM chamber is maintained at 2.5 mW throughout the experiment. The temperature increase due to laser illumination is around 20 mK.

7.3 Results and Discussion

The topographic images of Si(111) 7×7 surface is shown in Fig. 7.1. Individual C_{60} molecules appear as protrusions with multiple lobed features corresponding to their electronic structures. The appearances of the molecules vary in the STM images, depending on their absorption sites and orientations. The surface has a low density of intrinsic defects. A single Si atom defect can be created by pulling a Si atom out from the surface with 2.0 V bias and 0.5 nA tunneling current, leaving a single atom vacancy and a Si adatom. The Si adatom is mobile on the surface and can recombine with the vacancy by manipulation with STM tip (Fig. 7.1.C-E).

The local density of state (LDOS) measured over the center a C_{60} and a Si atom vacancy at 80 K are presented in the *dI/dV* spectra in Fig. 7.2. The measured LDOS of different C_{60} molecules reproducibley shows multiple peaks in the range from 1.3 V to 2.5 V. The peak positions vary among the molecules, probably due to the difference in their adsorption geometries. For the molecule shown in the inset of Fig. 7.2.A, two peaks centering at 1.75 V and 2.28 V are

FIG. 7.2. LDOS of a C_{60} molecule and a Si vacancy measured at 80 K. (A) *dI/dV* spectra taken with (red) and without (black) laser illumination over the center of the C_{60} molecule shown in the inset. (B) *dI/dV* spectra taken with (red) and without (black) laser illumination over the center of the Si vacancy circled in the inset image. Junction is set at V_B = 1.5 V, I_T = 0.1 nA for all the spectra.

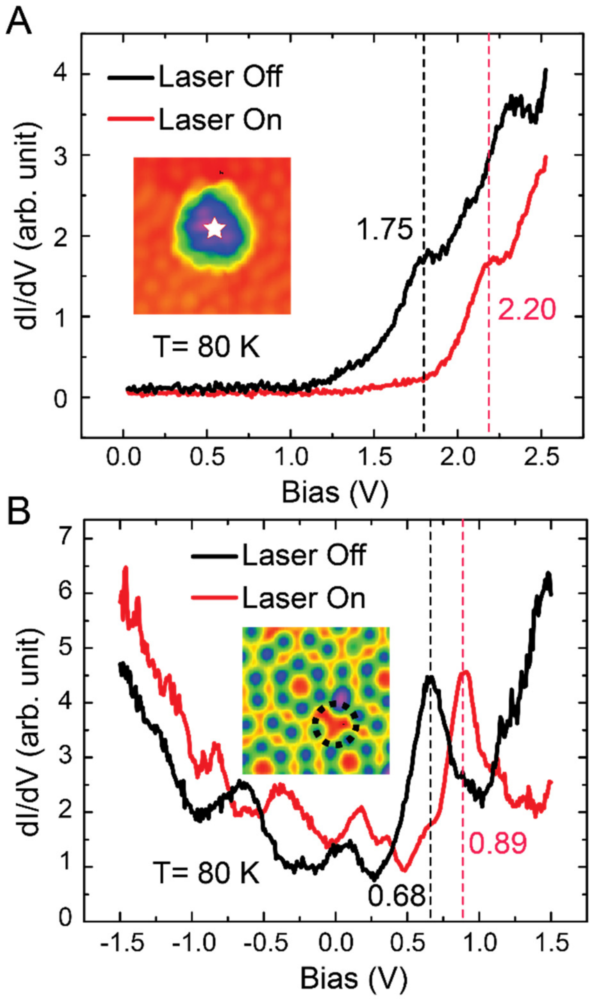
A
Laser Off
Laser On
T= 80 K
1.75
2.20
dI/dV (arb. unit)
Bias (V)
0
1
2
3
4
0.0
0.5
1.0
1.5
2.0
2.5
B
Laser Off
Laser On
T= 80 K
0.68
0.89
dI/dV (arb. unit)
Bias (V)
0
1
2
3
4
5
6
7
-1.5
-1.0
-0.5
0.0
0.5
1.0
1.5

resolved without laser illumination, which are attributed to the lowest unoccupied molecular orbital (LUMO) and second lowest unoccupied orbital (LUMO+1) of a C_{60} respectively. The *dI/dV* taken over the Si vacancy site shows a prominent peak at 0.68 V without laser illumination, which is not resolved over the same position before removing the Si atom. This feature is attributed to the surface defect state at this missing atom site. The peak position and amplitude is quantitatively robust for the same type of defects at different positions. Weaker peaks corresponding to the surface states of Si(111) 7×7 reconstructed surface can be resolved over the background.

The LDOS of both C_{60} and Si vacancy shift significantly under laser illumination. The bias of the defect state increases by 0.21 V, from 0.68 V to 0.89 V. A larger increase is measured over the C_{60} molecule shown in Fig. 7.2.A. The LUMO state shift up to 2.20 V, with an increase of nearly 0.45 V compared with the spectrum taken without light. The LUMO+1 state is not resolved in the bias window of the measurement. The amount of the shifting doesn't show significant power dependence when as the laser power increases, indicating a saturated laser induced effect.

The laser induced up-shift of the LDOS of C_{60} and Si vacancy can be explained by the surface photovoltage due to the photo-induced band flattening. For the p-type semiconductor in this metal-vacuum-semiconductor junction, a downward band bending is expected near the sample surface as shown in Fig. 7.3.A. With laser illumination, the diffusion and recombination of the charge carriers lead to a flattened band under saturation condition, resulting in an up-shift of the Fermi level at the surface as shown in Fig. 7.3.B. Since both the Si vacancy state and LUMO of C_{60} are pinned to the Fermi level of the surface, the photovoltage will also up-shift the LDOS as measured in the STM *dI/dV* spectra.

The larger amplitude of energy shift measured for LUMO of C_{60} compare to the Si vacancy state indicates a stronger local band bending near the C_{60} molecule. It can be explained by the

FIG. 7.3. Schematic diagrams of the band bending (A) and laser induced band flattening (B).

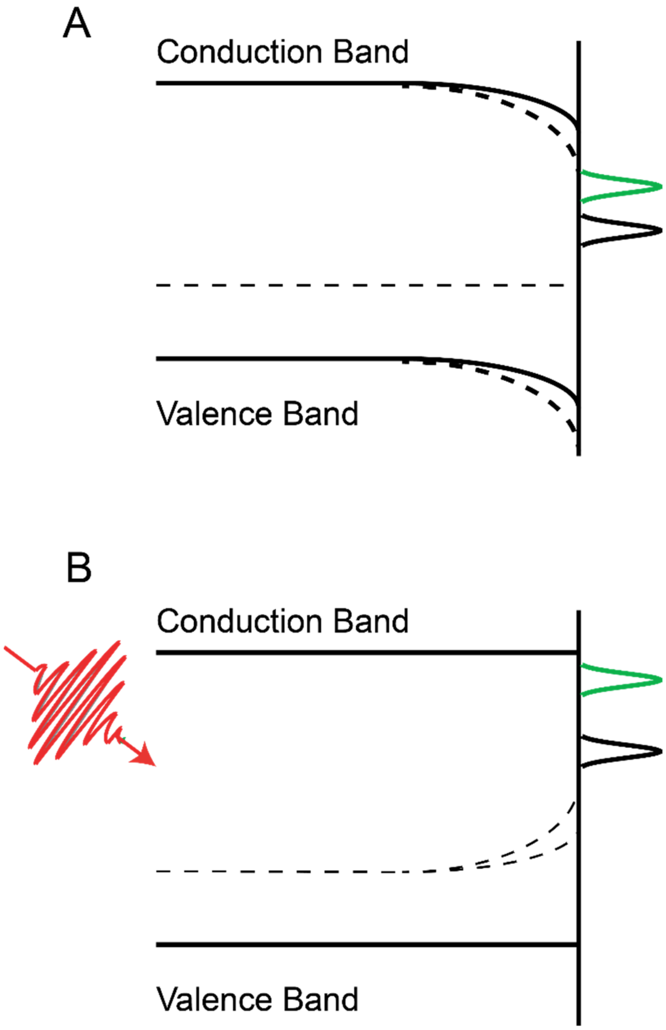
A
Conduction Band
Valence Band
B
Conduction Band
Valence Band

charge transfer between C_{60} and Si(111) surface. C_{60} has been well-known as a strong electron acceptor on surfaces. Photoemission, inverse photoemission, and electron energy loss spectroscopy have all show an electron gain of C_{60} in the range from 0.02 to 1.7 electrons per molecule on metal or semiconductor surfaces [23-34]. Similarly, the electrons are expected to transfer from Si(111) to C_{60} and increase the local electron density near the interface. This will result in the stronger local band bending near C_{60} measured experimentally.

The occupation of surface states and the thermal equilibrium of band bending are subject to the sample temperature. As the temperature increases, both the charge carrier density and mobility should increase, leading to a reduced band bending near the sample surface, which is also measured in the *dI/dV* spectra taken at a higher sample temperature. The STS measurements conducted at 90 K is shown in Fig. 7.4. For the C_{60} presented in Fig. 7.4.A, a weak LUMO peak near 1.60 V and a stronger LUMO+1 peak near 2.25 V are resolved before laser illumination. Fig. 7.4.B shows the LDOS of the same type of Si vacancy with the one in Fig. 7.2.B. The prominent defect state is resolved at 0.80 V without light. Laser illumination up-shift the LDOS of both C_{60} and Si vacancy by a much smaller amplitude compared to the one measured at 80 K. The LUMO peak of C_{60} and the defect state up-shift to 1.75 V and 0.92 V respectively under laser irradiation. The decrease in laser induced energy shift of both C_{60} LUMO and Si vacancy further confirm the origin of the energy shift as the laser induced band flattening.

No obvious power dependence is observed in our study when the laser power is regulated between 0.5 mW to 1.5 mW at the entrance of the STM chamber, indicating a saturated surface photovoltage even with 0.5 mW laser power. The diameter of the laser spot at the junction is around 20 μm, giving an average power density in the order of 10^7 W/m^2 at the junction. The laser could excite the junction plasmon which quickly relaxes into hot carriers locally. The effective

FIG. 7.4. LDOS of a C_{60} molecule and a Si vacancy measured at 90 K. *dI/dV* spectra are taken with same setpoints as FIG. 7.2 for a C_{60} (A) and a Si vacancy (B).

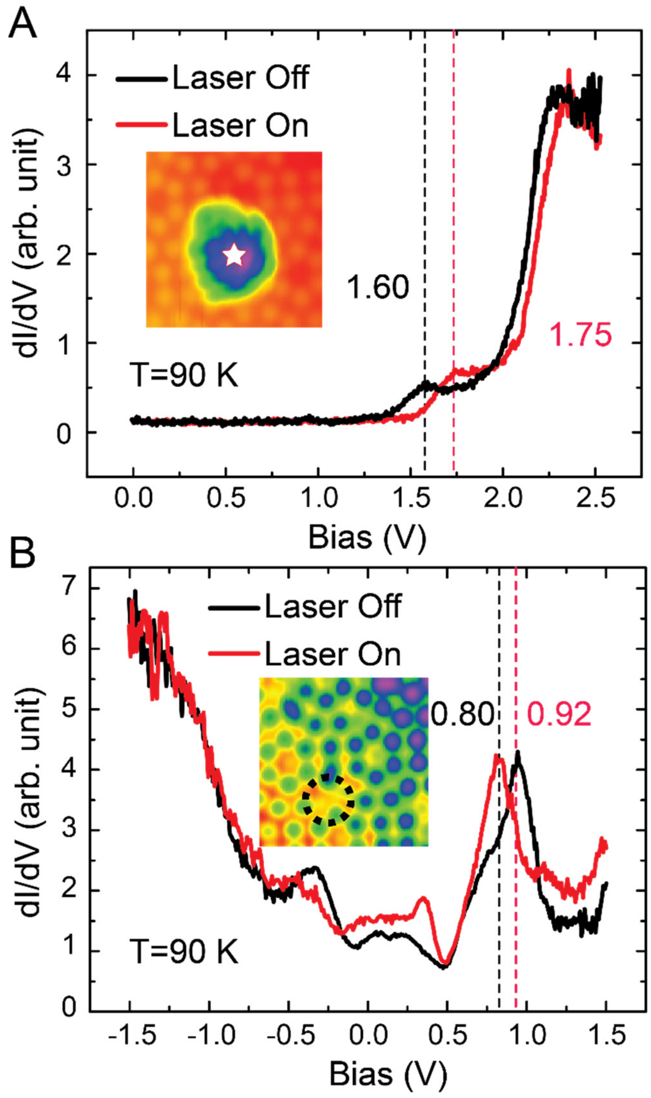
A
Laser Off
Laser On
1.60
1.75
T=90 K
dI/dV (arb. unit)
0
1
2
3
4
0.0
0.5
1.0
1.5
2.0
2.5
Bias (V)
B
Laser Off
Laser On
0.80
0.92
T=90 K
dI/dV (arb. unit)
0
1
2
3
4
5
6
7
-1.5
-1.0
-0.5
0.0
0.5
1.0
1.5
Bias (V)

photo induced band flattening is probably largely due to the strong plasmonic enhancement of the laser field in the STM tunnel junction by using Ag tips.

7.4 Conclusions

In summary, the band bending and laser induced band flattening of a Si(111) surface is observed in real-space using an STM combined with a Ti-sapphire laser. The photo-induced changes in the electronic structures are visualized with STM at single molecule level. Individual C_{60} molecules are found to locally enhance the band bending, probably due to its electron acceptor nature on surfaces. This study provides fundamental insight into the nano-scale electronic properties of molecular interfaces as well as an experimental basis towards designing of the single molecule photo-electronic devices.

Bibliography

[1] L. Sun, Y. A. Diaz-Fernandez, T. A. Gschneidtner, F. Westerlund, S. Lara-Avilab, and K. Moth-Poulsen, Chem. Soc. Rev. **43**, 7378 (2014).

[2] M. Ratner, Nat. Nanotechnol. **8**, 378 (2013).

[3] D. A. B. Miller, Appl. Opt. 49, 59 (2010).

[4] J. Correa-Baena, S. Turren-Cruz, W. Tress, A. Hagfeldt, C. Aranda, L. Shooshtari, J. Bisquert, and A Guerrero, ACS Energy Lett. **2**, 681 (2017).

[5] K. Appavoo, M. Liu, C. T. Black, and M. Y. Sfeir Nano Lett., **15**, 1076 (2015).

[6] A. Higuera-Rodriguez, B. Romeira, S. Birindelli, L. E. Black, E. Smalbrugge, P. J. van Veldhoven, W. M. Kessels, M. K. Smit, A. Fiore, Nano Lett. **17**, 2627 (2017).

[7] Z. Zhang and J. T. Yates, Chem. Rev. **112**, 5520 (2012).

[8] J. P. Long and V. M. Bermudez, Phys. Rev. B **66**, 121308 (2002).

[9] H. Sezen, S. Suzer, Surf. Sci. **604**, 21 (2010).

[10] D. C. Gleason-Rohrer, B. S. Brunschwig, and N. S. Lewis, J. Phys. Chem. C, **117**, 18031 (2013).

[11] G. Binnig, H. Rohrer, C. Gerber and E. Weibel, App. Phys. Lett. **40**, 178 (1982).

[12] R. M. Feenstra, J. A. Stroscio and A. P. Fein, Surf. Sci. Lett. **181**, 295 (1987).

[13] G. Binnig, H. Rohrer, C. Gerber and E. Weibel, Phys. Rev. Lett. **49**, 57 (1982).

[14] R. Balog, B. Jørgensen, L. Nilsson, M. Andersen, E. Rienks, M. Bianchi, M. Fanetti, E. Lægsgaard, A. Baraldi, S. Lizzit, Z. Sljivancanin, F. Besenbacher, B. Hammer, T. G. Pedersen, P. Hofmann, and L. Hornekær, Nat. Mater. **9**, 315 (2010).

[15] G. Hörmandinger, Phys. Rev. B **49**, 13897 (1994).

[16] W. Ho, J. Chem. Phys. **117**, 11033 (2002).

[17] S. W. Wu, N. Ogawa, and W. Ho, Science **312**, 1362 (2006).

[18] S. W. Wu and W. Ho, Phys. Rev. B **82**, 085444 (2010).

[19] L. Bartels, F. Wang, D. Möller, E. Knoesel, T. F. Heinz, Science **305**, 648 (2004).

[20] S. Yoshida, Y. Aizawa, Z.-H. Wang, R. Oshima, Y. Mera, E. Matsuyama, H. Oigawa, O. Takeuchi, and H. Shigekawa, Nature Nanotechnol. **9**, 588 (2014).

[21] T. L. Cocker, D. Peller, P. Yu, J. Repp, and R. Huber, Nature **539**, 263 (2016).

[22] B. C. Stipe, M. A. Rezaei and W. Ho, Rev. Sci. Instrum. **70**, 137 (1999).

[23] X. Lu, M. Grobis, K. H. Khoo, S. G. Louie, and M. F. Crommie, Phys. Rev. Lett. **90**, 096802 (2003).

[24] X. Lu, M. Grobis, K. H. Khoo, Steven G. Louie, and M. F. Crommie, Phys. Rev. B, **70**, 115418 (2004).

[25] C.-T. Tzeng, W.-S. Lo, J.-Y. Yuh, R.-Y. Chu, and K.-D. Tsuei, Phys. Rev. B **61**, 2263 (2000).

[26] J. H. Weaver, J. Phys. Chem. Solids **53**, 1433 (1992).

[27] D. Purdie, H. Bernhoff, and B. Reihl, Surf. Sci. **364**, 279 (1996).

[28] K. D. Tsuei and P. D. Johnson, Solid State Commun. **101**, 337 (1997).

[29] A. J. Maxwell, P. A. Brühwiler, D. Arvanitis, J. Hasselstrom, and N. Mårtensson, Phys. Rev. Lett. **79**, 1567 (1997).

[30] A. J. Maxwell, P. A. Brühwiler, D. Arvanitis, J. Hasselstrom, M. K.-J. Johansson, and N. Mårtensson, Phys. Rev. B **57**, 7312 (1998).

[31] K. Sakamoto, M. Harada, D. Kondo, A. Kimura, A. Kakizaki, and S. Suto, ibid. **58**, 13951 (1998).

[32] C. Cepek, M. Sancrotti, T. Greber, and J. Osterwalder, Surf. Sci. **454**, 467 (2000).

[33] T. R. Ohno, Y. Chen, S. E. Harvey, G. H. Kroll, J. H. Weaver, R. E. Haufler, and R. E. Smalley, Phys. Rev. B **44**, 13747 (1991).

[34] S. Modesti, S. Cerasari, and P. Rudolf, Phys. Rev. Lett. **71**, 2469 (1993).

CHAPTER EIGHT

Summary and Prospects

8.1 Concluding Remarks

Several studies to extend the chemical and temporal sensitivities of a scanning tunneling microscope (STM) have been presented in this dissertation. They show that the STM can contribute extensively to the cross-disciplinary studies by providing valuable information of individual molecules. These studies mature our understanding to the fundamental physical and chemical phenomena on the single-molecule scale.

The experiments discussed in this dissertation have extended STM-IETS to the studies of rotational transitions of a single molecule trapped in the STM junction. The vibrational and rotational properties of a gaseous molecule such as a hydrogen molecule weakly adsorbed on surfaces can be probed in real-space. The physical and chemical properties of the molecule including bond length, bond strength, binding geometry, intermolecular interaction, and orbital hybridization can now be characterized by rotational spectroscopy and microscopy at the single-molecule level. The distinct rotational and vibrational features measured between hydrogen and its isotopes demonstrate the improved chemical resolution of STM. The shift in hydrogen rotational excitation energy measured at different positions of a substrate proves the sensitivity of STM rotational spectroscopy to the site-dependent chemical potential. The sub-Ångström tunability of the dimension of the tunneling junction provides a unique approach to exploring how the properties of a molecule vary in response to its nano-scale chemical environments.

In this dissertation, STM shows its versatility and has been applied to various research fields. The ability to use STM to identify, manipulate and characterize single molecules provides inhomogeneous molecular characters which are not accessible in previous ensemble measurements. The experimental demonstration of the H-H bond breakage induced by the mechanical motion of STM tip presents a model example of using STM to trigger and monitor a mechanochemical reaction. It provides insight into the mechanism behind this mechanochemical process with unparalleled real-space visibility. The ability to trap and move a hydrogen molecule with STM tip facilitates the detection of reaction barrier at different chemical environments modified by the surface geometries or molecular dopants. The catalytic effect of single molecules and atoms can be visualized. The observation of C-H bond activation of single azulene molecule proves STM's capability to study photochemical transformations of single molecules. It demonstrates the atomic-scale coupling of photons to the tunneling electrons at the STM junction. The sub-molecular scale localization and meV range energy tunability of the photo-assisted tunneling electrons may allow the bond-selective control of photochemical pathways. We expect our experiments to open a new avenue to the studies of mechanochemistry and photochemistry at the single-molecule level.

By combining a femtosecond laser with an STM, we ultimately achieve simultaneous spatial-temporal resolution. This femtosecond laser STM allows the probing of coherent dynamics of a single molecule in the time domain, which enables the assessment of the inhomogeneous dynamics of individual molecules in this local environment. We detect the coherent structural transformations of single pyrrolidine molecule with joint femtosecond-Ångström sensitivity. The visualization of changes in single molecule dynamics due to intermolecular interaction showcases the unique power of real-space measurement with STM. This novel experimental approach provides a route to probe chemical and physical events on surfaces with unprecedented sensitivity in space-time domain.

8.2 Related Research: Hydrogen Rotational Spectroscopy and Microscopy

Besides the experiments discussed in chapters two to four, additional studies concerning the rotational excitation of a single hydrogen molecule in the tunneling junction of a scanning tunneling microscope (STM) have been performed. These studies include rotational spectroscopy measurement of hydrogen-molecule interaction on a metal surface as well as theoretical explanations to the line-shape differences in rotational inelastic tunneling spectra. Details information of these studies can be found in the literature [1, 2].

8.2.1 Rotational Imaging of Single Magnesium Porphyrin Molecules

The paper "Single-Molecule Rotational and Vibrational Spectroscopy and Microscopy with the Scanning Tunneling Microscope" by Arthur Yu, Shaowei Li, Gregory Czap, and W. Ho has been published in *The Journal of Physical Chemistry C*, Volume 119, pages 14737-14741, 2015. In this study, we apply rotational spectromicroscopy to study the interaction between hydrogen and magnesium porphyrin (MgP) molecules adsorbed on Au(110) surface. Both vibrational and rotational modes of the trapped H_2 molecule show variations in the energies due to the highly localized position-dependent adsorption potential, which reveals salient features in the chemical structure of the MgP molecule. This study shows that the hydrogen rotational spectromicroscopy can be used to visualize the interaction potential between hydrogen and another molecule [1].

8.2.2 Line-shape Variations in Rotational IETS

The paper "Trapping and Characterization of a Single Hydrogen Molecule in a Continuously Tunable Nanocavity" by Hui Wang, Shaowei Li, Haiyan He, Arthur Yu, Freddy Toledo, Zhumin Han, W. Ho, and Ruqian Wu has been published in *The Journal of Physical Chemistry Letters*, Volume 6, pages 3453-3457, 2015. In this study, we study the hydrogen molecule trapped in the cavities formed by STM tip and an atop atom or a trough atom of a Au(110) surface. We find the IETS line-shape of hydrogen $j=0$ to $j=2$ excitation is different in these two cases. This is due to the distinct chemical properties of the trapped hydrogen in different environments given by Density Function Theory (DFT) calculations [2].

8.3 Related Research: Tunneling Electron Induced Luminescence

In addition to the experiments described in chapters five and six, another approach we use to obtain optical spectra below diffraction limit involves the measurement of photon emission excited by tunneling electrons. A. Yu, W. Ho and I have also used this method to probe plasmonic, vibrionic, and electronic structures of individual molecules or nanoclusters. The essences of these studies are briefly discussed below. Details of these experiments are described in the literature [3-5].

8.3.1 Vibronically Resolved Light Emission from Single Panhematin Molecules

The paper "Tunneling Electron Induced Charging and Light Emission of Single Panhematin Molecules" by Arthur Yu, Shaowei Li, Bharat Dhital, H. Peter Lu and W. Ho has been published in *The Journal of Physical Chemistry C*, Volume 120, pages 21099-21103, 2016. We observed the charging and light emission from single Panhematin molecules induced by STM tunneling electrons. The lowest unoccupied state of a neutral Panhematin molecule was observed at 1.3 V bias, which formed the singly occupied molecular orbital (−0.8 V) and singly unoccupied molecular orbital (2.3 V) states when the molecule is charged into a negative ion by the electrons injected from the tip into the molecule. Vibronic states were resolved in the light emission spectrum for the charged hemin ion. The vibronic features in the light emission spectrum arise from the radiative decay from a doublely charged transient state into the substrate [3].

8.3.2 Plasmonic Properties of Single Gold Nanoclusters

The paper "Tunneling Electron Induced Light Emission from Single Gold Nanoclusters" by Arthur Yu, Shaowei Li, Gregory Czap, and W. Ho has been published in *Nano Letters*, Volume 16, pages 5433-5436, 2016. This paper concerns the light emission from exciting the tip-nanocluster-substrate junction plasmon with tunneling electrons. We have found gold nanoclusters with radius from 3 to 7 nm can be formed by thermal evaporation onto Al_2O_3 bilayers over a NiAl(110) surface. Quantum-confined electronic states are revealed in *dI/dV* spectra. Spatially resolved photon imaging showes localized emission hot spots corresponding to the optical transitions between two different quantum-confined states. Size-dependent study and light emission from nanocluster dimers further indicate that the light emission is from the radiative decay of the junction plasmon [4].

8.3.3 Plasmon Mediated Light Emission from Single Azulenes

The paper "Visualization of Nano-Plasmonic Coupling to Molecular Orbital in Light Emission Induced by Tunneling Electrons" has been submitted to *Physical Review Letters* for publication. This study demonstrates the coupling between a localized plasmon and a molecular orbital in the STM induced light emission processes. The light emission intensity can be enhanced when the energy difference between the tunneling electrons and the azulene molecular orbital matches the energy of a plasmon mode of the nanocavity defined by the Ag-tip and Ag(110) substrate. The spatially resolved image of the light emission intensity matches the spatial distribution of the molecular orbital. This result highlights the near-field coupling of a molecular orbital to the radiative decay of a plasmonic excitation in a confined nanoscale junction. [5]

8.4 Prospects for Future Research

The experiments conducted in this dissertation have revealed a need to continuously pursue additional technology developments towards the extension of STM's chemical sensitivity and temporal resolution. The following section discusses several future studies that can make use of the previously introduced techniques to solve some problems in physics and chemistry and propose additional experimental methods to further expand the applicability of an STM.

8.4.1 Excitation of Different Secondary Angular Momentum Quantum Number

When a hydrogen molecule is placed in an anisotropic potential well, the degeneracy of its rotational states with different secondary angular momentum quantum number *m* will be lifted [6]. The rotational excitation peak observed in STM-IETS is expected to split into multiple peaks. The energy differences between these peaks are expected to be determined by the depth of the adsorption potential well. This splitting has been observed in the high-resolution electron energy loss spectra but has not been seen in the STM-IETS measurements introduced in this dissertation. A possible reason is the lack of spectral resolution at the operating temperature of 10 K. One possible way to detect these transitions with different *m* is to increase the depth of the adsorption well [7]. We have found that the decrease of the tip-substrate distance can increase the hydrogen-junction binding. The rotational motion of the hydrogen molecule can be hindered leading to resolvable energy gaps between different *m* states. However, it may be difficult to obtain a stable enough junction for IETS measurements when the tip is very close to the surface. Another possible approach is to increase spectral resolution by lowering the operating temperature. The sub-Kelvin STM in Ho lab has observed the fine splitting of CO hindered translational and rotational vibration energies due to surface anisotropy. The fine splitting due to different *m* states may be resolvable at 600 mK.

8.4.2 Real-space Study of Hydrogen Ortho-Para Conversion

The mechanism behind fast ortho-para transitions of hydrogen molecules at low temperature has been an interesting topic among surface scientists for years. At room temperature, the ratio of ortho-H_2 and para-H_2 is 3:1 at thermal equilibrium. When the molecules are cooled to low temperature, the spontaneous ortho-para transition should be highly forbidden due to the vanished transition matrix between an asymmetric singlet state and a symmetric triplet state. However, the ortho-H_2 have been observed to rapidly relax into the para-state when adsorbed on noble metal surfaces at low temperature [8]. The origin of this fast ortho-para transition is still under debate. A possible explanation is that the large spin-spin interaction terms induced by magnetic impurities on surfaces lead to a non-vanished transition matrix [9]. Rotational spectroscopy with STM-IETS can be a unique technique to investigate H_2 ortho-para transition in real-space. Since ortho-H_2 and para-H_2 have distinct rotational quantum numbers, they can be easily distinguished by STM rotational spectroscopy and microscopy. Previously, we have observed the $j=1$ to the $j=3$ transition of ortho-H_2 immediately after dosing hydrogen from a room temperature bottle. The single intensity of this transition got weaker with time and became unresolvable within 30 min after dosing. This result proves that the STM-IETS could be used to monitor the temporal and spatial variations of the ortho-para transition of hydrogen. It can provide real-space information to reveal the mechanism behind this phenomenon.

8.4.3 Probing Photon Emission Induced by Photo-assisted Tunneling Electrons

The STM in Ho group has been proven to resolve the photon emission from single molecules excited by tunneling electrons [3-5]. We have also shown in this dissertation that the femtosecond laser photon can couple with the tunneling electrons to form photo-assisted tunneling electrons. It may be possible to observe the single molecule luminance excited by photo-assisted tunneling electrons. Since the photo-excitation occurs in an ultrashort time scale, the photo-assisted tunneling electrons combine both temporal sensitivity from femtosecond pulses and the spatial resolution from tunneling. The main difficulty in achieving this is the low ratio of photo assisted tunneling electron in the tunneling current, which may be improved by the proper alignment of the laser to the junction as well as the careful tuning of the junction plasma mode. The photon emission induced by photo-assisted tunneling can be distinguished from the luminescence due to regular tunneling electrons by its up-converted energy. This method is expected to be applicable to the systems previously studied by time-resolved photoluminescence spectroscopy and can be used to probe the molecular dynamics without the needs of detecting the structural transformations.

8.4.4 Application of Lock-in Techniques in STM Pump-probe Spectroscopy

The traditional femtosecond pump-probe spectroscopy usually uses the lock-in method to measure optical properties of samples. The power of the probe pulse is often modulated with a sine wave using a shaker or chopper [10]. A lock-in amplifier is used to extra the signal with the same frequency from the measurable outputs. However, power modulation cannot be used in the STM pump-probe spectroscopy. The thermal expansion of STM tip responding to the laser power change leads to an unstable junction which prohibits the STM measurements.

One approach that has been applied in the previous STM pump-probe studies is to modulate the pulse delay. The piezo shaker described previously in this dissertation can be used to apply a sine-wave modulation to one arm of the Michelson interferometer. Yoshida and coworkers have adopted this technique to detect the spin dynamics of GaAs [11]. However, the variation of the signal in the time domain is relatively small and nonlinear. Previous studies done by Ho group members have failed to show an enough signal noise ratio using delay modulation.

In the experiments previously discussed in this dissertation, we have found that the coupling between laser and tunneling junction depends strongly on the laser polarization. With same power, the maximized photon-junction coupling is observed for p-polarized light whose electric field direction is parallel to the plane of incidence. Experimentally, we have noticed that the changes in tip expansion are negligible between junctions irradiated by p-polarized light and s-polarized light. This result indicates that a modulation may be applied to the polarization of laser pulses to extra laser induced signal from the tunneling current without causing junction instability. Possible approaches to applying the polarization modulation include using an electrooptic modulator or simply a polarizer mounted on a motorized rotational stage. The application of lock-in techniques in STM pump-probe measurements would yield a higher signal-to-noise ratio and therefore faster and more sensitive interrogation of samples.

Bibliography

[1] A. Yu, S. Li, G. Czap, and W. Ho, J. Phys. Chem. C **119**, 14734 (2015).

[2] H. Wang, S. Li, H. He, A. Yu, F. Toledo, Z. Han, W. Ho, and R. Wu J. Phys. Chem. Lett, **6**, 3453 (2015).

[3] A. Yu, S. Li, B. Dhital, H. P. Lu, and W. Ho, J. Phys. Chem. C, **120**, 21099 (2016).

[4] A. Yu, S. Li, G. Czap, and W. Ho, Nano Letters, **16**, 5433 (2016).

[5] A. Yu, S. Li, H. Wang, S. Chen, R. Wu, and W. Ho, submitted to Phys. Rev. Lett.

[6] K. Svensson and S. Andersson, Surf. Sci. 392 L40 (1997).

[7] K. Svensson, L. Bengtsson, J. Bellman, M. Hassel, M. Persson, and S. Andersson, Phys. Rev. Lett. **83**, 124 (1999).

[8] E. Ilisca, Phys Rev Lett. **66**, 667 (1991).

[9] I. F. Silvera, Rev. Mod. Phys. **52**, 393 (1980).

[10] A. Stolow, A. E. Bragg, and D. M. Neumark, Chem. Rev, **104**, 1719 (2004).

[11] S. Yoshida, Y. Aizawa, Z.-H. Wang, R. Oshima, Y. Mera, E. Matsuyama, H. Oigawa, O. Takeuchi, and H. Shigekawa, Nature Nanotechnol. **9**, 588 (2014).

Appendix A

Hardware Instrumentation

One of the belief that is shared by all Ho group members is that the breakthrough in science always follows from the development of new techniques and instrumentations. This includes the design and fabrication of homemade and unique apparatuses. As a tradition, all the Ho group members need to learn fundamentals of machining and CAD drawing and keep improving their STM systems by adding new gadgets. This appendix includes detailed introductions of a few hardware projects the author finished in Ho group. Most of the designs described here are based on the existing apparatus constructed by previous group members. One main reason the author decided to modify or redesign them was to standardize them so they could be easily constructed and interchangeable among different STMs. By writing this appendix, the author does not claim full credit for the invention of every part listed here but try to document all the necessary information in one place. The author sincerely hopes these documents can be valuable for the future Ho group members.

A.1 Design and Fabrication of a Molecular Evaporator

A.1.1. Introduction

Here we introduce a compact thermal evaporator (Fig. A.1.1) designed to use for dosing molecule below 600 Celsius and without the need for water cooling. Alumina crucible is directly heated by a tungsten filament. The electric and rotary feedthroughs can be mounted and operated

FIG. A.1.1 Picture of a finished molecular evaporator

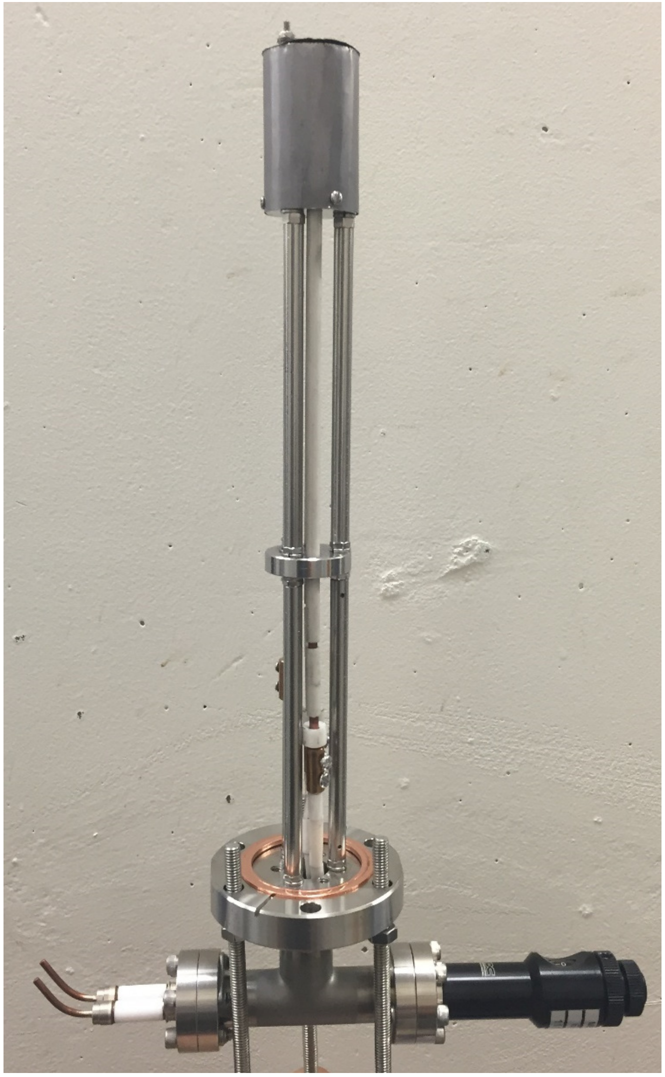

from the side to minimize the space required for installation. The fabrication requires a low amount of machining and no welding.

A.1.2. Machined Parts

A.1.2.1 Base Flange

Fig. A.1.2 is the CAD drawing of the base flange, which is a modified stainless steel 304 CF 2.75” to CF 1.33” zero-length reducer. Six mounting holes with 8-32 thread and 0.3” depth are added to the vacuum side of the flange. The orientation of the mounting holes is offset with the CF 1.33” screw holes by 30 degrees to avoid any possible interference. Each mounting hole is 0.42” away from the center of the flange.

A.1.2.2 Top plate and shaft collar

The top plate is used below the crucible to mount the thermal shield. The shaft collar is used in the middle of the evaporator to secure the supporting standoffs as well as the electrodes. Fig. A.1.3 and Fig. A.1.4 are the CAD drawings of the top plate and shaft collar, respectively. Both parts are made from stainless steel 304 or 316. These two pieces are nearly identical. The only difference is the top plate has three additional 2-56 mounting holes at the side for the thermal shield. The 3 through holes with 0.164” clearance are for 2-56 threaded rods to mount the standoffs. The two 0.188” through holes are for the electrodes with a ceramic insulator. The ceramic insulators used here are the alumina tube with 1/8” ID ordered from Mcmaster-Carr. The clearance of these two holes should be adjusted based on the OD of the alumina tubes, which can vary from order to order. The last through hole with 0.1” ID is for the 2-56 threaded rod used to operate the shutter.

A.1.2.3 Copper electrodes

Two copper electrodes (Fig. A.1.5) are needed to provide power to the tungsten filament.

FIG. A.1.2 CAD drawing of the base flange

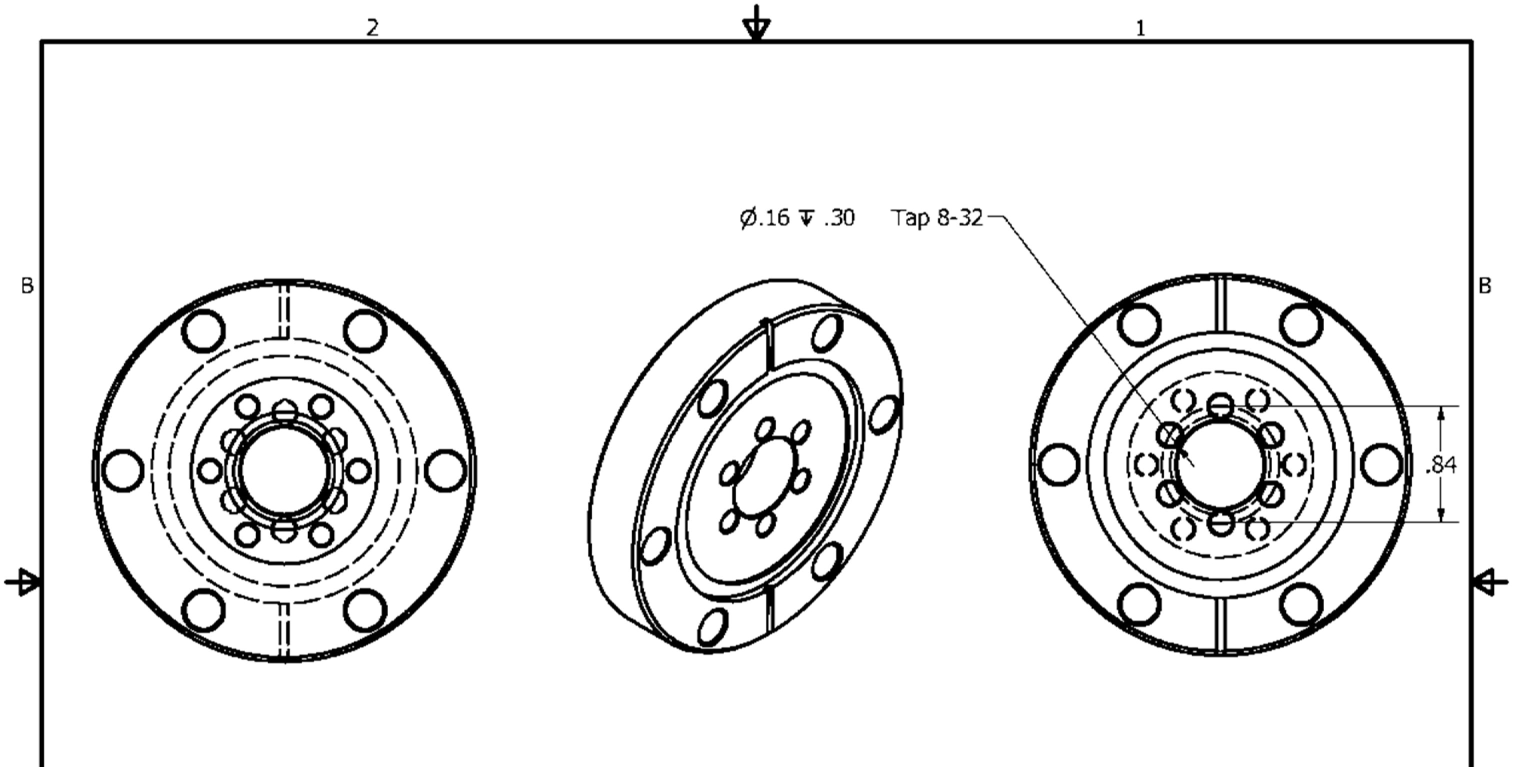
2
1
B
B
Ø.16 ⊽ .30
Tap 8-32
.84

DRAWN Shaowei Li	1/30/2015	
CHECKED		TITLE
QA		
MFG		
APPROVED		
		SIZE A · DWG NO Zero-length Reducer 1 · REV
		SCALE · SHEET 1 OF 1

A
A
2
1

FIG. A.1.3 Pictures of a finished base flange

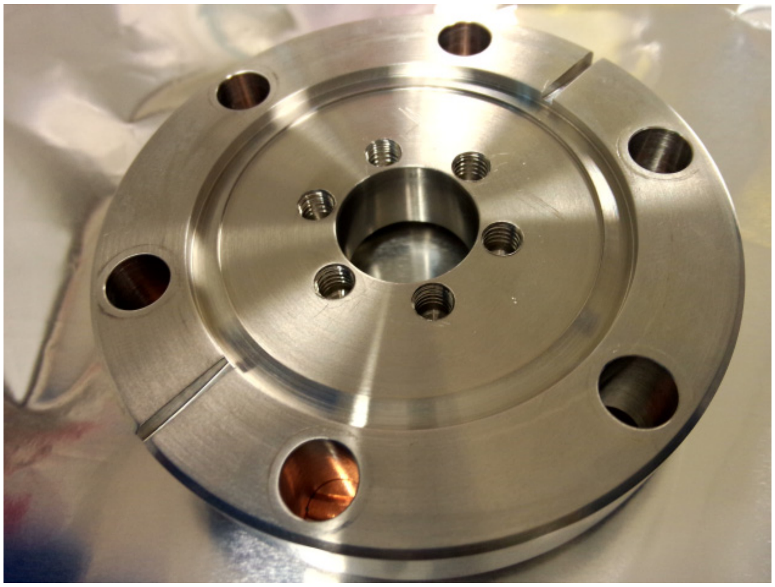

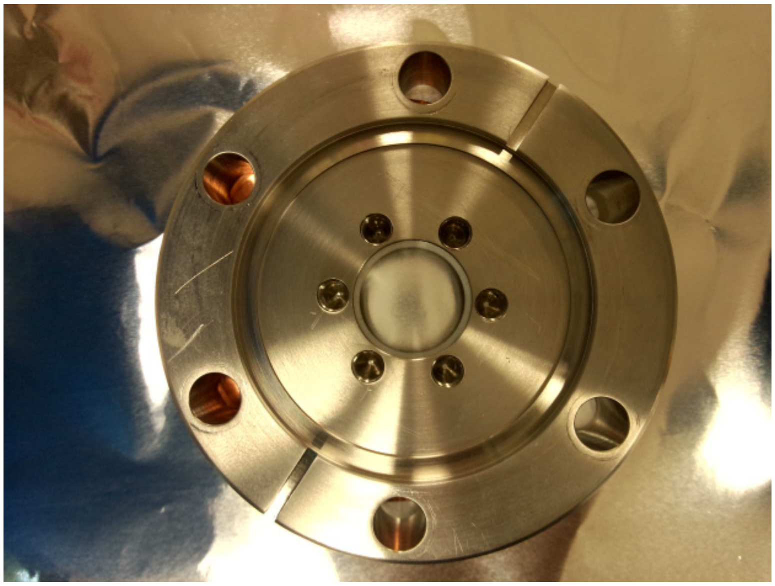

FIG. A.1.4 CAD drawing of the top plate

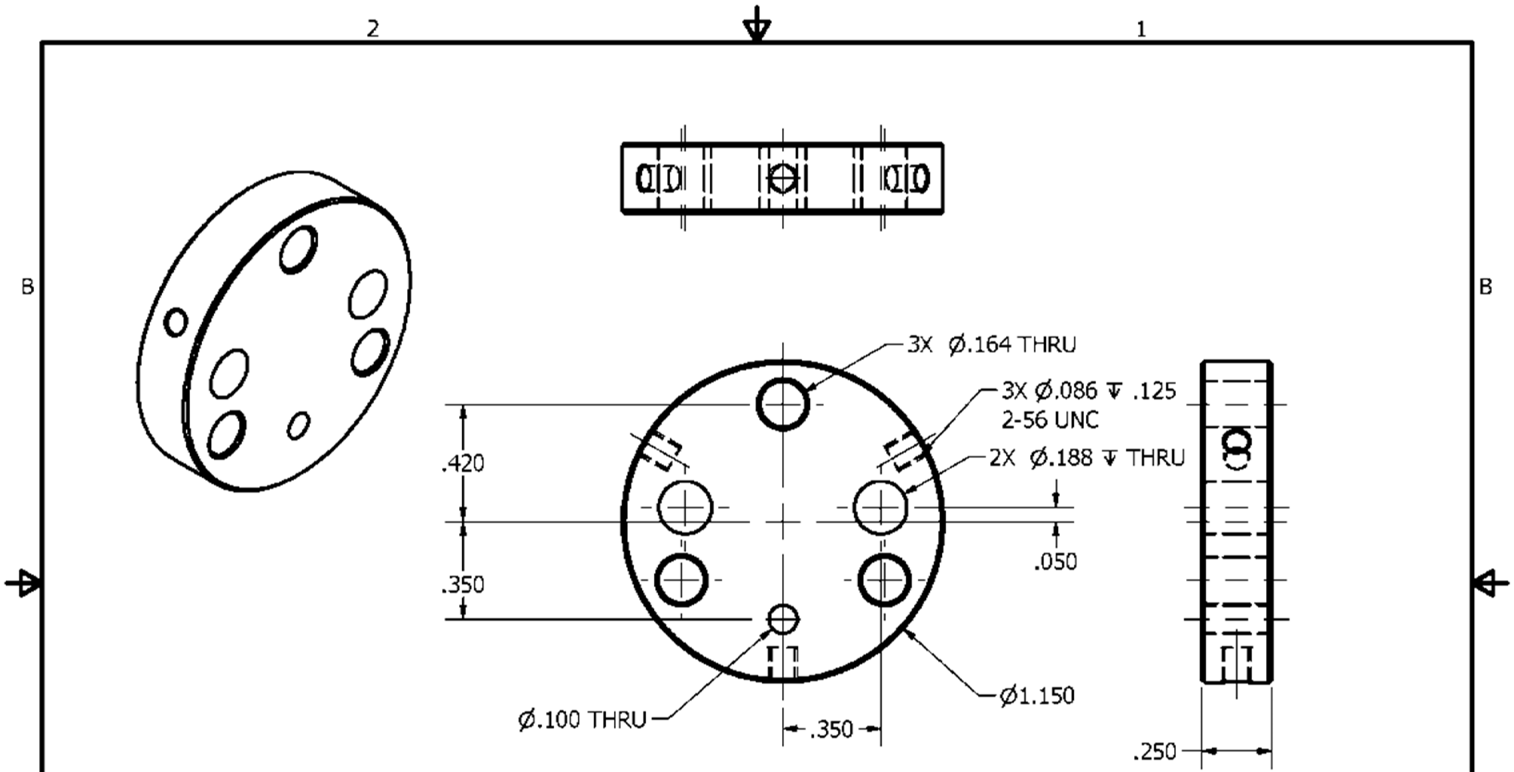
2
1
B
A
3X Ø.164 THRU
3X Ø.086 ↧ .125
2-56 UNC
2X Ø.188 ↧ THRU
.050
.420
.350
Ø.100 THRU
.350
Ø1.150
.250

DRAWN Shaowei Li	11/7/2014			
CHECKED		TITLE Base Plate For Molecular Doser		
QA				
MFG				
APPROVED				
		SIZE A	DWG NO Base Plate	REV
		SCALE		SHEET 1 OF 1

FIG. A.1.4 CAD drawing of the shaft collar

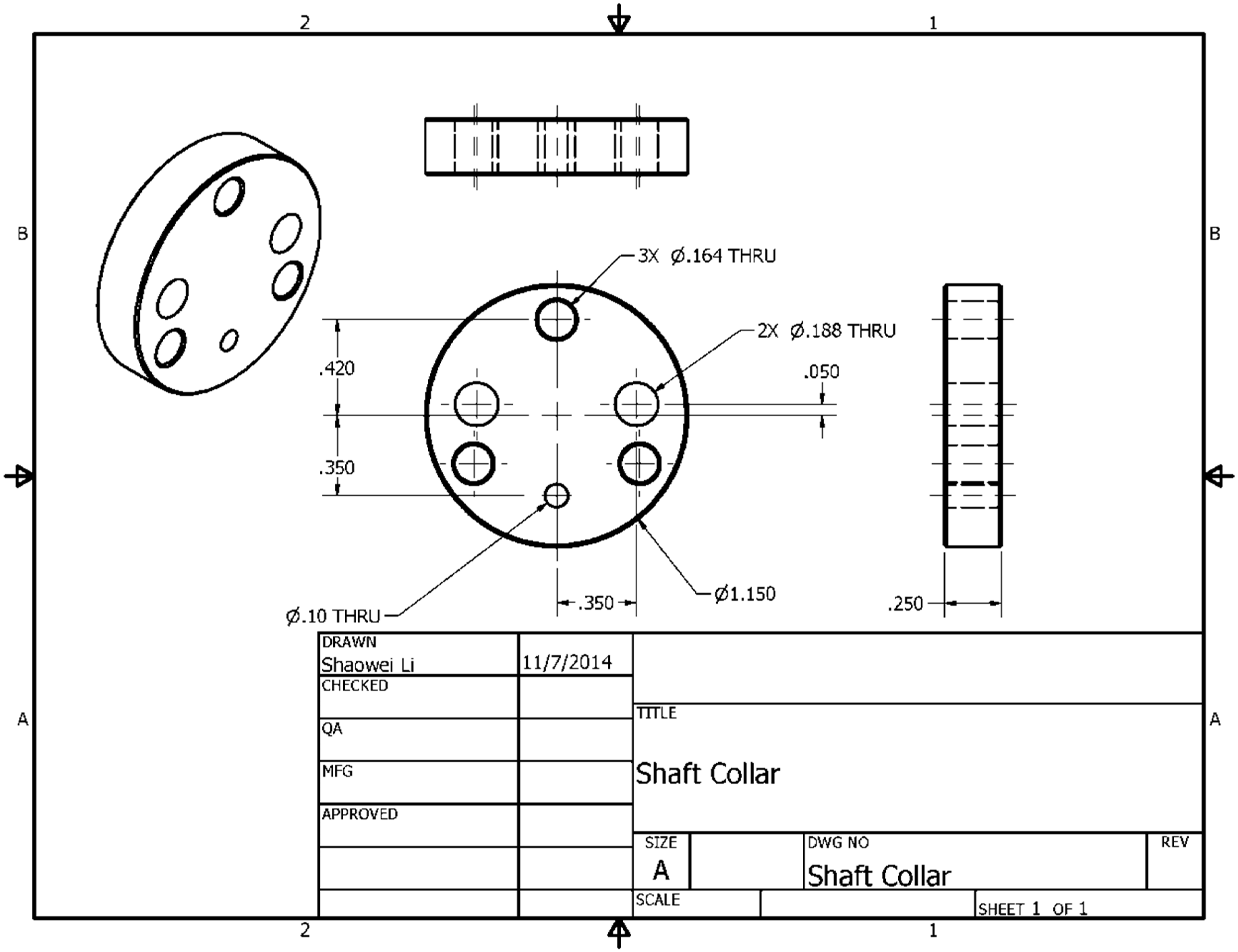
2
1
B
A
3X Ø.164 THRU
2X Ø.188 THRU
.050
.420
.350
.350
Ø.10 THRU
Ø1.150
.250

DRAWN
Shaowei Li 11/7/2014
CHECKED
QA
MFG
APPROVED
TITLE
Shaft Collar
SIZE A
DWG NO Shaft Collar
REV
SCALE
SHEET 1 OF 1

FIG. A.1.5 CAD drawing of the copper electrode

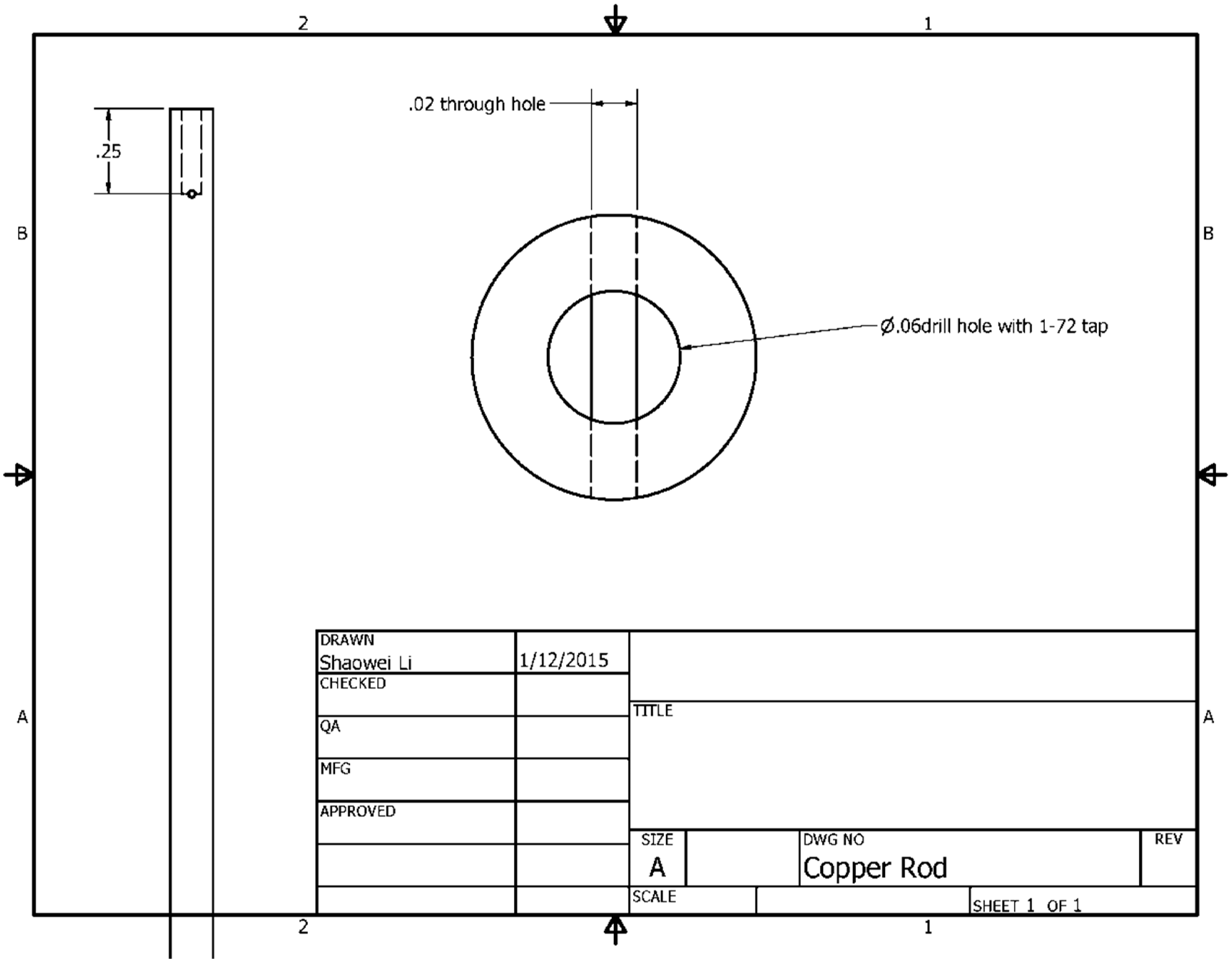
2
1
B
A
.25
.02 through hole
Ø.06drill hole with 1-72 tap
DRAWN
Shaowei Li
1/12/2015
CHECKED
QA
MFG
APPROVED
TITLE
SIZE
A
DWG NO
Copper Rod
REV
SCALE
SHEET 1 OF 1

FIG. A.1.5 Pictures of a shaft collar (top) and a copper electrode (bottom)

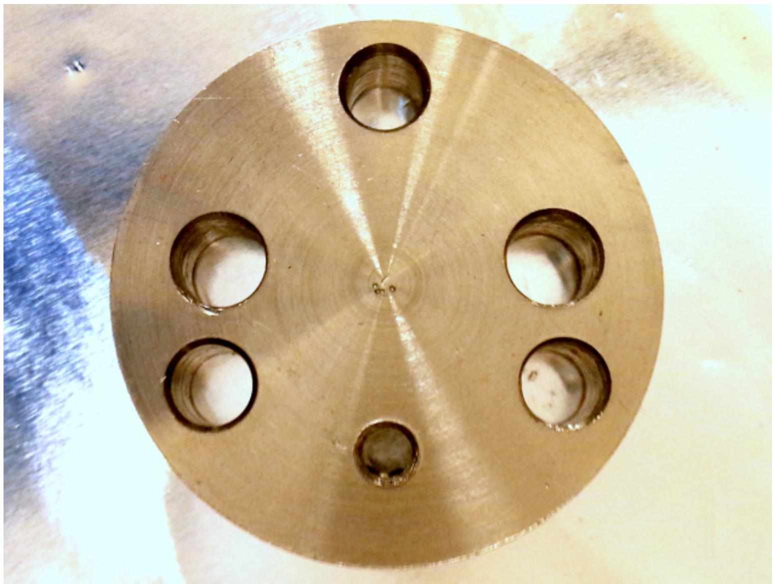

The electrodes are machined from 1/8” OD copper rods with ~10” length. We have found the 1/8” OD copper rods ordered from Mcmaster-Carr may not always fit the 1/8” ID alumina tube, 3 mm OD copper rods can be used as an alternative. Each electrode has a 1-72, 1/4” depth tapped hole at one end. A side hole with ~0.03” clearance need to be drilled at the bottom of the tapped hole to pass through the tungsten filament. The actual diameter of this side hole may depend on the filament thickness.

A.1.2.4 Standoffs

Six cylindrical 1/4" OD stainless steel standoffs with 8-32 tapped holes at both ends are used to support the shaft collar and the top plate. The length of the standoff depends on the required length of the evaporator. For the standard 11” evaporator, 4” long standoffs are used. The desired material should be either stainless steel 304 or 316. Other types of stainless steel may also be acceptable as long as the outgassing rate is low enough. A small venting hole needs to be added at each end of each standoff (Fig. A.1.6) to prevent the virtual leak from the trapped gases.

A.1.2.5 Thermal Shield

The thermal shield is a cylindrical bucket made from tantalum sheet with 0.01” thickness. The tantalum sheet can be cut by scissor to 2” x 4” to be used as the side wall of the shield. Three mounting holes with ~0.1” diameter and ~1.2” separation need to be punched along the long edge of the sheet before spot-welding [Fig. A.1.7 (a)]. The sheet should then be rolled around a 1.15” tube (a homemade jig should be available in the Ho lab specific for this purpose) and spot-welded on the overlapping part [Fig. A.1.7 (B)]. A round tantalum sheet is used as the cap of the shield. A center hole for dosing and a small hole for shutter should be punched at the appropriate positions of the cap before spot-welding it to the side wall. When spot-welding the cap, please make sure the orientation of the shutter hole is appropriate [Fig. A.1.7 (C-D)].

FIG. A.1.6 CAD drawing of the vent hole on the stand off

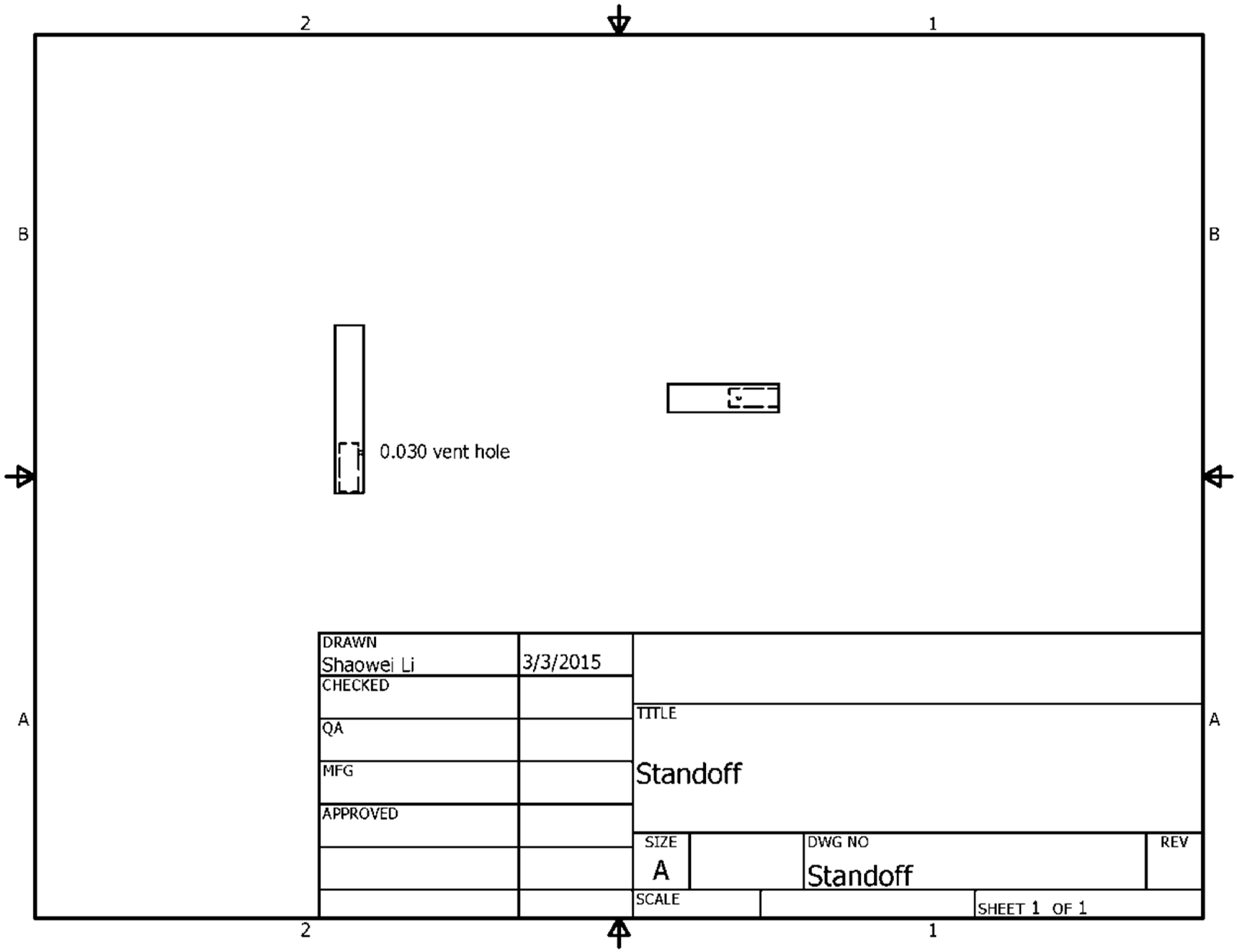
2
1
B
A
0.030 vent hole

DRAWN Shaowei Li	3/3/2015	
CHECKED		TITLE Standoff
QA		
MFG		
APPROVED		SIZE A
		DWG NO Standoff
		REV
		SCALE
		SHEET 1 OF 1

FIG. A.1.7 Procedures of making the thermal shield

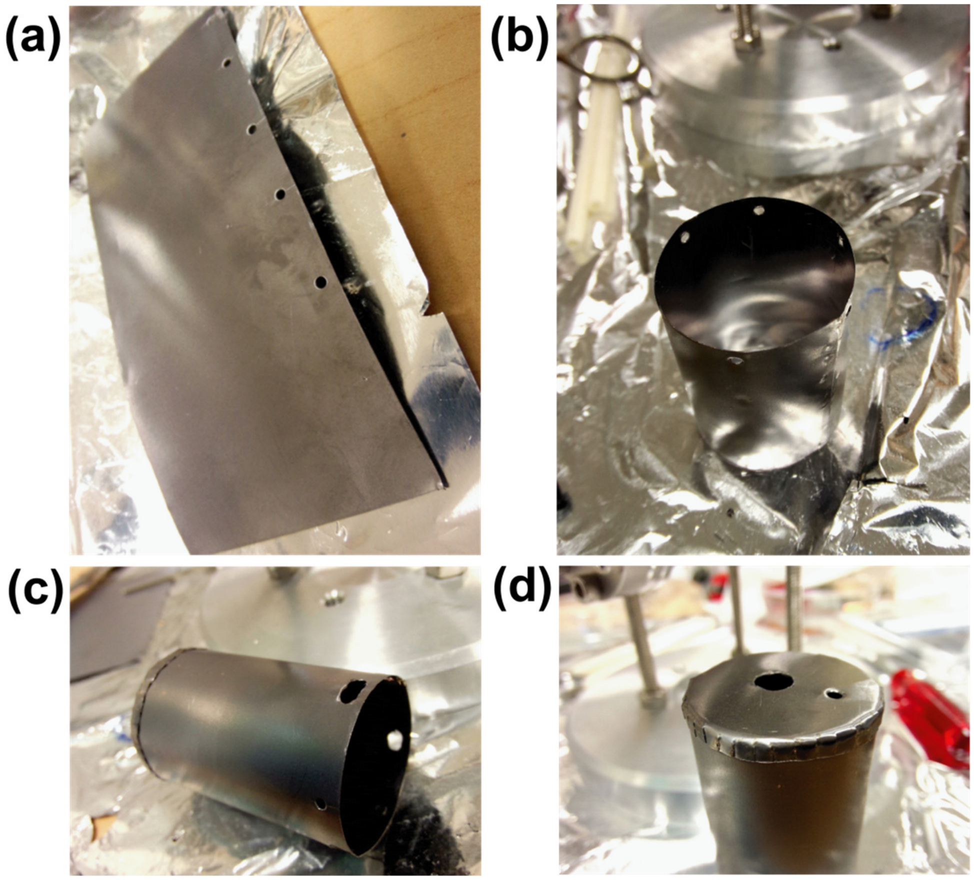
(a)
(b)
(c)
(d)

A.1.2.6 Crucible

The crucible is made from a 3/8” OD alumina tube with one end sealed. Spiral slots are cut on the outer surface of the tube for the tungsten filament to engage. Ho group has a homemade jig for making the crucible. To make the slots, we secure the ceramic tube onto the jig using set screws [Fig. A.1.8 (a)]. Turn on the wheel grinder increase the speed to level 4. Adjust the position of the jig and ceramic tube until gentle touch occurs between ceramic tube and the wheel. Then slowly rotate the jig to cut the spiral slots [Fig. A.1.8 (b)]. Keep rotating the jig backward and forward until the slot is deep enough [Fig. A.1.8 (c)].

In most cases, the filament is made from 0.02” or 0.03” tungsten wire. We need to first roll and bend the tungsten wire around the thread of a 1/4-20 threaded rod. Then slowly screw the crucible into the filament. The filament should be as tight as possible [Fig. A.1.8 (d)].

A.1.3. Assembling

A.1.3.1 Supporting structure

Screw three 8-32 and 3/4’’ long threaded rod into the three non-adjacent holes at the vacuum side of the base flange. Tighten the threaded rods using 8-32 undersized nuts. Lock washers are encouraged to be used between the nuts and the flange.

Screw the standoffs onto the threaded rod and screw another 8-32, 1-1/4’’ threaded rod with an 8-32 undersized nut into the other end of the standoff. Tighten these three nuts to secure the standoffs. Place the shaft collar onto the 1-1/4’’ threaded rod. The hole for shutter should be aligned with the vent gap on the bottom flange. Secure the shaft collar by putting another 8-32 undersized nut onto each threaded rods. Again, lock washers are encouraged to be used between the shaft collar and the nuts at both sides.

FIG. A.1.8 Procedures of making the crucible

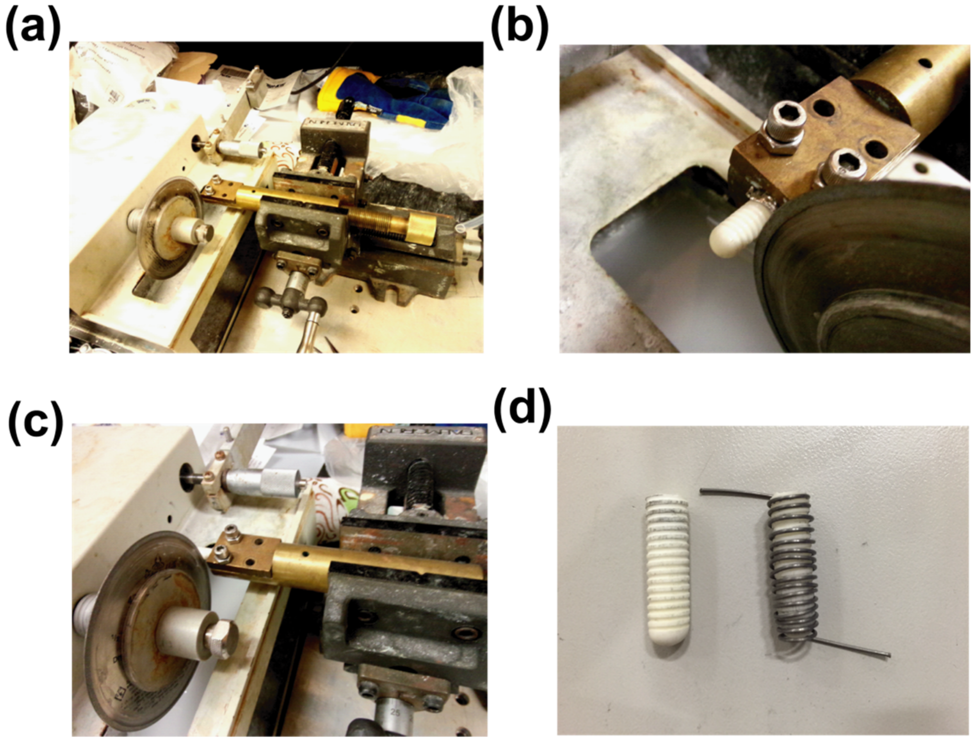
(a)
(b)
(c)
(d)

Screw in another three standoffs onto the open ends of the 1-1/4” threaded rod and lock them with an 8-32 male-to-male adapter. Put the top plate on and temporarily hand tighten with nuts. Make sure the orientation of the top plate is appropriately aligned with the shaft collar.

If the assembling follows all above procedures with appropriate parts, the distance between the top plate and the base flange should be 9”.

A.1.3.2 Rotary and electric feedthroughs

Insert a 2-56 threaded rod into the small shutter hole on the top plate. Screw two pairs of 2-56 nuts each with a lock washer sandwiched in between onto the threaded rod. Those nuts pairs are used to prevent the unnecessary movement of the threaded rod. Similarly, another two pairs of nuts are placed above and beneath the base plate and shaft collar, respectively

A 2 copper leads mini-flange power feedthrough used to provide power to the electrodes. The current rating of the feedthrough needs to be at least 20A. Place ceramic beads onto the copper pins and bend the conductor until it could go through the top port of a mini-flange tee from one side port. Use the thinnest ceramic beads available to allow maximum clearance for the flexible shaft connecting the rotary feedthrough. Tow copper pins at the air side of the electrical feedthrough should be parallel with the base flange.

We use miniature CF1.33” rotary feedthrough from MDC which is the most compact one among the commercially available products. The rotary feedthrough is installed at the other side port of the CF1.33” tee. We use a flexible shaft and two beryllium copper (Be-Cu) couplers to connect the rotary feedthrough and the threaded rod for the shutter. The flexible shaft goes in from the top port, pass through the gap between two copper pins and come out from the side port. The Be-Cu couplers are used at each side of the shaft.

Connect the tee to the CF 1.33” port of the base flange. Adjust the orientation of the tee so that the horizontal axis of the tee is parallel to the vent line of the base flange. The flexible shaft coming out from the base plate should be aligned with the shutter holes on the top plate and shaft collar. Use set-screws on the Be-Cu couplers to secure the shaft at both ends. If the gap between the coupler and the cable is excessively large, place a small piece of tantalum sheet in between as a gasket. Setscrews should be tightened as hard as possible. Fix the rotary motion feedthrough to the CF 1.33” tee. Adjust the orientation of the rotary feedthrough so its indicator can be easily monitored.

A.1.3.3 Electrodes

0.187” OD and 1/8” ID ceramic tubes are used as the insulating shield for the electrodes. Cut the copper electrodes as well as the ceramic tubes to the desired length based on the distance between the copper pins of the electrical feedthrough and the top plate as well as the length of the crucible. One of the electrodes should be 1” longer than the other one.

Insert the copper electrodes along with the ceramic tubes into the two 1.88” holes on the top plate and shaft collar. The longer electrode should go through the hole on the right side as shown is the Fig.A.1.9. This is to help the crucible with right-hand thread sit in the middle of the base plate. Connect the electrodes and the copper pins of the electric feedthrough with two Be-Cu couplers. A larger ceramic bid should be added at the bottom of each electrode to prevent short between Be-Cu coupler and the standoffs.

Due to the poor flexibility of the ceramic tubes, one may feel difficult to have it pass through all the holes freely. Losing and re-tightening the nuts on the standoffs may help the assembling.

A.1.3.4. Crucible and shield

Cut both ends of the filament to the appropriate length base on the distance between the electrodes using a tungsten wire cutter. Make sure the ends of the filament are smooth and free of crack. Even a small crack on the filament can grow and break when heating up. Insert the filament to the side holes on both copper rods and genteelly bend the filament to align crucible to the center of the top plate. Make sure the filament is not short with other parts of the evaporator. Use two 1-72 socket cap screw to secure the filament. Choose the screws of the right length to prevent the short to the thermal shield.

Place the shield onto the top plate at the appropriate orientation. Tighten the shield using three 2-56 and 1/8'' length pan slotted screws. Cut a small piece of tantalum sheet as a shutter plate. Secure the shutter plate onto the 2-56 threaded shutter rod using two nuts and a lock washer. Adjust the orientation of the shutter so it is closed when the rotary feedthrough indicates zero.

Now the assembling of the evaporator should have been finished. Test the continuity of the filament. The resistance between two electric feedthrough pins should be below 1 ohm at room temperature while the resistance between electrode and standoffs should be at least several mega ohms.

A.1.4. Performance

We have tested an evaporator with 0.03" OD tungsten filament and an empty crusible. Fig. A.1.11 is the temperature of the crucible as a function of the filament current. The temperature is measured by a thermal couple wire in direct contact with the crucible 30 min after setting the filament current to each value. The temperature curve shows a good reproducibility bewteem different dosers with same type of filament and crucible. The temperature curve depends linearly with filament current in the range from 3 nA to 7 nA, corresponding to a crucible temperature from

100 degree celcius to 500 degree celcius. The author would like to note that a cursible with 0.02” OD tungsten filament requires a much lower current.

FIG. A.1.9 Pictures of assembling the molecular evaporator.

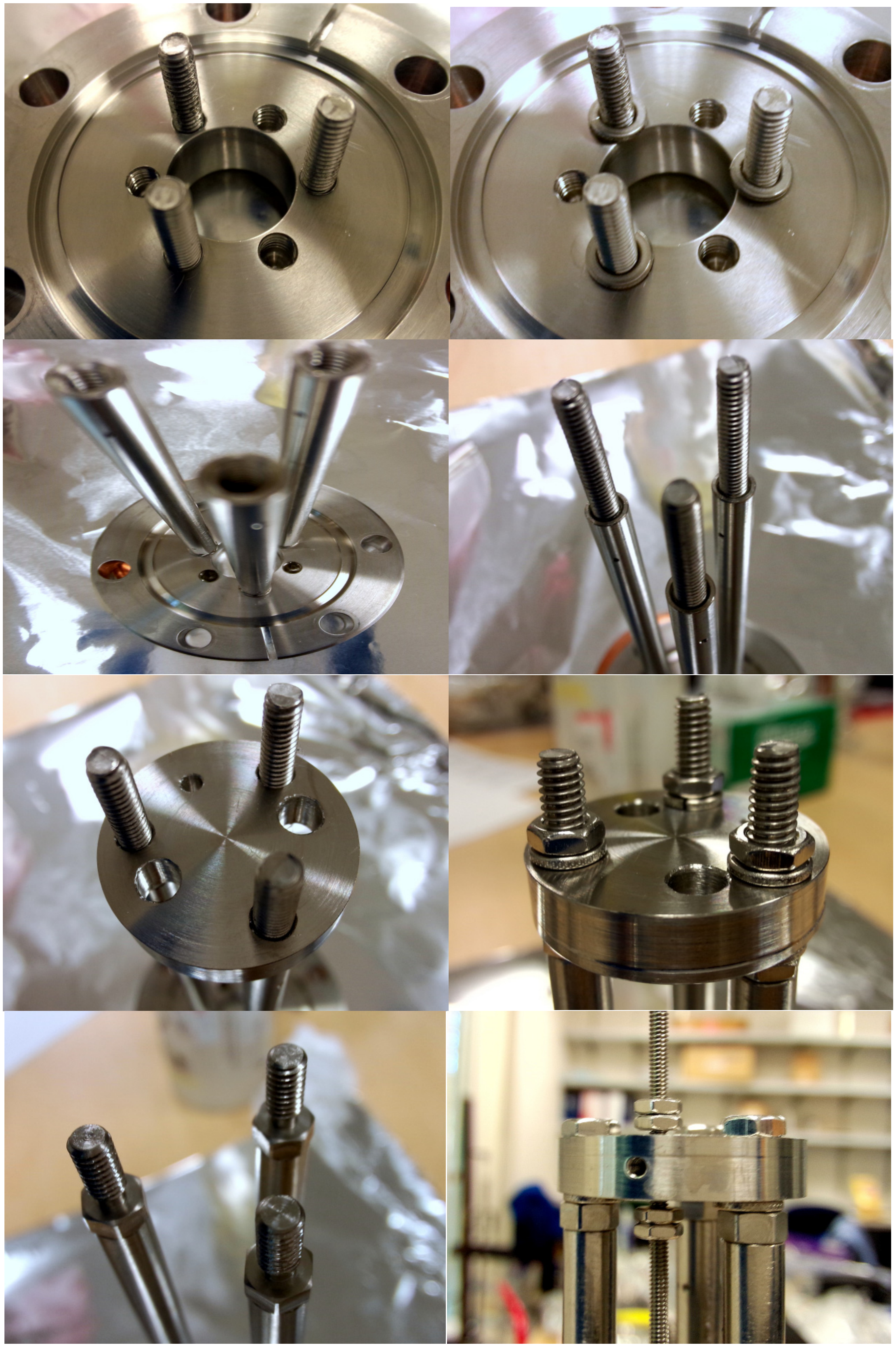

FIG. A.1.10 Pictures of assembling the molecular evaporator (continued).

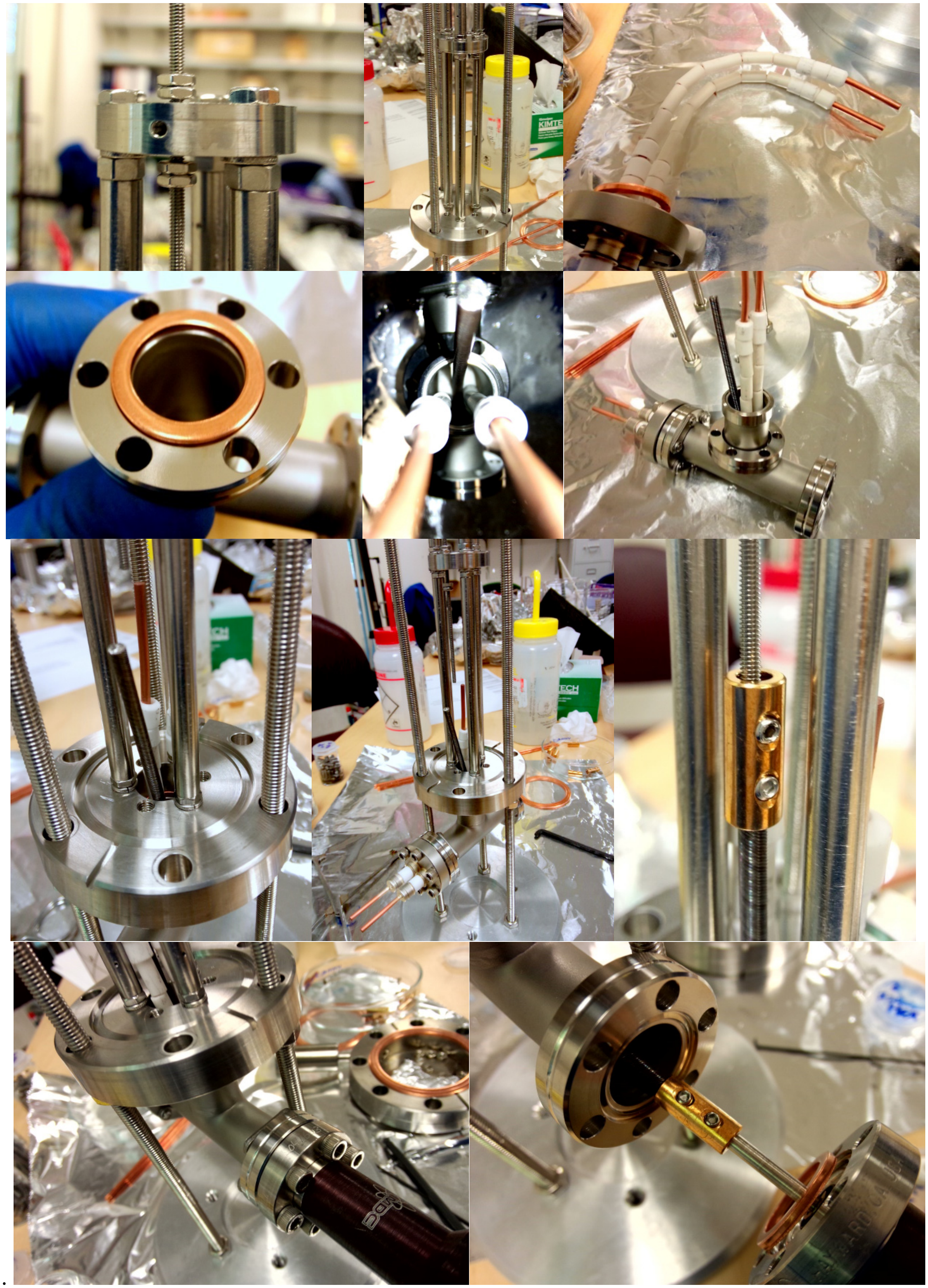

FIG. A.1.11 Crucible temperature as a function of filament current.

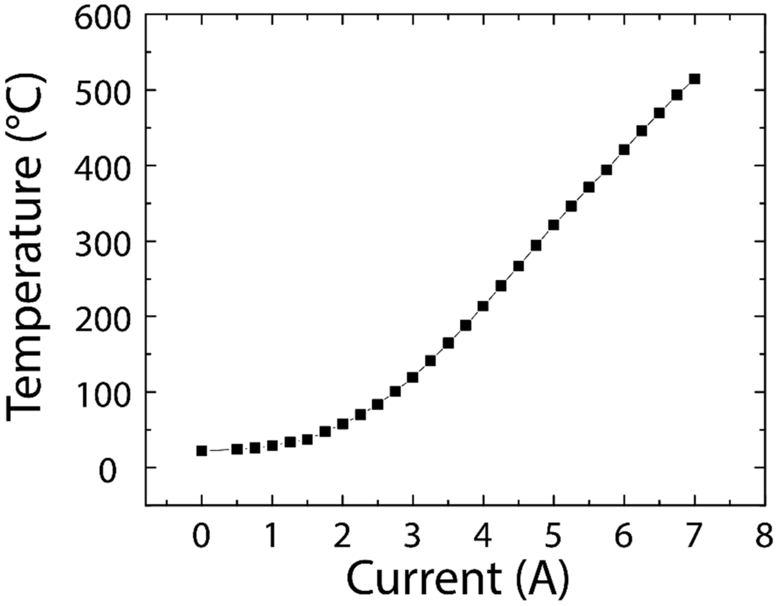
600
500
400
300
200
100
0
Temperature (°C)
0
1
2
3
4
5
6
7
8
Current (A)

A.2 Design and Fabrication of a Water-cooling Evaporator

A.2.1. Introduction

To evaporate molecule or metal at a temperature above 600 Celsius, water cooling is required to avoid overheating the shield or chamber. Here the author designed a compact water cooling doser which can fit into the doser interlock system with CF 2.75” flange (Fig. A.2.1). This design has been used to dose iron (melting point 1538 Celsius). The main innovation in this design is the interchangeable water tank, which can have a different length between different STM systems. This design has also minimized the amount of welding required to avoid the risk of leaking.

A.2.2. Machined Parts

A.2.2.1 Base flange

The base flange is a modified CF 2.75” to CF 1.33” zero length reducer. The item can be ordered from either MDC or A&N. The CAD drawing of the base flange is shown in Fig. A.2.2.

A.2.2.2 Water tank and water feedthrough

The water tank (Fig. A.2.3) is a ½” OD bucket with 3/8” ID with two 4-40 tapped holes. The water tank will be welded with the water feedthrough which is made from a pair of concentric stainless steel tubes. The outer tube has an OD of 3/8” and should be used as the water supply. The inner tube OD is ¼” and should serve as water return. It is not recommended to reverse the water flow direction which may decrease the cooling efficiency. The wall thickness of the inlet and out let tubes are not critical but we have found the 0.28” wall thickness inlet tube to be most economically friendly as well as easy to bend. The inlet and outlet tubes should be pre-cut to the appropriate length depending on the doser length. Dimensions in the drawings here are based on the standard 11” doser that can be shared in STM1, 2, 4 and MK. The 1/4” outlet tube should

FIG. A.2.1. Picture of a finished water-cooling evaporator.

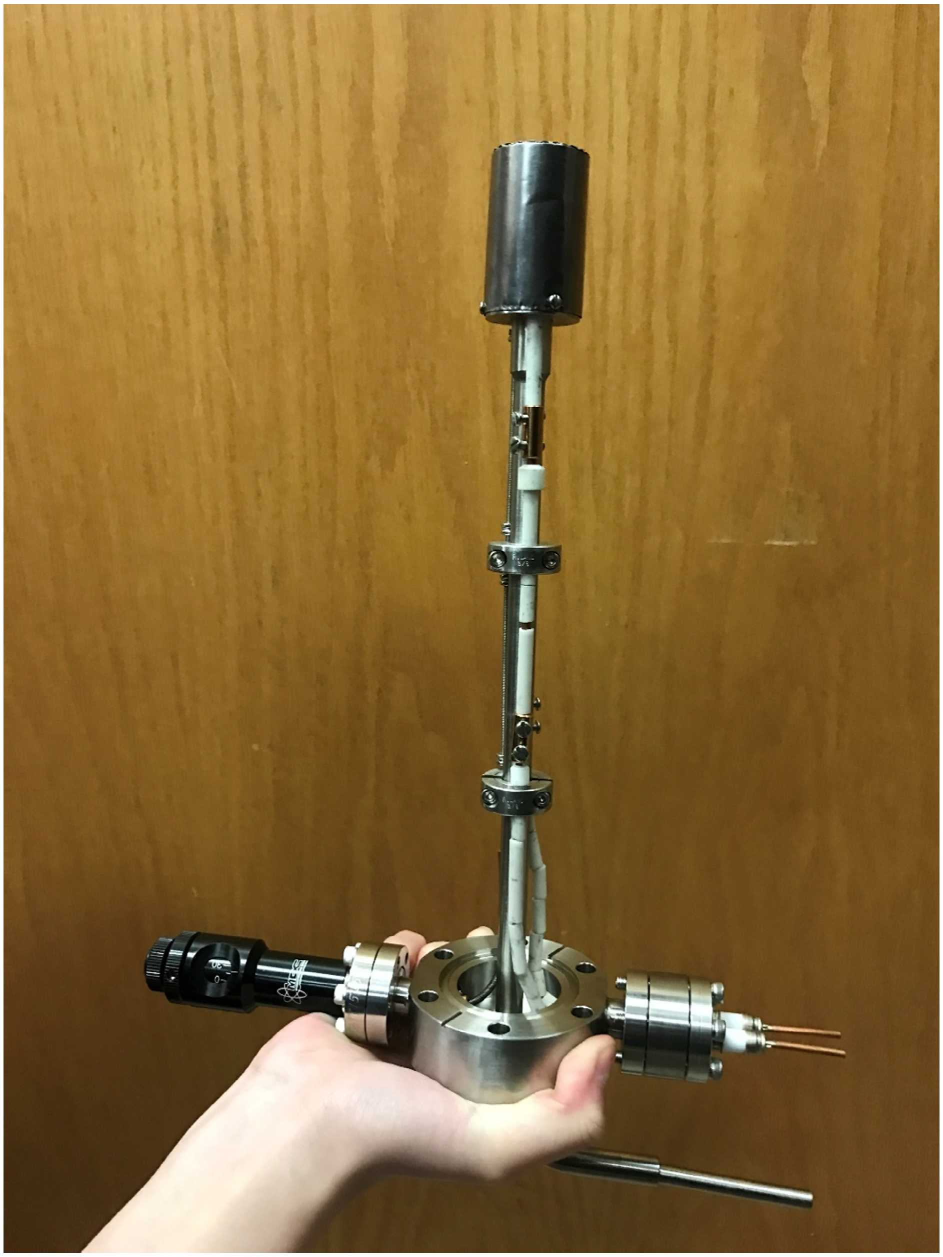

FIG. A.2.2. CAD drawing of the base flange.

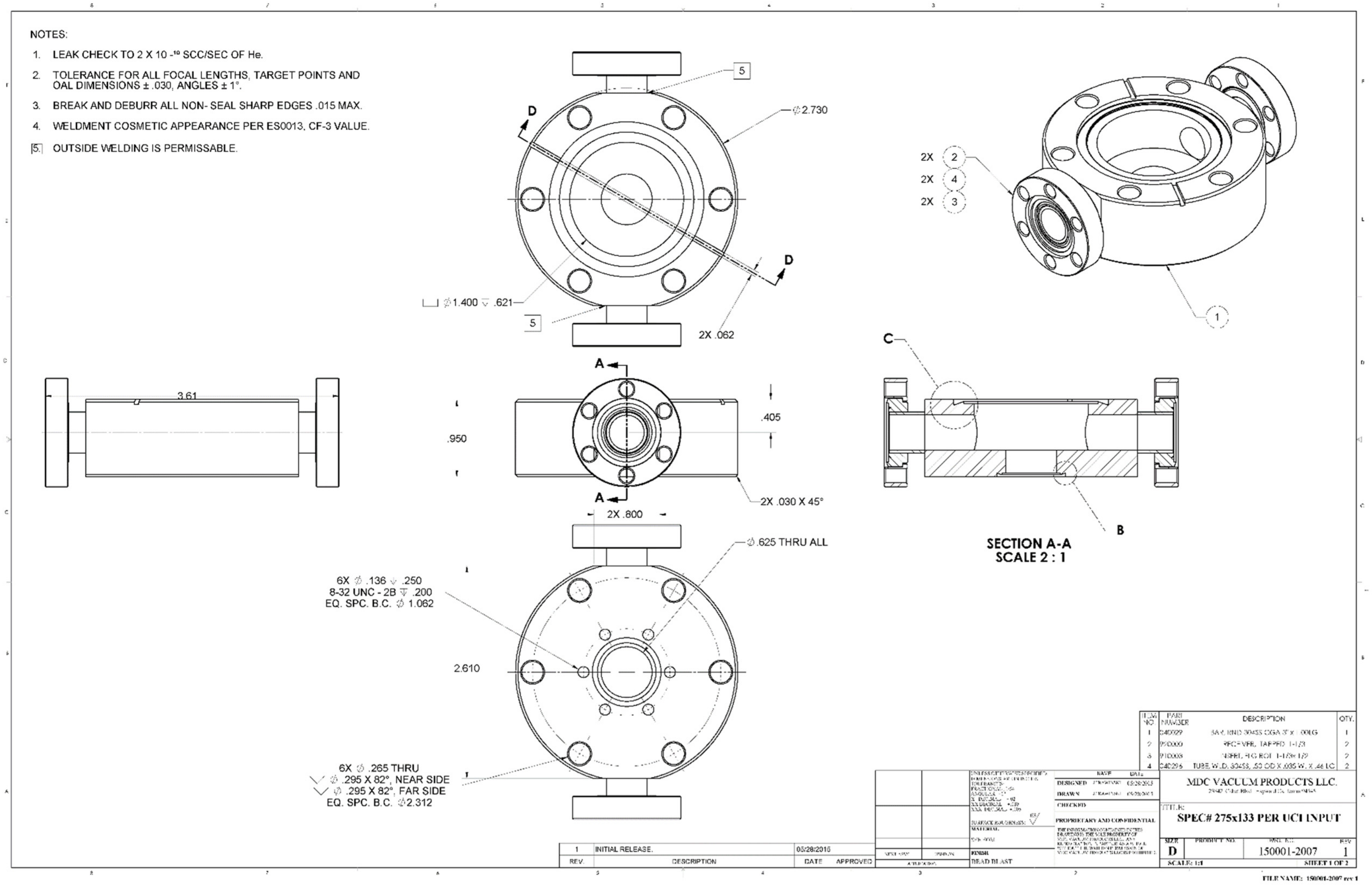
NOTES:
1. LEAK CHECK TO 2 X 10 -10 SCC/SEC OF He.
2. TOLERANCE FOR ALL FOCAL LENGTHS, TARGET POINTS AND OAL DIMENSIONS ± .030, ANGLES ± 1°.
3. BREAK AND DEBURR ALL NON- SEAL SHARP EDGES .015 MAX.
4. WELDMENT COSMETIC APPEARANCE PER ES0013, CF-3 VALUE.
5 OUTSIDE WELDING IS PERMISSABLE.
3.61
D
D
5
5
⌀2.730
⌴ ⌀1.400 ↧ .621
2X .062
A
A
.950
.405
2X .030 X 45°
2X .800
⌀.625 THRU ALL
6X ⌀.136 ↧ .250
8-32 UNC - 2B ↧ .200
EQ. SPC. B.C. ⌀1.062
2.610
6X ⌀.265 THRU
⌵ ⌀.295 X 82°, NEAR SIDE
⌵ ⌀.295 X 82°, FAR SIDE
EQ. SPC. B.C. ⌀2.312
2X 2
2X 4
2X 3
1
C
B
SECTION A-A
SCALE 2 : 1
ITEM NO. | PART NUMBER | DESCRIPTION | QTY.
1 | 040029 | BAR, RND 304SS CGA 3" x 1.00LG | 1
2 | 990009 | RECEIVER, TAPPED 1-1/3 | 2
3 | 910003 | INSERT, FLG ROT 1-1/3x 1/2 | 2
4 | 040296 | TUBE, WLD, 304SS, .50 OD X .035 W. X .46 LG | 2
1 | INITIAL RELEASE. | 05/28/2015
REV. | DESCRIPTION | DATE | APPROVED
UNLESS OTHERWISE SPECIFIED
SURFACE ROUGHNESS: 63
MATERIAL
FINISH
BEAD BLAST
NAME | DATE
DESIGNED | 05/28/2015
DRAWN | 05/28/2015
CHECKED
PROPRIETARY AND CONFIDENTIAL
MDC VACUUM PRODUCTS LLC.
TITLE:
SPEC# 275x133 PER UCI INPUT
SIZE D
PRODUCT NO.
150001-2007
REV 1
SCALE: 1:1
SHEET 1 OF 2
FILE NAME: 150001-2007 rev 1

FIG. A.2.3. CAD drawing of the water tank.

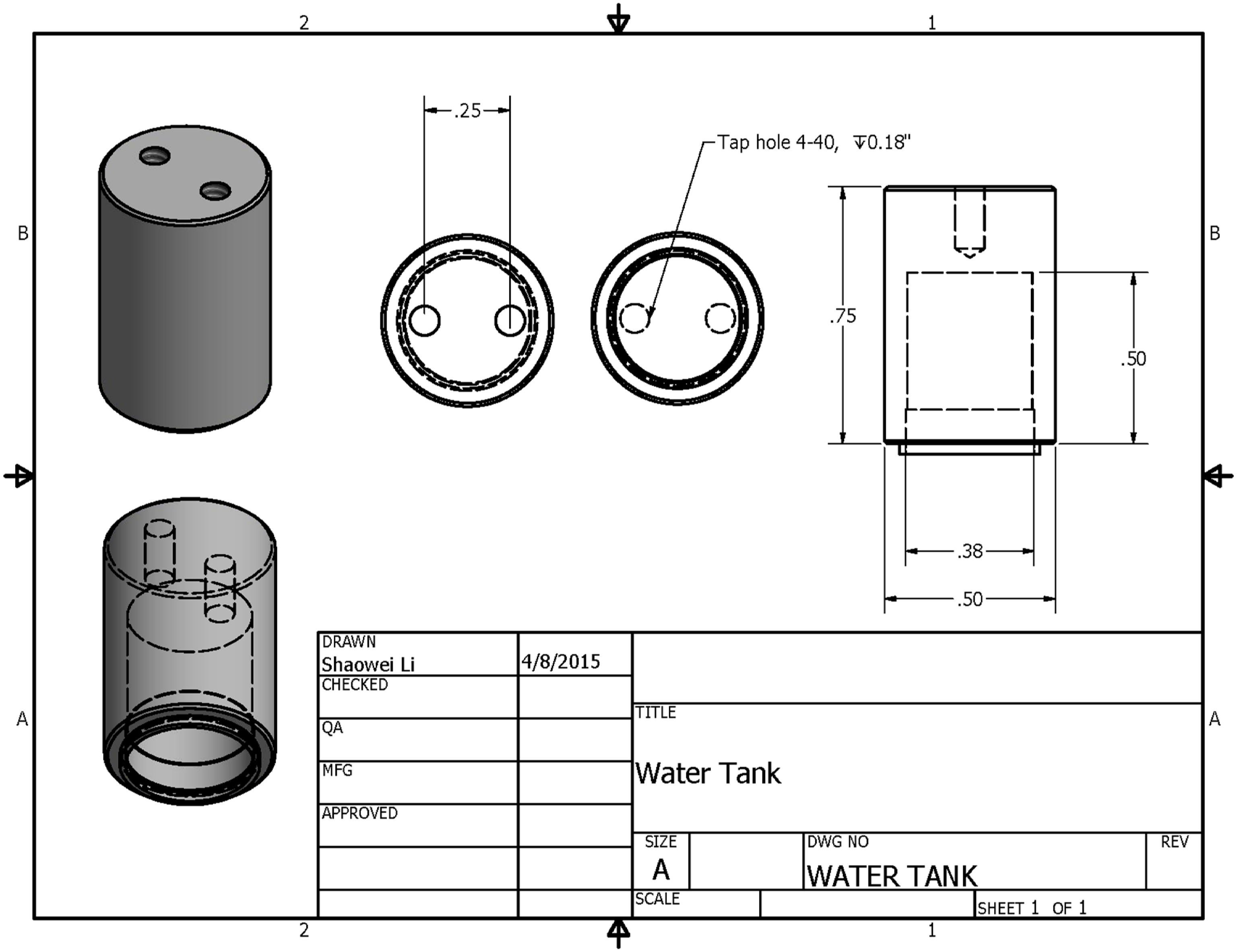
2
1
B
A
.25
Tap hole 4-40, ↧0.18"
.75
.50
.38
.50

DRAWN Shaowei Li	4/8/2015	TITLE Water Tank
CHECKED		
QA		
MFG		
APPROVED		SIZE A · DWG NO WATER TANK · REV
		SCALE · SHEET 1 OF 1

be roughly 2” longer than the inlet tube. After debris, one should bend the two tubes together to 90 degrees with the ends flush with each other at the water tank side. A miniflange with a 3/8” center hole will be welded to the tubes. Ideally, the miniflange should be as close to the 90 degrees’ corner as possible to save space. If a non-rotatable miniflange is used here, the orientation of the miniflange respect to the 4-40 tapped holes on the water tank and the water tubes is very critical. Follow the drawing in Fig. A.2.4 if the doser is made for STM2 doser interlock.

A.2.2.3 Base plate

The base plate (Fig. A.2.5) is a ¼” thick and 1.15” OD stainless steel disk that is attached to the water tank and used to support the tantalum thermal shield. It acts as a heat sink that transfers the heat from the shield to the water tank. Two 1/8” holes are drilled for the tantalum electrodes. Both sides of the base plate are machined down by 0.1” depth with ½” diameter at the center, which should be a tight fit with the water tank to ensure best thermal contact. Two 0.12” diameter through holes at the center of the base plate are used to mount the water tank. Three 2-56 side holes are used mount the tantalum thermal shield. A small 0.1” hole is used for the threaded rod to operate the shutter.

A.2.2.4 Shaft collars

The shaft collars (Fig. A.2.6) are modified from SS316 two pieces split shaft collars made by Ruland. It is important to use the “metric with 3/8 inch bore” type which is slightly larger than the standard 3/8” one. Similar to the base plate, two 0.188” holes are used for electrodes, and the small hole is used for the shutter. At least two sets of shaft collars are needed for one doser, more may be necessary for a longer doser.

FIG. A.2.4 CAD drawing of the water tank together with the water feedthrough

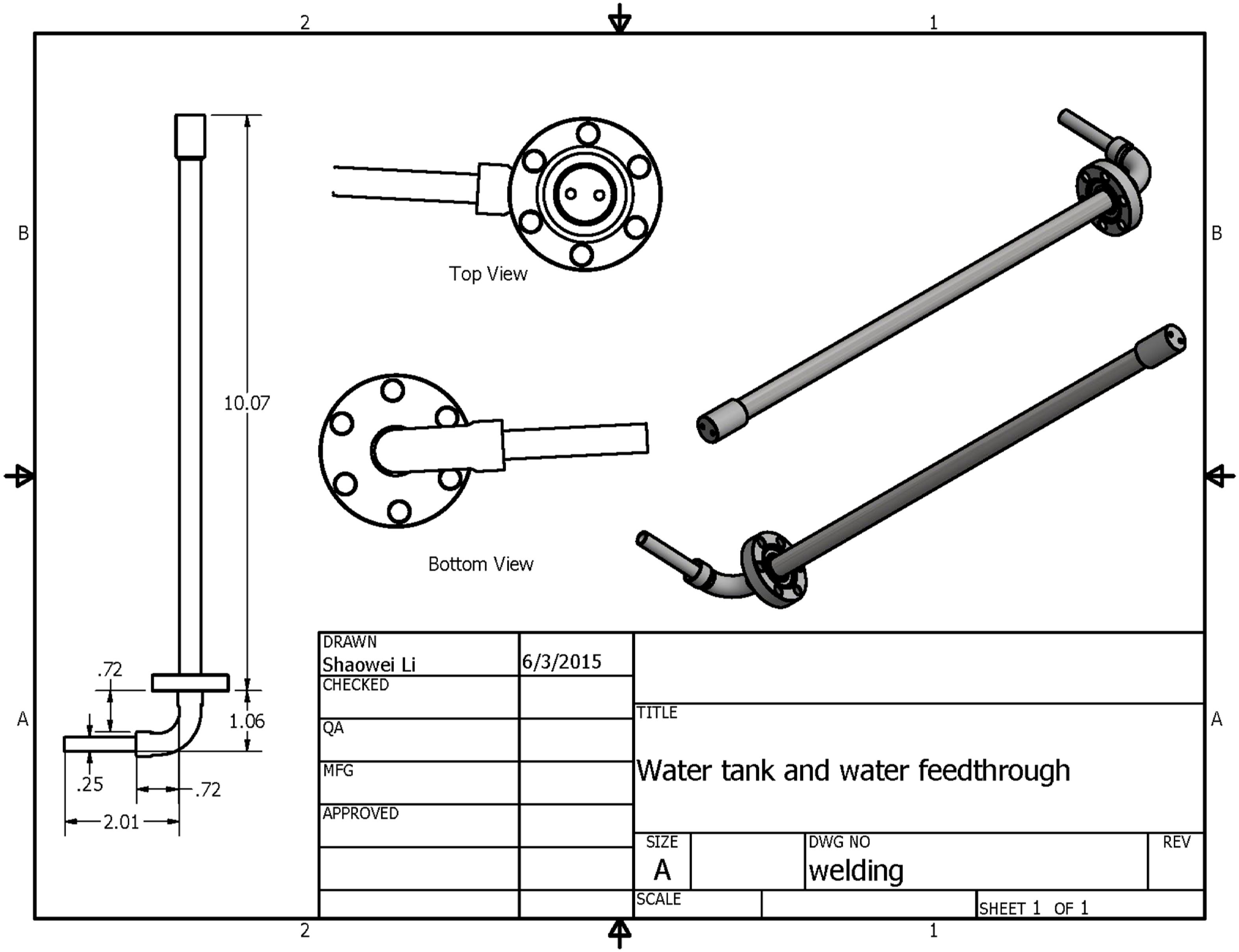
2
1
B
A
10.07
.72
1.06
.25
.72
2.01
Top View
Bottom View

DRAWN Shaowei Li	6/3/2015
CHECKED	
QA	
MFG	
APPROVED	

TITLE

Water tank and water feedthrough

SIZE		DWG NO	REV
A		welding	

SCALE		SHEET 1 OF 1

FIG. A.2.5 CAD Drawing of the base plate.

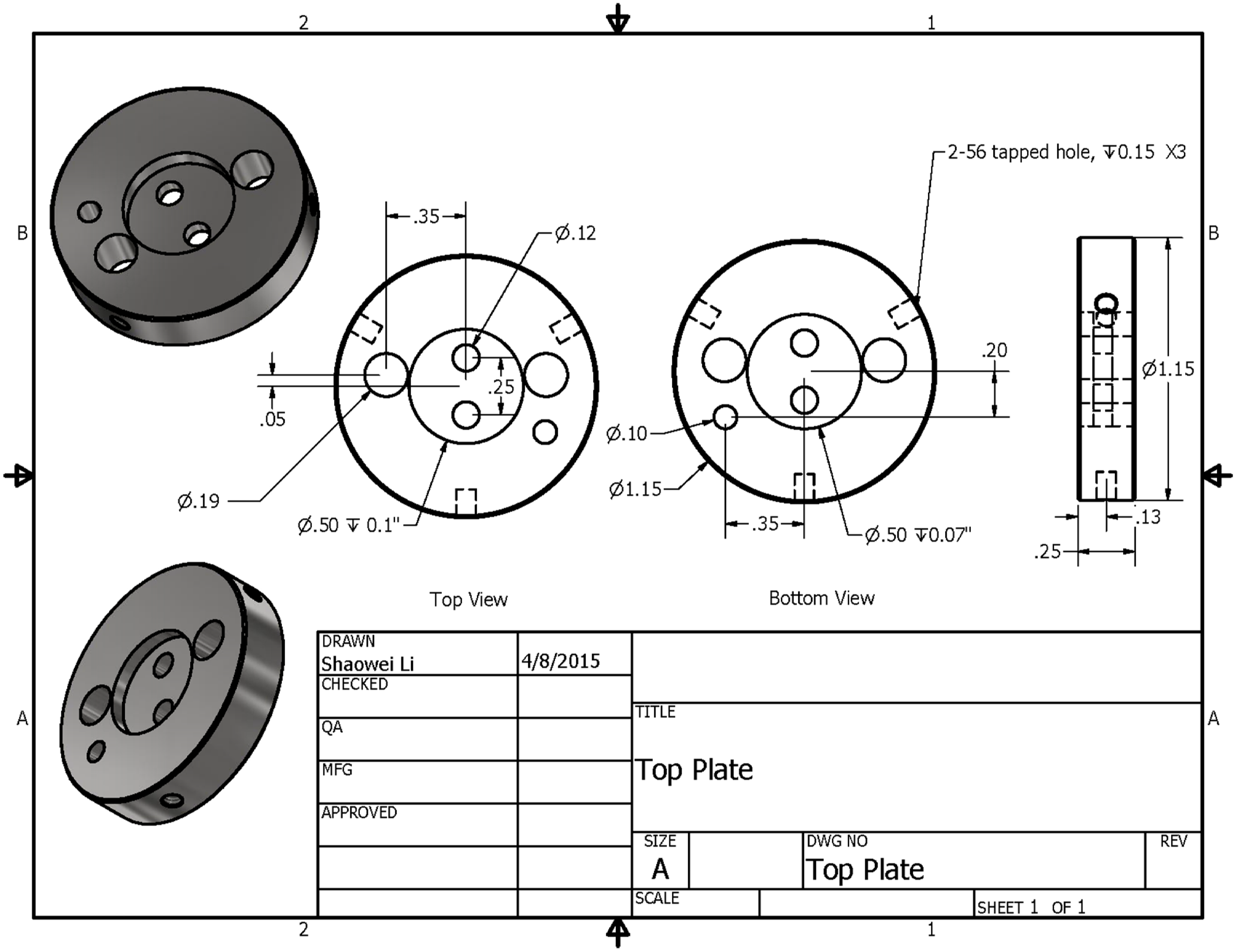
2
1
B
A
2-56 tapped hole, ⌴0.15 X3
.35
Ø.12
.25
.05
Ø.19
Ø.50 ⌴ 0.1"
.20
Ø.10
Ø1.15
.35
Ø.50 ⌴0.07"
Ø1.15
.13
.25
Top View
Bottom View

DRAWN
Shaowei Li 4/8/2015
CHECKED
QA
MFG
APPROVED

TITLE
Top Plate

SIZE
A

DWG NO
Top Plate

REV

SCALE

SHEET 1 OF 1

FIG. A.2.6 CAD Drawing of the shaft collar.

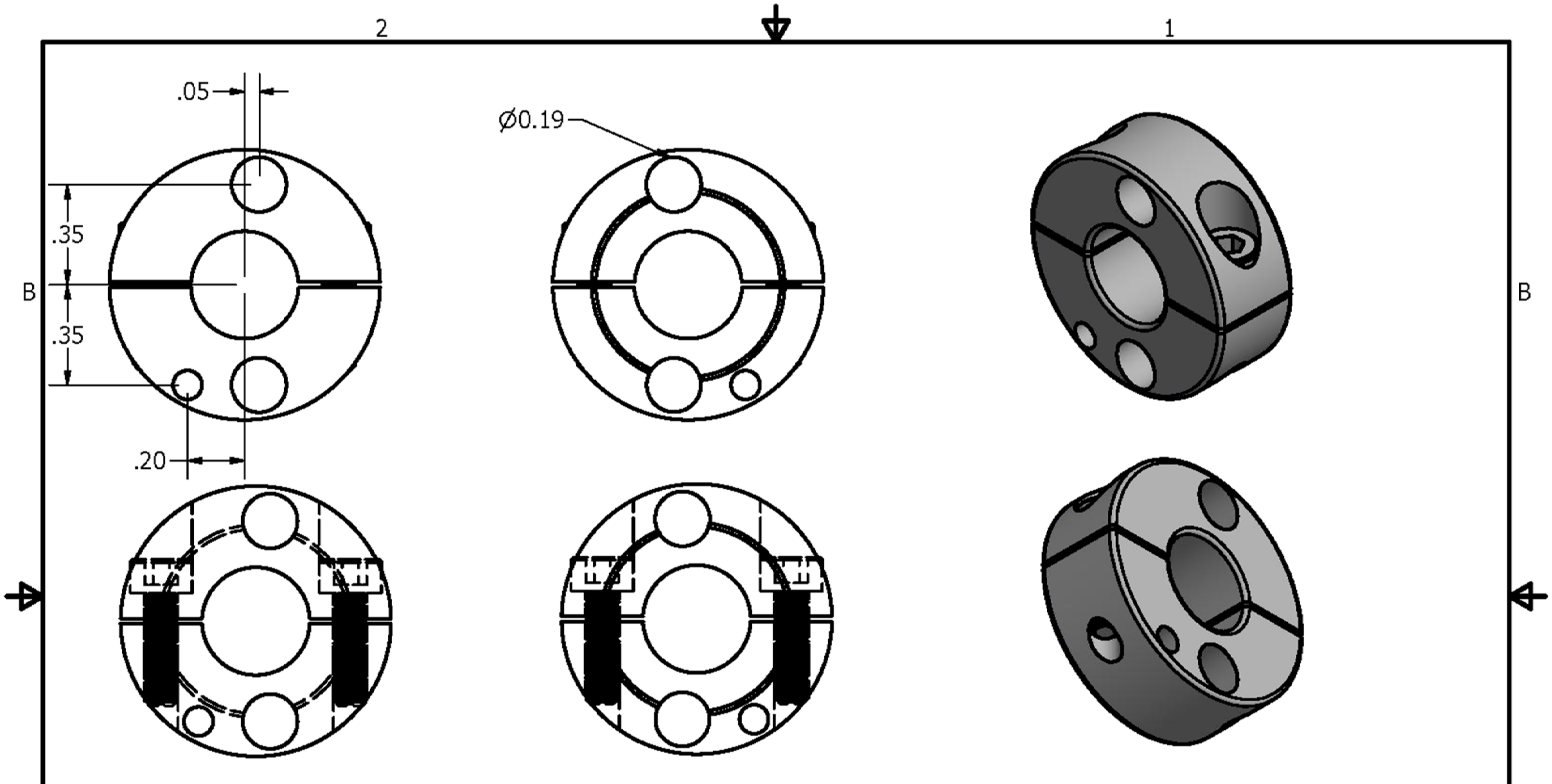
2
1
B
.05
Ø0.19
.35
.35
.20

DRAWN Shaowei Li	4/13/2015	
CHECKED		TITLE Shaft Collar
QA		
MFG		
APPROVED		

SIZE		DWG NO	REV
A		Shaft Collar	
SCALE		SHEET 1 OF 1	

A
A
2
1

A.2.2.5 Tantalum and copper electrodes

A pair of tantalum electrodes (Fig. A.2.7) is used here to provide power to the filament. These tantalum electrodes are similar to the copper electrodes used in the molecular evaporators introduced in A.1.2.3. Tantalum replaces copper here due to its high melting point as well as low outgassing rate. Due to the high cost of tantalum, we only use it near the crucible. Two copper rods are used to connect the tantalum electrodes with the power feedthrough installed on the flange. The length of the copper rods depends on the length of the doser.

A.2.2.6 Crucible and shield

The procedures of making a thermal shield and a crucible are same with the ones used in making a molecular evaporator. Refer to A.1.2.5 and A.1.2.6 for detailed information. It is recommended to increase the thickness of the tantalum thermal shield to provide better thermal conductivity or use multiple layers. 0.03” filament is required to provide enough support to the crucible.

A.2.3. Assembling

A.2.3.1 Rotary and electrical feedthroughs

The rotary feedthrough and electrical feedthrough we use for a water cooling doser are same as those used in the molecular doser as described in A.1.3.2. The feedthroughs are mounted on the two miniflange side ports of the base flange. A 1/2” thick doubled sided miniflange (a standard part ordered from A&N) is needed as a spacer at the power feedthrough side since side ports ID is too small for the ceramic ends of the copper leads. Ceramic beads are used on the copper leads for insulating. The rotary feed through is connected with the flexible shaft by Be-Cu connectors. Compare to the molecular doser, the flexible shaft used in a water cooling doser is

FIG. A.2.7. CAD Drawing of the tantalum electrodes.

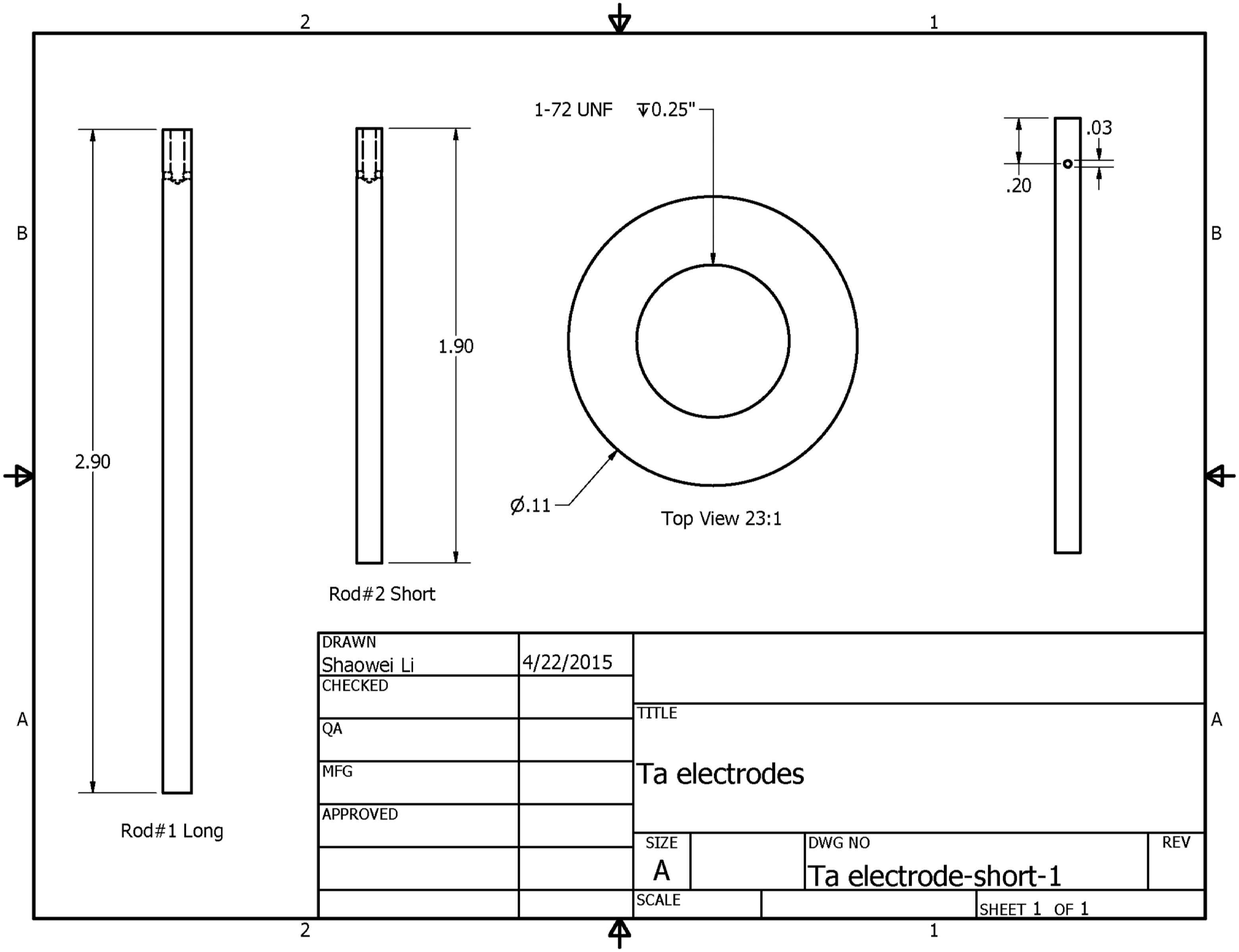
2
1
B
A
2.90
Rod#1 Long
1.90
Rod#2 Short
1-72 UNF ↧0.25"
∅.11
Top View 23:1
.03
.20

DRAWN
Shaowei Li 4/22/2015
CHECKED
QA
MFG
APPROVED

TITLE
Ta electrodes

SIZE A
DWG NO Ta electrode-short-1
REV
SCALE
SHEET 1 OF 1

shorter and thus has a larger curvature. Epoxy can be used to glue the shaft with the Be-Cu couplers to prevent the shaft from detaching.

A.2.3.2 Shaft collars and electrodes

We use 3 mm or 1/8” OD copper rods with 1.87” OD and 1/8” ID ceramic tubes as islutating shields to connect the copper leads of the electrical feedthrough to the tantalum electrodes. Be-Cu couplers are used to connected the junctions. The shaft collars are mounted on the water feedthrough with appropriate separation (bottom of Fig.A.2.8). The copper rods and ceramic shields need to pass through the 0.188” holes on the shaft collars. The electrodes are secured solely by the friction between ceramic and shaft collars. A little bit miss alignment between the shaft collars may help them stay in place. Same ceramic tubes are also used as the insulating shield for the tantalum electrodes.

A.2.3.3 Base plate

The base plate is mounted on the water tank using two 4-40 1/8” length screws. Moly or tantalum screws are recommended here though the author has been using regular stainless steel screws. The tantalum electrodes with ceramic shield pass through the 0.188” holes on the base plate.

A.2.3.4. Crucible and shield

The installation procedues of the thermal shield and the crucible are same as those described in A.1.3.4. It is recommended to use a tantalum threaded rod to operate the shutter. If a stainless steel rod is used, a ceramic tube needs to be used to cover the section within the tantalum shield near the crucible. The 1-72 screws used to secure the crucible should also be either tantalum or molybdenum.

FIG. A.2.8. Pictures of assembling the water cooling doser.

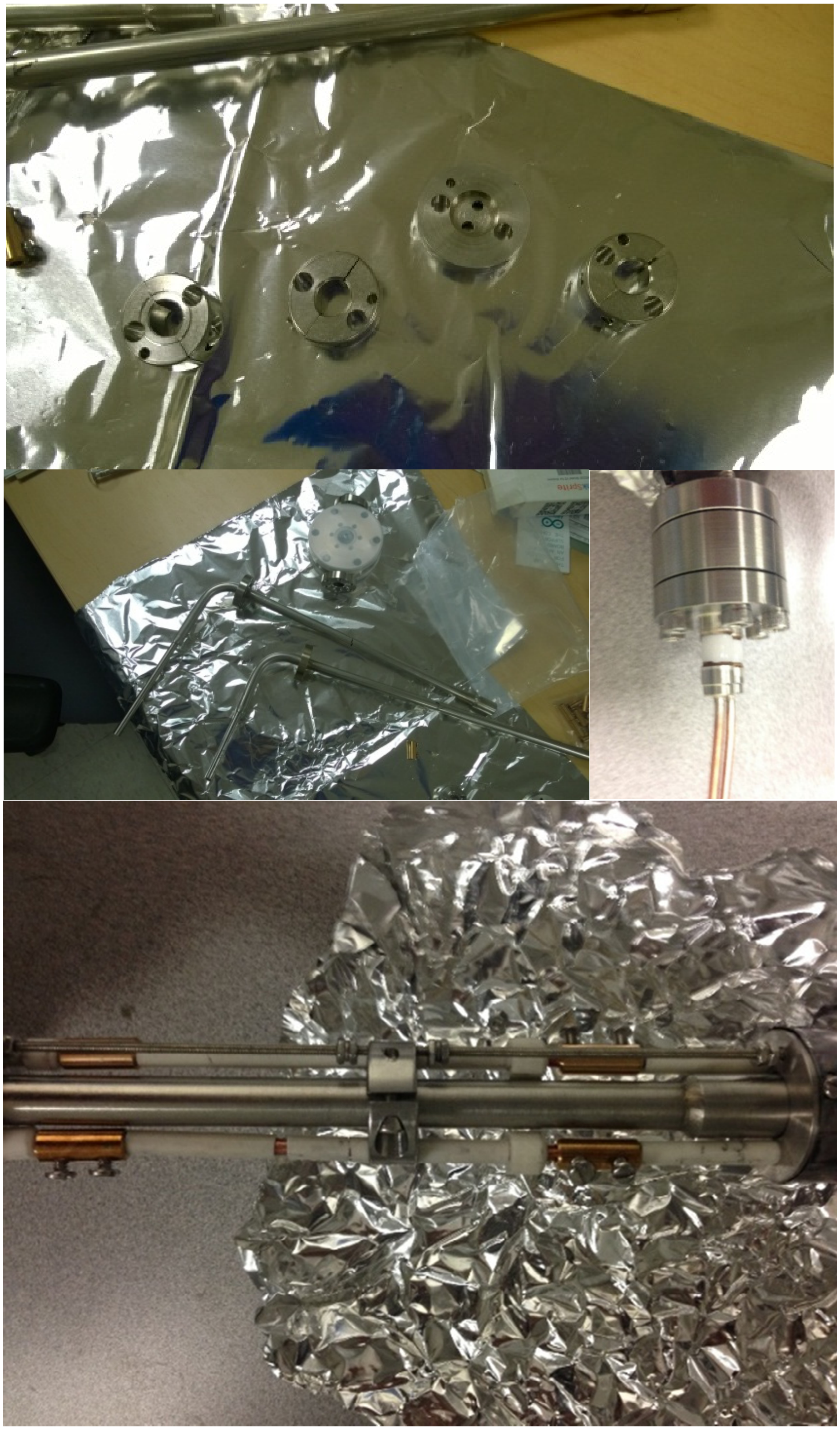

Appendix B

Software Development

One of the unique advantages of home-made apparatus is the versatility. Ho group have developed a customized computer control software for the home-built STM systems. The software has been continuously modified and upgraded by different generations of Ho group members. There have been three major versions after the initial release. The original software (version 1) was written by M. A. Rezaei and S. Na in 1998 using C and runs under Windows 3.11. As the Windows operation systems later than Windows 95 are not running in real-time, it became necessary to perform some of the functions by a stand along digital signal processor (DSP) whose operation will not be interrupted by the Windows operating system. T. M. Wallis updated the software (version 2) and converted the core functions including tip approaching and data acquisition into assembling language to be run with a Motorola DSP563xx series DSP board. After that, H. Lee, S. W. Wu, U. Ham, X. W. Tu and C. Xu create different versions of updates base on the specialties of each STM. The author (S. W. Li) adapts some of these updates and adds additional functions to the program (version 3). As a fundamental programing language, C is relatively old fashioned and less user-friendly. LabVIEW has been widely used by Ho group members as well as scientific instrument companies due to its convenient graphic user interface. In the current version, the STM control software can send triggers to LabVIEW or other programs, allowing these programs to synchronize with the STM. The author use LabVIEW 2012 together with a Data Aqucistion Module (NI DAQ 6 series). This section details the new functions of the STM control software added by the author as well as a series of different LabVIEW programs used for data acquisition and processing.

B.1 STM Control Software

The "Scan" dialog of the STM program is shown in Fig. B.1.1. Two new functions are added in this dialog as circled by the dashed lines. A new section “Sequence” is used to save or load the current image sequence. The “save” bottom can be used to save the current sequence setting into a .SEQ file. The “load” bottom can be used to override the current setting with the previously saved sequence. Since sequence #1 is usually used for constant current topographic image and should not be modified, a warning message “You are overwriting Sequence #1, continue?” will show up if the user is attempting to override the sequence #1. Another new section “Triggering” can be found right underneath the “Sequence”. This function is used to change the output voltage of a specific output channel which can be used to trigger other programs. The input box “Ch.” is used to specify the output channel. Our STM electronic box has totally 14 output channels labeled from 0 to 11. Channel 7, 9, 10 and 11 are usually not occupied and can be used for triggering. The bottom “To 5V” is used to ramp the output voltage of the triggering channel to 5 V within 1 ms, corresponding to a logic high. The bottom “To 0V” is used to ramp the voltage back to 0 V. If the bottom “Pulse” is pressed, the program will send out a 5 V TTL pulse with 50 ms duration.

Fig. B.1.2. shows the “Spectroscopy” dialog and “Spectroscopy Option” dialog. The most important modification here is allowing the STM electronics to send out trigger pulses during a spectroscopy measurement. In “Spectroscopy Option” dialog, the pulse parameter can be specified in the “Triggering” section. If the “Each Pass” box is enabled, a triggering pulse will be sent before each pass of spectroscopy. If the “Each Step” box is enabled, a pulse will be sent at each step of one pass. The triggering function is disabled if none of these two boxes is clicked. The “Ch.” box is used to specify the trigger output channel during spectroscopy. This box is independent with the

FIG. B.1.1. Screenshot of the “Scan” dialog.

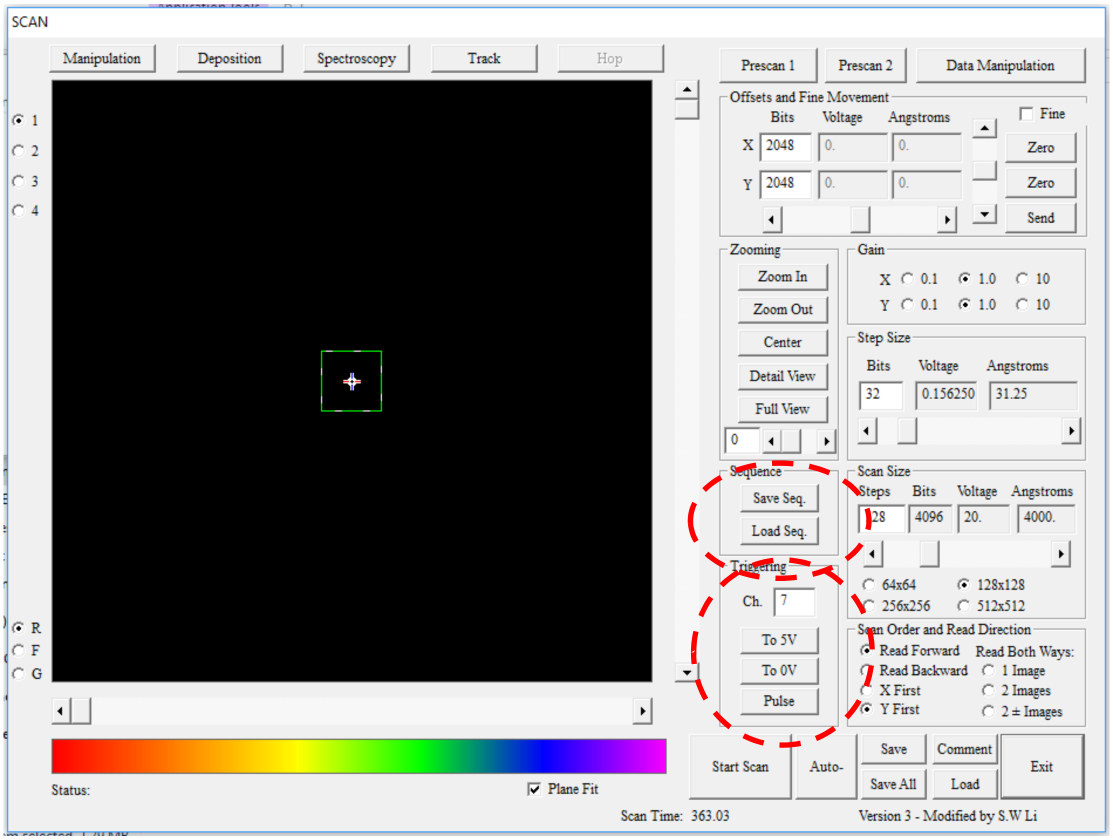
SCAN
Manipulation
Deposition
Spectroscopy
Track
Hop
Prescan 1
Prescan 2
Data Manipulation
Zero
Zero
Send
Zoom In
Zoom Out
Center
Detail View
Full View
Save Seq.
Load Seq.
To 5V
To 0V
Pulse
Start Scan
Auto-
Save
Comment
Save All
Load
Exit
Status:

● 1 ○ 2 ○ 3 ○ 4

● R ○ F ○ G

☑ Plane Fit

Offsets and Fine Movement

	Bits	Voltage	Angstroms
X	2048	0.	0.
Y	2048	0.	0.

☐ Fine

Zooming: 0

Gain

X ○ 0.1 ● 1.0 ○ 10

Y ○ 0.1 ● 1.0 ○ 10

Step Size

Bits	Voltage	Angstroms
32	0.156250	31.25

Sequence

Triggering

Ch. 7

Scan Size

Steps	Bits	Voltage	Angstroms
128	4096	20.	4000.

○ 64x64 ● 128x128

○ 256x256 ○ 512x512

Scan Order and Read Direction

● Read Forward
○ Read Backward
○ X First
● Y First

Read Both Ways:
○ 1 Image
○ 2 Images
○ 2 ± Images

Scan Time: 363.03

Version 3 - Modified by S.W Li

FIG. B.1.2. Screenshots of the “Spectroscopy Options” and “Spectroscopy” dialogs.

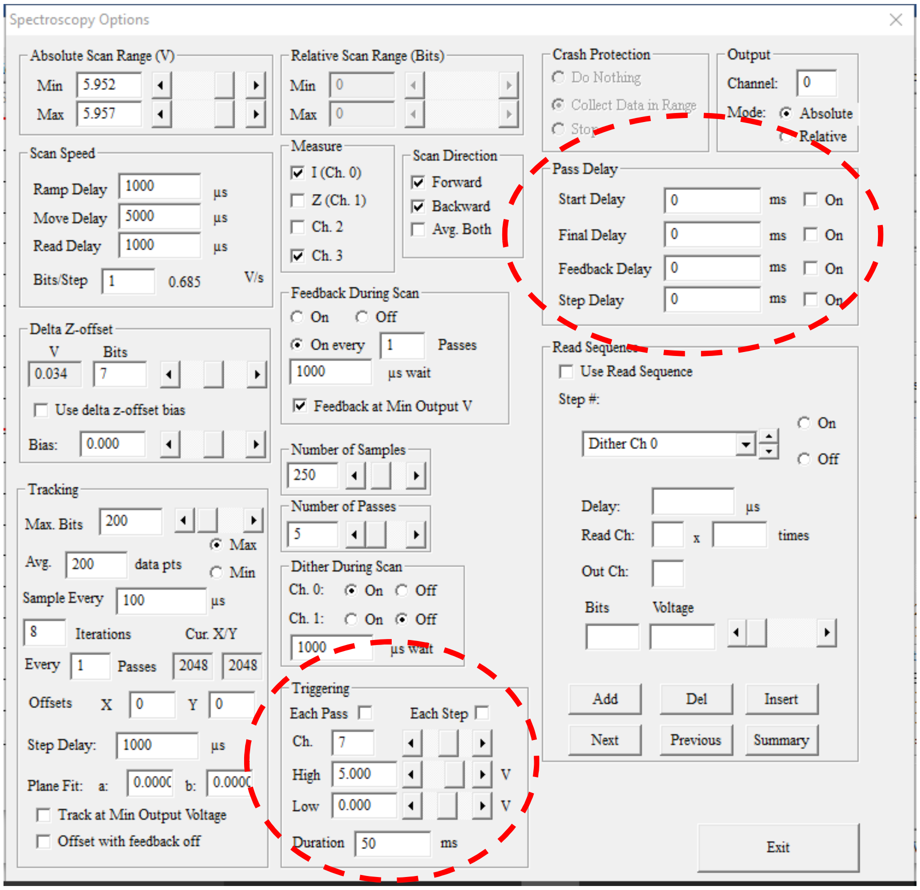
Spectroscopy Options

Absolute Scan Range (V)
Min 5.952
Max 5.957

Relative Scan Range (Bits)
Min 0
Max 0

Crash Protection
○ Do Nothing
● Collect Data in Range
○ Stop

Output
Channel: 0
Mode: ● Absolute ○ Relative

Scan Speed
Ramp Delay 1000 µs
Move Delay 5000 µs
Read Delay 1000 µs
Bits/Step 1 0.685 V/s

Measure
☑ I (Ch. 0)
☐ Z (Ch. 1)
☐ Ch. 2
☑ Ch. 3

Scan Direction
☑ Forward
☑ Backward
☐ Avg. Both

Pass Delay
Start Delay 0 ms ☐ On
Final Delay 0 ms ☐ On
Feedback Delay 0 ms ☐ On
Step Delay 0 ms ☐ On

Delta Z-offset
V 0.034 Bits 7
☐ Use delta z-offset bias
Bias: 0.000

Feedback During Scan
○ On ○ Off
● On every 1 Passes
1000 µs wait
☑ Feedback at Min Output V

Read Sequence
☐ Use Read Sequence
Step #:
Dither Ch 0 ○ On ○ Off
Delay: µs
Read Ch: x times
Out Ch:
Bits Voltage

Number of Samples 250

Number of Passes 5

Tracking
Max. Bits 200 ● Max ○ Min
Avg. 200 data pts
Sample Every 100 µs
8 Iterations Cur. X/Y
Every 1 Passes 2048 2048
Offsets X 0 Y 0
Step Delay: 1000 µs
Plane Fit: a: 0.0000 b: 0.0000
☐ Track at Min Output Voltage
☐ Offset with feedback off

Dither During Scan
Ch. 0: ● On ○ Off
Ch. 1: ○ On ● Off
1000 µs wait

Triggering
Each Pass ☐ Each Step ☐
Ch. 7
High 5.000 V
Low 0.000 V
Duration 50 ms

Add
Del
Insert
Next
Previous
Summary
Exit

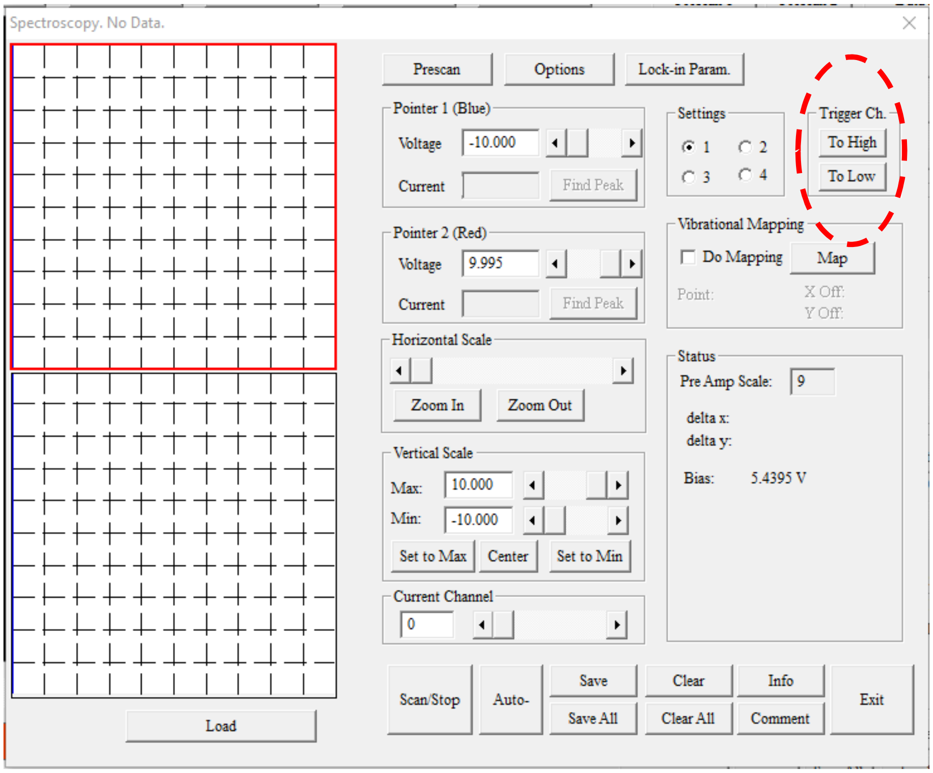
Spectroscopy. No Data.

Pointer 1 (Blue)
Voltage -10.000
Current

Pointer 2 (Red)
Voltage 9.995
Current

Settings
● 1 ○ 2
○ 3 ○ 4

Vibrational Mapping
☐ Do Mapping
Point: X Off: Y Off:

Vertical Scale
Max: 10.000
Min: -10.000

Current Channel 0

Status
Pre Amp Scale: 9
delta x:
delta y:
Bias: 5.4395 V

Prescan
Options
Lock-in Param.
Find Peak
Find Peak
Trigger Ch.
To High
To Low
Map
Horizontal Scale
Zoom In
Zoom Out
Set to Max
Center
Set to Min
Load
Scan/Stop
Auto-
Save
Save All
Clear
Clear All
Info
Comment
Exit

“Ch.” box in “Scan” dialog. The “High” box is used to define the voltage of logic high of the TTL pulse while the “Low” box defines the logic low. Default values for logic high and low are 5 V and 0 V respectively. Duration of the TTL pulse can be changed in the “Duration” box from 1 ms to 10000 s.

Another new section in the “Spectroscopy Option” dialog is “Pass Delay”, where different delay time can be specified in order to appropriately synchronize between programs. The “Start Delay” is the time system wait at the beginning of each pass. The “Final Delay” is the wait time at the end of each pass. “Feedback Delay” is the delay time between passes when the feedback is turned on and off. “Step Delay” is the additional wait time between each step. The “on” boxes after each delay are used to enable the corresponding delay time. The delay time will only take effect when the triggering function is also enabled. The “To High” and “To Low” bottoms in the “Trigger Ch.” section in “Spectroscopy” dialog can be used to manually switch the trigger channel output voltage to logic high or logic low.

The auto ramping function added to the “Pre-Scan Controls” dialog is circled in Fig. B.1.3. this function is used to ramp the bias or current to the desired set point with a constant speed. The top section “Tunneling current” is used to ramp the set point current. The when a “Ramp To” bottom is clicked, the system will ramp the current to the corresponding “Target Current”. The “Ramp Delay” determine the speed of ramping. The “Stop” bottom can be used to interrupt the auto-ramping. Similarly, the bottoms in “Sample Bias” section are used to ramp the sample bias to the desired set point automatically. To avoid crashing the tip, the auto ramping function cannot be used to ramp the bias across zero.

Fig. B.1.4. shows the modifications in “Deposition” and “Pulse Options” dialogs. The most important feature added here is the “Repeated Pulses” function which allows the software to

FIG. B.1.3. Screenshot of the “Pre-Scan Controls” dialog.

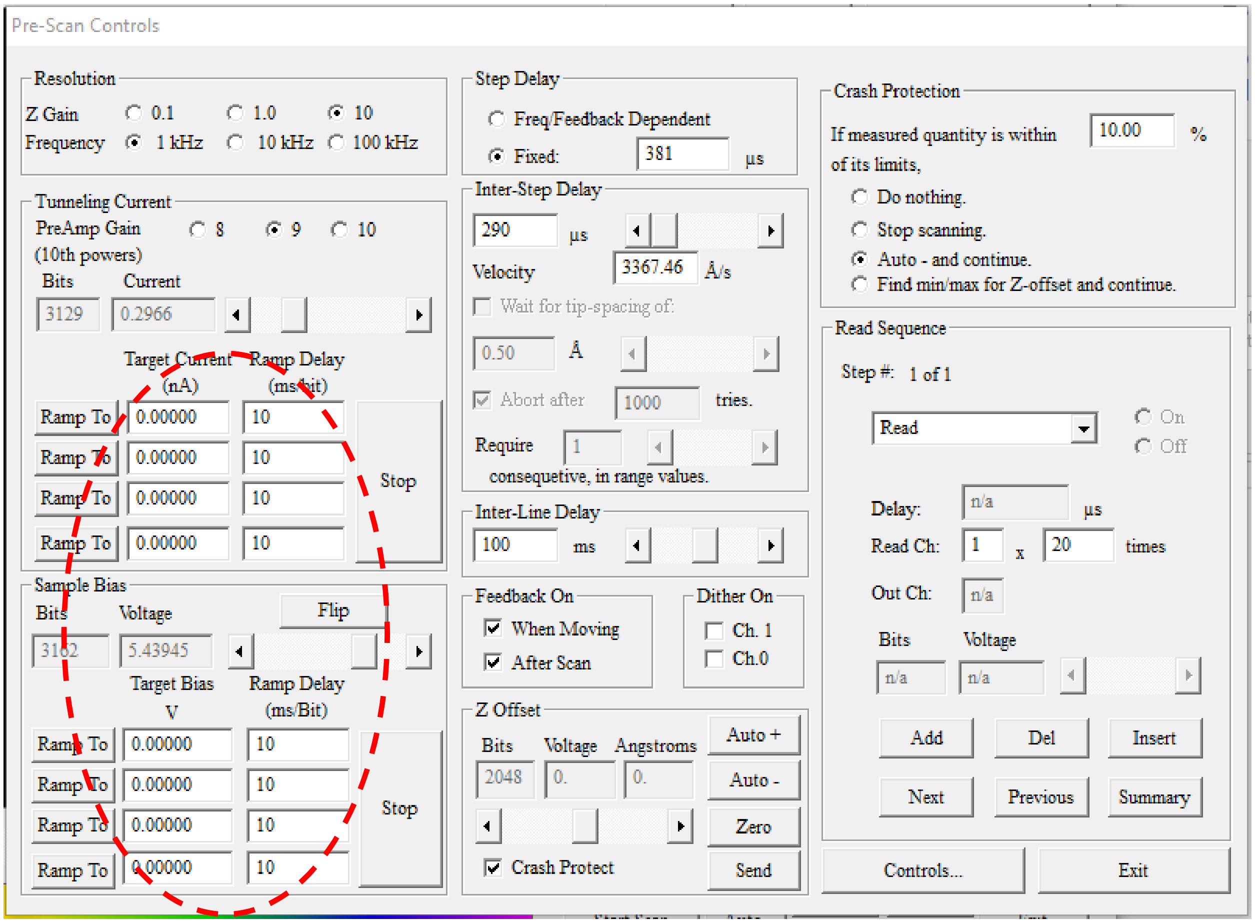
Ramp To
Ramp To
Ramp To
Ramp To
Stop
Flip
Ramp To
Ramp To
Ramp To
Ramp To
Stop
Auto +
Auto -
Zero
Send
Add
Del
Insert
Next
Previous
Summary
Controls...
Exit

Pre-Scan Controls

Resolution
Z Gain ○ 0.1 ○ 1.0 ● 10
Frequency ● 1 kHz ○ 10 kHz ○ 100 kHz

Tunneling Current
PreAmp Gain (10th powers) ○ 8 ● 9 ○ 10
Bits 3129 Current 0.2966

Target Current (nA)	Ramp Delay (ms/bit)
0.00000	10
0.00000	10
0.00000	10
0.00000	10

Sample Bias
Bits 3162 Voltage 5.43945

Target Bias V	Ramp Delay (ms/Bit)
0.00000	10
0.00000	10
0.00000	10
0.00000	10

Step Delay
○ Freq/Feedback Dependent
● Fixed: 381 µs

Inter-Step Delay
290 µs
Velocity 3367.46 Å/s
☐ Wait for tip-spacing of: 0.50 Å
☑ Abort after 1000 tries.
Require 1 consequetive, in range values.

Inter-Line Delay
100 ms

Feedback On
☑ When Moving
☑ After Scan

Dither On
☐ Ch. 1
☐ Ch.0

Z Offset
Bits 2048 Voltage 0. Angstroms 0.
☑ Crash Protect

Crash Protection
If measured quantity is within 10.00 % of its limits,
○ Do nothing.
○ Stop scanning.
● Auto - and continue.
○ Find min/max for Z-offset and continue.

Read Sequence
Step #: 1 of 1
Read
○ On
○ Off
Delay: n/a µs
Read Ch: 1 x 20 times
Out Ch: n/a
Bits n/a Voltage n/a

apply a series of voltage or z pulses to the sample automatically. “# of Pulses” box is used to set the number of repeated pulses. “Inter Pulse Delay” is the wait time between the starting points of two adjacent pulses. Therefore, the “Inter Pulse Delay” must be larger than the pulse duration. If “# of Pulses” is not 1, a warning message “You are doing repeated pulses, continue?” will pop up when clicking the “Do it” bottom in the “Deposition” dialog. The “Stop” bottom can be used to interrupt the repeated pulses before they finish. The “Post pulse Tip movement” section determine what to do after applying repeated pulses. The software can retract the tip, auto minus, or do nothing depending on with box is clicked.

Triggering is also added to the deposition. Similar to the one in the “Spectroscopy Option”, the “Triggering” section in “Pulse Options” determines the triggering channel and logic levels. If the “Step” box and “Low” box are enabled, the triggering channel will be ramped to the low logic level before starting the repeated pulses and ramped to the high logic level after they finish. Similarly, if “High” box is enabled, the triggering channel will be ramped to high at the beginning and low at the end. If “Pulse” is enabled, a TTL pulse will be sent at the beginning or end depending on if “Start” or “End” is clicked. The “Trigger Ch.” section in “Deposition” dialog is also for manually switching the trigger channel output voltage to logic high or logic low.

The “Tip Approach” dialog is shown in Fig. B.1.5. A “Translate” function is added here. Once enabled, the feedback control box will switch from rotation mode to translation mode, allowing the sample to move left or right to compensate the sliding during tip approach. Limited by the current version of DSP codes, the sample can only move left or right. Update to the DSP code is required to enable translation to other directions.

Note that the triggering function can only operate correctly together with with the DSP code upgraded by the author.

FIG. B.1.4. Screenshots of the “Pulse Options” and “Deposition” dialogs.

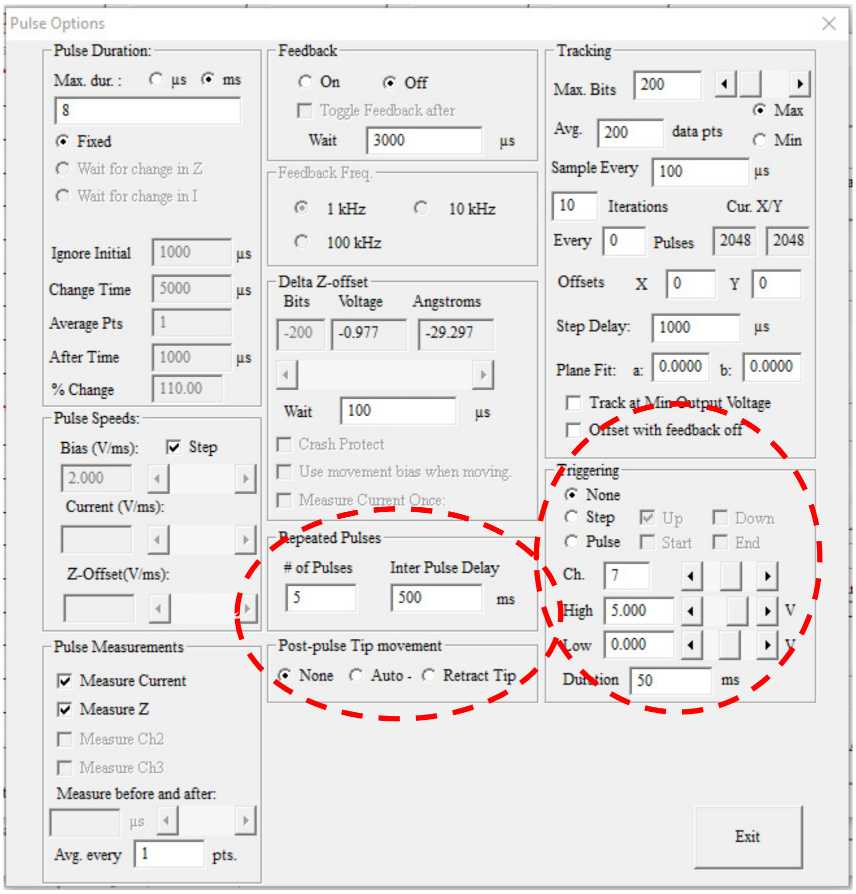
Pulse Options
Exit

Pulse Duration:
Max. dur. : ○ µs ● ms
8
● Fixed
○ Wait for change in Z
○ Wait for change in I
Ignore Initial 1000 µs
Change Time 5000 µs
Average Pts 1
After Time 1000 µs
% Change 110.00

Pulse Speeds:
Bias (V/ms): ☑ Step
2.000
Current (V/ms):
Z-Offset(V/ms):

Pulse Measurements
☑ Measure Current
☑ Measure Z
☐ Measure Ch2
☐ Measure Ch3
Measure before and after: µs
Avg. every 1 pts.

Feedback
○ On ● Off
☐ Toggle Feedback after
Wait 3000 µs

Feedback Freq.
● 1 kHz ○ 10 kHz
○ 100 kHz

Delta Z-offset
Bits -200
Voltage -0.977
Angstroms -29.297
Wait 100 µs
☐ Crash Protect
☐ Use movement bias when moving.
☐ Measure Current Once:

Repeated Pulses
# of Pulses 5
Inter Pulse Delay 500 ms

Post-pulse Tip movement
● None ○ Auto - ○ Retract Tip

Tracking
Max. Bits 200 ● Max ○ Min
Avg. 200 data pts
Sample Every 100 µs
10 Iterations
Every 0 Pulses
Cur. X/Y 2048 2048
Offsets X 0 Y 0
Step Delay: 1000 µs
Plane Fit: a: 0.0000 b: 0.0000
☐ Track at Min Output Voltage
☐ Offset with feedback off

Triggering
● None
○ Step ☑ Up ☐ Down
○ Pulse ☐ Start ☐ End
Ch. 7
High 5.000 V
Low 0.000 V
Duration 50 ms

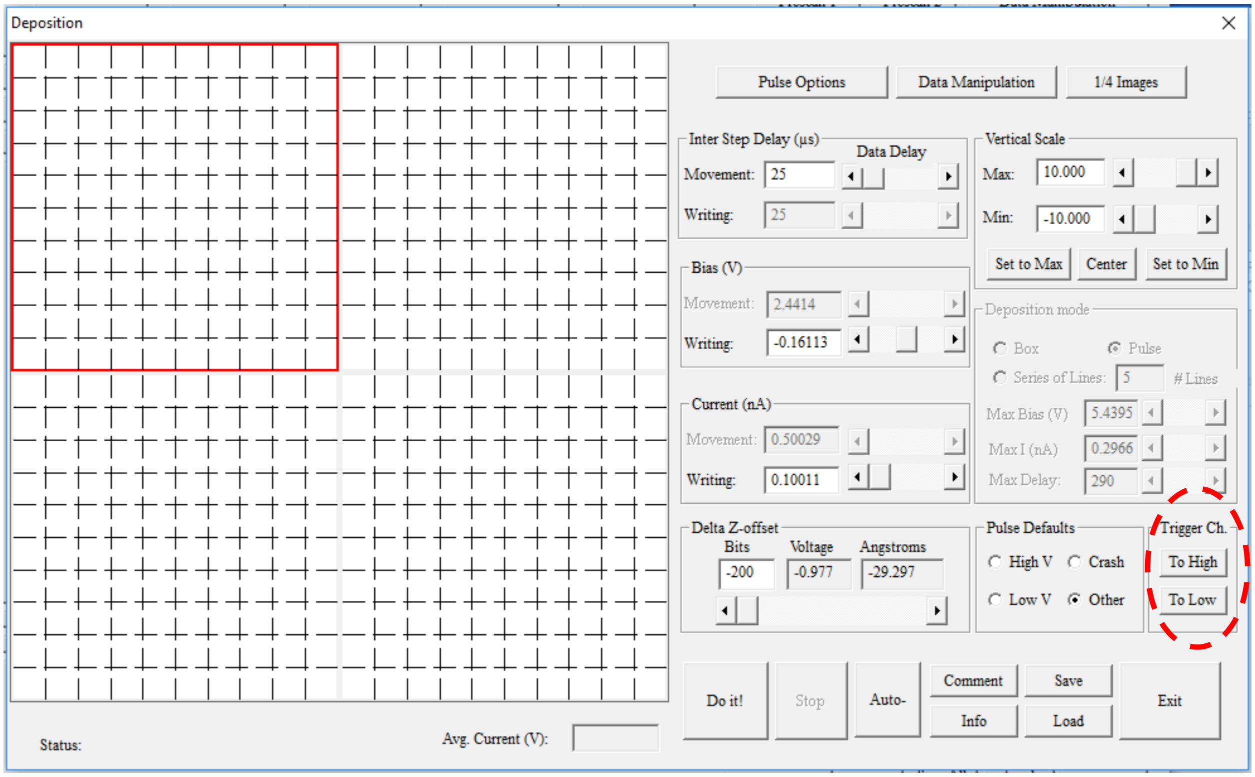
Deposition
Pulse Options
Data Manipulation
1/4 Images
Set to Max
Center
Set to Min
To High
To Low
Do it!
Stop
Auto-
Comment
Save
Info
Load
Exit

Inter Step Delay (µs) Data Delay
Movement: 25
Writing: 25

Vertical Scale
Max: 10.000
Min: -10.000

Bias (V)
Movement: 2.4414
Writing: -0.16113

Deposition mode
○ Box ● Pulse
○ Series of Lines: 5 # Lines
Max Bias (V) 5.4395
Max I (nA) 0.2966
Max Delay: 290

Current (nA)
Movement: 0.50029
Writing: 0.10011

Delta Z-offset
Bits -200
Voltage -0.977
Angstroms -29.297

Pulse Defaults
○ High V ○ Crash
○ Low V ● Other

Trigger Ch.

Status:
Avg. Current (V):

FIG. B.1.5. Screenshot of the “Tip Approach” dialog.

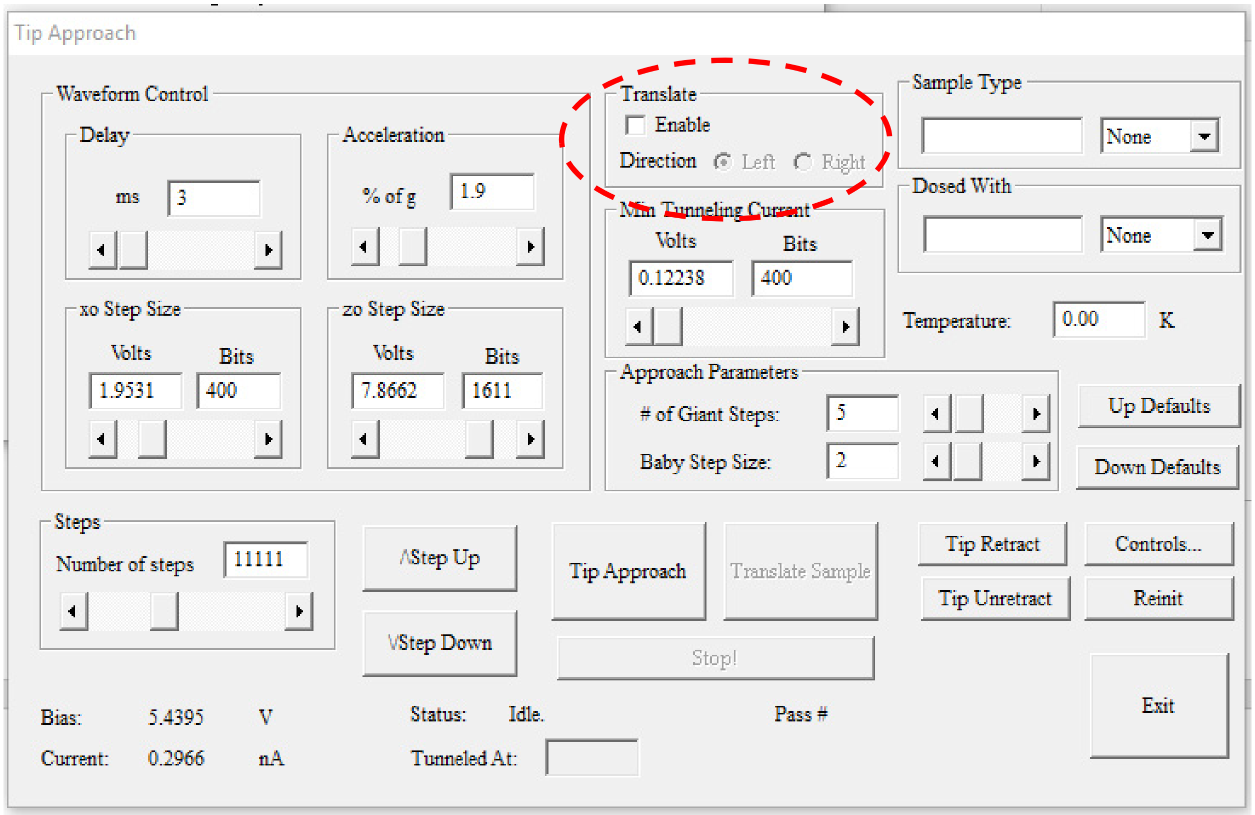
Tip Approach
Waveform Control
Delay
Acceleration
xo Step Size
zo Step Size
Translate
Sample Type
Dosed With
Min Tunneling Current
Approach Parameters
Steps
Up Defaults
Down Defaults
/\Step Up
\/Step Down
Tip Approach
Translate Sample
Stop!
Tip Retract
Tip Unretract
Controls...
Reinit
Exit

Delay: ms 3

Acceleration: % of g 1.9

xo Step Size: Volts 1.9531 Bits 400

zo Step Size: Volts 7.8662 Bits 1611

Translate: ☐ Enable

Direction ● Left ○ Right

Min Tunneling Current: Volts 0.12238 Bits 400

Sample Type: None

Dosed With: None

Temperature: 0.00 K

# of Giant Steps: 5

Baby Step Size: 2

Number of steps 11111

Bias: 5.4395 V

Current: 0.2966 nA

Status: Idle.

Pass #

Tunneled At:

B.2 LabVIEW Programs

B.2.1. Auto Annealing

Cleaning sample by ion bombardment and annealing is one of the routine tasks that every Ho group member does to acquire clean surfaces for experiments. Careful controls need to be applied for some samples which may go over irreversible phase transitions if their temperature changes too rapidly. The annealing process used to be manually controlled and the reproducibility of different annealing cycles are not guaranteed. The author automates this process using a LabVIEW controlled DC power supply (HP 6643A). This section serves as a manual of the LabVIEW program the author developed. The reader is assumed to have sufficient knowledge about the sample cleaning mechanism and procedures before using this program.

The screenshot of the LabVIEW auto-annealing program is shown in Fig. B.2.1. The left side of the front panel is the control panel where the annealing parameters can be changed. The first section "Power Supply Configurations" is used to initialize the HP 6643 power supply. The "VISA resource name" specifies the GPIB port of the power supply. If all the drivers are installed correctly and the power supply is connected to the computer, the GPIB address corresponding to the power supply should automatically show up in the drop-down menu. The "Current" and "Voltage" boxes specify the default initial output current and voltage. Since we usually run the power supply using current mode control mode, the "Voltage" need to be sufficient and the "Current" should be set as "0". The "RESET" bottom can be used to reset the power supply output to these default values. The "Protection" menu can be used to set the protection mode of the power supply. "Overvoltage protection" is usually used in the current control mode. "Overvoltage prot value" box specifies the maximum output voltage under overvoltage protection mode. Default values as shown in Fig. B.2.1 should be used for other parameters in this section.

FIG. B.2.1. Screenshot of the Auto-Annealing program.

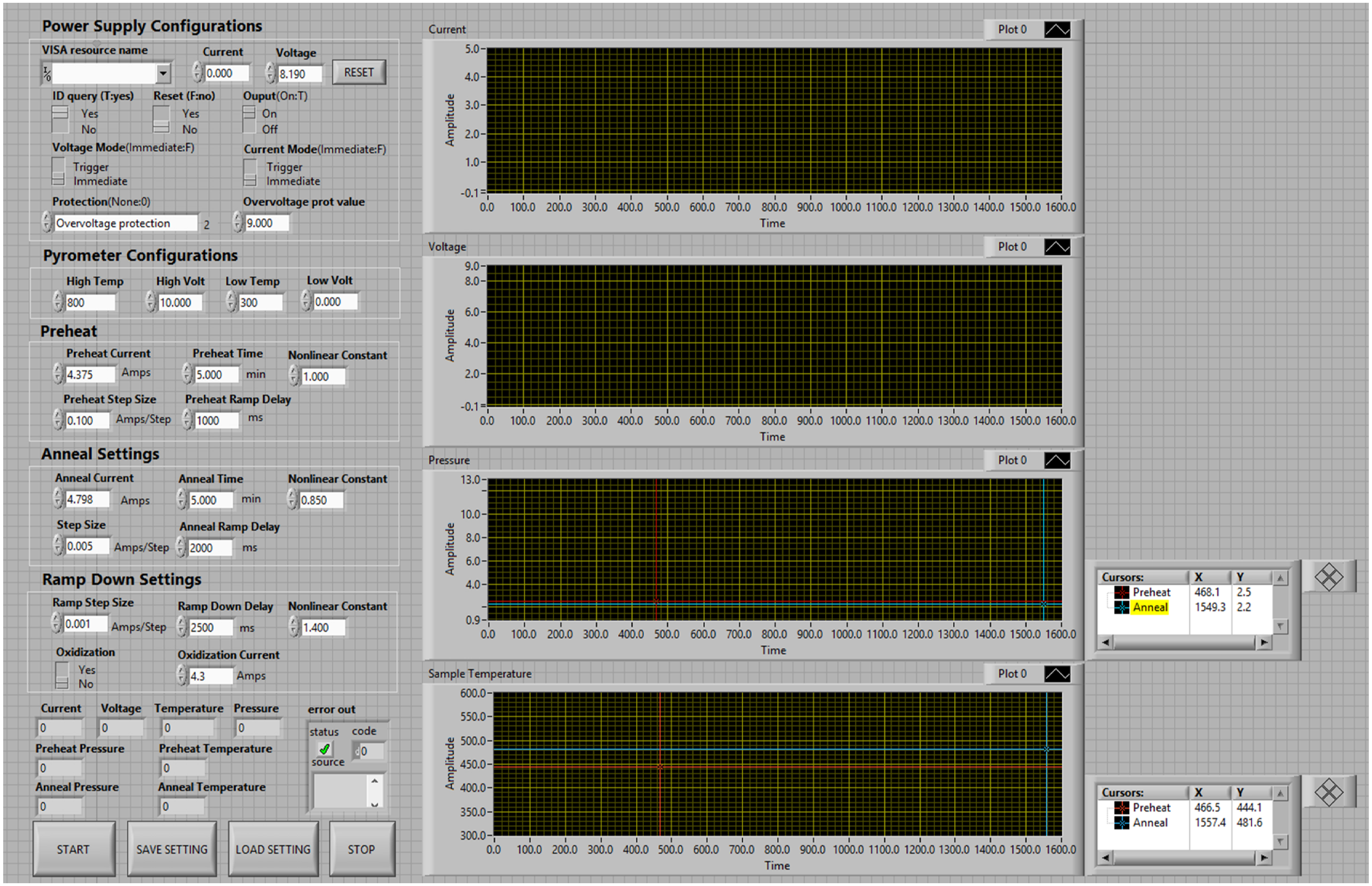
Current
Voltage
Pressure
Sample Temperature
Plot 0
Amplitude
Time
0.0
100.0
200.0
300.0
400.0
500.0
600.0
700.0
800.0
900.0
1000.0
1100.0
1200.0
1300.0
1400.0
1500.0
1600.0
5.0
4.0
3.0
2.0
1.0
-0.1
9.0
8.0
6.0
13.0
10.0
0.9
600.0
550.0
500.0
450.0
400.0
350.0
300.0
RESET
START
SAVE SETTING
LOAD SETTING
STOP

Power Supply Configurations

VISA resource name:
Current: 0.000
Voltage: 8.190
ID query (T:yes): Yes / No
Reset (F:no): Yes / No
Ouput(On:T): On / Off
Voltage Mode(Immediate:F): Trigger / Immediate
Current Mode(Immediate:F): Trigger / Immediate
Protection(None:0): Overvoltage protection 2
Overvoltage prot value: 9.000

Pyrometer Configurations

High Temp: 800
High Volt: 10.000
Low Temp: 300
Low Volt: 0.000

Preheat

Preheat Current: 4.375 Amps
Preheat Time: 5.000 min
Nonlinear Constant: 1.000
Preheat Step Size: 0.100 Amps/Step
Preheat Ramp Delay: 1000 ms

Anneal Settings

Anneal Current: 4.798 Amps
Anneal Time: 5.000 min
Nonlinear Constant: 0.850
Step Size: 0.005 Amps/Step
Anneal Ramp Delay: 2000 ms

Ramp Down Settings

Ramp Step Size: 0.001 Amps/Step
Ramp Down Delay: 2500 ms
Nonlinear Constant: 1.400
Oxidization: Yes / No
Oxidization Current: 4.3 Amps

Current: 0
Voltage: 0
Temperature: 0
Pressure: 0
Preheat Pressure: 0
Preheat Temperature: 0
Anneal Pressure: 0
Anneal Temperature: 0

error out
status ✓
code 0
source

Cursors:	X	Y
Preheat	468.1	2.5
Anneal	1549.3	2.2

Cursors:	X	Y
Preheat	466.5	444.1
Anneal	1557.4	481.6

The second section “Pyrometer Configurations” is used to input the settings configured in the pyrometer to define the slope of the linear relationship between DC output voltage (V) of and the measured temperature (T) it measures [$T = V \times (T_{High} – T_{Low})/(V_{High} – V_{Low})$]. These settings need to be exactly same as the ones set in the pyrometer.

The sample cleaning usually involves three steps: preheat, anneal, and ramp down. The parameters of each step can be set in the “Preheat Settings”, “Anneal Settings” and “Ramp Down Settings” sections respectively. The “Step Size” in each section is the current change (ΔI) at each step. The “Ramp Delay” defines the delay time between two ramping steps. When ramping up, the output current increase with step number n as $I = (n \times \Delta I)^{m}$ until the set current is reached. When ramping down, $I = (n \times \Delta I)^{m.}$ The value of m can be set in the “Nonlinear Constant” boxes. When m is larger than 1, the ramping speed decrease as n increases. When m is smaller than 1, the ramping speed decreases with n. If the “Oxidization” switched is enabled when preparing an Al_2O_3 surface, the program will stop after the output current ramps down to the value set in the “Oxidization Current”. Otherwise, the program will stop after the current ramps down to zero.

The “Current”, “Voltage”, “Temperature”, and “Pressure” indicators and windows show the live status during annealing. The “Preheat Pressure” and “Preheat Temperature” record the final pressure and temperature after preheating. The “Anneal Pressure” and “Anneal Temperature” record the final pressure and temperature after annealing. The parameters can be saved into a .INI to load later using the “Save” and “Load” bottoms.

B.2.2. Dosing Control

Dosing Control is a simple LabVIEW program that is used to monitor the chamber pressure and the temperature read by the pyrometer. It can also be used to monitor the dosage in Langmuir. The screenshot of the program is shown in Fig. B.2.2.

FIG. B.2.2. Screenshot of the Dosing Control program.

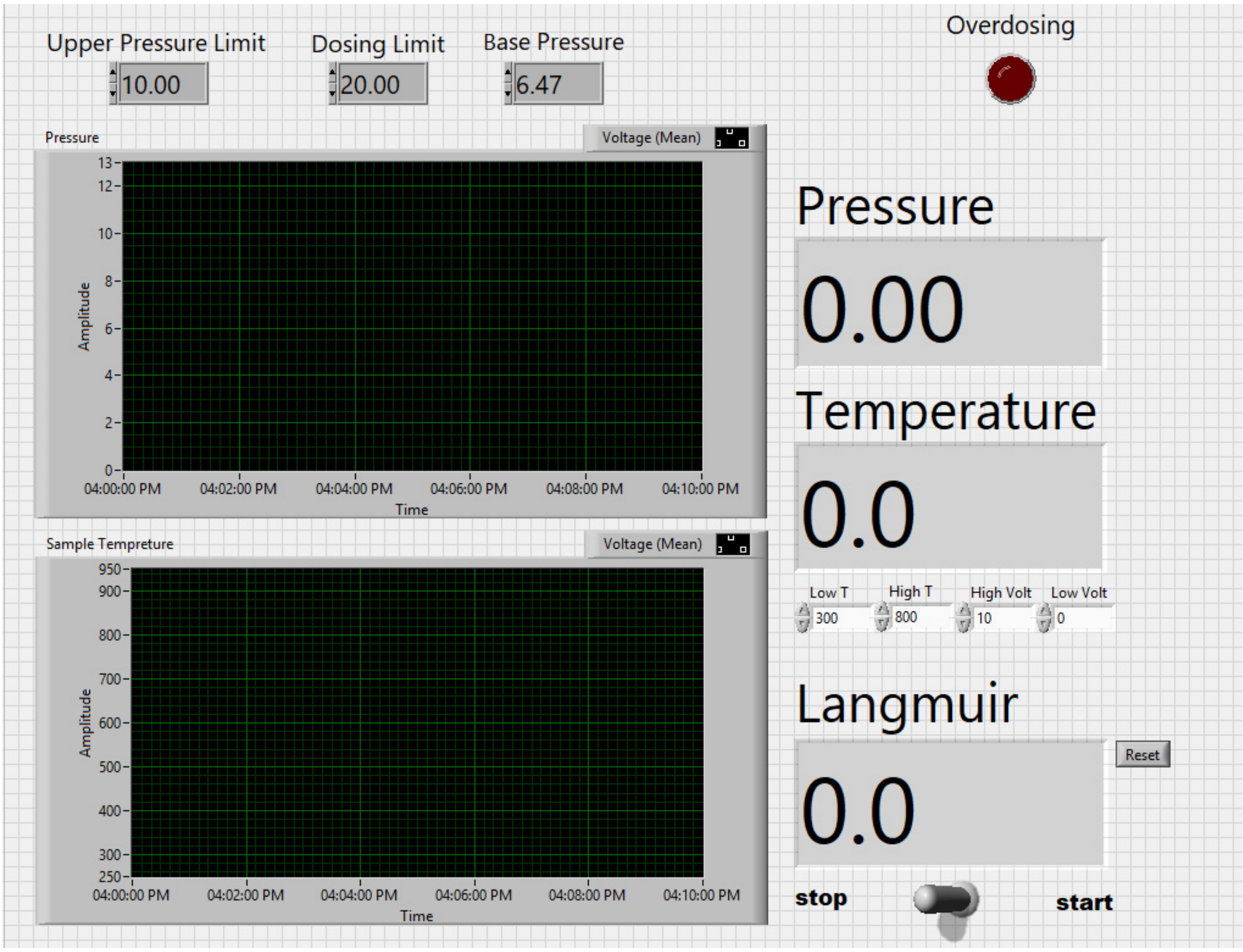
Overdosing
Pressure
Voltage (Mean)
Amplitude
13
12
10
8
6
4
2
0
04:00:00 PM
04:02:00 PM
04:04:00 PM
04:06:00 PM
04:08:00 PM
04:10:00 PM
Time
Sample Tempreture
Voltage (Mean)
Amplitude
950
900
800
700
600
500
400
300
250
04:00:00 PM
04:02:00 PM
04:04:00 PM
04:06:00 PM
04:08:00 PM
04:10:00 PM
Time
Reset
stop
start

Upper Pressure Limit 10.00

Dosing Limit 20.00

Base Pressure 6.47

Pressure 0.00

Temperature 0.0

Low T 300

High T 800

High Volt 10

Low Volt 0

Langmuir 0.0

When the program is running, the real-time pressure and pyrometer reading are displayed in the “Pressure” and “Temperature” windows and indicators. Similar to the “Pyrometer Configurations” section in the auto-annealing program, the “Low T”, “High T”, “High Volt” and “Low Volt” boxes are used to define the temperature-voltage relationship of the pyrometer output. The pressure reading only show the first three scientific digits since the analog ion gauge controller we use doesn’t output the order of the pressure reading.

The switch at the bottom of the program is used to turn on the dosage monitoring. The “Langmuir” window displays the calculated dosage base on (Pressure – Base Pressure) × Time. The “Reset” bottom is used to reset the “Langmuir” value to zero. Again, the user needs to be aware that the actual dosing among depends on the order of the dosing pressure. The base pressure needs to be manually set in the “Base Pressure” box. If the Langmuir value exceeds the value set in the “Dose Limit”, the “Overdosing” indicator will light up. A warning sound will play if the measured pressure exceeds the “Upper Pressure Limit”.

B.2.3. Fourier Transform Signal Analyzer

The Fourier Transform Signal Analyzer program can perform Fast Fourier Transform (FFT) of the DAQ. This is very useful to find out the noise frequency in the input signals. Fig. B.2.3 shows a screenshot of the program. The program reads four signals (I, Z, dI/dV and d^2I/dV^2) at the same time. The channel to perform FFT can be chosen in the “Source Channel” menu in the “Fourier Transform Settings” section. Please refer to the block diagram for the physical channels in DAQ corresponding to these signals. The window function can be chosen in the “Window” menu. The averaging mode and weighting mode can be chosen as the corresponding menus in the same section. If “No averaging” is chosen, the program will run continuously. In other average

FIG. B.2.3. Screenshot of the Fourier Transform Signal Analyzer program.

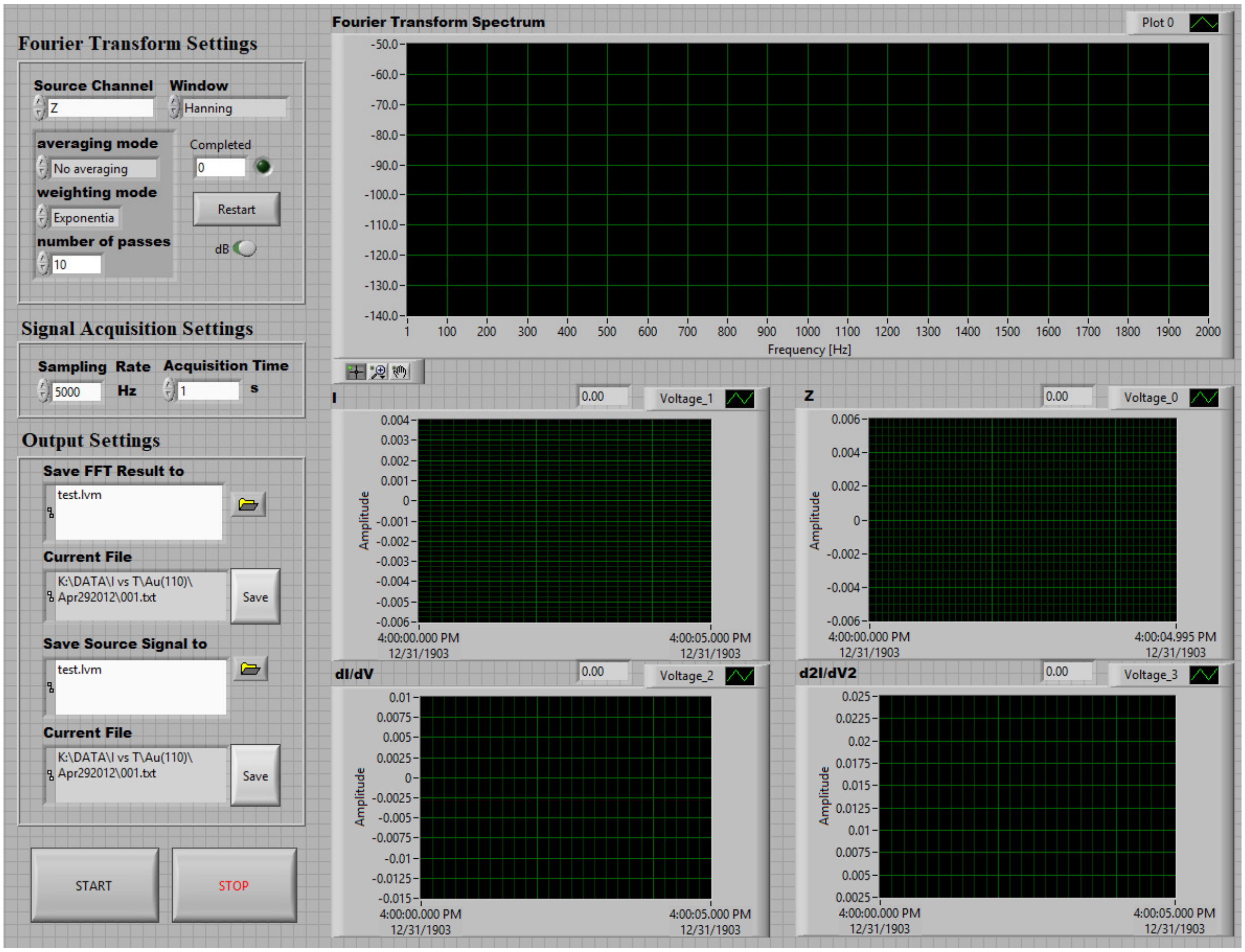

Fourier Transform Settings

Source Channel: Z
Window: Hanning
averaging mode: No averaging
weighting mode: Exponentia
number of passes: 10
Completed: 0

Signal Acquisition Settings

Sampling Rate: 5000 Hz
Acquisition Time: 1 s

Output Settings

Save FFT Result to: test.lvm
Current File: K:\DATA\I vs T\Au(110)\Apr292012\001.txt
Save Source Signal to: test.lvm
Current File: K:\DATA\I vs T\Au(110)\Apr292012\001.txt

Restart
dB
Save
Save
START
STOP
Fourier Transform Spectrum
Plot 0
-50.0
-60.0
-70.0
-80.0
-90.0
-100.0
-110.0
-120.0
-130.0
-140.0
1
100
200
300
400
500
600
700
800
900
1000
1100
1200
1300
1400
1500
1600
1700
1800
1900
2000
Frequency [Hz]
I
0.00
Voltage_1
Amplitude
0.004
0.003
0.002
0.001
0
-0.001
-0.002
-0.003
-0.004
-0.005
-0.006
4:00:00.000 PM 12/31/1903
4:00:05.000 PM 12/31/1903
Z
0.00
Voltage_0
Amplitude
0.006
0.004
0.002
0
-0.002
-0.004
-0.006
4:00:00.000 PM 12/31/1903
4:00:04.995 PM 12/31/1903
dI/dV
0.00
Voltage_2
Amplitude
0.01
0.0075
0.005
0.0025
0
-0.0025
-0.005
-0.0075
-0.01
-0.0125
-0.015
4:00:00.000 PM 12/31/1903
4:00:05.000 PM 12/31/1903
d2I/dV2
0.00
Voltage_3
Amplitude
0.025
0.0225
0.02
0.0175
0.015
0.0125
0.01
0.0075
0.005
0.0025
4:00:00.000 PM 12/31/1903
4:00:05.000 PM 12/31/1903

modes, the program will conduct several runs of measurements base on the “number of passes” and average them.The “completed” box displays the current pass number. The green indicator will light up when all the passes are completed. The “dB” switch specifies whether the results are expressed in decibels.

The “Signal Acquisition Settings” section defines the sampling rate and total acquisition time of each pass, which further define the frequency resolution and the frequency range of the FFT result. The FFT result is displayed in the “Fourier Transform Spectrum” window, the raw data of each channel are displayed in the 4 smaller windows underneath. Both the FFT result and raw input data can be saved into a .TXT file using the options in the “Output Settings” section.

B.2.4. Reaction Control

As presented in *Chapter 4* and *Chapter 5*, molecules in the tunneling junction can often be dissociated by energetic tunneling electrons. The Reaction Control program shown in Fig. B.2.4 is intended to use DAQ to apply an additional bias to the sample to induce the reaction, and automatically ramp down the bias as soon as the reaction is detected. This is very important to catch the intermediate product in a multi-step reaction.

The physical channels of DAQ corresponding to Z, I, dI/dV and d^2I/dV^2 can be set in the “Input Channels” menu. The DAQ output channel needs to be wired to the bias dither input (output channel 1) in the STM electronics. Both the physical toggle switch in electronics as well as the dither switch in STM software should be turned on.

The “DAQ Voltage” is the additional bias apply to the sample on top of the bias applied by the STM software. The bias set by STM software should be manually inputted into the “STM Voltage” box to ensure appropriate operation of the program. The “Step Size” defines the voltage change in each step during voltage ramp-up and ramp-down. The “Ramp down delay” and “Ramp up delay" define the delay time between two steps during bias ramp-down and ramp-up respectively. The "Ramp down delay" should be relatively short since we want the bias to be reduced immediately after a reaction event is detected.

A reaction event is usually detected by a change in Z (feedback on) or I (feedback off). The "Dissociation Logic" is used to define the signal change associated with the event. The options in this menu are described in the following table:

Option	Description
STD DEV BELOW THRESHOLD	The standard deviation of the detect signal drops below the threshold.
VALUE ABOVE THRESHOLD	The detect signal is higher than the threshold.
VALUE BELOW THRESHOLD	The detect signal is lower than the threshold.
VALUE CHANGED DOWNWARD BY THRESHOLD	The detect signal drops by an amount larger than the threshold.
VALUE CHANGED UPWARD BY THRESHOLD	The detect signal increase by an amount larger than the threshold.

The threshold voltage can be set in the "Threshold" box. "Reaction time" shows the time it takes to detect the reaction event. The program will also ramp down the bias and stop if a reaction event not detected with in the time set in "Time Target".

The program can output two record files if enabled. The "Notes file" records the conditions used in the experiment includes reaction time and bias. The "Time Trace file" records the raw data of the input channels acquired by DAQ.

FIG. B.2.4. Screenshot of the Reaction Control program.

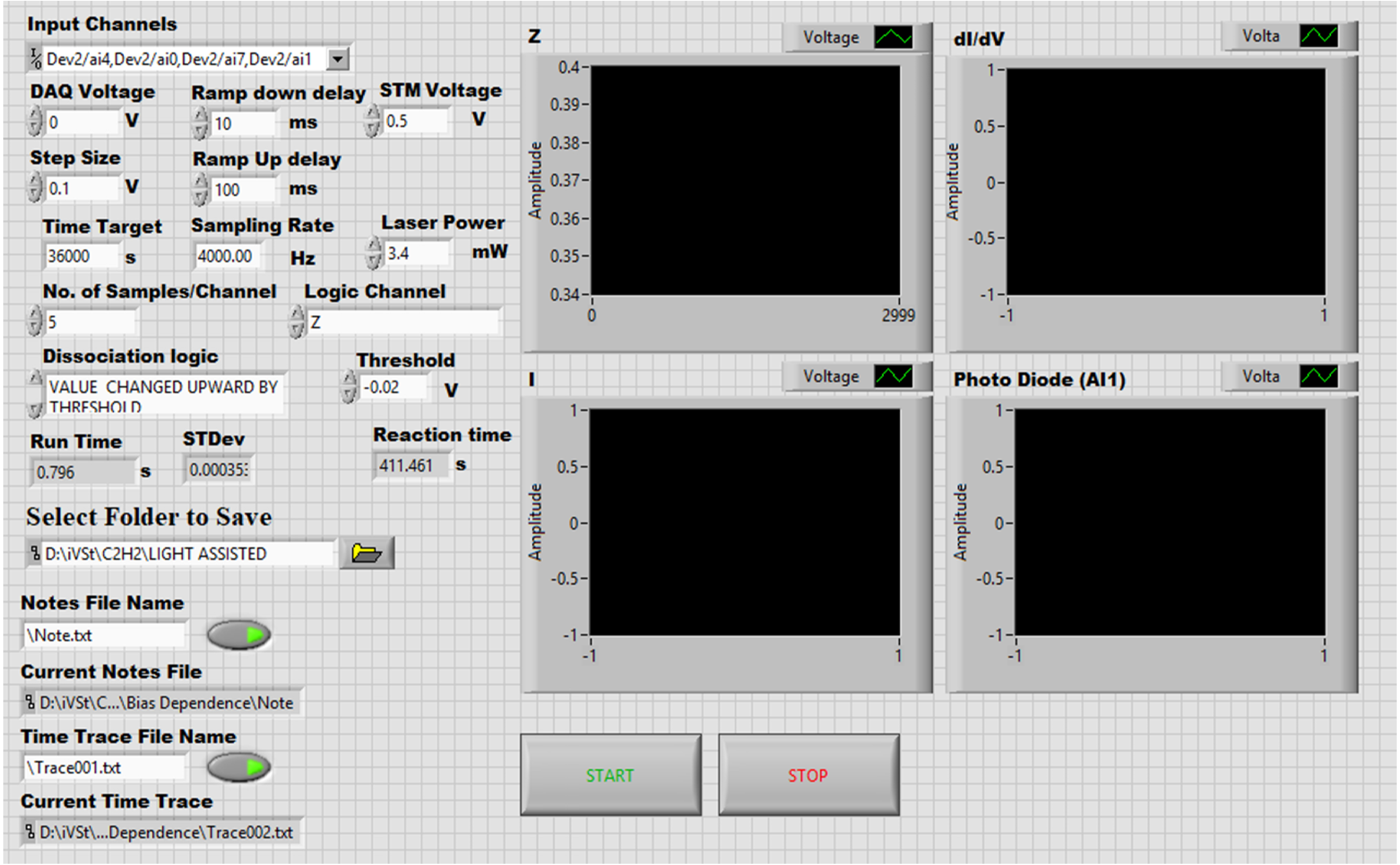

Input Channels: Dev2/ai4,Dev2/ai0,Dev2/ai7,Dev2/ai1

DAQ Voltage: 0 V

Ramp down delay: 10 ms

STM Voltage: 0.5 V

Step Size: 0.1 V

Ramp Up delay: 100 ms

Time Target: 36000 s

Sampling Rate: 4000.00 Hz

Laser Power: 3.4 mW

No. of Samples/Channel: 5

Logic Channel: Z

Dissociation logic: VALUE CHANGED UPWARD BY THRESHOLD

Threshold: -0.02 V

Run Time: 0.796 s

STDev: 0.00035:

Reaction time: 411.461 s

Select Folder to Save: D:\iVSt\C2H2\LIGHT ASSISTED

Notes File Name: \Note.txt

Current Notes File: D:\iVSt\C...\Bias Dependence\Note

Time Trace File Name: \Trace001.txt

Current Time Trace: D:\iVSt\...Dependence\Trace002.txt

Z
Voltage
Amplitude
0.4
0.39
0.38
0.37
0.36
0.35
0.34
0
2999
dI/dV
Volta
Amplitude
1
0.5
0
-0.5
-1
-1
1
I
Voltage
Amplitude
1
0.5
0
-0.5
-1
-1
1
Photo Diode (AI1)
Volta
Amplitude
1
0.5
0
-0.5
-1
-1
1
START
STOP

B.3 Combine STM and LabView Programs to Acquire and Process Data

The following section describes a few experimental measurements which require the combination of STM program and a few LabVIEW programs.

B.3.1. Bias Dependent Electron Induced Light Emission Spectra

This experiment uses the monochromator and CCD camera to measure a series of wavelength resolved spectra at different sample bias, and plot the light emission intensity at different wavelengths as a function of bias. The bias is ramp by the STM program in spectroscopy mode. At each bias, a TTL trigger is sent to the CCD controller to acquire a spectrum. The light emission spectra are then processed by a LabVIEW program.

Fig. B.3.1 shows a screenshot of a sample spectroscopy setting in STM software. The important settings are highlighted. The scan direction should be "Forward". Feedback should always be on during the measurement since we want to keep the tunneling current constant for all the spectra. Dither should be turn off for both channels. The "Each step" in the "Triggering" section and the "Step Delay" in "Pass Delay" section should both be enabled. The time set in "Pass Delay" should equal the exposure time of each CCD spectra plus 0.5 s for data transfer.

The CCD and monochromator are controlled by the Winspec program. Readers should get familiar with this program by reading the manual provided by Princeton Scientific. "Spectroscopy" mode should be chosen in the program. "Timing" should be set as "external trigger". The "number of spectra" should be same as the number of steps defined by the spectroscopy scan range and step size in the STM program.

To acquire data, users should start in the Winspec first, the CCD will then wait for the TTL signals. Within 5 s, users should start a spectroscopy measurement using the STM program. The

FIG. B.3.1. Screenshot of the spectroscopy settings for a photon intensity vs bias measurement.

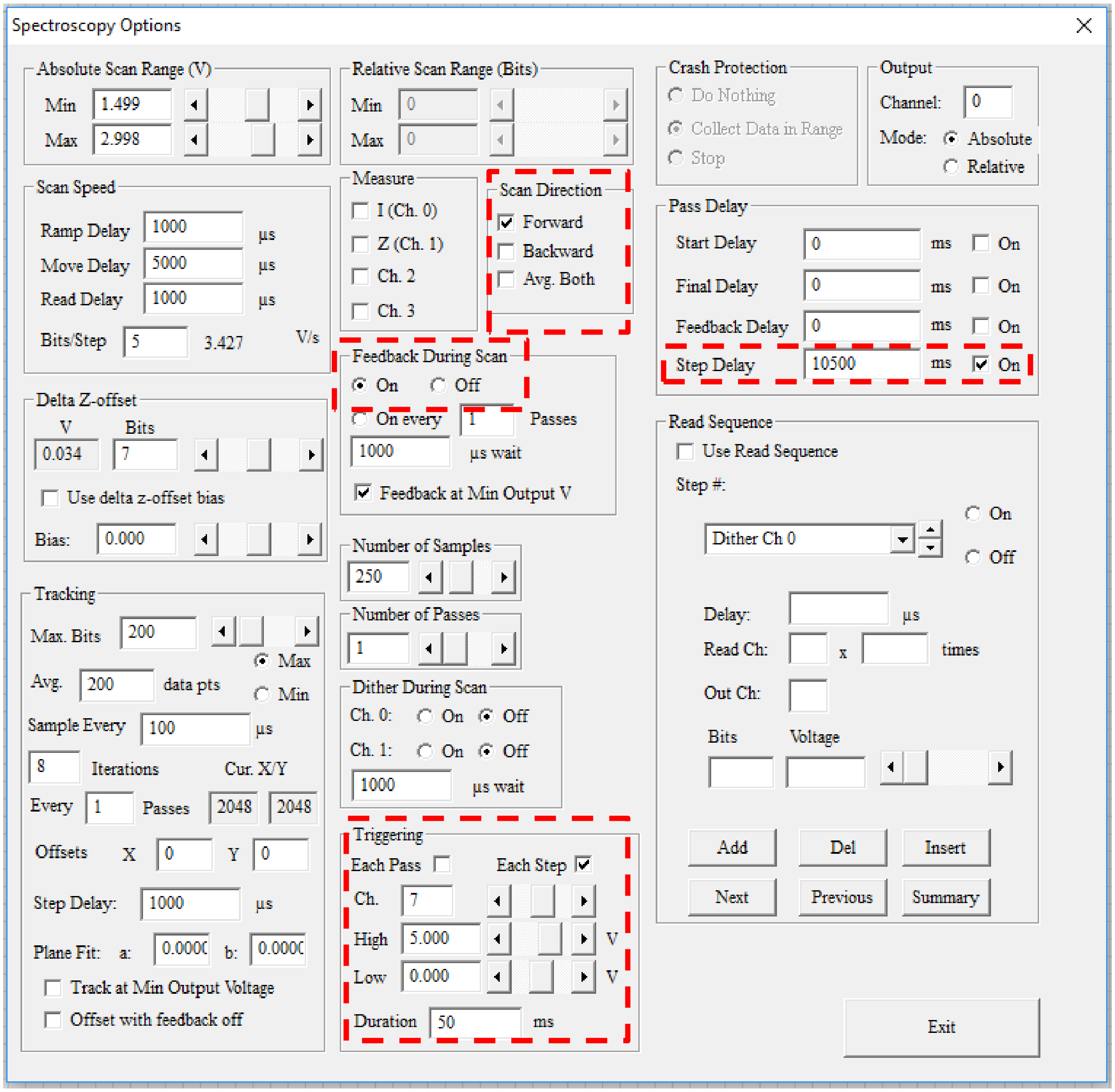

Absolute Scan Range (V)
Min 1.499
Max 2.998

Relative Scan Range (Bits)
Min 0
Max 0

Crash Protection
○ Do Nothing
● Collect Data in Range
○ Stop

Output
Channel: 0
Mode: ● Absolute ○ Relative

Scan Speed
Ramp Delay 1000 µs
Move Delay 5000 µs
Read Delay 1000 µs
Bits/Step 5 3.427 V/s

Measure
☐ I (Ch. 0)
☐ Z (Ch. 1)
☐ Ch. 2
☐ Ch. 3

Scan Direction
☑ Forward
☐ Backward
☐ Avg. Both

Pass Delay
Start Delay 0 ms ☐ On
Final Delay 0 ms ☐ On
Feedback Delay 0 ms ☐ On
Step Delay 10500 ms ☑ On

Feedback During Scan
● On ○ Off
○ On every 1 Passes
1000 µs wait
☑ Feedback at Min Output V

Delta Z-offset
V 0.034 Bits 7
☐ Use delta z-offset bias
Bias: 0.000

Number of Samples
250

Number of Passes
1

Read Sequence
☐ Use Read Sequence
Step #:
Dither Ch 0
○ On
○ Off
Delay: µs
Read Ch: x times
Out Ch:
Bits Voltage

Tracking
Max. Bits 200
● Max
Avg. 200 data pts ○ Min
Sample Every 100 µs
8 Iterations Cur. X/Y
Every 1 Passes 2048 2048
Offsets X 0 Y 0
Step Delay: 1000 µs
Plane Fit: a: 0.0000 b: 0.0000
☐ Track at Min Output Voltage
☐ Offset with feedback off

Dither During Scan
Ch. 0: ○ On ● Off
Ch. 1: ○ On ● Off
1000 µs wait

Triggering
Each Pass ☐ Each Step ☑
Ch. 7
High 5.000 V
Low 0.000 V
Duration 50 ms

STM program then will ramp the bias to the initial value and trigger the CCD to start data acquisition.

Once all the spectra are acquired, the user can convert the .SPE file into a .TXT file in ASCII format using Winspec. The output data should be in multiple columns without headers. The .TXT file can be load into the LabVIEW program shown in Fig. B.3.2. The user can use the program to process two files each time by switch the toggle switch to “2 Files” and select two different .TXT files using the bottom two file selection windows. The program will output the sum of these two spectra. Usually, the toggle switch should be at the “1 File” side and only the 1st file selection window should be used. The user needs to input the accurate wavelength range of the spectra into the “Spectra Range”, and the bias range set in the STM program into the “Bias Range”. The “Offset” and “Gain” can be used if the user wants to add a constant offset to the output spectrum or multiply the data by a constant gain. The “Activate Window” switch is used to choose which output window to display the processed spectrum. The user can set the integration range in wavelength at the bottom of each output window, or enable the “Full Range” switch to integrate the whole spectrum. The “Cosmic Ray Removal” function can be turned on to remove the sharp and tall peaks in the light emission spectra caused by cosmic rays using a simple “sigma clipping” algorithm.

The user can click the “DO IT” bottom to start processing data. The intensity vs bias spectrum of the selected wavelength should be displayed in the chosen window. The “Save” bottom under each display window can be used to output the spectrum into a .TXT file in ASCII format.

FIG. B.3.2. Screenshot of the LabVIEW program for photon intensity vs bias data processing.

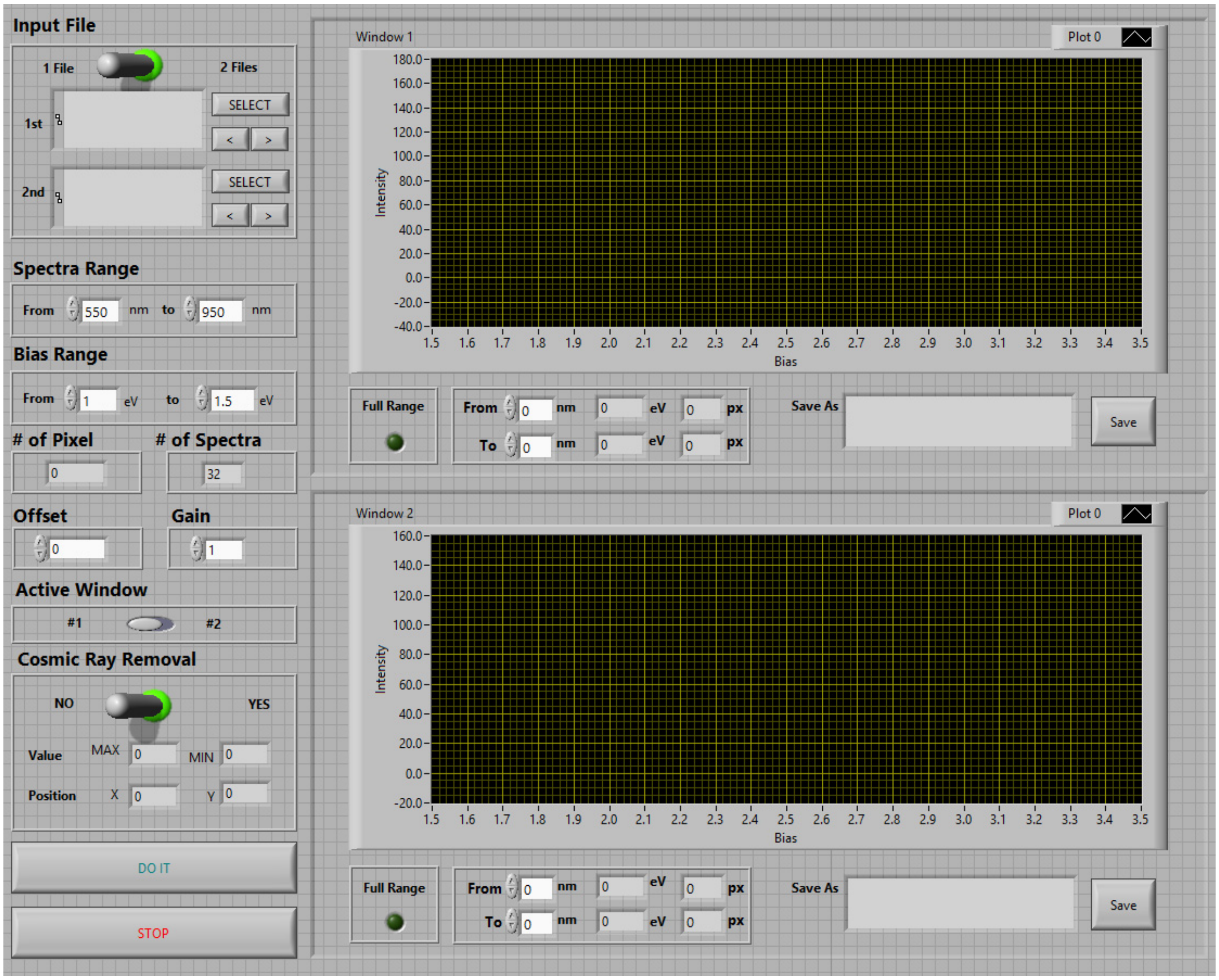
Input File
1 File
2 Files
1st
SELECT
<
>
2nd
SELECT
<
>
Active Window
#1
#2
Cosmic Ray Removal
NO
YES
DO IT
STOP
Window 1
Plot 0
Intensity
180.0
160.0
140.0
120.0
100.0
80.0
60.0
40.0
20.0
0.0
-20.0
-40.0
1.5
1.6
1.7
1.8
1.9
2.0
2.1
2.2
2.3
2.4
2.5
2.6
2.7
2.8
2.9
3.0
3.1
3.2
3.3
3.4
3.5
Bias
Full Range
Save As
Save
Window 2
Plot 0
Intensity
160.0
140.0
120.0
100.0
80.0
60.0
40.0
20.0
0.0
-20.0
1.5
1.6
1.7
1.8
1.9
2.0
2.1
2.2
2.3
2.4
2.5
2.6
2.7
2.8
2.9
3.0
3.1
3.2
3.3
3.4
3.5
Bias
Full Range
Save As
Save

Spectra Range: From 550 nm to 950 nm

Bias Range: From 1 eV to 1.5 eV

# of Pixel: 0

# of Spectra: 32

Offset: 0

Gain: 1

Cosmic Ray Removal: Value MAX 0 MIN 0; Position X 0 Y 0

Window 1: From 0 nm 0 eV 0 px; To 0 nm 0 eV 0 px

Window 2: From 0 nm 0 eV 0 px; To 0 nm 0 eV 0 px

B.3.2. Molecular Switching Rate as a Function of Sample Bias

This experiment uses a LabVIEW program to measure the switching rate of a molecule as a function of sample bias. The bias is ramped by the STM program in the spectroscopy mode. At each bias, a TTL pulse is sent to the DAQ to acquire a time trace of the molecular switching, and determine the switching rate at this bias using the measured trace.

The spectroscopy settings used in this measurement is same as the ones introduced previously in Fig. B.3.1. The trigger channel of the STM electronics should be wired with one of the digital input channels of the DAQ. In most case, we use the "Feedback on every one pass" option so the feedback will be off during ramping since we want to keep the tip-molecule distance constant for all the measurements. The switching rate can be normalized later by dividing the measured current later. The user can also turn the feedback on if the tunneling current needs to be constant throughout the measurement. The time set in "Pass Delay" should equal the length of the time trace acquire at each bias plus a few seconds for initialization and data processing.

The screenshot of the LabVIEW program screenshot used to measure the switching rate is shown in Fig. B.3.3. The "Scan Setting" section is used to specify the settings used in the STM software. This program is relatively complicated compared to the ones introduced above. Most settings in the program are fairly straight forward. The following section only focuses on the non-trivial parts of the program. The "Start Bias" and "Final Bias" should be same as the "Min" and "Max" used in the spectroscopy range settings in STM program. "Passes" should be same as the number of passes set in the STM spectroscopy options. The "Step Size" is the delta voltage between steps and depends on the "bits/step" setting in the STM software. The user needs to fine tune the "Start Bias", "Final Bias", and "Step Size" settings so that the number of data points in LabVIEW (as displayed in the "Total Pts" box) is exactly same as the number of steps in the STM

FIG. B.3.3. Screenshot of the control panel of the Switching vs Bias program.

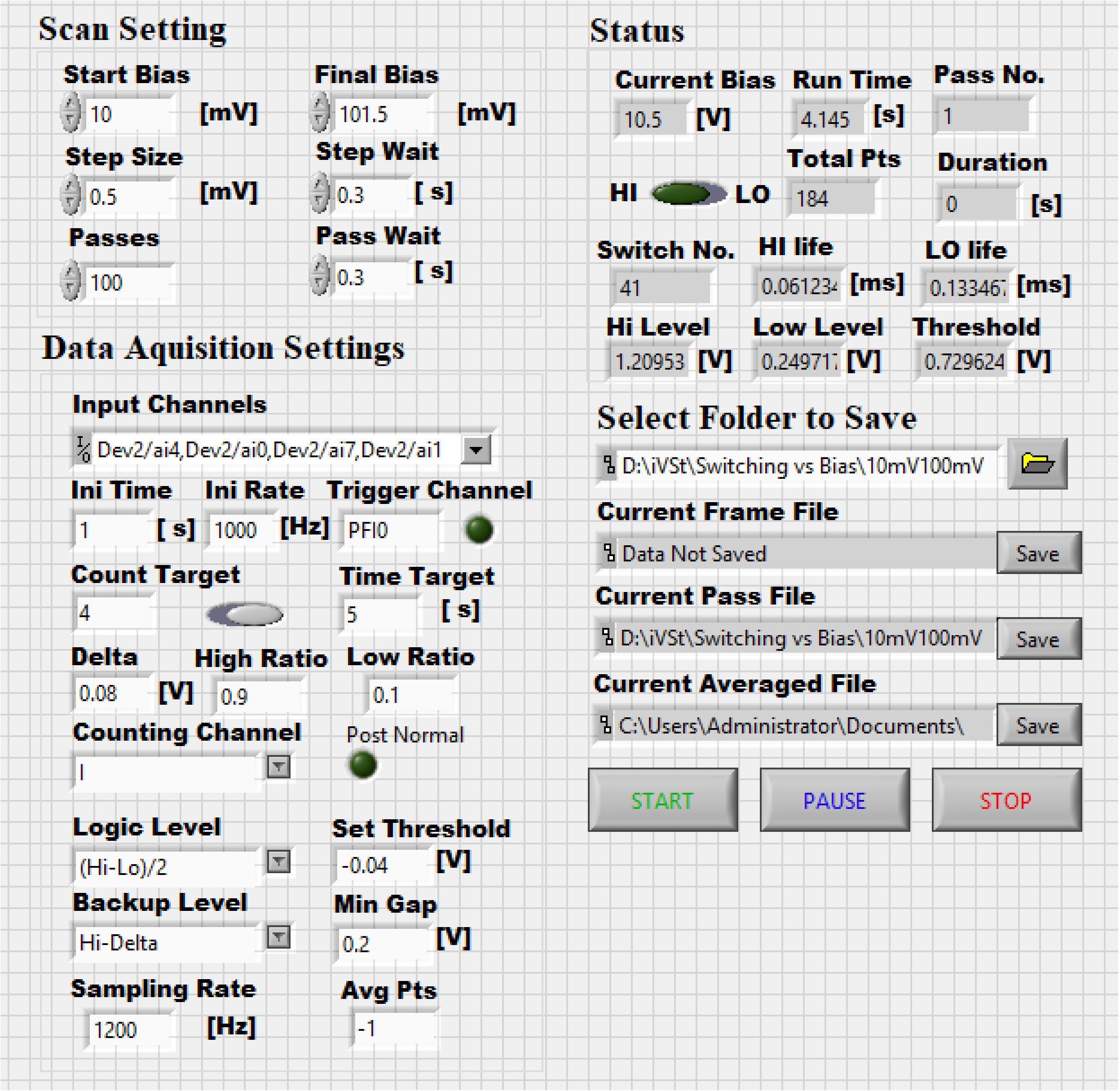

Scan Setting

Start Bias 10 [mV]
Final Bias 101.5 [mV]
Step Size 0.5 [mV]
Step Wait 0.3 [s]
Passes 100
Pass Wait 0.3 [s]

Data Aquisition Settings

Input Channels Dev2/ai4,Dev2/ai0,Dev2/ai7,Dev2/ai1
Ini Time 1 [s]
Ini Rate 1000 [Hz]
Trigger Channel PFI0
Count Target 4
Time Target 5 [s]
Delta 0.08 [V]
High Ratio 0.9
Low Ratio 0.1
Counting Channel I
Post Normal
Logic Level (Hi-Lo)/2
Set Threshold -0.04 [V]
Backup Level Hi-Delta
Min Gap 0.2 [V]
Sampling Rate 1200 [Hz]
Avg Pts -1

Status

Current Bias 10.5 [V]
Run Time 4.145 [s]
Pass No. 1
HI LO
Total Pts 184
Duration 0 [s]
Switch No. 41
HI life 0.06123 [ms]
LO life 0.13346 [ms]
Hi Level 1.20953 [V]
Low Level 0.24971 [V]
Threshold 0.729624 [V]

Select Folder to Save

D:\iVSt\Switching vs Bias\10mV100mV

Current Frame File Data Not Saved
Current Pass File D:\iVSt\Switching vs Bias\10mV100mV
Current Averaged File C:\Users\Administrator\Documents\

program. The “Step Wait” is the extra wait time the LabVIEW program will wait between steps. The “Pass Wait” define the delay time before each pass.

The “Data Acquisition Settings” defines the settings used in the LabVIEW program to acquire the time trace and determine the switching rate. “Input Channels” menu is used to specify the DAQ physical channels corresponding to the I, Z, dI/dV and d^2I/dV^2. If the slide switch is at the “Count Target” side, the program will record data until the number of switching events is reached. If the switch is at the “Time Target” side, the program will stop after a fixed time length at each bias. The “Trigger Channel” is the DAQ physical channel used to receive TTL pulse from the STM electronics. The LED switch next to this box needs to be enabled, otherwise, the program will run continuously without synchronizing with the STM software. The “Sampling Rate” and “Avg Pts” defines DAQ sampling rate and how many adjacent data points should be averaged.

Other settings in this section define how the program counts the switching. The “Counting Channel” specify the signal channel that will be used to detect the switching. A switching event is defined as the detected signal changes from high level to low level or the other way. The “High Ratio” and “Low Ratio” define the percentile point of the sorted input data which defines the high and low states voltage levels. If the “Post Normal” bottom is not enabled, the program will take a separated length of time trace defined by the “Ini Time” and “Ini Rate” boxes to determine high and low voltage levels. If “Post Normal is disabled”, the program will determine the high and low levels using the time trace recorded in the previous step. The “Logic Level” defines how to determine the voltage threshold of a switching event. The descriptions of “Logic Level” and “Back Level” can be found in the following table:

Logic Level	**Description**	**Backup Channels**
Hi-Delta	The high state voltage level – “Delta”	N/A
Lo+Delta	The low state voltage level + “Delta”	N/A
(Hi+Lo)/2	The average of high state and low state voltage levels	If the Hi-Lo is smaller than the “Min Gap”, a Backup Channel will be used
Set Threshold	A value set in “Set Threshold” box	N/A
Previous Step	Use the average of high and low levels determined using the previous time trace	If the threshold voltage is smaller than the “Min Gap”, a “Backup Level” will be used
dx/dt	Use the number of peaks in the time derivative of the signal with a higher peak value than the “Set Threshold”	N/A
(dx/dt)/x	Use the number of peaks in time derivative divided by the signal amplitude with a higher peak value than the “Set Threshold”	N/A

The once the program is running, the real-time status including the bias, time, pass number etc. will be displayed in the “Status” section. The acquired data will also be displayed on the windows at the right-hand side of the program. The data can be saved into .TXT files using the settings in “Select Folder to Save” section. The “Frame File” records the time trace of the selected channel at each bias step of each pass. The “Pass” file records the switching count as a function of bias for at each pass. The “Averaged” file records the final averaged switching rate as a function of bias after all passes are finished. The “Select Folder to Save” box is used to choose the folder where all files will be saved to.

B.3.3. Molecular Switching Rate as a Function of Delay Time

This experiment uses a LabVIEW program to control the Newport UTM100PP stepping motor to measure the switching rate of a molecule as a function of laser pulse delay. In this measurement, the tip is park over the molecule with tracking function turned on using the STM program. The LabVIEW ramps the delay and records the time trace at each delay time to determine the switching rate. This program uses the same method as introduced in section B.3.2. to determine switching rate from time trace. This section focuses on the details of how this program can be used to control the delay time.

The screenshot of the sections concerns the delay control of the "Switching vs Delay" LabVIEW program is shown in Fig. B.3.4. The stepping resolution, display unit and GPIB address of the stepping motor can be set in the "Motion Controller Settings". Please remember that "resolution" setting will not change the actual resolution of the stepping motor, which is defined by the minimum step size. It only changes conversion ratio used by the controller so that the program can be used with different stepping motor with different step resolution. For the UTM100PP stepping motor we use, the resolution setting should always be 0.1 um. The "display unit" can be used to change the unit displayed by the stepping motor controller.

The "Delay Scan Setting" sections concern the range and wait time used in a delay scan. The range of the scan is defined by the "Start Step" and "Final Step". The unit used here is the step encoder. The corresponding delay time will be automatically displayed in the "Start Delay Time" and "End Delay Time" boxes. The "Set Point" defines the encoder number the stepping motor moves to before and after each scan. The "Ini Wait" box defines how long the program waits at the set point before start ramping the delay. The number of passes and the wait time between two passes can be set in the "Passes" and "Pass Wait" boxes respectively. The "Step Wait" defines the

FIG. B.3.4. Screenshot of the delay scan settings in the Switching vs Delay program.

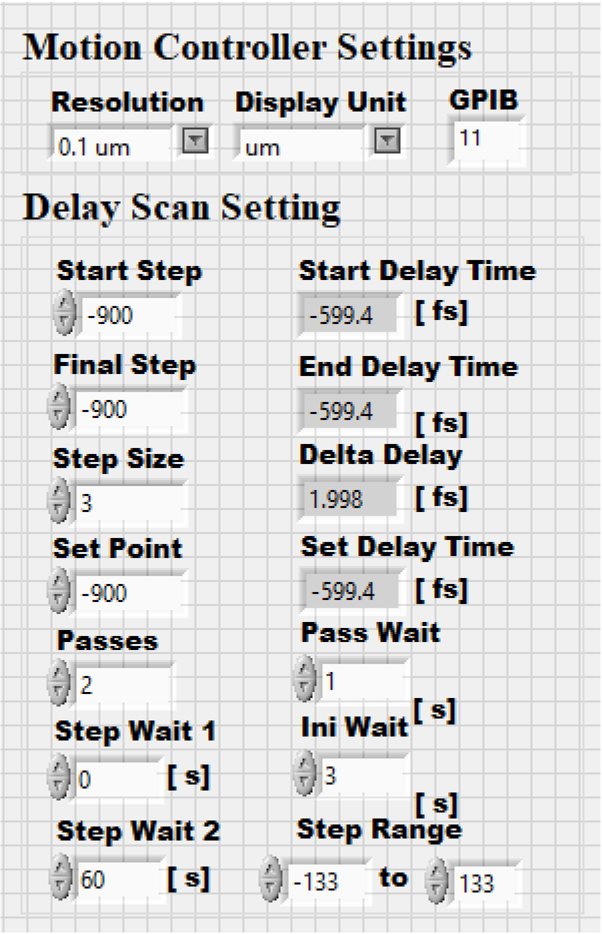

Motion Controller Settings

Resolution: 0.1 um

Display Unit: um

GPIB: 11

Delay Scan Setting

Start Step: -900

Start Delay Time: -599.4 [fs]

Final Step: -900

End Delay Time: -599.4 [fs]

Step Size: 3

Delta Delay: 1.998 [fs]

Set Point: -900

Set Delay Time: -599.4 [fs]

Passes: 2

Pass Wait: 1 [s]

Step Wait 1: 0 [s]

Ini Wait: 3 [s]

Step Wait 2: 60 [s]

Step Range: -133 to 133

wait time between two adjacent delay steps. Usually, we need to wait for a longer time to let the junction stabilize when two beams are temporally overlapping. This can be done by using the “Step Wait 2”. The range where longer wait time should be used can be set in the “Step Range” boxes.

B.3.4. Spatially Resolved Molecular Switching Rate Imaging

Spectrally resolved switching rate images could be obtained by synchronizing the LabVIEW and the STM. The STM imaging sequence is configured in a way that it will set out a TTL pulse to the DAQ at each image pixel. The LabVIEW will record a time trace at each location and determine the switching rate to construct an image. The following table shows a sample sequence used in the STM program:

Sequence	Operation	Description
1	Wait 381 (step delay)	
2	Read Ch.1, average 10 times	Read Z
3	Wait 1000	
4	Read Ch.0, average 10 times	Read current
5	Wait 1000	
6	Step Ch.7 to 5.000 volts	Ramp trigger channel to high
7	Wait 5000000	Wait for the LabVIEW to acquire data
8	Step Ch. 7 to 0.000 volts	Ramp trigger channel to low
9	Wait 1500000	Additional time for the LabVIEW to process data

The screenshot of the control panel of the LabVIEW program is shown in Fig. B.3.5. Most of the settings here are same as the ones shown in Fig. B.3.2. The “Time Target” should be same as the wait time used in sequence #7 set in the STM software. The sum of “Ini Time” and “Step Wait” need to be shorter than the wait time used in sequence #9. The “Step Point” specifies the

FIG. B.3.5. Screenshot of the control panel of the Switching Mapping program.

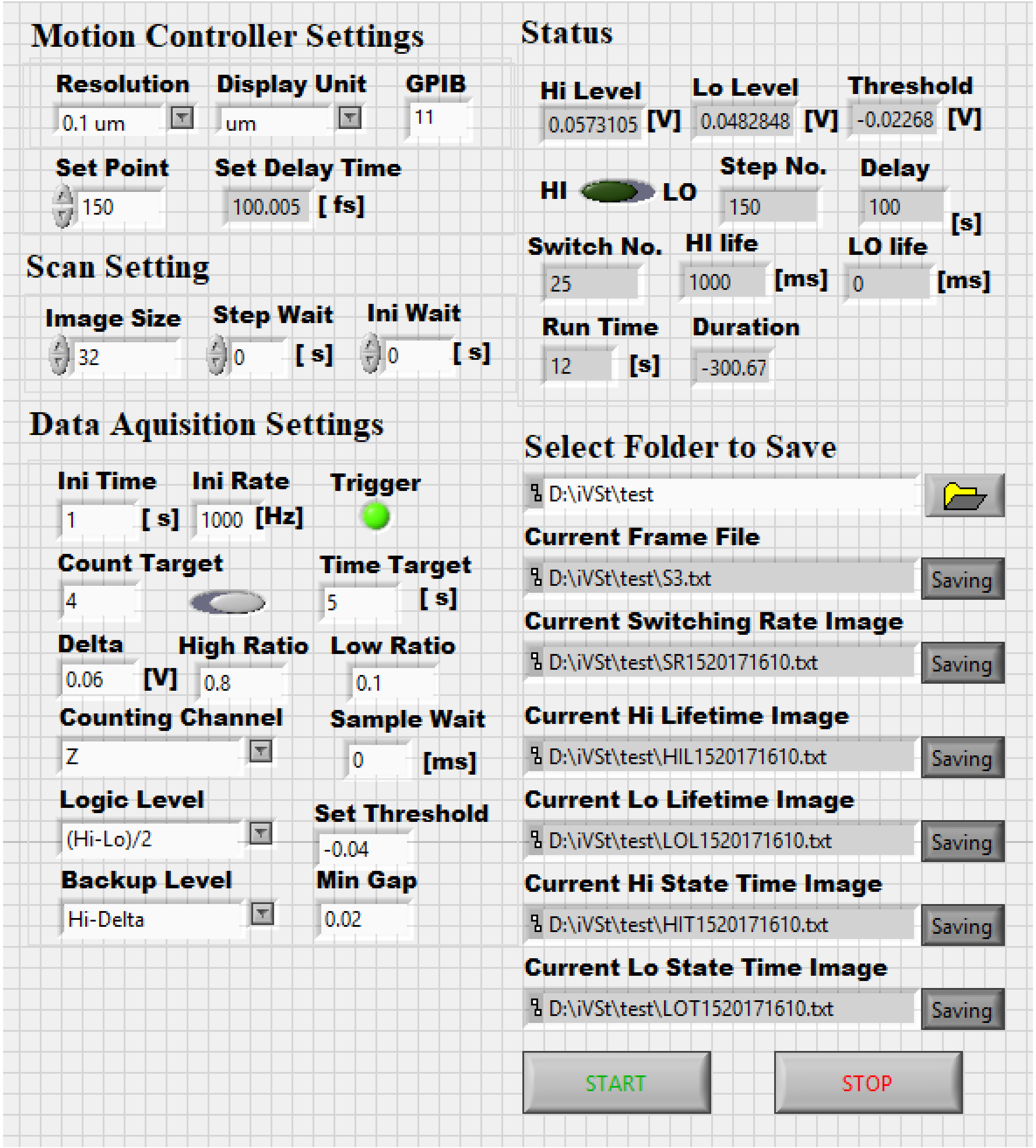

Motion Controller Settings

Resolution 0.1 um

Display Unit um

GPIB 11

Set Point 150

Set Delay Time 100.005 [fs]

Scan Setting

Image Size 32

Step Wait 0 [s]

Ini Wait 0 [s]

Data Aquisition Settings

Ini Time 1 [s]

Ini Rate 1000 [Hz]

Trigger ●

Count Target 4

Time Target 5 [s]

Delta 0.06 [V]

High Ratio 0.8

Low Ratio 0.1

Counting Channel Z

Sample Wait 0 [ms]

Logic Level (Hi-Lo)/2

Set Threshold -0.04

Backup Level Hi-Delta

Min Gap 0.02

Status

Hi Level 0.0573105 [V]

Lo Level 0.0482848 [V]

Threshold -0.02268 [V]

HI ● **LO**

Step No. 150

Delay 100 [s]

Switch No. 25

HI life 1000 [ms]

LO life 0 [ms]

Run Time 12 [s]

Duration -300.67

Select Folder to Save

D:\iVSt\test

Current Frame File

D:\iVSt\test\S3.txt

Current Switching Rate Image

D:\iVSt\test\SR1520171610.txt

Current Hi Lifetime Image

D:\iVSt\test\HIL1520171610.txt

Current Lo Lifetime Image

D:\iVSt\test\LOL1520171610.txt

Current Hi State Time Image

D:\iVSt\test\HIT1520171610.txt

Current Lo State Time Image

D:\iVSt\test\LOT1520171610.txt

stepping motor position which determines the pulse delay time used during the imaging. The "Image Size" in "Scan Setting" should be same as the image resolution used in the STM program.

The program can generate five images at the same time, which are the images of switching rate, dwell time of the high state, dwell time of the low state, the total time the molecule spent in the high state and total time the molecule spent in the low state. All the images are also displayed at the right-hand side of the program during the measurement.